EPFL

Ferroelectric Effects Probed by in situ Transmission Electron Microscopy

■ École
polytechnique
fédérale
de Lausanne

2022

Acknowledgments

My greatest and foremost gratitude is given to Professor Vasiliki Tileli, who has guided me through the PhD studies. I have learned a lot from her, especially the way, how to think about the scientific challenges from unique yet rigid point of view. When a PhD student inevitably gets lost in the scientific fog, she will nudge him/her in to the right direction. Additionally, I want to thank Professor Dragan Damjanovic without whom this PhD endeavor in Switzerland would not be possible as it was he, who introduced me to Prof. Tileli and vice versa. He has given a lot of great ideas during our meetings and has also directly influenced these PhD thesis and publications. The conversations with him are always enlightening.

Whenever something went south with the electron microscopes, there was always someone from CIME to rescue me. Therefore, CIME team and especially director of CIME Dr. Marco Cantoni is greatly appreciated. He picked up phone even on Sundays, when the focused ion beam machine usually starts to misbehave.

Huge thanks to my current and former lab colleagues: Tzu-Hsien, Jan, Robin, Michele, Morgan, Saltanat, Pierpaolo, Martina, Jing, My, Nikos, Junjie. All of you create jolly yet scientific atmosphere in the lab. Special thanks to Morgan and Robin, who kindly help with French translations, when in need.

Nothing would be possible without my parents - Irēna and Ivars. They always encouraged me to go one step beyond and try my best. Additionally, I want to thank my sister Gunda and brother Viesturs, when in doubt, their advice was much appreciated.

Unmeasurable gratitude goes to my dear Līga, whose patience with me during these last PhD steps has been enormous. You bring the greatest joy and happiness.

<div align="right">Reinis Ignatans</div>

Lausanne, Switzerland, 2022

Résumé

Les oxides de pérovskite ferroélectriques sont largement utilisés dans des capteurs, des actionneurs et des modulateurs optiques et, dans le même temps, ils sont prometteurs pour être implémentés dans de futures applications comme le stockage d'énergie ou des dispositifs de mémoire et de refroidissement. Aux balbutiements de la découverte des ferroélectriques polycristallins, le $BaTiO_3$ était considéré comme un candidat pour diverses applications, mais la découverte capitale pour la commercialisation des ferroélectriques arriva en 1952 quand le système de solution solide ferroélectrique $PbZrO_3 - PbTiO_3$ (PZT) fut découvert. Le PZT et d'autres oxides de pérovskite contenant du plomb sont restés au premier plan des intérêts scientifiques et industriels. Cependant, des inquiétudes relatives aux dangers environnementaux et pour la santé posées par ces matériaux toxiques dans les équipements électroniques et électriques ont induits un changement de législation. De nos jours, tous les produits concernés en Europe doivent être en conformité avec la directive RoHS (*Restriction of Hazardous Substances*, aussi connu comme Directive 2002/95/EC). Ce changement dans les standards industriels a alimenté une nouvelle fois la recherche dans les matériaux ferroélectriques sans plomb. L'attention est actuellement portée sur les matériaux à base de $BaTiO_3$, $BaZrO_3$, $(Na/K)NbO_3$, $Na_{1/2}Bi_{1/2}TiO_3$. Comme leurs propriétés physiques sont faibles comparées au PZT, leurs applications à large échelle est encore à réaliser. La miniaturisation des pérovskites polaires, pour lesquelles les effets à l'échelle nano- et microscopique deviennent dominants, inhibant ainsi leur performance, posent encore des défis considérables.

Dans cette thèse, l'une des pérovskites ferroélectriques sans plomb les plus connues, le $BaTiO_3$, est étudiée par des techniques de microscopie électronique en transmission (MET) combinées avec un contrôle *in situ* de la température et du champ électrique. En détail, une préparation fiable à la sonde ionique focalisée d'échantillons pour des polarisations électriques *in situ* en MET pour des ferroélectriques est établie. La méthode est testée sur du $BaTiO_3$ à température ambiante, pour lequel la réponse électrique est observée aux valeurs de champ attendues, et confirmée par des calculs d'éléments finis. Les zones des domaines (polarisation) – les boucles de polarisation électrique appliquées sont directement mesurées, révélant un fort attachement à faibles champs, tandis que des champs plus forts décrochent les murs des domaines, permettant des mouvements plus libres suivant la loi de Rayleigh.

En augmentant la température, le BaTiO$_3$ manifeste des transformations morphologiques dans ses structures de domaines, d'un état ferroélectrique 180° (proche de la température ambiante) à un état ferroélastique 90° (en-dessous de la température de Curie). Des expériences de polarisation électrique de domaines en aiguille ferroélastique montrent deux mécanismes différents de croissance vers l'avant. Dans un cas, les domaines en aiguille sont montrés bougeant librement, influencés principalement par des potentiels ressemblant à ceux de Peierls, tandis que quand des domaines perpendiculaires se rencontrent, leurs mouvements sont entravés par de forts attachements entre domaines arbitrés par des champs électromécanique. Dans ce dernier cas, des boucles P-E de forme carrée sont produites, avec des marches distinctes, qui indiquent des sauts de Barkhausen.

Finalement, l'effet des transitions de phase ferroélectrique sur la structure électronique est étudié avec de la spectroscopie de perte d'énergie des électrons (EELS, sigle pour *electron energy loss spectroscopy*) *in situ* et des calculs de théorie de la fonctionnelle de la densité (DFT, sigle pour *density functional theory*). Les mesures des pertes des couches internes par EELS montrent que les changements dans l'état électronique 3d du Ti sont qualitativement en accord avec les calculs DFT. Les mesures EELS à faible perte effectuée en dehors de l'axe permettent des mesures précises de la bande interdite dans toutes les phases. Des méthodologies de traitement expérimental et de traitement de données personnalisées sont développées pour extraire les fonctions diélectriques déterminées par le moment, qui montrent des résultats en adéquation avec ceux calculés par DFT à petit transfert de moment. Une voie pour étudier les pérovskites déficientes en oxygène avec la EELS est théoriquement démontrée avec la DFT.

Mots-clés : ferroélectriques, BaTiO$_3$, sonde ionique focalisée, microscopie électronique en transmission *in situ*, polarisation électrique, transitions de phase, mouvement de domaines, spectroscopie de perte d'énergie des électrons, densité d'états électroniques, théorie de la fonctionnelle de la densité.

Abstract

Ferroelectric perovskite oxides are widely used in sensors, actuators and optical modulators and, at the same time, they show promise for implementation in future applications such as energy storage, memory and cooling devices. At the infancy of the discovery of polycrystalline ferroelectrics, $BaTiO_3$ was considered as a candidate for various applications, but the breakthrough for the commercialization of ferroelectrics came in 1952 when the ferroelectric $PbZrO_3$ - $PbTiO_3$ (PZT) solid solution system was discovered. PZT and other lead containing perovskite oxides remained on the forefront of scientific and industrial interest. However, concerns over the environmental and health hazards posed by these toxic materials in the electronic and electrical equipment created a legislation change. Nowadays, all applicable products in the EU must pass RoHS (Restriction of Hazardous Substances also known as Directive 2002/95/EC) compliance. This change in the industrial standards fueled research in lead-free ferroelectric materials once again. Attention is currently placed on materials based on $BaTiO_3$, $BaZrO_3$, $(Na/K)NbO_3$, $Na_{1/2}Bi_{1/2}TiO_3$. Their widespread application is yet to be realized as their physical properties pale in comparison to PZT. Substantial challenges also lie in the miniaturization of polar perovskites where effects at nano and microscopic scales become dominant, which inhibit their performance.

In this thesis one of the most prominent lead-free ferroelectric perovskites $BaTiO_3$ is studied by transmission electron microscopy (TEM) techniques in combination with *in situ* temperature and electric field control. In detail, a reliable focused ion beam sample preparation for *in situ* TEM electrical biasing for ferroelectrics is established. The method is tested on $BaTiO_3$ at room temperature, where the electrical response is observed at the expected field values, further confirmed by finite element calculations. Domain area (polarization) - applied bias loops are directly measured revealing strong pinning at lower fields, while higher fields depin domain walls allowing for more free movement following Rayleigh's law.

Upon increasing the temperature, $BaTiO_3$ exhibits morphological transformations in its domain structure from ferroelectric 180° (close to room temperature) to ferroelastic 90° state (below the curie temperature). Electrical biasing experiments of ferroelastic needle domains show two different forward growth mechanisms. In one case, the needle domains are shown to move freely, influenced mainly by Peierls-like

potentials, while when perpendicular domains meet, their movement is hindered by strong domain-domain pinning mediated by electromechanical fields. The latter one produces square shaped P-E like loops with distinct steps, indicative of Barkhausen pulses.

Finally, the effect of ferroelectric phase transition on the electronic structure is studied with *in situ* electron energy loss spectroscopy (EELS) and density functional theory (DFT) calculations. Core-loss EELS measurements show that changes in the Ti 3d states qualitatively agree with DFT calculations. Off-axis low-loss EELS allows precise bandgap measurements in both phases. Custom experimental and data treatment methodologies are developed to retrieve momentum resolved dielectric functions, which show excellent fit with DFT calculated ones at small momentum transfer. A pathway to study oxygen deficient perovskites with EELS is theoretically demonstrated with DFT.

Keywords: ferroelectrics, $BaTiO_3$, focused ion beam, *in situ* transmission electron microscopy, biasing, phase transitions, domain motion, electron energy-loss spectroscopy, density of states, density functional theory.

Contents

1 Introduction

Ferroelectricity was discovered by Joseph Valasek in 1920 with a subsequent publication in 1921, which has a historic statement that the dielectric displacement $\mathbf{D}$, electric intensity $\mathbf{E}$, and the polarization $\mathbf{P}$ in Rochelle salt is analogous to magnetic flux $\mathbf{B}$, magnetic field $\mathbf{H}$, and magnetization $\mathbf{I}$ (nowadays the symbol $\mathbf{M}$ is more prominent) in the case of magnetism [1]. However, speculations on the existence of ferroelectricity can be dated back to 1912, when Erwin Schrödinger used German word *"ferroelektrisch"* in context of possible substances with spontaneous polarization [2].

Analogous to ferromagnetic materials, ferroelectrics are defined by the appearance of a spontaneous dielectric polarization $\mathbf{P_s}$, that is, a ferroelectric crystal exhibits an electric dipole moment even in the absence of an external electric field [3].

The second ever ferroelectric material was potassium dihydrogen phosphate (KDP) and it was discovered in 1935 by Paul Scherrer and Georg Busch [2, 4], which indicates some difficulties in identification of ferroelectrics at that time.

Considerable breakthrough was made by Arthur R. von Hippel in 1946 with the discovery of ferroelectricity in $BaTiO_3$ [2, 5]. $BaTiO_3$ was the first commercial ferroelectric material that directed research to explore perovskite type oxides (ABO_3, where A and B are positively charged metal cations and O is oxygen anion). This led to the discovery of the famous $PbZrO_3$ - $PbTiO_3$ (PZT) solid solution system in 1952 [6]. PZT was developed at the Tokyo Institute of Technology with a large input of Gen Shirane.

Discovery of robust oxide based ferroelectrics led to various practical applications. Ferroelectrics, compared to normal dielectric materials, exhibit large relative dielectric constant. For instance, the dielectric constant of $BaTiO_3$ based materials at room temperature can be several thousands, whereas for conventional dielectric materials it is in the one to two digit range. Large dielectric response enables ferroelectrics to be used in the energy storage applications as well as in high performance/small form factor capacitor manufacturing [7]. If the material is ferroelectric, by definition it must be also piezoelectric, meaning that the deformation of such material generates surface charges. The opposite is also true where application of electric potential on the surfaces of a ferroelectric induces macroscopic deformation. For this reason, ferroelectrics are used as sensors, transducers and actuators [7]. Excellent high fre-

quency response of oxide based ferroelectrics enables their usage in the ultrasonic acoustics. The applications ranges from medical ultrasonic imaging to sonar devices for various sea vessels [7]. Spontaneous polarization is associated with the breakage of the inversion symmetry within the material, which leads to anisotropic and non-linear optical phenomena to appear in ferroelectrics [7]. Ferroelectrics are associeted with optical second harmonic generation and electro-optical properties. A famous example is lanthanum doped PZT (PLZT), which is used as ultra-fast (response in the range of ~ 10 ns) electro-optical light switch [7, 8].

Highly tunable PZT is still considered to be best suited for various sensors, actu-ators and transducers utilizing ferroelectric effects [9]. On the other hand, $BaTiO_3$ is widely used in research as a model ferroelectric due to its simple chemical compo-sition and rich phase diagram (three ferroelectric phases and one paraelectric phase) [10]. Many of the phenomena and the associated physical models found in $BaTiO_3$ can be projected to other, more complex ferroelectric perovskite oxides.

A turning point in the field of ferroelectrics was the European Union's directive of "Restriction of Hazardous Substances" (RoHS), which came into force in 2000's [9, 11]. As PZT contains lead, it falls under the class of hazardous materials, but at that time (and even now) PZT was exempt from this directive as there simply were no alternatives for it. RoHS reignited scientists to study materials beyond PZT and its derivatives. However, up to this date, no system or material has come close to fulfilling all the high standards set by PZT. [6, 9]. Nevertheless, lead-free ferroelectrics start to find the niche applications in high temperature and high power applications [12].

Lead-free ferroelectrics similarly to PZT are designed as solid solutions, which is necessary in order to tune the desired physical properties. The most prominent components in them are barium titanate, barium zirconate, sodium-bismuth titanate ($Na_{1/2}Bi_{1/2}TiO_3$) and potassium/sodium niobate. Formation of binary, tertiary and sometimes even quaternary systems complicates the interpretation of the observed effects due to the induced chemical disorder and highly sensitive phase diagrams [12, 13]. Rejuvenated interest in the lead-free ferroelectrics has also motivated researchers to perform fundamental studies with modern experimental techniques on the plain components of the lead-free materials. For example, it was understood that previous limitations of the experimental methods mis-characterized $Na_{1/2}Bi_{1/2}TiO_3$. As it turns out, native ground state of this material contains at least two crystallographic phases (there are still discussions on exactly which symmetries describe them), while one distinct phase is only possible after the material has been subjected to the electric field [14]. Such findings are enabled by modern equipment and facilities. Precise and accurate characterization of the lead-free solid solution's components is crucial in the design of more complicated systems. This example illustrates the need for modern fundamental research of even "simple" ferroelectrics, especially important are *in situ* (temperature and electric field) studies of them, which shed light on

the internal processes at operating conditions. Control of the material's properties with temperature and electric field is relevant for the possible future applications such as silicon compatible ferroelectric memories (based on the ferroelectric HfO_2 - ZrO_2 system), neuromorphic computing, as well as the still unrealized dream of the practical electro-caloric refrigeration devices [2, 15, 16].

Transmission electron microscopy (TEM) in combination with *in situ* temperature and electric field control offers a platform for imaging and characterization capabilities from microscopic to atomic scale. Versatility of modern TEM instrumentation permits not only imaging, but also usage of the electrons as a probe in generating secondary signals, which enable characterization of the chemical constituents, bonding and electronic structure.

In this thesis a TEM sample preparation method is developed, which is suitable for silicon based micro electro-mechanical (MEMS) *in situ* heating and biasing systems. The viability of the method is demonstrated in probing the classical ferroelectric $BaTiO_3$ at different stimuli.

In detail, **chapter 2** introduces the fundamental physical concepts of the ferroelectrics followed by the specifics of $BaTiO_3$. Additionally, contrast origins at various TEM imaging length-scales and imaging modes is discussed. Finally, a discussion on various *in situ* TEM biasing and heating methods used for ferroelectrics is given.

Chapter 3 provides information on the experimental and theoretical methods utilized in this thesis. First, I introduce the *in situ* TEM heating and biasing system used in the experiments, followed by the description of the generalized sample preparation method and the theoretical electrostatic characterization of the system using finite elements method. Transmission electron microscopy imaging modes and electron-matter interactions are also discussed, with special emphasis on the electron energy loss spectroscopy. Experimental considerations, concepts behind the spectra formation and description of density functional theoretical methods used to calculate electron energy loss spectra of $BaTiO_3$ are also provided.

Chapter 4 demonstrates the viability of the *in situ* sample preparation method by analyzing the temperature and field induced effects in $BaTiO_3$. The experimental results are discussed in combination with finite element calculations. The results reveal that biasing of the $BaTiO_3$ at room temperature leads to strong pinning of the domain walls at low electric fields and weak domain wall pinning at high fields.

Chapter 5 details the results of simultaneous heating and biasing of $BaTiO_3$. Heating of $BaTiO_3$ TEM specimen introduces domain wall morphological transformation from 180° to 90° state. Biasing of 90° needle domains at non-ambient conditions reveals a new manifestation of Barkhausen noise, which hinders polarization switching and is responsible for so called crackles. Interestingly, the mechanism involves strong mutual domain-domain interactions.

Chapter 6 is dedicated to the electron energy loss spectroscopy of cubic and tetragonal $BaTiO_3$. Differences in the core loss spectra are analyzed with simple

point charge model describing distortions of the oxygen octahedra. Additionally, more involved first principle calculations are used to model the spectra. Theoretically calculated spectra are compared to the experimental ones, revealing the impact of the density of states. Low loss electron energy loss spectroscopy is used to measure the bandgap of cubic and tetragonal $BaTiO_3$ and aids in retrieving the dielectric function in wide energy range (0 - 100 eV). Custom methodologies and measurements are developed to retrieve the dielectric function in non-optical regime (with momentum transfer).

Chapter 7 summarizes the results achieved herein and suggests future prospects and possibilities of the *in situ* TEM methods for ferroelectrics.

2 Background

This chapter introduces key physical aspects to aid the understanding of the properties of ferroelectric materials and more specifically barium titanate. A discussion on various TEM imaging modes followed by a small review of the most relevant *in situ* transmission electron microscopy (TEM) techniques for ferroelectrics is also given.

2.1 Ferroelectric state and the structural changes

A ferroelectric materials are defined by the appearance of a spontaneous dielectric polarization $\mathbf{P_s}$ [17]. Usually for a ferroelectric phase F there exists a "parent" phase G with a higher symmetry, which is not ferroelectric. From the group-theoretical stand point it can be written like this:

$$F \subset G, \tag{1}$$

where group G contains symmetry elements of the non-ferroelectric (paraelectric) "parent" phase and F contains symmetry elements of the ferroelectric phase. Therefore, F is a subgroup of G [17]. A characteristic trait of the ferroelectric group F is the lack of inversion symmetry, which is present in the group G. Although such notion seems subtle, it implies the possibility to use second-order phase transition to describe the evolution between states F and G. For a second-order phase transition the first derivatives of the Gibbs free energy $[G(T, P, E, N)$, where T is temperature, P is pressure, E is electrical field and N - number of moles] are continuous, which reduces the complexity of the analysis.

Group-theoretical description of the ferroelectric/paraelectric state and the phase transition between them is abstract and rather general. To better illustrate the differences between the ferroelectric and paraelectric states, it is useful to inspect the ferroelectric materials from an atomistic point of view. The spontaneous dipole moment implies a physical separation of positive and negative charge center of masses. In general, in solid materials this can be achieved by two distinct phase transition mechanisms - order-disorder and displacive.

2.1.1 Order-disorder mechanism
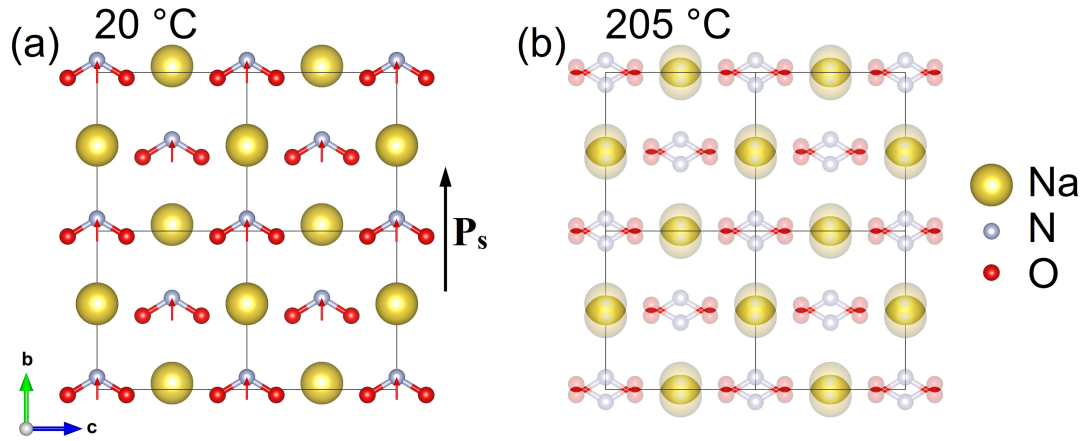
Figure 2.1: Crystallographic models of NaNO₂ at two different temperatures. (a) Ordered - ferroelectric - phase at 20 °C characterized by asymmetric NO_2 units pointing in the same direction, small red arrows show dipole moment associated within each NO_2 unit, black arrow indicates net spontaneous polarization. (b) Disordered - paraelectric - phase at 205 °C. Thermally activated atomic jumps between equilibria positions are depicted with semi-transparency. At this temperature NO_2 units do not have preferred direction, therefore there is zero net spontaneous polarization.

If the atoms controlling the symmetry change at the transition perform thermally activated jumps between two or more equilibria positions, the transition is classified as order-disorder type [17]. A prototypical material exhibiting order-disorder phase transition to a ferroelectric state is sodium nitrite ($NaNO_2$), Fig. 2.1 [17–19]. Ferroelectricity in $NaNO_2$ originates from the asymmetric NO_2 units due to the bent NO_2 molecule. From an ionic point of view, oxygen ions are negatively charged while the nitrogen ion is positively charged, due to the non-180° angle between O-N-O bonds, an electric dipole moment emerges in a NO_2 molecule. At room temperature NO_2 molecules align themselves in the crystal as seen in Fig. 2.1(a), in turn giving rise to a macroscopic spontaneous polarization.

If the temperature is increased, the phase transition occurs at 163 °C, leading to a high temperature paraelectric phase. Now the NO_2 molecules become thermally activated and lose their preferential direction, meaning that NO_2 units stochastically "flip" between up and down equilibria positions as schematically shown in Fig. 2.1(b). Although each NO_2 molecule retains its dipole moment, their lack of ordering prohibits the emergence of macroscopic spontaneous polarization.

When the transition is analyzed from the symmetry considerations, the ferroelectric state F is characterized by the space group Nr. 44 (*Im2m*), but the paraelectric state G with the space group Nr. 71 (*Immm*). Indeed, group-subgroup relation

holds, as the difference betwen F and G is the transformation from simple two-fold rotation axis along **b** in a ferroelectric state to two-fold rotation axis with addition of inversion center (a mirror plane) in the paraelectric state [17, 20]. It may seem counter-intuitive, but the disordered paraelectric phase has higher symmetry.
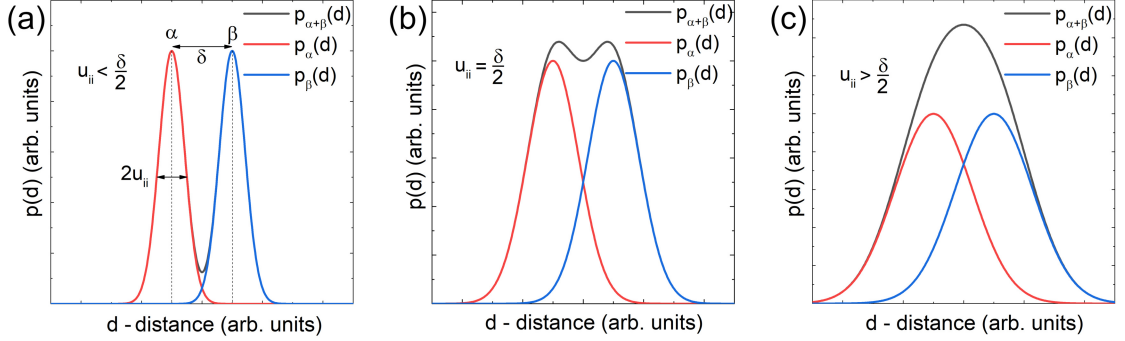
Figure 2.2: Schematic representation of probability density of two atoms separated by distance δ assuming disordered high temperature phase with different thermal displacement parameters. (a) Thermal displacements are small and two distinct positions α and β are resolved, which is characteristic of true disordered phase. (b) Larger thermal displacements, limit-case of disordered phase, positions α and β are almost unresolvable. (c) Large thermal displacements, assumption of two distinct positions α and β is not valid, this case corresponds to displacive mechanism.

A quantitative distinction of the order-disorder and displacive mechanisms follows from the analysis of the atomic thermal motion. When the high temperature disordered phase is considered, a single atom occupies two positions (α and β) separated by a distance δ in a unit cell, where atoms stochastically hop in-between the two positions. At each position an atom experiences natural thermal motion characterized by temperature dependent root-mean-squared atomic displacement parameter u_{ii} (usually measured in nm or Å). The probability density $p(d)$ of finding an atom around its mean position is characterized with a Gaussian distribution having full width at half maximum (FWHM) of $2u_{ii}$, Fig. 2.2(a).

If root-mean-squared displacement is smaller than half of the separation distance, then two positions of a single atom [$p_\alpha(d)$ and $p_\beta(d)$] can be distinguished as shown in Fig. 2.2(a). That is, if:

$$u_{ii} < \frac{\delta}{2}, \tag{2}$$

then the high temperature phase is disordered and the phase transition is order-disorder type [18, 21].

Figure 2.2(b) represents the boundary case $u_{ii} = \delta/2$, in which case the thermal motion is large and it is almost impossible to distinguish two distinct positions since the total probability density of finding an atom at some point [$p_{\alpha+\beta}(d)$] has only a

small dimple.

Finally, if:

$$u_{ii} > \frac{\delta}{2},$$ (3)

it is unreasonable to assume two separate atomic positions and hopping in-between them, as effectively there exists only a single atomic position with probability density $p_{\alpha+\beta}(d)$ - see Fig. 2.2(c). This case corresponds to displacive transition mechanism since the atom has moved from one distinct position to another within the unit cell and does not exhibit thermally activated jumps [18, 21].

2.1.2   Displacive mechanism

Traditionally, the phase transitions in $BaTiO_3$ are attributed to displacive mechanism, Fig. 2.3 [17]. The spontaneous polarization in $BaTiO_3$ originates from anti-parallel displacement of the oxygen atoms with respect to the central titanium atom. Assuming an ionic model, oxygen ions have -2 charge, while barium and titanium
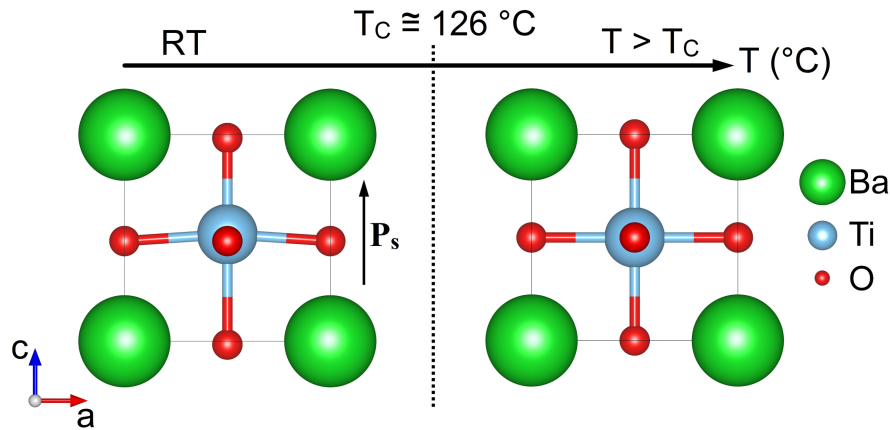
Figure 2.3: BaTiO₃ crystallographic models at room temperature (RT) and T > T$_C$. RT phase is associated with titanium and oxygen atom anti-parallel displacement along **c** axis giving rise to spontaneous polarization and tetragonal unit cell. Upon temperature increase, atoms move towards high symmetry points and at T $\cong$ 126 °C phase transition to high temperature - highly symmetric cubic phase occurs. There are no polar cubic space groups, therefore spontaneous polarization is lost.

ions have positive charges of +2 and +4 respectively. As seen in Fig. 2.3, in room temperature, oxygen ions are displaced anti-parallel **c** axis, whereas titanium ions are displaced along the **c** axis. Therefore positive and negative charge centres of masses do not coincide (barium ions are not considered to be ferro-active, although they also show displacement with respect to high symmetry parent phase) giving rise to electric dipole moment within the unit cell and macroscopic spontaneous polarization.

An increase in temperature leads to phase transition at the Curie temperature (T_C) to the cubic phase, in which spontaneous polarization is lost as the atoms reside in highly symmetric positions. The space groups of tetragonal and cubic phases are *P4mm* and *Pm3m* respectively, therefore the group-subgroup relation is fulfilled.
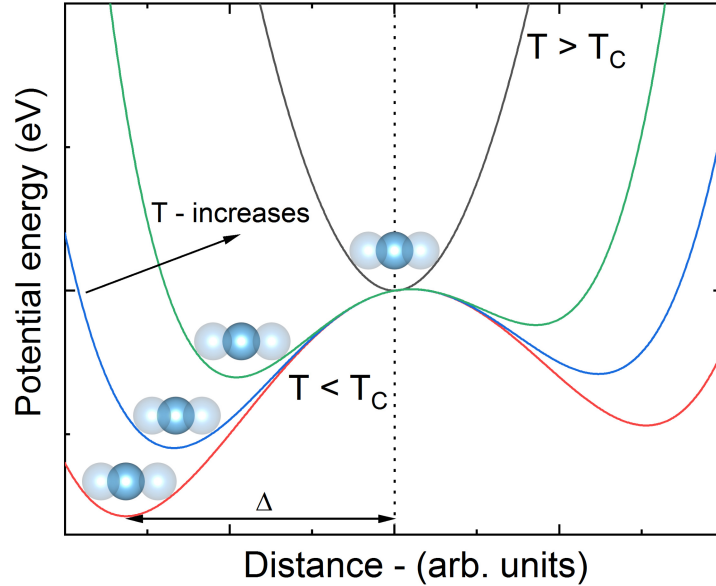
Figure 2.4: Schematic representation of the evolution of Ti potential well with respect to the temperature increase. At $T < T_C$ potential well has two minima, the distance between global minimum and high symmetry point is depicted with Δ. As T increases, Δ decreases, at $T > T_C$ Ti atom oscillates around central high symmetry point (indicated by the dashed line) and the potential well has a single minimum.

Physically, the symmetry change at the transition is controlled by displacements of bottoms of the potential wells, where the atoms oscillate as shown in Fig. 2.4 [17]. As the temperature increases, the minimum of the potential well, where Ti ions reside, moves closer to the high symmetry point. It is noted that Ti displacement at room temperature is small: $\Delta \sim 0.07$ Å, however, its impact on the overall macroscopic properties of the material is substantial.

Additionally, ferroelectric phase transitions are not reconstructive, that is bonds between atoms do not break [17]. Here both order-disorder and displacive mechanisms are represented as two distinct possibilities. However, in reality, it is probably more correct to think of them as boundary cases of a continuous spectrum. Hence, a real ferroelectric phase transformation falls somewhere closer to the order-disorder or displacive region (there are also suggestions on true mixed regime). It has been shown, that traditional order-disorder ferroelectric $NaNO_2$ has displacive component (with respect to Na atoms) and there are still discussions whether the ferroelectricity in classical $BaTiO_3$ originates from displacive, order-disorder or mixed mechanism

[18, 22–25].

2.2 Thermodynamics of the ferroelectric phase transition

As per Landau - Ginzburg approach, an order parameter is attributed to the ferroelectric and paraelectric phases. The order parameter in the ordered, ferroelectric phase takes a finite value, while in the disordered, paraelectric phase it is zero [17]. Conveniently for the ferroelectrics an order parameter can have the value of the spontaneous polarization. To analyze the behavior of the macroscopic properties in the vicinity of T_c, the differential of Gibbs free energy in such form is used:

$$ \mathrm{d}\Phi = E_i \, \mathrm{d}P_i - \varepsilon_{ij} \, \mathrm{d}\sigma_{ij} \,, \tag{4} $$

where E_i is electric field in the direction i, P_i is the polarization, σ_{ij} and ε_{ij} is the stress and strain tensors respectively. The stress-strain part will be neglected to simplify the analysis and only the electric part will be considered. The ferroelectric is assumed to be uni-axial, meaning that the polarization vector can point only in two anti-parallel directions.

Expansion of the Gibbs free energy is done with respect to the order parameter with even powers since the parent phase is non-polar:

$$ \Phi = \Phi_0 + \frac{1}{2}\alpha P_y^2 + \frac{1}{4}\beta P_y^4 + ... \tag{5} $$

Expansion until the fourth power is enough to analyze the transition within second order phase transformation framework [17] since the simplified second order phase transition mechanism already captures the essence of the macroscopic properties with respect to temperature and electric field in the vicinity of T_c. The parameter α is set to be temperature dependent, as per temperature driven transition, and beta is a positive constant:

$$ \begin{aligned} \alpha &= \alpha_0(T - T_c), \\ \alpha_0 &> 0, \\ \beta &> 0. \end{aligned} \tag{6} $$

With such assumptions, the Gibbs free energy Φ at $T < T_c$ shows two minima, corresponding to the two equivalent spontaneous polarization directions of uni-axial ferroelectric, while at $T > T_c$ the energy minimum is located at $P_y = 0$, which corresponds to the expected behavior from the observations of real materials.
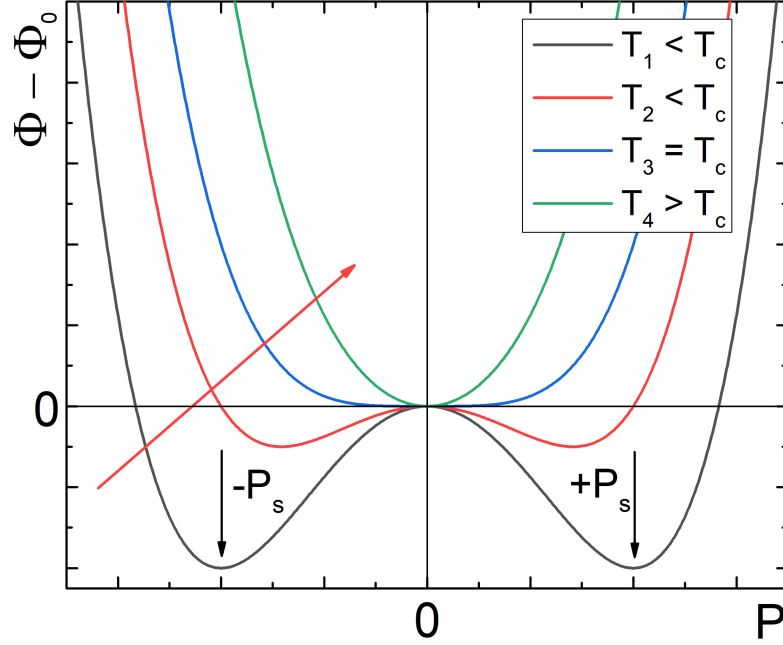
Figure 2.5: Gibbs free energy dependence on the temperature. Red arrow indicates the direction of increasing temperature. At $T < T_c$ potential is double-well, with equivalent minima corresponding to $+P_s$ and $-P_s$. At $T > T_c$ only one stable minimum remains, corresponding to $P_y = 0$.

Following from the relation:

$$\left(\frac{\partial \Phi}{\partial P_y} \right)_\sigma = E_y. \tag{7}$$

The equation of state can be obtained:

$$E_y = \alpha_0(T - T_c)P_y + \beta P_y^3. \tag{8}$$

As the characteristic of a ferroelectric is the appearance of macroscopic polarization without external field, E_y is set to zero and the solutions are sought. For the paraelectric phase $(T > T_c)$ only one valid solution is obtained $P_y = 0$. However, for a ferroelectric phase $(T \lesssim T_c)$ two temperature dependent solutions are found:

$$P_y = \pm P_s = \pm \sqrt{\frac{(\alpha_0(T_c - T))}{\beta}} \tag{9}$$

The dielectric susceptibility $(\chi = \partial P_y / \partial E_y)$ also follows from the Eq. 8 and the solutions of P_y at the temperatures over and under T_c. For paraelectric phase $(T < T_c)$ Curie-Weiss law is fulfilled [17]:

$$\chi = \frac{1}{\alpha_0(T - T_c)} \equiv \frac{\varepsilon_0 C}{T - T_c}. \tag{10}$$

11

Similarly for the ferroelectric phase $(T < T_c)$:

$$\chi = \frac{1}{2\alpha_0(T_c - T)}. \tag{11}$$

Fig. 2.6(a) shows the graphical representation of the solutions, which show singularity of χ at the transition point and onset of spontaneous polarization $P_S \propto \sqrt{T_c - T}$.

Similarly P_s and χ curves can be obtained for the first order phase transition, if Eq. 5 is expanded to higher power. The main differences between second order and the first order phase transition are the loss of singularity of χ at the transition and onset of the spontaneous polarization with a jump to a finite value. Additionally the dielectric susceptibility in the ferroelectric regime obeys slightly different relationship. However, in the paraelectric phase, Eq. 10 is still valid, that is the Curie-Weiss law still applies. For a graphical representation see Fig 2.6(b). Additionally, as per first order phase transitions, ferroelectric and paraelectric phase coexistence in the near vicinity of T_c is permitted.
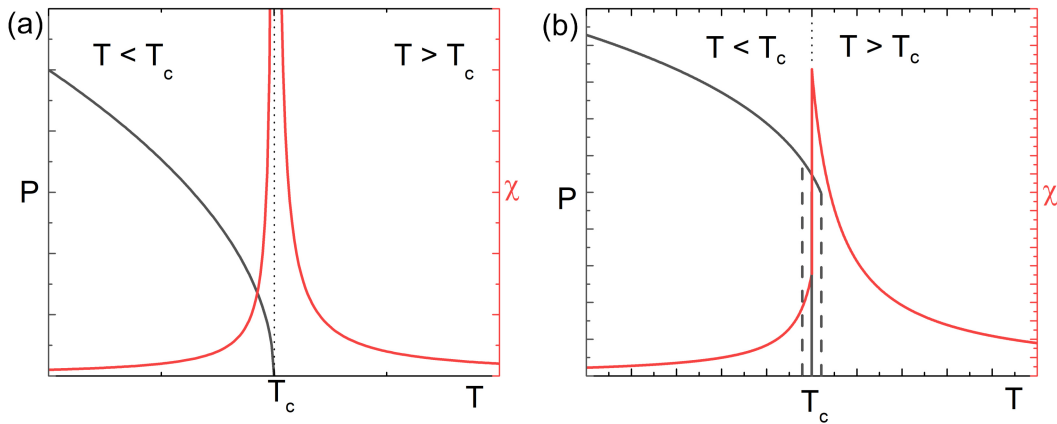
Figure 2.6: Dielectric susceptibility of and spontaneous polarization in the vicinity of T_c. (a) T_c is marked with a thin dashed line, red curves represent dielectric susceptibility and the dark grey line represents spontaneous polarization. Region of phase coexistence is marked with grey dashed lines with respect to spontaneous polarization. (a) Second order phase transition. (b) First order phase transition.

2.3 Ferroelectric domain structures

A fictitious, infinite, ideal ferroelectric crystal at thermodynamic equilibrium would exhibit a single macroscopic polarization direction through-out the whole medium (a single domain state) [26]. However, real crystals are inherently imperfect. They have finite dimensions and a surface (arguably the largest crystal defect possible, a termination of a crystal).

2.3.1 Free energy minimization of a finite size ferroelectric

The finite size of a real crystal gives rise to a depolarizing field of bound charges, Fig. 2.7(a), which points in the opposite direction of the spontaneous polarization [27]. The slabs in Fig. 2.7 have finite sizes in the direction of the spontaneous polarization
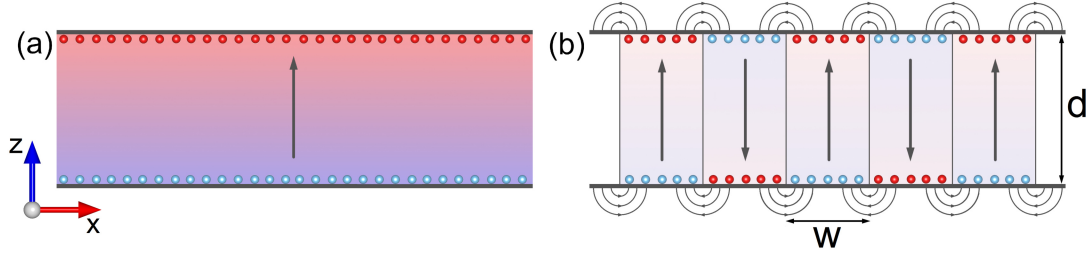
Figure 2.7: Cross-sections of ferroelectric slabs. The slabs are infinite in the **x** and **y** directions, but have finite size d in the **z** direction. Positive and negative bound charges are depicted as red and blue circles, direction of the spontaneous polarization is shown with the arrows within the slabs. (a) Slab is in a single domain state, which gives rise to a strong depolarization field (depicted as dark shading within the slab). (b) The slab is split domains with opposite polarization directions, the domain structure is highly periodic with the domain size w, such configuration reduces overall depolarization fields within domains.

(**z**). Assuming a single domain state as shown in Fig. 2.7(a), a large depolarization field is induced in the slab, which is also associated with high electrostatic energy. The strength of the depolarization field can be reduced if the ferroelectric slab splits in periodic domain structure with opposite polarization in each successive domain with width w, as seen in Fig. 2.7(b) [26, 28]. Reduction of w by half, reduces the electrostatic energy associated with the depolarization field by half (surrounding domains compensate each others' depolarization field). However, this increases the density and the total surface area of the domain walls and, hence, it increases the associated domain wall surface energy [3, 28, 29]. Nevertheless, there must be an equilibrium state, with optimal electrostatic and domain wall surface energy. The domain structure seen in Fig. 2.7(b) was theoretically studied by C. Kittel in the ferromagnetic materials and later introduced to ferroelectrics under a similar theoretical approach by T. Mitsui [28, 29]. It is termed 180° domain structure or c-c domain pattern.

Quantitatively, the description of the domain wall formation follows from the minimization of the free energy. In the most simple case only the energy of the electrostatic depolarization field and the surface energy of the domain walls are considered. The other influences such as elastic effects, finite width of a domain walls, screening charges, crystalline defects and external electric field are neglected for simplicity. The full derivation of the expressions can be found in references

[28, 30]. In short, the total free energy per unit area of the slab consists of two terms:

$$F = F_{\text{dep}} + F_{\text{walls}}. \tag{12}$$

The term F_{walls} is propotional to the thicknees of a slab d (the thicker the slab, the larger the area of the domain walls) and inversely proportional to the domain width w ($1/w$ is essentially the density of the domain walls), therefore:

$$F_{\text{walls}} = \gamma \frac{d}{w}. \tag{13}$$

The parameter γ indicates the surface energy of the domain wall (measured in J/m^2). It can be both theoretically estimated and experimentally measured and it depends on the material, domain wall type and configuration [26, 29, 31]. The expression for the depolarization field energy per unit area is:

$$F_{\text{dep}} = \frac{8.42}{\pi^3} \frac{P_s^2 w}{\varepsilon_0 (1 + \sqrt{\varepsilon_x \varepsilon_z})}, \tag{14}$$

where P_s is the spontaneous polarization, ε_0 is the absolute value of the dielectric permittivity of vacuum, ε_z and ε_x are the relative dielectric permittivities of a ferroelectric material in the direction of the spontaneous polarization and orthogonal to it (the same coordinate system as in Fig. 2.7).

To better illustrate the previous formulas, it is assumed that the slab in Fig. 2.7(b) corresponds to BaTiO$_3$ at room temperature with the values of the physical constants taken from reference [31], that is $P_s = 0.25$ C/m^2, $\varepsilon_z = 200$, $\varepsilon_x = 4000$, $\gamma = 1 \cdot 10^{-2}$ J/m^2, $d = 1$ mm). The resulting curves are shown in Fig. 2.8. For such a slab the equilibrium domain width is 2 µm. The general equilibrium width (w_{eq}) dependency on the other parameters follows from $\partial F / \partial w = 0$.

$$w_{eq} = \sqrt{\frac{\pi^3 \varepsilon_0 \gamma (1 + \sqrt{\varepsilon_x \varepsilon_z})}{8.42 P_s^2}} \sqrt{d}. \tag{15}$$

The equilibrium domain width is proportional to the square root of the slabs thickness, $w_{eq} \propto \sqrt{d}$. This proportionality seems to be fundamental to all *ferroic* materials even if more complicated expressions of the free energy are analysed [31]. Additionally, it indicates that the observable domain structure is highly dependent on the dimensions and the shape of the ferroelectric material.

2.3.2 Non-180° domain walls

The 180° (c-c) domain structure is one possibility for the polar domains to arrange themselves, which is quite often found in the ferroelectric materials. However, it is
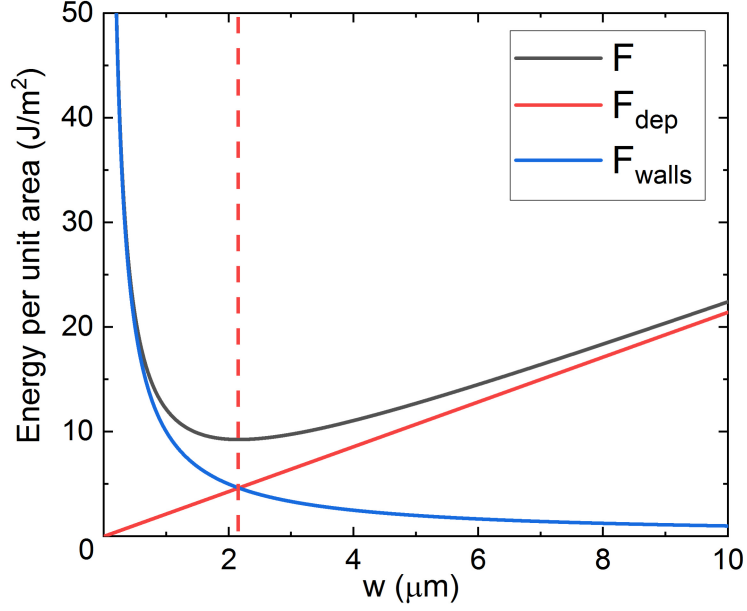
Figure 2.8: Free energy dependency on the width of the domains in BaTiO₃, d = 1 mm. Energy is expressed per unit area, black line represents total free energy F, red line - free energy associated with the depolarization field and the blue line is the free energy of the domain walls. Red, dashed vertical line corresponds to the equilibrium domain width.

not the only domain structure possible. One of the governing factors of the domain structure is the electrical compatibility, which follows from the Poisson equation:

$$\rho_b = -\boldsymbol{\nabla} \cdot \mathbf{P}. \tag{16}$$

If a ferroelectric domain wall is oriented arbitrary in the material, bound charge ρ_b would appear on its surface. However, such situation is energetically unfavourable, but not impossible if there are free charge carriers, which can compensate the bound charge [17]. If there are no free charge carriers and the elastic properties are neglected, then the domain wall electric neutrality plays a major role in the formation of the domain pattern according to the equation:

$$(\mathbf{P_{SA}} - \mathbf{P_{SB}}) \cdot \mathbf{n} = 0, \tag{17}$$

where $\mathbf{P_{SA}}$ and $\mathbf{P_{SB}}$ are the spontaneous polarization directions in the adjacent domains and $\mathbf{n}$ is the normal vector of the domain wall's surface. The possible domain structures are governed by the crystallographic symmetry of the ferroelectric material's unit cell [17]. All ferroelectric materials form 180° domain walls (the angle represents rotation of the polarization vector across the domain wall). Materials with hexagonal and trigonal symmetry only form 180° walls whereas materials with lower

symmetry, tetragonal for example, already have two possibilities to form 180° and 90° domain walls. Orthorhombic symmetry permits 180°, 90°, 120° and 60° domain walls, Fig. 2.9 [26]. Monoclinic symmetry has 24 different domain wall types and the lowest possibility symmetry, which corresponds to the triclinic structure, gives rise to 48 different domain wall types. In the non-180° cases, polarization across the domain
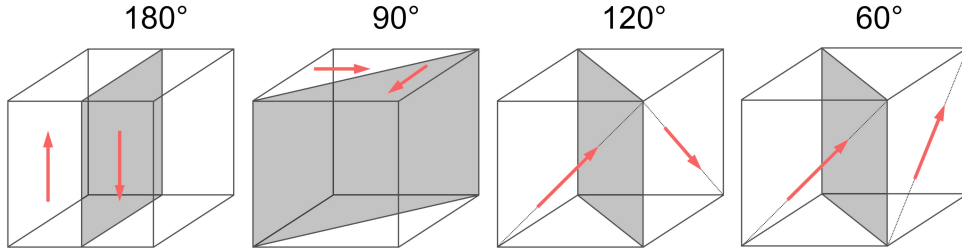
Figure 2.9: Geometric representation of the 180°, 90°, 120° and 60° domain walls. Name of the specific domain wall originates from the angle of the polarization vector (red arrow) change in the adjacent domains, the domain wall is depicted as a light gray plane within a cube.

wall forms a *head-to-tail* pattern to keep the wall electrically neutral (polarization component along the normal of the wall is continuous) [17].

Non-180° ferroelectric domain walls are associated with the minimization of the mechanical stress fields originating upon the transition to the ferroelectric state. As it was already discussed, the appearance of the spontaneous polarization implies a loss of inversion center within the unit cell and physical movement of the atomic equilibria positions, therefore the appearance of spontaneous strain is also expected [17].

When the transition from the paraelectric parent phase G to the ferroelectric phase F involves a change in the crystal system, then the transition is also ferroelastic. This is the necessary and sufficient condition for the ferroelastic transition [32]. For example, $NaNO_2$ upon transition does not change the crystal system (ferroelectric and paraelectric phases are both orthorhombic), while $BaTiO_3$ changes the crystal system from cubic to tetragonal.

Tetragonal $BaTiO_3$ at room temperature can form 180° and 90° domain walls. 180° domain walls are mechanically compatible, however 90° domain walls need local readjustment of the unit cells [17].

The high symmetry cubic phase of $BaTiO_3$, Fig. 2.10(a), is characterized by a single unit cell parameter a_c while the transition to a tetragonal phase [Fig. 2.10(b)] leads to two distinct lattice parameters a_t and c_t with $c_t/a_t > 1$. Changes in the crystal system give rise to a situation where spontaneous polarization can point to six different directions in space. When two orthogonal polarization directions come into contact, Fig. 2.10(b), the lattice must elastically deform to accommodate such situation. It is mechanically advantageous for the unit cells to locally *"rotate"* into
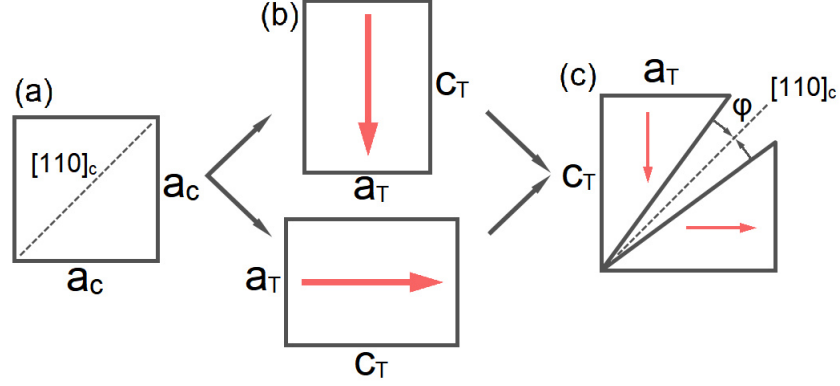
Figure 2.10: Formation of ferroelastic 90° domain wall. (a) Parent cubic phase, with characteristic lattice parameter a_c, dashed line represents $[110]_c$ direction. (b) Upon transition to a ferroelectric tetragonal phase six different spontaneous polarization directions are possible (here two of them are shown with red arrows). (c) Formation of 90° ferroelastic domain boundary, it is mechanically advantageous to form the boundary along previous $[110]_c$ direction with two unit cells *"rotating"* to each other by an angle ϕ.

each other by an angle ϕ (clapping angle), as shown in Fig. 2.10(c). A ferroelastic domain wall then forms along the parent phase $[110]_c$ direction [17]. It is noted that the clapping angles are usually small. For example, tetragonality of $BaTiO_3$ at room temperature is $c_t/a_t = 1.004$. That is the distortion from the ideal cubic phase is just 0.4 %.

Similar considerations of free energy minimization lead to the conclusion that ferroelastic domain walls also form periodic patterns with the same relationship as in ferroelectric case, $w_{eq} \propto \sqrt{d}$ [33]. While in the ferroelectric case the energy of the electrostatic depolarization field is reduced by forming domain walls, in the ferroelastic case the energy associated with the spontaneous elastic stress fields is being reduced via the formation of ferroelastic domain walls [34]. Of course, this also implies coupling of the mechanical and electrical properties of ferroelectrics.

2.3.3 Charged domain walls

The previously described domain wall configurations are all electro-neutral (polarization vectors form head-to-tail pattern), however it has been theoretically and experimentally confirmed that the polarization across the domain wall's normal vector can also be discontinuous [35]. Such discontinuity leads to the appearance of bound charges on the domain wall with the surface charge density:

$$(\mathbf{P_{SA}} - \mathbf{P_{SB}}) \cdot \mathbf{n} = \sigma_b. \tag{18}$$

Usually strongly charged and weakly charged domain walls are distinguished. In
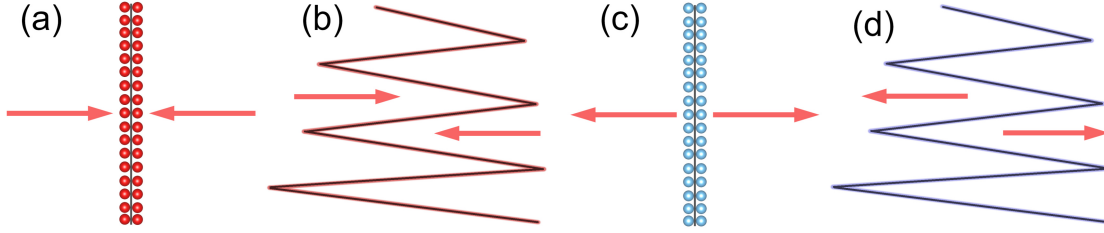
**Figure 2.11: Schematic drawings of charged domain walls.** Red and blue spheres represent positive and negative charges, similarly red and blue shading represent weaker positive and negative charges. (a) Strongly positively charged domain wall. (b) Weakly positively charged domain wall. (c) Strongly negatively charged domain wall. (d) Weakly negatively charged domain wall.

the case of strongly charged domain walls, the polarization vectors of the adjacent domains point directly along the normal vector of the wall, Fig. 2.11(a)/(c). In this case, the bound charge density is equal to $\sigma_b = 2P_s$ (theoretically) and the domain wall is positively charged if the polarization vectors meet head-to-head [Fig. 2.11(a)], and negtively charged when they meet tail-to-tail [Fig. 2.11(c)]. The polarization vectors in the adjacent domains in weakly charged cases are pointing head-to-head or tail-to-tail, however the domain wall is inclined, as shown in Fig. 2.11(b)/(d). In this case, the bound charge is dependent on the angle between the normal of the wall and the direction of the spontaneous polarization, and it is greatly reduced when compared with strongly charged walls [35]. In many cases, strongly charged domain walls will be stabilized by transformation into weakly charged domain walls at the expense of the domain wall's surface energy [27].

Charged domain walls are almost always associated with the presence of screening free charges, which stabilize electro-statically unfavourable conditions. This creates a unique situation, where adjacent highly insulating domains are separated by a thin conductive domain wall [35].

2.3.4 The local structure of domain walls

From theoretical and experimental studies, it is clear that domain walls have a local polarization structure and a finite width.

The domain wall's thickness, in simple terms, is conceived as the width of the region where significant departures of the spontaneous polarization from its values deep inside the two adjacent domains occur [17] (although the definition is somewhat vague). Additionally, the polarization change across a domain wall may be fulfilled in several ways, giving rise to distinct domain wall types, Fig. 2.12 [36]. The theoretically calculated 90° domain wall thickness for $BaTiO_3$ at room temperature is approximatelly 5 nm. This agrees with the experimental microscopic studies, which estimate the thickness to be between 5 - 10 nm [17].
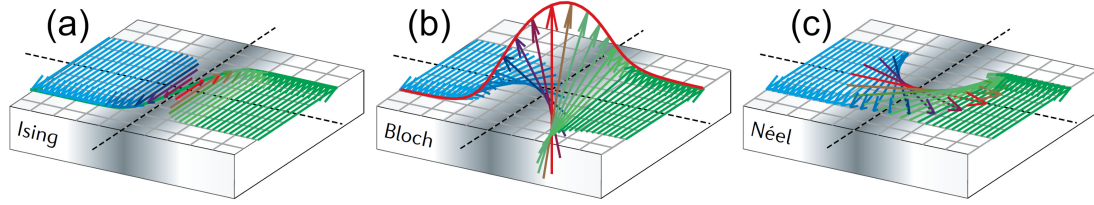
Figure 2.12: Some of the domain wall types. Approximate wall width is represented with the shaded region. (a) Ising wall - polarization smoothly decreases across both sides of the wall, at the center being zero. (b) Bloch wall - polarization rotates in 3D space across the wall. (c) Néel wall - polarization rotates across the wall, but it is locked in two dimensions. Image adapted by permission from *Springer Nature Customer Service Centre GmbH: Springer Nature, Nature Review Physics*, from ref. [36], Copyright (2021).

2.4 Polarization switching

Hysteresis (memory effect of the material's previous state) is a characteristic of *ferroic* materials. For the ferroelectrics, as demonstrated by Joseph Valasek in 1921, it concerns polarization - electric ($\mathbf{P}$ - $\mathbf{E}$) field hysteresis loops [1]. Hysteresis in the ferroelectrics is closely related to the previously discussed domain structure. When the major part of a sample changes its domain state, a switching process takes place, which is characterised by a hysteresis loop, Fig. 2.13 [17, 37].

Ferroelectrics in their native, non-poled state form domain patterns, where contributions from each domain's polarization cancel each other out, therefore their macroscopic polarization is zero (Fig. 2.13 point A). Application of external electric field induces domain wall movement, domain growth and coalescence. Domains with polarization in the direction of the electric field grow, while the ones with opposite polarization direction shrink. In a single crystal, a ferroelectric state similar to the one shown in Fig. 2.13 point B can be achieved and they can exhibit a single domain state. Point B is characterized by a saturation polarization $\mathbf{P_{max}}$. Decrease of the electric field brings the loop to point C, where the electric field is zero, however the crystal is now poled, which is characterized with a remnant polarization $\mathbf{P_{rem}}$. Only when sufficient electric field is applied, polarization decreases to zero and point D is characterized by the coercive field $\mathbf{E_c}$. Further, more "negative" electric field application would induce a similar state as in point B, but with the opposite direction of polarization. Of course, on the positive side of the loop, the magnitude of the $\mathbf{E_c}$ is the same, but the sign is opposite.

The coercive field $\mathbf{E_c}$ is the minimal field necessary to induce a poled state (albeit, if $\mathbf{E} \gtrsim \mathbf{E_c}$ the crystal may not be fully poled). $\mathbf{P_{max}}$ is slightly larger than $\mathbf{P_{rem}}$ due to the conventional dielectric response of the material $\mathbf{P} = \chi \varepsilon_0 \mathbf{E}$, where χ is the electric susceptibility of the material. Additionally, at high fields the non-linear
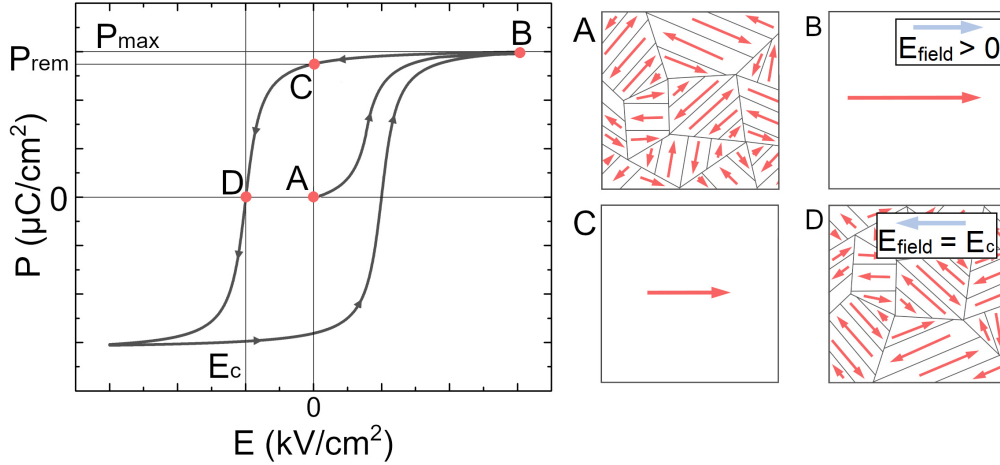
Figure 2.13: Schematic of a P-E loop of a ferroelectrc single crystal. Relationship of **P** - **E** is inherently non-linear in ferroelectrics, direction of the applied electric field is indicated with blue arrow, red arrows represent the direction of spontaneous polarization in the domains. Several relevant points of the loop are marked. A - polarization of a ferroelectric prior the application of the electric field is macroscopically zero, such state is associated with dense domain structure, where the polarization of the domains cancel each other out. B - application of sufficiently large field in the direction of the spontaneous polarization, single domain state can be achieved, characterised by **P$_{max}$**. C - although the electric field is reduced to zero the crystal retains polarization state with the value **P$_{rem}$**. D - application of the electric field in the opposite direction (negative side of the loop), leads to a situation, where polarization is zero with applied electric field **E$_c$** - coercive field.

relationship between polarization and electric field may play a role. The spontaneous polarization from the polarization loop (if it is saturated, the branches of the loop will merge before the tip of the loop) of a single crystal can be estimated by the intersection of the tangent taken at the tip of the loop with the axis at **E** = 0. For example BaTiO$_3$ at room temperature along the **c** axis has **P$_s$** ≈ **P$_{max}$** ≈ **P$_{rem}$**. The area encapsulated by the loop is equal to the energy required to fully switch the polarization twice.

Hysteresis loops can be approached also from a macroscopic, thermodynamic point of view by plotting **P − E** relationship from Eq. 8 at $T < T_c$, $T = T_c$ and $T > T_c$ as shown in Fig. 2.14. In the case of $T = T_c$ and $T > T_c$, the response corresponds to paraelectric material. However, in the case of $T < T_c$ at $E = 0$, the polarization has non-zero value and therefore the response is indeed ferroelectric. Dashed lines correspond to the critical field or thermodynamic coercive field, which can be calculated via $dE_y/dP_y = 0$ from Eq. 8. At $\pm E_c$, the unfavorable polarization state loses its stability and the switching to the opposite state is inevitable, therefore P values in the interval enclosed by $-E_c$ and E_c actually cannot be reached [17].
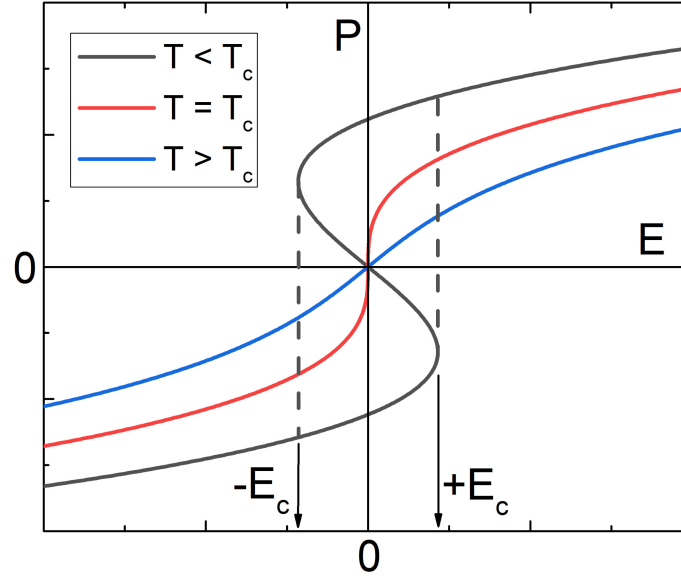
Figure 2.14: P − E response around T_c **if second order phase transition is assumed.** Blue line corresponds to classical paraelectric response at $T > T_c$, red curve is set at $T = T_c$, increase in the polarization with respect to electric field is seen. Dark grey line corresponds to ferroelectric state $\mathbf{T} < \mathbf{T_c}$, dashed lines show thermodynamic coercive field.

2.5 Barium titanate

Barium titanate is a prototypical ferroelectric material. It is tetragonal and ferroelectric at room temperature and heating to ~ 126 °C induces a phase transition to the paraelectric cubic phase. It has overall four different phases, three of them are ferroelectric. It is noted that there is an additional hexagonal phase, but it is not relevant for the ferroelectric phase transitions, as the transformation is reconstructive [38]. The lower symmetry phases can be accessed by cooling the material bellow 0 °C. Its ferroelectric properties, its rich phase diagram, the rigidness of the oxide structure and the convenient phase transition temperatures have always attracted researchers to $BaTiO_3$ for fundamental studies of ferroelectrics and phase transitions.

Crystallographic models of the perovskite $BaTiO_3$ and their respective temperature intervals are shown in Fig. 2.15. The structural parameters are taken from Ref. [39]. In all cases, except orthorhombic $Amm2$, unit cell axis directions coincide with the cubic, parent phase's one (considering that the rhombohedral angle for $R3m$ is just $\sim 89.5° \approx 90°$, such approximation is valid). Also the magnitude of the unit cell parameters is ~ 4 Å. However, in the case of $Amm2$ at $T = -83$ °C, the lattice parameters are $a = 3.9828$ Å, $b = 5.6745$ Å and $c = 5.6946$ Å and the unit cell (black thin line in Fig. 2.15 $Amm2$ case) is 45° rotated with respect to the cubic phase's lattice basis vectors. For easier comparison with the other $BaTiO_3$ phases,
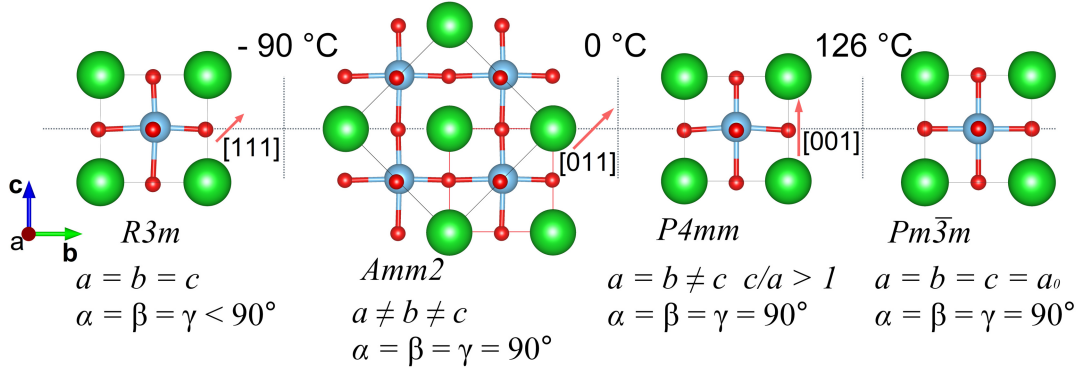
Figure 2.15: Crystallographic models of BaTiO₃ phases. High temperature, parent phase of BaTiO$_3$ is cubic, it is stable starting from 126 °C. Tetragonal phase (space group $P4mm$ is stable between 0 - 126 °C, polarization points along [001] direction with respect to cubic phase. Orthorhombic phase (space group $Amm2$) of BaTiO$_3$ is stable between -90 to 0 °C, polarization points along [011] direction with respect to parent cubic phase. Ground state of BaTiO$_3$ is rhombohedral (space group $R3m$), it is stable bellow -90 °C, there are no indications of lower symmetry phases at low temperatures.

the orthorhombic lattice parameters are recalculated with respect to pseudocubic unit cell, marked with thin red line in Fig. 2.15 for the $Amm2$ case. As it turns out, pseudocubic unit cell fragment in $Amm2$ can be considered to be monoclinic. The relations to the orthorhombic lattice parameters are as follows [39]:

$$a = a_m, \tag{19}$$

$$b = 2c_m \sin(\alpha/2), \tag{20}$$

$$c = 2c_m \cos(\alpha/2). \tag{21}$$

The subscript m denotes the monoclinic parameter and α is the monoclinic angle. This side note is important in understanding the reason that when the orthorhombic parameters of BaTiO$_3$ are reported, only two lattice parameters are shown as seen in Fig. 2.16(a) or even some non-90° angle is shown for the orthorhombic case as seen in Fig 2.16(b), which actually is the angle α.

The lattice parameters shown in Fig. 2.16(a) reveal hysteresis with respect to the temperature. That is, the phase transition temperature shows different values whether it is approached from the high temperature phase or lower temperature phase. At the phase transitions clear discontinuities in the unit cell volume [Fig 2.16(a)] and overall in the lattice parameters [Fig 2.16(b)] are seen, which is characteristic of first order phase transitions.
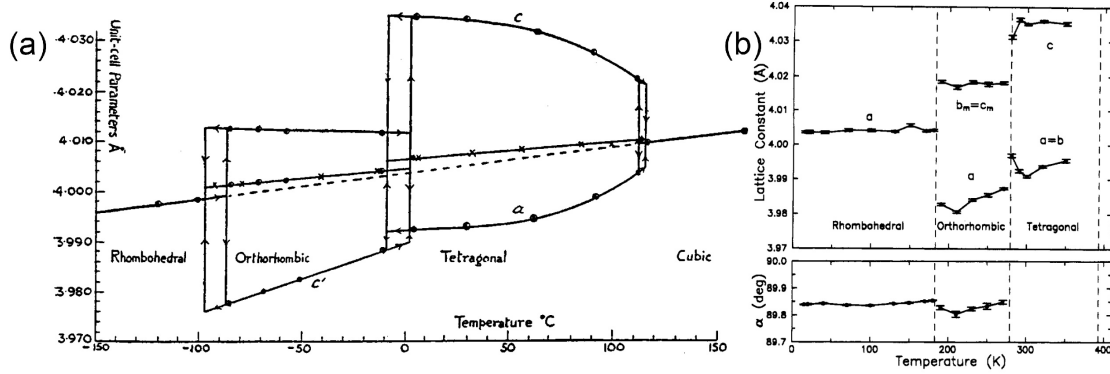
Figure 2.16: Unit cell parameters of BaTiO$_3$ as a function of temperature. (a) Unit cell parameters for all phases, crosses represent cubic root of the unit cell's volume $V^{1/3}$ reproduced by permission of *Taylor & Francis* from the ref. [40]. (b) Unit cell parameters and the angle α of the polar phases only, Reprinted with permission from ref. [39]. *Copyright (2021) American Chemical Society.*

The drastic changes in the structure are also reflected in the dielectric properties of BaTiO$_3$. First, the appearance of the spontaneous polarization is signified by the steep $\mathbf{P_s}$ onset in Fig. 2.17(a) around ~ 120 °C. The form of the polarization onset highly resembles the theoretically calculated one for the first order transition, as shown in Fig. 2.6. At lower temperatures similarly as with the structural parameters, thermal hysteresis is detected around the phase transition regions, Fig 2.17(a)/(b). It is noted that the values reported in Fig. 2.17(a) are systematically underestimated. Despite this, a distinct transition from paraelectric to ferroelectric state is visible and the room temperature value of polarization $P_s \sim 25$ µC/cm^2 reported in Fig. 2.17(b) is widely accepted for BaTiO$_3$ [10, 17, 41].

The relative dielectric constant of BaTiO$_3$ is high across the whole temperature interval and it is anisotropic with respect to the crystal orientation (Fig. 2.18). The phase transition regions are signified with the characteristic jumps in the dielectric constant. It follows from:

$$\mathbf{P} = \varepsilon_0 \chi \mathbf{E}, \tag{22}$$

$$\chi \propto \frac{\partial \mathbf{P}}{\partial \mathbf{E}}, \tag{23}$$

$$\varepsilon_r = \chi + 1. \tag{24}$$

In the vicinity of the phase transition, the spontaneous polarization jumps $\Delta \mathbf{P}$ are large. If one considers $\mathbf{E}$ in the proportionality of Eq. 23 to be small measurement field, then large $\Delta \mathbf{P}$ is reflected as a sudden large jump in the χ and ε_r, the dielectric susceptibility and relative dielectric constant respectively.

Also the form of the dielectric constant dependence in the vicinity of $T_c \sim 120$
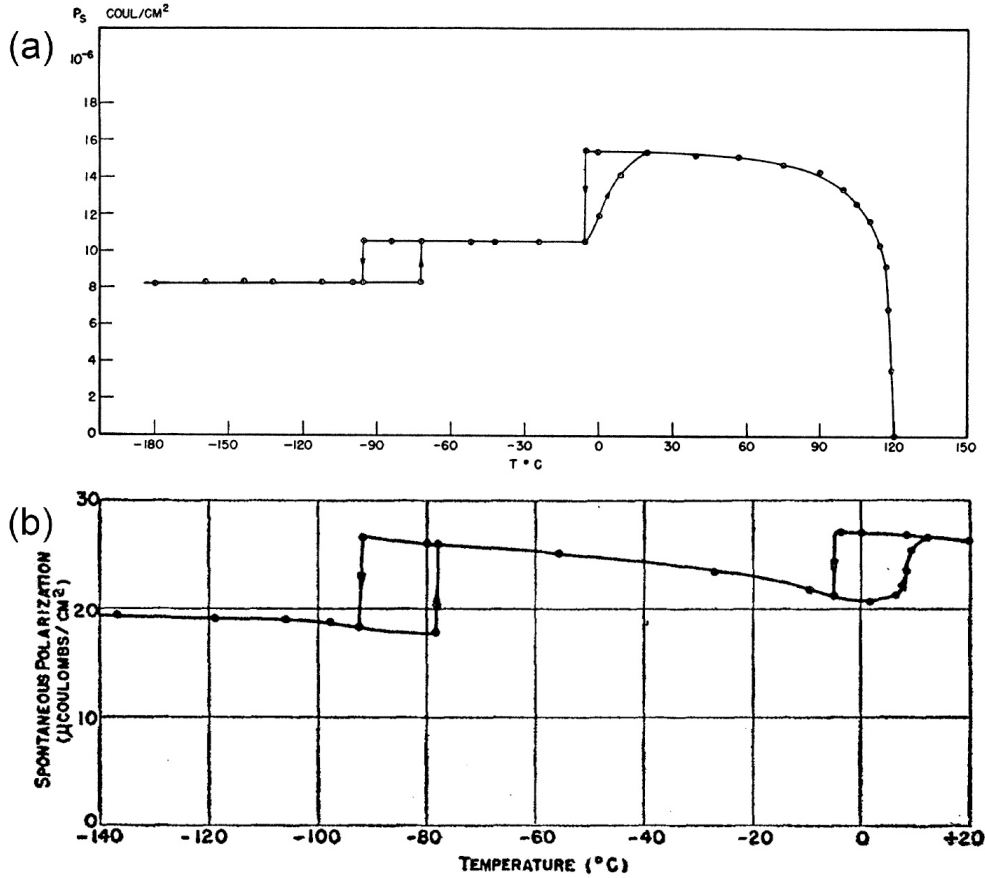
Figure 2.17: Spontaneous polarization of BaTiO₃ as a function of temperature. (a) Reprinted figure with permission from [10] *Copyright (2021) by the American Physical Society.* (b) Reprinted figure with permission from [41]. *Copyright (2021) by the American Physical Society.*

°C resembles the theoretical one for the first order phase transition following Devonshire's theory *Theory of Barium Titanate*, as shown in Fig. 2.6. Devonshire's approach can be thought as an extension of Landau-Ginzburg approach, which only deals with the macroscopic properties of a feroelectric around the paraelectric-ferroelectric transition. Sometimes it is called Landau-Ginzburg-Devevonshire theory, although it seems that Devonshire created it independently from Landau and Ginzburg. Devonshire's theory successfully shows (Fig. 2.19) and analyses macroscopic properties of BaTiO₃ across the full temperature range [42–44].

To switch the tetragonal BaTiO₃ at room temperature, moderate electric fields of $\mathbf{E_c} = 0.5$ kV/cm² are needed. Additionally, $\mathbf{P_s}$ is 24 µC/cm² in the particular experiment [45]. Optical imaging of switching process in BaTiO₃ involving 90° domain walls as shown in Fig. 2.20, shows similar domain behavior as discussed with the schematic in Fig. 2.13.
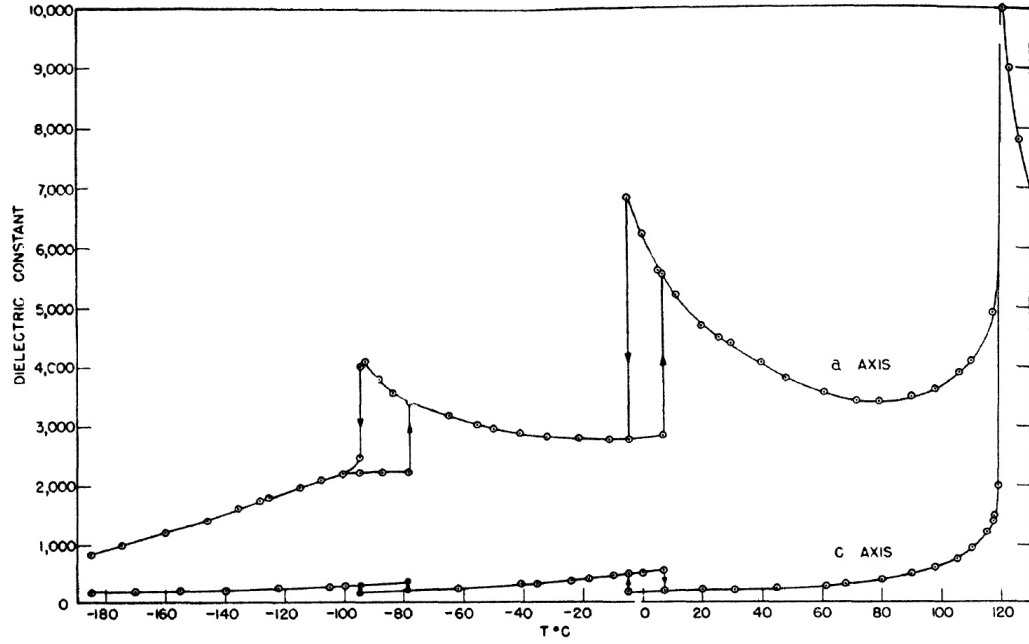
Figure 2.18: Dielectric constants of BaTiO₃ single crystal as a function of temperature. Reprinted figure with permission from [10]. *Copyright (2021) by the American Physical Society.*
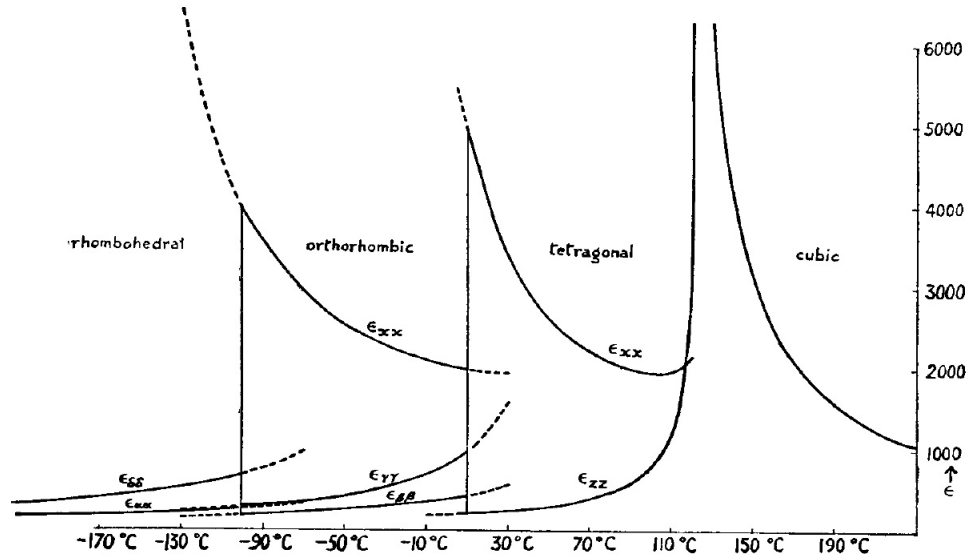
Figure 2.19: Principal dielectric constants of BaTiO₃ (theoretical). Reproduced by permission of *Taylor & Francis* from the ref. [42].
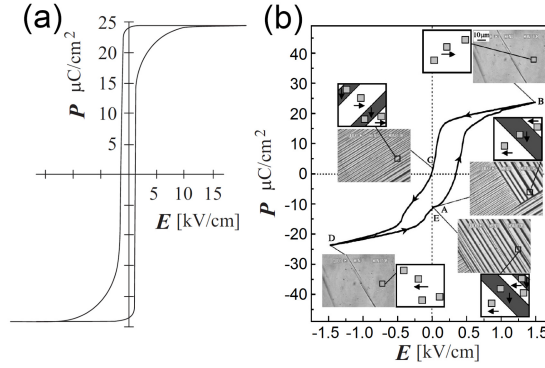
Figure 2.20: P-E loops of BaTiO$_3$ single crystals. (a) Loop of a pure BaTiO$_3$ containing only 180° domain walls switched along c axis in room temperature, Image adapted by permission from *Springer Nature Customer Service Centre GmbH: Springer Nature, Nature Review Physics*, from ref. [45], Copyright (2021). (b) Slightly doped (0.3 mol % Mn doping with respect to Ti) BaTiO$_3$ single crystal containing 90° domain walls, loop and optical images of the crystal at relevant points. Reprinted figure with permission from [46]. *Copyright (2021) by the American Physical Society.*

2.6 *In situ* TEM methods for ferroelectrics

As established before, the two main stimuli influencing a ferroelectric material are temperature and electric field. Usually these two stimuli are combined with experimental methods to study relationships relevant for ferroelectrics.

Temperature and electric field control coupled with electron microscopy techniques allows to study atomic and microscopic (domain) structure directly at relevant conditions. Additionally, secondary signals originating from electron-matter interactions can be used to retrieve information on the local chemical composition and electronic structure.

2.6.1 Contrast origins in TEM of ferroelectrics

To better understand the changes observed in the *in situ* experiments, the origins of TEM contrast associated with ferroelectrics are first discussed. Except for conventional mass-thickness contrast (denser and/or thicker parts absorb more electrons as compared to "lighter" and/or thinner parts), the ferroelectric materials also show specific contrast associated with diffraction [47]. As the ferroelectric splits in domains, regions with different crystallographic orientations appear in the material. Electrons passing through the crystal diffract in them, however the distortion from the "parent" high-symmetry phase is small and the formed diffraction pattern is in close resemblance of the parent phase.
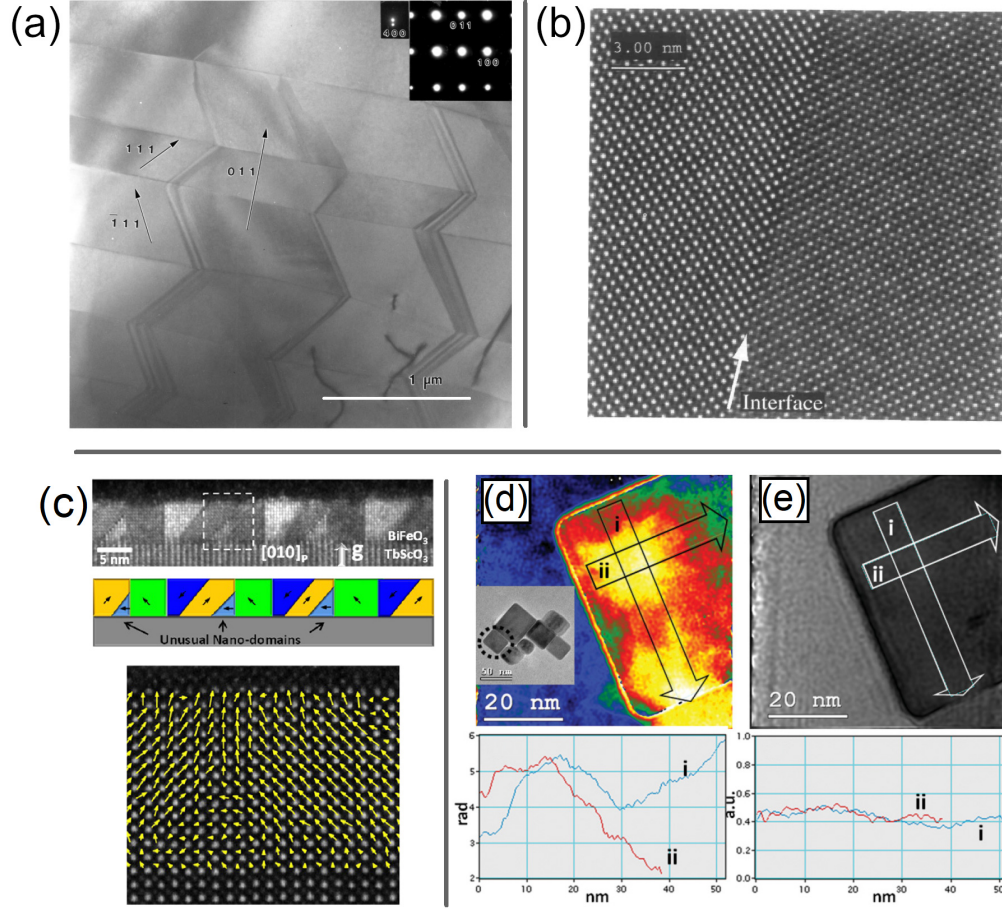
Figure 2.21: Examples of various contrast origins in TEM of ferroelectric materials. (a) TEM bright field micrograph of PZT ceramics showing a herringbone-like ferroelectric domain configuration, viewed along [0$\bar{1}$1] (see larger inset). The 400 reflection is enlarged to show the splitting of the spots (smaller inset). Republished with permission of *IOP Publishing Ltd*, from [48]; permission conveyed through *Copyright Clearance Center, Inc.* (b) HR-TEM micrograph of a 90° ferroelectric domain wall in $PbTiO_3$ crystal, taken on a [010] zone axis, reproduced from ref. [49] by permission of *Oxford University Press.* (c) Top, Cross-sectional dark-field TEM image revealing the domain patterns of a 5 nm thick (001) $BiFeO_3$ film grown on a (110) $TbScO_3$ substrate. Middle, a schematic of the observed domain pattern. Bottom, Z-contrast STEM image of the rectangular highlighted part in the top image. Arrows indicate Fe displacement with respect to the center of unit cell formed by Bi atoms. Adapted with permission from [50]. *Copyright 2021 American Chemical Society.* (d) Phase and (e) amplitude images of a $BaTiO_3$ nano-cubes below the Curie temperature. In (d) the phase image is color scaled to emphasize the change of phase, inset shows displays a low-magnification image of the nano-cubes under inspection marked by a dashed circle. The plots shown underneath are corresponding phase and amplitude profiles along scan lines "i" and "ii". Reprinted figure with permission from [51]. *Copyright (2021) by the American Physical Society.*

Still, if electron diffraction pattern is acquired from a large enough region, splitting in the "parent" phase diffraction spots conveying distorted structure can be observed [see the small inset in Fig 2.21(a)]. Under the bright field imaging conditions (image formed by the directly transmitted electron beam and some diffracted beams, depending on the size of the aperture used), Fig. 2.21(a), domain walls (i.e. twin boundaries) can be probed [47].

Fig 2.21(a) (ceramic sample of PZT) also shows contrast differences in the bulk part of the domains (some are brighter, some are darker) and not only on the domain walls. This is associated with the breakage of Friedel's law in polar materials, i.e. diffraction spots in the direction of spontaneous polarization are brighter than in its opposite ($\bar{h}\bar{k}\bar{l} \neq hkl$) [47]. This contrast originates due to the strong dynamic scattering of electrons in matter. The effect can be used to image domains containing polarization in certain hkl direction. The top part of Fig 2.21 (thin film of $BiFeO_3$) shows dark-field TEM image, which is formed by selecting a specific diffracted beam using an aperture. The domains containing polarization in that particular direction are considerably brighter when compared to other domains [for comparison use domain orientation schematic seen in Fig. 2.21(c)].

Underneath the schematic in Fig. 2.21(c), a high angle annular dark field scanning transmission electron microscopy (HAADF-STEM) image is appended. The image is formed by incoherent electron scattering on the nuclei of the matter. Bright parts correspond to atomic columns and brightness of the column is associated with the atomic number Z (the theoretical intensity on an atomic column is proportional to Z^2 [47]). HAADF-STEM allows direct interpretation of high resolution images, which is demonstrated in 2.21(c). The arrows represent Fe atom displacement within individual unit cells, revealing local polar ordering and nano-domains within the thin film.

Figure 2.21(b) is a high resolution transmission electron microscopy (HR-TEM) image of a 90° domain wall in $PbTiO_3$ crystal. It shows similar features as seen in Fig. 2.21(c). However, the image formation mechanism and the interpretation is different. In HR-TEM, the image is formed by interference of transmitted and diffracted beams. It is essentially an interference pattern of the transmitted and diffracted electrons on the periodic lattice potential. In many cases HR-TEM analysis require rigorous image simulation and very thin specimens for quantitative interpretation [47].

Figure 2.21(d - e) depicts $BaTiO_3$ nano-cubes probed with electron holography. In short, as the electron wave is traveling through the medium, it experiences the electrostatic potential of the atoms, in turn this potential induces phase phase shift of the wave. Similarly, electron beam traveling through the ferroelectric medium experiences local potential due to the spontaneous polarization. Relative phase difference between the beams traveling through vacuum and medium can be measured with electron holography. The projected electric field due to the ferroelectric fields is proportional to the negative gradient of the phase shift ($\mathbf{E_{proj}} \sim -\boldsymbol{\nabla}\phi$), where

$\mathbf{E_{proj}}$ is the electric field integrated along the thickness of the sample and ϕ is the electron wave phase shift) [51, 52] . Electron wave phase map of such measurements are shown in Fig. 2.21(d), while Fig. 2.21(e) depicts the amplitude of the interfering beams (essentially it corresponds to pure bright field image). It can be shown that the electron wave phase shift upon traveling through polar medium strongly influences the diffracted beams and is the main contribution in breaking the Friedel's law [52].

2.6.2 Furnace type heating
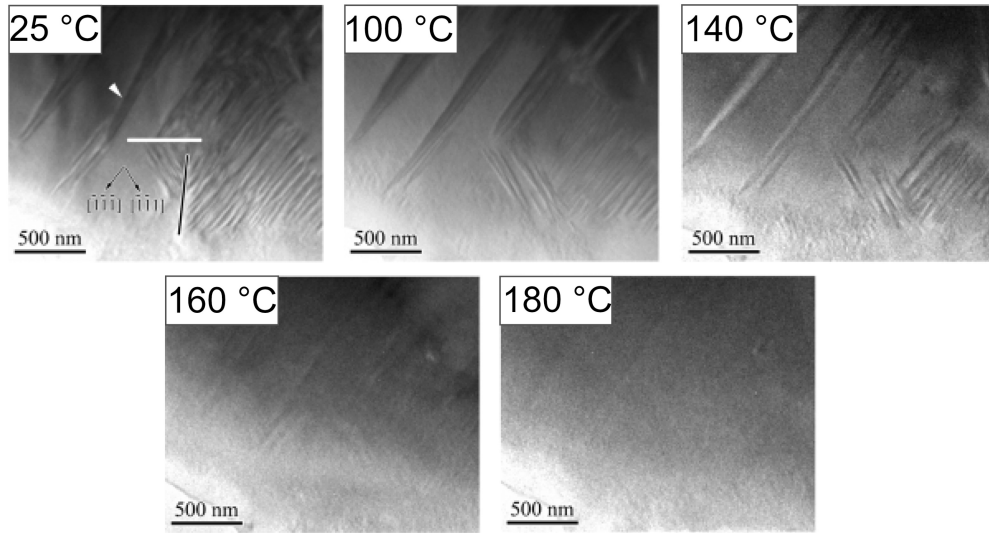
Figure 2.22: Domain structure evolution in $0.885(\mathbf{Bi_{1/2}Na_{1/2}})\mathbf{TiO_3} - 0.05(\mathbf{Bi_{1/2}K_{1/2}})\mathbf{TiO_3} - 0.015(\mathbf{Bi_{1/2}Li_{1/2}})\mathbf{TiO_3} - 0.05\mathbf{BaTiO_3}$ complex ceramics wtih respect to temperature increase. Loss of long range order is indicated by gradual disappearance of the macroscopic domains. White and black lines show (101) and (011) domain walls. Images acquired in bright field TEM mode. Reproduced from the ref. [53] by respecting *Creative Commons Attribution License.*

Specimen heating inside electron microscopes is a well established technique. The first reports on using heating within the microscope dates back to 1960 [54]. The furnace-type holder contains tantalum wire through which current is passed inducing Joule heating. The use of tantalum allows to achieve ~ 1200 °C *in situ* due to its high melting temperature [55]. The surroundings of the furnace are usually cooled to prevent unnecessary heating of the components within the microscope and the holder [55].

The main advantages of the furnace-type system is the capability to hold standard microscopy sample grids, therefore no specialized sample preparation is needed. However, there are several disadvantages of this system. High resolution imaging may

be hindered due to the furnace's large thermal mass, which gives rise to temperature instability ($\sim$ 0.1 °C/min), which in turn prompts movement at nano/micro scale [54]. To mitigate the thermal drift, stabilization at wanted temperature is sometimes needed for one to two hours [55]. Although furnace-type electron microscopy heating holders are difficult to use for high resolution imaging, they are convenient for the domain structure observation as shown in Fig. 2.22, where gradual increase of the temperature destroys macroscopic domain structure and leaves only polar regions with the size of $\sim$ 30 nm (not shown here) [53].

2.6.3 Electrical biasing of mechanically polished samples
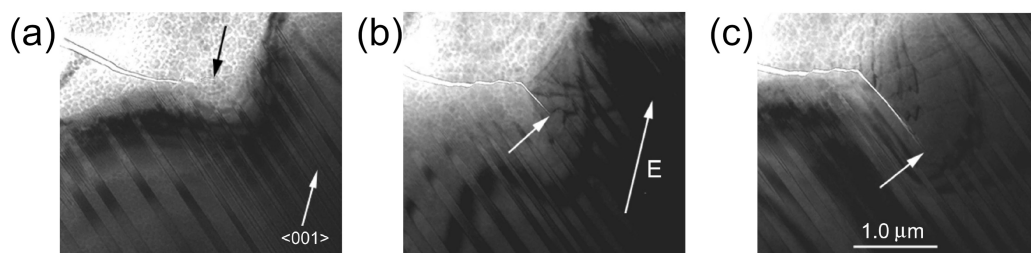
Figure 2.23: Bright-field TEM images showing the electric field-induced fracture in a $0.65\text{Pb}(\text{Mg}_{1/3}\text{Nb}_{2/3})\text{O}_3 - 0.35\text{PbTiO}_3$ single crystal with tetragonal structure. (a) The preexisting crack and the regular 90° domain stripes. The in-plane $\langle 001 \rangle$ direction is indicated by the bright arrow. The domain wall is parallel to the (101) plane. (b) Crack growth after the first application of a static field of 20 kV/cm. The field was applied along the $\langle 001 \rangle$ direction. (c) Crack growth after the second application of the same field. Adapted by permission from *Springer Nature Customer Service Centre GmbH, Journal of Materials Research.* [56]. Copyright (2021).

Traditionally, biasing experiments were performed on TEM holders that could accommodate mechanically polished samples connected with electrodes far away from the area of interest, which could be contacted in several ways (wire bonding, silver paste, etc.) [56–58]. A thin disk of a ferroelectric material is first coated with gold in a shape of half circles. Then the disk is mechanically polished until perforation appears in the center and the final polishing is done with an Ar^+ ion beam, which expands the central hole and removes mechanically damaged layers [56]. The finished specimen is loaded in a holder, which has electrical contacts and wires leading to a power supply. The sample disk is wire-bonded to the electrical contacts of the specimen holder. The main advantages of this method are that excellent TEM sample quality can be achieved and reliable electrical contact between the dielectric material and conductive layer is established. However, the resulting electric field in a mechanically polished sample cannot be uniform and it is also difficult to control the geometry

of the region of interest with respect to the direction of the electric field [57, 59]. Example images of this method are shown in Fig. 2.23. Interestingly, these images may reveal another disadvantage of a mechanical disk polishing method, as not only domain structure is modified with the field, but cracks propagate from the edge of the perforation. Such behavior has previously been reported where this sample preparation method was used [56, 58]. Undeniably, this may also be associated with the material properties.

2.6.4 Probe based electrical biasing
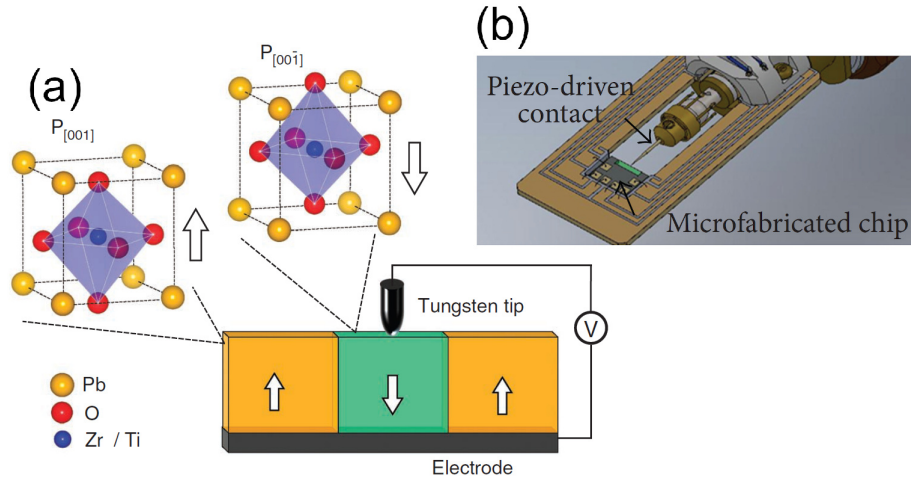
Figure 2.24: Probe based electrical biasing approach. (a) Schematic of the formation of a downward polarized ($P_{[00-1]}$) region within an upward polarized ($P_{[001]}$) film cross-section by the application of a local electric field via a surface probe. Adapted by permission from *Springer Nature Customer Service Centre GmbH, Springer Nature, Nature Communications.* [60]. Copyright (2021). (b) Schematic of a TEM specimen holder with nano-contacting probe, arrow denoting micro-fabricated chip's ferroelectric sample position. Reproduced from the ref. [54] by respecting *Creative Commons Attribution License.*

The probe based technique is also used for biasing ferroelectric structures in the TEM. It offers better control of the electric field as compared to the mechanical polishing method. In this case highly specialized TEM specimen holders are necessary. The holders contain a sharp metallic probe driven by piezo motors (similarly as in scanning tunnelling microscopy) as schematically shown in Fig. 2.24(b). Additionally, the specimen must contain at least one counter-electrode layer [depicted in the Fig. 2.24(a)]. The probe is pressed directly on the surface of a ferroelectric sample and bias voltage is applied [Fig. 2.24(a)]. The achievable results of this approach are shown in Fig. 2.25. Indeed, highly local switching can be induced in a ferroelectric, which allows further analysis at atomic scale.

The drawback of this biasing method is that it creates highly inhomogeneous local electric field, which could hinder interpretation of the results. Additionally, ferroelectrics are highly responsive to the applied external stress and pressing of a needle to a surface easily modifies the domain structure as shown in Ref. [61]. These issues can be mitigated by sandwiching the ferroelectric between conductive layers and pressing the probe on the conductor far away from the region of observation [62]. Nevertheless, such configuration is viable for thin films [63], but not for samples with larger areas such as single crystals or ceramics. Restrictions imposed on the sample geometry with the addition of conductive layers can influence the inherent switching properties of the ferroelectrics through interfacial effects.
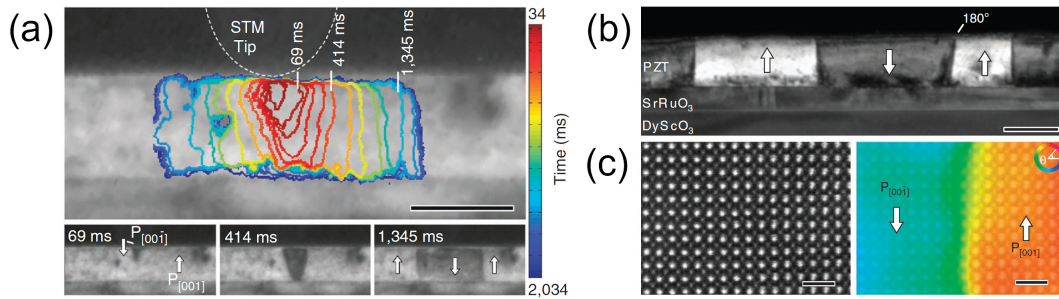
Figure 2.25: Electrical biasing of PZT thin film with the probe based method. (a) The PZT film undergoes cyclic switching using an 18 V peak-to-peak triangle wave. Domain nucleation with negative applied voltage. Contour plots depict domain size at given time intervals, scale bar is 100 nm. (b) Domain structure after switching event (no field applied), scale bar is 100 nm. (c) Analysis of a 180° domain wall showing Ti atoms shift downward in the nucleated domain and upward shifts in the parent domain, scale bar is 1 nm. Adapted by permission from *Springer Nature Customer Service Centre GmbH, Springer Nature, Nature Communications.* [60].

2.6.5 Methods based on silicon micro-technology

Recent advances in TEM holder instrumentation enabled microelectromechanical (MEMS) Si-based chips with patterned electrodes deposited on silicon nitride membranes to be used for heating and biasing experiments.

Figure 2.26 depicts a MEMS based *in situ* heating/biasing system. The metallic spiral acts as a heater and resistive thermometer and it is suspended on a comparably large nitride membrane, Fig. 2.26(b). Therefore, it drastically reduces thermal mass effects, which is the main drawback of the furnace-type heating systems. Small thermal mass enables easier high-resolution measurements, low thermal drift and precise thermal control [54]. Addition of several electrical lines for sample biasing is possible.

Procedures to load a sample on a chip ranges from simple drop-casting to focused
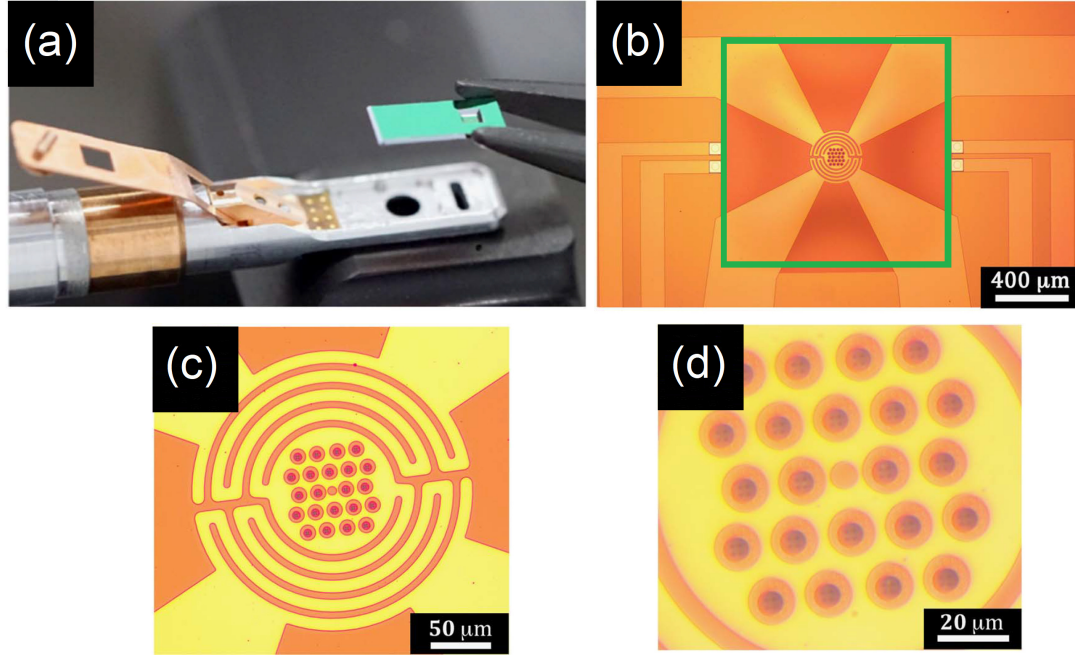
Figure 2.26: MEMS based *in situ* TEM heating system. (a) The tip of a TEM specimen holder containing contacts, MEMS chip is being held by tweezers, green, shiny layer on the chip is silicon nitride coating, backside of a chip is shown, a small hole is seen in the chip - a place of suspended silicon nitride membrane. (b) Front side of a chip, green square marks suspended silicon nitride membrane, x-shaped cross feature marks four electrodes used to pass current through the central heating spiral and also measure potential drop across it. Four electrodes connecting the green marked region in the horizontal way are electrodes used for biasing. (c) Magnified heating spiral, small holes are electron transparent windows, where a sample can be deposited. (d) Magnified image of the electron transparent windows. Reproduced by permission of *Cambridge University Press* from ref. [64].

ion beam milling [64]. If only heating is needed, then sample preparation methods can follow Refs. [64, 65]. However, preparation of a sample for electrical biasing of a ferroelectric is a more complex endeavor, which requires specialized and careful steps. Similar MEMS-based system as well as specimen preparation for ferroelectric biasing experiments that were used in this thesis will be discussed in the next chapter.

3 Methodology

Methods used within this thesis are described in this chapter. First, the *in situ* heating and biasing system and the focused ion beam (FIB) procedure of preparing samples are detailed. Further description of the finite element calculations of the electric field of the biasing device are given. Followed by details of transmission electron microscope working principles. Finally, electron energy loss spectroscopy (EELS) is described along with the density functional theory calculations of the spectra.

3.1 *In situ* heating and biasing system

The TEM heating and biasing specimen holder is shown in Fig. 3.1(a). The holder has the capability to tilt the MEMS chip (β tilt) inserted in the carriage [Fig. 3.1(b)], which is important for the alignment of the crystal axis with respect to incident electron beam. The temperature control is achieved via external power-supply, which has a convenient computer interface control. The chips used in the study contain six electrical lines as shown in Fig. 3.1(c). Four electric lines are used to power (apply potential) and measure the resistance of the metallic spiral heater/temperature sensor. The temperature is determined using the Calendar-Van Dusen equation [66]:

$$R(T) = R(0)(1 + AT + BT^2), \tag{25}$$

where $R(0)$ is the resistance of a platinum thermometer at 0 °C and T is the temperature in °C. The constants A and B are determined experimentally at 0 °C and 100 °C respectively. In practice, B is extrapolated from the resistance measurement at room temperature just before the experiment. Four point probe measurements allow to determine the exact resistance of the heating loop, ensuring precise temperature control. Proportional–integral–derivative (PID) loop is used to control the applied potential to the thermometer/heating spiral. The potential applied to the heating spiral can be adjusted three times per second with a resolution of up to 12 µV. The maximum attainable temperature is 800 °C (specialized MEMS chips are available with maximal achievable temperature of 1300 °C).
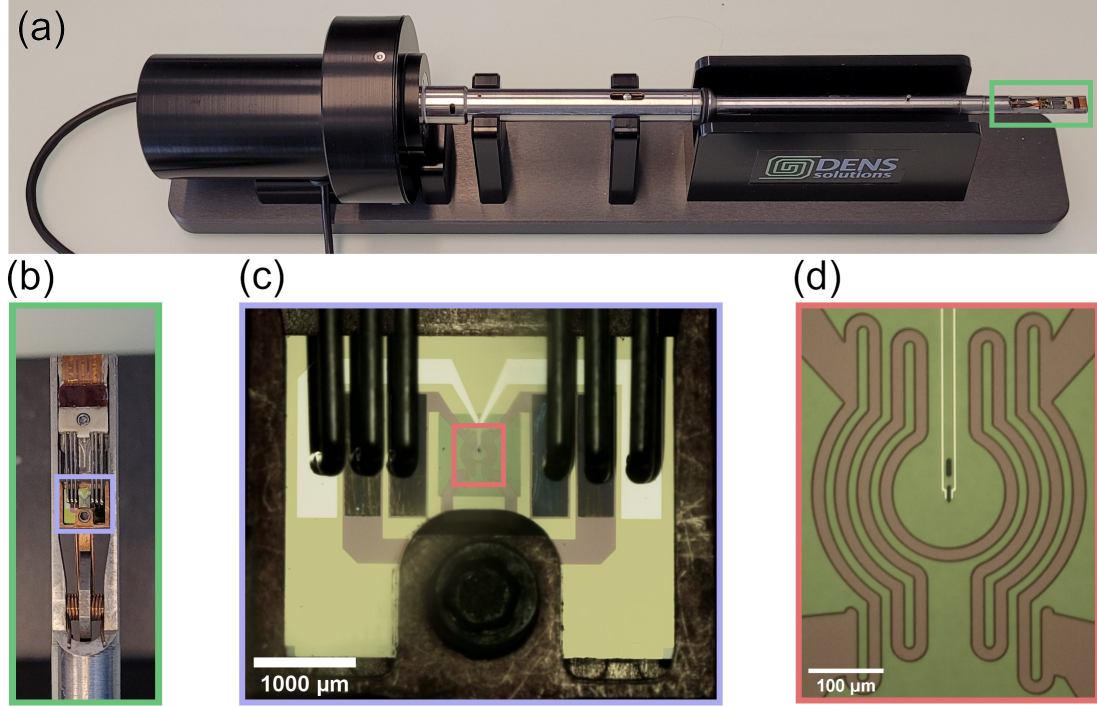
Figure 3.1: *In situ* **TEM double tilting heating and biasing system.** (a) Image of the TEM holder, one wire at the left hand side is used for the application of the temperature and electrical bias stimuli, the other is used to control tilt angle of the MEMS chip carriage (so called β tilt). (b) Magnified image of the tip region of the holder, blue box corresponds to the chip carriage. The holder has six pins available to deliver stimuli to the sample. (c) Optical microscope image of the chip, the pins are firmly pressed against large pads, the chip is fixed in the carriage with a locking screw (black circular region on the bottom part), the chip in use has six electrodes, four are used for the temperature control, the other two outer electrodes (silver color) are used to apply electrical bias), red box corresponds to the heating spiral region located on the suspended silicon-nitride membrane. (d) Heating spiral region, the tiny dark area in the center is a very thin (~ 20 nm) silicon nitride window, which is the optimal place for the specimen

The relative temperature stability is specified to be better than 0.3 °C with a temperature accuracy better than 10 %. The heating spiral and bias electrode lines, Fig. 3.1(d), are suspended on a thin (~ 50 - 100 nm) silicon-nitride membrane ensuring very low thermal mass and fast temperature set time (under 5 s for a temperature change of 300 °C). Low thermal mass radically reduces thermal drift as compared to furnace-type holders. For a MEMS system it is less than 1 nm/min at 800 °C.

For the bias control an external power supply [*Keithley 2450* source meter unit (SMU)] is used with a maximal power output of 20 W and maximal voltage output of $\pm$ 210 V at $I \leq 100$ mA range. The applied electrical bias can be either manually

controlled or the control can be achieved via software by generating voltage wave-shapes via Keithley's native scripting language (*Keithley Test Script Builder*). The custom made script used herein is shown in Appendix A. At relevant voltage ranges for ferroelectric electrical biasing applications (20 V), the accuracy is 0.015 % + 2.4 mV.

3.2 Focused ion beam sample preparation

For a successful *in situ* TEM electrical biasing experiment of a ferroelectric material strict requirements for the sample geometry mounted on the MEMS chip are imposed. The sample should not have any conductive channels, otherwise the applied voltage bias would drop across it, therefore creating a short circuit. In this case, consequences usually involve direct Joule heating of the lamella and complete failure of the experiment. Similarly, the MEMS chip should not allow for short circuit in-between the bias lines.
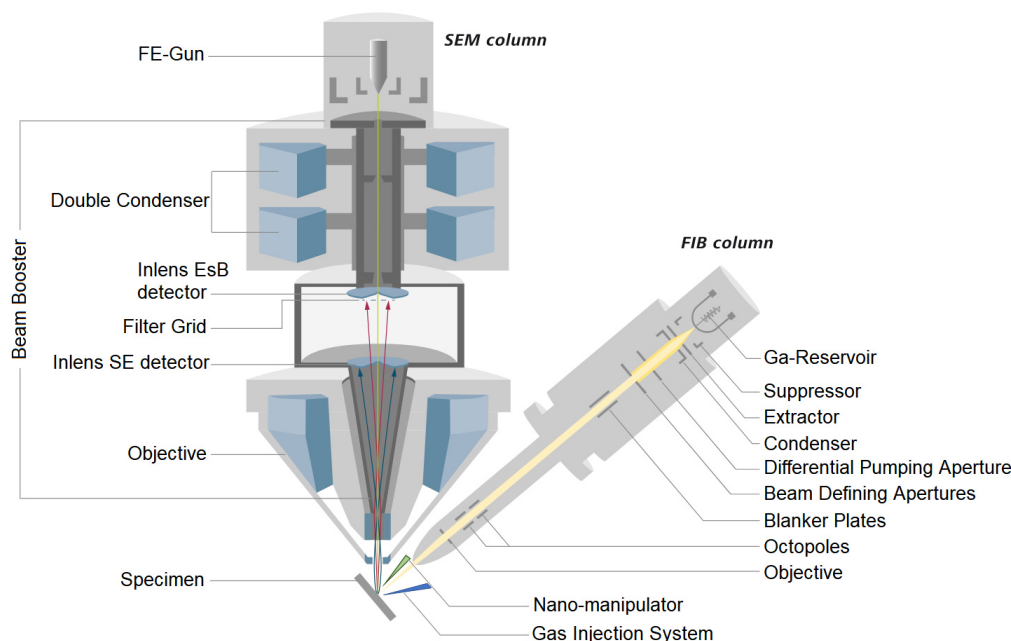
Figure 3.2: SEM-FIB system's construction. Electron optical column is vertical, ion optical column is tilted at 54° angle with respect to the electron optics. Reproduced from the Zeiss website [67].

For preparing the samples in this thesis, the *Zeiss NVision 40 CrossBeam* system (see Fig. 3.2) was used. In this system, electrons for the scanning electron microscope (SEM) column are electric field emitted (FE) and the microscope can be operated between 0.1 - 30 kV accelerating voltage. Three detectors are routinely used for imaging: a conventional Everhart-Thornley secondary electron detector (SE), an

in-lens SE detector and an in-lens energy selective backscattered (EsB) electron detector. The specimen is mounted on a stage, which can be tilted and rotated. The achievable resolution at 20 kV is 1.1 nm and at 1 kV 2.5 nm.

The ion column uses a liquid Ga source, which can be operated between 1 - 30 kV. The achievable resolution at 30 kV accelerating voltage is 4 nm. The current of the ion beam (from 1 pA to 45 nA) is managed via beam defining apertures and the conventional SE and in-lens SE detectors are used to form an ion beam image.

The gas injection system (GIS) is used to pass gases inside the column. It is essentially a tube connected with a reservoir that has gas precursors, which moves close to the working surface of the ion beam. During specimen preparation, it is used to form protective layers and to solder. The GIS injects the precursor gas of the preferred material and the gas interaction with the ion beam breaks the precursor molecules and deposits a layer of the material. Usually carbon or platinum layers are deposited during TEM specimen preparation.
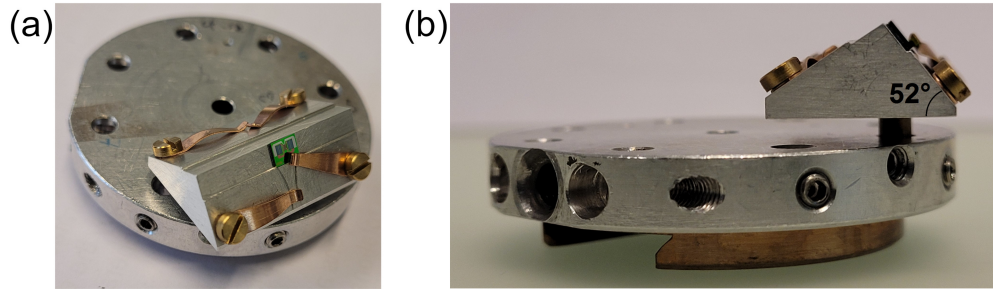
Figure 3.3: Triangular sample stage for a MEMS chip. (a) Overview of the stage. (b) Side view of the stage, the stage has 52° angle.

A nano-manipulator (manufactured by *Kleindiek Nanotechnik*) is used to control a tungsten needle, which is utilized for the lift-out of the prepared lamella.

Prior to any focused ion beam operations, the ferroelectric material and the MEMS chip are coated with an electrically conducting carbon layer outside the microscope to avoid charging effects. For this purpose *Cressington 108 series carbon coater* is used. $BaTiO_3$ single crystal samples were coated with 30 nm layer while the MEMS chip was coated with $\sim$ 7 - 8 nm since it needs to be removed by plasma cleaning before the *in situ* biasing experiment.

The chip is mounted on a specialized "triangular" stage with metal clips pressing against it, Fig. 3.3. The stage is angled slightly differently (52°) than the ion beam column (54°) in the particular microscope. The MEMS chip must be slightly modified before the lamella is mounted on it, Fig. 3.4. By trial and error it was found, that the hole in the silicon nitride membrane is too small for successful biasing experiments, therefore a simple cutting operation is done with FIB. The lamella mounting and polishing procedures create residues, which tend to deposit around the lamella. The

original hole is not long enough and the residues easily form a short circuit on the chip. The extension of the hole allows for the residues to fall through.
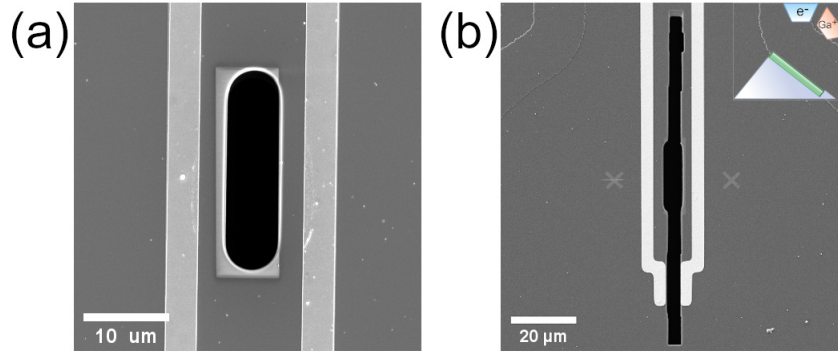
Figure 3.4: Extension of a hole of a MEMS chip. (a) Original hole as chip comes with is 23 µm in height. (b) The hole is extended to be 100 µm in length, inset shows schematic of the triangular stage with MEMS chip on it during this cutting operation.

3.2.1   Preparation of MEMS biasing device
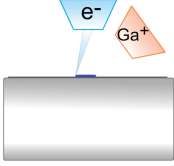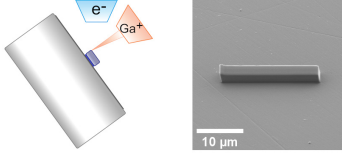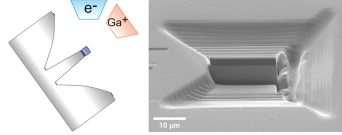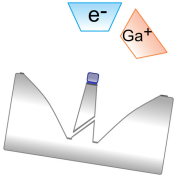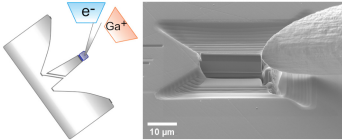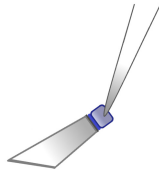
The preparation of a MEMS biasing device involves non-conventional manipulations in the FIB. The schematics of the process flow in the tables 1 and 2 are not to-scale, however, they are made in such way that they preserve the angles observed during the real preparation process.

The start of the procedure is conventional electron and ion deposition of protective layers on the bulk of a material, steps one and two in the table 1. The width of the lamella is dictated by the bias line distance on a chip which is about 20 µm. The deposition width is chosen slightly larger, as during lamella transfer some parts of the lamella are cut off.
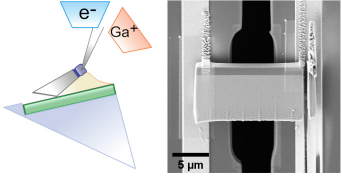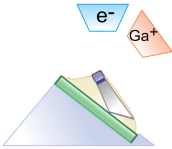
In the step three the depth of the cut is chosen so the final lamella would be ~ 7 - 8 µm large. At step four the so-called undercut is made, which can be seen in the step five SEM image. It is important to take out lamella of the crystal at 54° stage tilt angle to successfully mount it on the MEMS chip.

Table 1: Process flow of lamella mounting on a chip.

Schematics/images	Step description
	1. Deposition of protective layer with electrons. GIS is in, carbon or platinum deposition (blue thin layer in the schematic), stage tilt is 0°, target thickness $\sim$ 100 - 200 nm, target width and height is 21 µm and $\sim$ 2 µm, 5 kV accelerating voltage.
	2. Deposition of protective layer with ion beam. GIS in, carbon or platinum deposition (thick blue layer in the schematic), stage tilt is 54°, target thickness $\sim$ 1.5 µm, target width is 21 µm, height - $\sim$ 2 µm, ion beam parameters - 30 kV, 150 pA.
	3. Etching of the trenches. Stage tilt is 54°. Trench height is $\sim$ 13 µm. Ion beam parameters - 30 kV, 27 nA for rough cutting followed by 13, 6.5 and 0.7 nA, when approaching the final width of lamella ($\sim$ 1 µm).
	4. Creation of the undercut incision. Stage tilt is 9°, undercut is performed with ion beam parameters - 30 kV, 1.5 nA in deposition mode (all cutting region is exposed at the same time).
	5. Soldering the needle to the lamella. Needle is in, GIS is in, carbon or platinum deposition. Stage tilt is 54°, ion beam parameters - 30 kV, 10 pA.
	6. Lamella removal and stage switch. Stage tilt is still 54°. Lamella is removed with the needle by carefully moving it out of the bulk of the material. Stage is then switched to the specialized triangular chip holding one.

Table 2: Process flow of lamella mounting on a chip (continued).

Schematics/images	Step description
	7. Lamella docking on a chip. Needle is in, GIS is in, conductive platinum deposition. Chip is located on the triangular holder, stage tilt is 24°, angle between central line of the lamella and the chip is 8°, however the sides of the lamella ar not parallel, the actual contact angle is estimated to be ∼ 9°. Platinum deposition is made in such way that it fills the void underneath the lamella (yellow layer), ion beam parameters - 30 kV, 40 pA.
	8. Front side platinum deposition. Stage tilt is 0°, GIS is in. Stage is rotated, so the lamella faces ion column directly, the sides of the lamella are found in such way, that the central part of it is not exposed to the ion beam. Platinum electrodes are deposited on the face of lamella (yellow layer) and contacted to the bias lines on the chip, ion beam parameters - 30 kV, 40 pA.

During step six, while the lamella is still on the needle, the stage is switched to the triangular one (see Fig. 3.3), which contains the already modified MEMS chip. Step seven shows the geometry within the SEM-FIB chamber during the lamella mounting on the chip. The lamella does not lay flat on the chip but on an angle. This landing angle (in degrees) for the general case can be calculated from simple geometry considerations:

$$\alpha_{landing} = (90° - \alpha_{column}) - (\alpha_{stage} - \alpha_{tilt}). \qquad (26)$$

The angles used in Eq. 26 are shown in Fig. 3.5. While $\alpha_{column} = 54°$ and $\alpha_{stage} = 52°$ are fixed by the geometry of the system and the stage in use, α_{tilt} can be adjusted freely.

Two considerations for the α_{tilt} are taken into account. The first is associated with the safe operation of the FIB and in particular with the GIS system, which could make a contact due to the non-conventional geometry during operation. The other consideration is the visibility of the lamella during the polishing steps. At the last step low voltage ion beam polishing is usually done at a few degree angle (typically

$\sim$ 2° - 7°) from both sides. It was found that $\alpha_{tilt} = 24°$ fulfils these requirements giving $\alpha_{landing} = 8°$. The actual contact angle between the lamella and the chip is slightly larger as depicted in Fig. 3.5 because FIB does not produce parallel sided lamella without additional procedures. When the lamella is positioned as in step
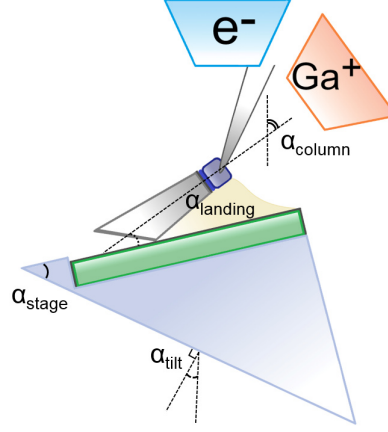
Figure 3.5: Geometry of the stage with a chip and the lamella on the needle during mounting procedure. Chip is the green rectangle, stage is light blue, lamella and the needle are depicted grey, Pt filling the void underneath is yellow. Electron and ion columns are depicted as blue and orange.

seven in Table 2, the void underneath is filled using platinum precursor gas. In the following step eight, the stage tilt is set to zero and the triangular stage is rotated, so the chip faces the ion column. Then, the front face of the lamella is covered with platinum contact electrodes.

3.2.2 Isolating cuts and polishing

Isolating cuts ensure that the lamella stays electrically non-conductive. First, the protective layer (made of either ion beam deposited carbon or platinum) is disconnected from the deposited electrodes on the sides. It is noted that the undercut region has been found to become conductive due to excessive damage during step four in the process flow (Table 1). The positions of the isolating cuts are shown in Fig. 3.6. The cuts are made with ion beam settings of 30 kV and 80 pA.

As shown in Fig. 3.7(a), the ion beam forms a trapezoid shape cross-section of the lamella, with the bottom part wider and the top part narrower. However, the parallel sided samples are beneficial for the interpretation of the domain structure.

To create parallel sided sample, the polishing angle must be determined. Firstly, the lamella is tilted so it faces the ion beam column directly and the faces of the lamella are polished at 30 kV and 80 pA, Fig. 3.7(a). This forms a trapezoid of the lamella. At this step the projected lamella height L_m can be measured. The lamella is tilted back, so it faces the electron column and careful measurements of the top

and bottom widths w_1 and w_2 are performed. The angle α is the deviation angle. From simple geometry it can be determined that:

$$\alpha = \mathrm{atan}\left(\frac{w_2 - w_1}{2L}\right) = \mathrm{atan}\left(\frac{(w_2 - w_1)\sin(54°)}{2L_m}\right), \tag{27}$$

where L can be either directly measured by rotating the lamella at an appropriate angle to the electron column or recalculated from $L = L_m/\sin(54°)$ (which gives close value to the true L). If the lamella is tilted to an angle $T = 54° + \alpha$, the
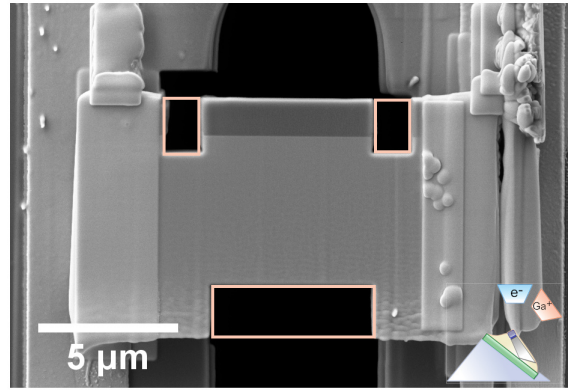
Figure 3.6: Isolating cuts of the lamella. Deposited electrodes are seen on the sides of the lamella. Isolating cuts are depicted with orange rectangles, the top cuts isolate protective layer from the bias lines, while bottom one removes highly damaged undercut region. Inset in the right-bottom part depicts geometry of the stage while making the cuts.
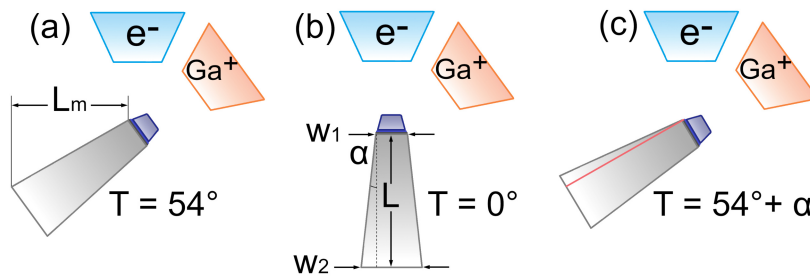
Figure 3.7: Determination of polishing angle. (a) Lamella is tilted directly against ion column (T = 54°), two cuts from both sides are made, which create trapezoid shape. Projected lamella height L_m can be also measured at this step. (b) Lamella is tilted to a position directly facing electron column (T = 0°), measurements of w_1 and w_2 are made. (c) Lamella is tilted at an angle $T = 54° + \alpha$, side facing the electron beam is polished, forming the first parallel side.

same beam settings are used and the face visible by electron beam is polished, then

the deviation angle is counteracted and parallel sides can be established (backside polishing is done at T = 54° - α).

When a lamella is mounted on a chip (i.e. triangular stage is used) and 24° stage tilt is used, then the polishing is done at T = 24° $\pm\alpha$. For BaTiO$_3$ polished at 30 kV and 80 pA, the deviation angle is α = 0.7°. Approximately 2 $\times$ 3 µm^2 electron transparent window with parallel faces is polished with 30 kV 80 pA ion beam settings followed by another isolation cut (red rectangle in Fig. 3.8) exactly under the electron transparent window. This cut is made very carefully so the freshly made thin window is not exposed to the ion beam. Finally, 5 kV and 30 pA polishing is done at 24° $\pm$ 4° angle to reduce the thickness of the amorphized layer formed on the faces by 30 kV Ga$^+$ ion beam. An example of the finished lamella on a MEMS chip is shown in Fig. 3.8. A chip containing the lamella is then plasma cleaned to remove the conductive layer formed by carbon coater on the MEMS chip as well as for the general cleaning of the specimen.
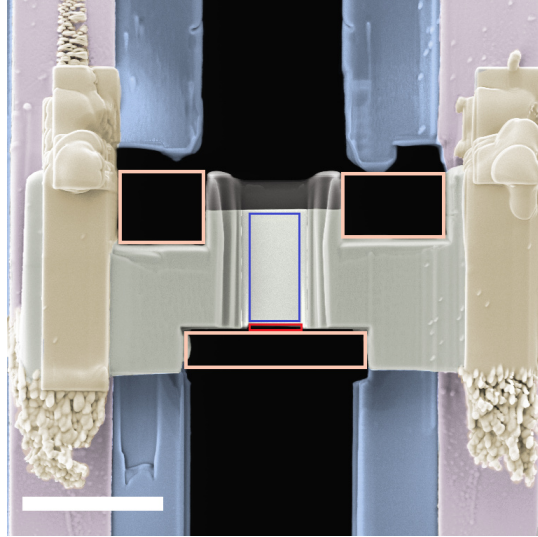
Figure 3.8: False color SEM image of a finished BaTiO$_3$ lamella on a chip. Orange coloured rectangles depict isolation cuts, red small rectangle shows the final isolation cut made directly underneath electron transparent window, which is depicted with blue rectangle. Black area corresponds to the vacuum region, blue to the silicon nitride membrane, pink to the Pt electrodes on the membrane, yellow to the FIB deposited Pt contact electrodes, grey to the bulk part of BaTiO$_3$, light grey to the electron transparent window, and dark grey to the protective carbon layer. Scale bar is 5 µm.

3.3 Finite element calculations

The planar geometry of the electrodes, the varying thickness across the lamella and the isolating cuts make it difficult to estimate the magnitude and the homogeneity

of the electric field within the electron transparent region. Therefore, electrostatic calculations of the lamella region were performed with finite element method (FEM). The goal is to link the sample geometry and the dielectric constant of the specimen to the magnitude of the electric field within the electron transparent region.

The electrostatic FEM model of the device was created with COMSOL MULTI-PHYSICS 5.4 package. The governing equation involved is:

$$\boldsymbol{\nabla} \cdot (\varepsilon_0 \varepsilon_r \boldsymbol{\nabla} V) = \rho, \tag{28}$$

where ε_0 is dielectric permittivity of vacuum, ε_r is the relative dielectric constant of the medium, ρ is the charge density and V is the electric potential.
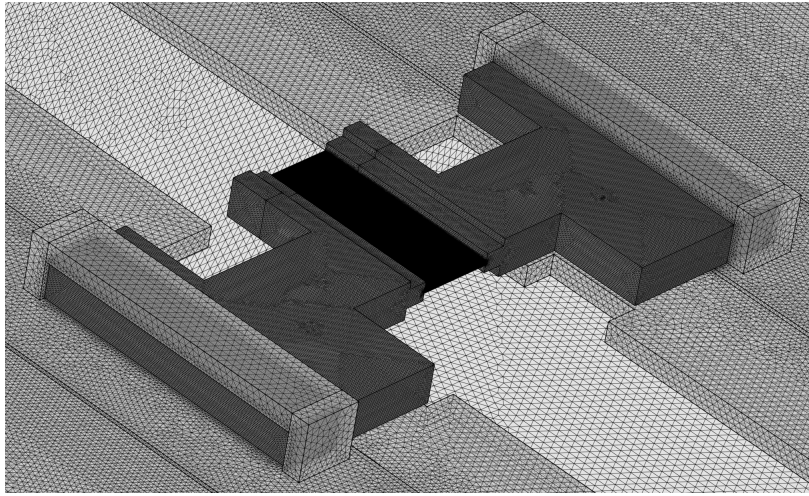
Figure 3.9: Geometry and the tetrahedral mesh used for the FEM model of the biasing MEMS device. The mesh in the electron transparent region is very fine, that is the reason, why it looks black in the image.

As input for the electrostatic model, the dimensions of the device were measured from SEM images. The dimensions of the simulation box were 40 µm width, 30 µm height, and 30 µm in depth. A tetrahedral adaptive mesh was used for the simulation. The general mesh element characteristics involved the electron transparent window of 0.02 µm max and 0.008 µm min, the bulk part of the lamella of 0.05 µm max and 0.008 µm min, the surface of the electrodes of 2.2 µm max and 0.16 µm min, the SiNx membrane of 0.2 µm max and 0.008 µm min, and the vacuum region around the device 0.25 µm max and 0.008 µm min. The geometry and the resulting mesh can be seen in Fig. 3.9. The bulk part of the lamella was set to 1 µm thick and the thickness of the electron transparent region was varied in order to understand the electric field's dependency on it. The relative dielectric constant of silicon nitride was used as per the COMSOL database ($\varepsilon = 9.7$), while the relative dielectric constant of the lamella was varied. The potential difference between the electrodes in the calculations was set to 1 V and it was used as a boundary condition.

3.4 Transmission electron microscopy

Transmission electron microscopes use fast electrons to image and probe electron transparent specimen. The electrons are manipulated by electric and magnetic lenses within column of the microscope. TEMs are complex instruments and herein I will describe some of their important elements.

Typical accelerating voltage of a laboratory TEM is between ~ 60 to 300 kV. The electron column and specimen are kept under high vacuum, which is ensured by mechanical, turbo-molecular and ion getter pumps.

The electron source that is prevalent in modern instruments is field emission electron gun. A schematic of it is shown in Fig. 3.10. An extraction voltage is applied to a sharp tungsten tip which creates a strong electric field at the sharp point. The electric field is approximately $E = V/r$, where V is the applied potential and r is the tip radius ($r < 0.1$ µm). The strong electric field reduces the workfunction barrier of the tungsten and allows electrons to tunnel out in free space. Free electrons are then accelerated with high potential [47]. The gun crossover acts as an electron source for
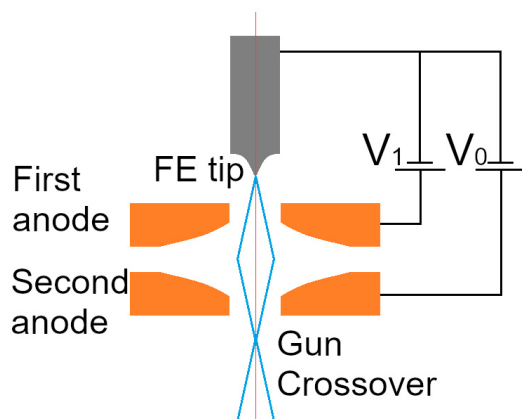
Figure 3.10: A schematic of a field emission gun (FEG). A sharp tungsten tip (grey) is positioned on the axis with two anode plates (orange), which have round holes. First anode is kept at voltage V_1 - extraction voltage - while the second anode is used to accelerate electrons (blue lines) to the desired kinetic energy ($V_0 \sim 60$ - 300 kV). After exiting the gun, electrons form the first crossover. Schematic based on image from ref. [47].

the illumination system of the rest of the transmission electron microscope's optical system.

The illumination system consists of various magnetic lenses, apertures, scan coils and electrostatic shutters. Two operating modes are used in the transmission electron microscope. In conventional transmission mode the sample is illuminated with a comparably large, parallel electron beam, Fig. 3.11(a), whereas in scanning transmission mode the electron beam is formed into a fine probe, which is raster scanned

across the area of interest, Fig. 3.11(b). The two modes require different excitations of the magnetic lenses as depicted in Fig. 3.11. In case of scanning TEM (STEM), Fig. 3.11(b), the upper objective lens is not shown because it acts as a transfer lens (or is turned off) and does not influence the ray diagram. In the case of conventional
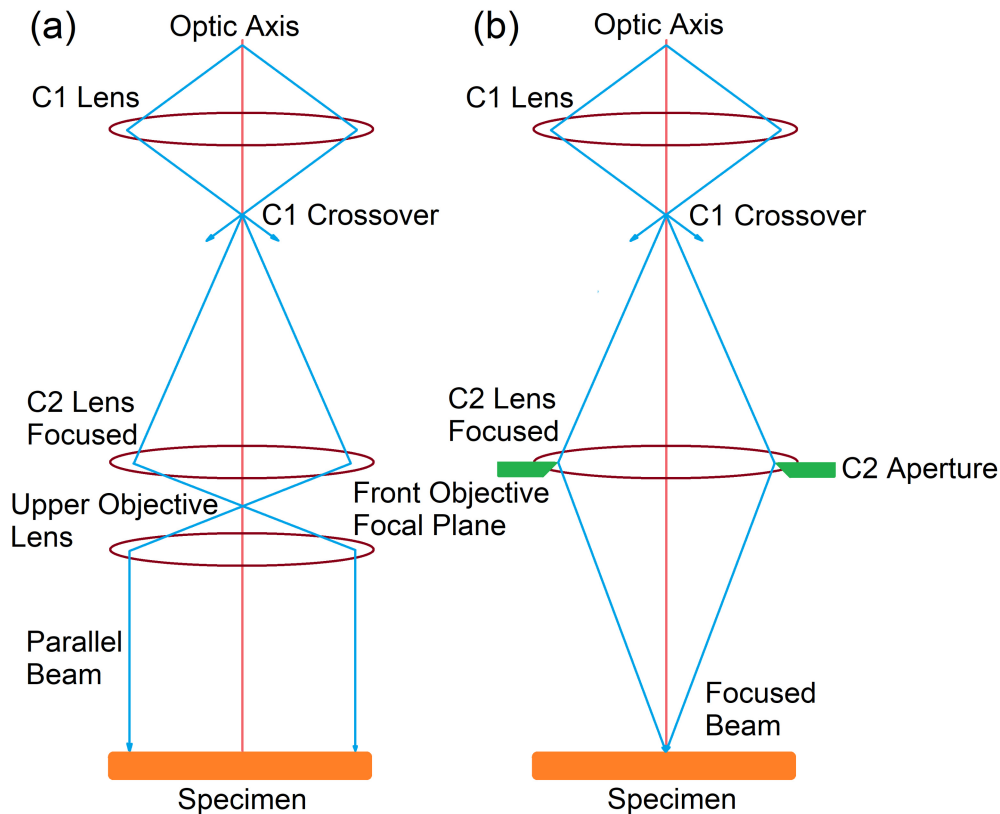
Figure 3.11: Illumination system of a transmission electron microscope. Electron beam is depicted as blue lines, electromagnetic lenses are brown ovals, optic axis is the red line. (a) Parallel beam formation in conventional TEM mode. (b) Fine electron probe formation on the surface of a specimen in STEM mode. Schematic based on image from ref. [47].

TEM mode, the imaging system can be used in two different ways, either to form a magnified image of the area or to form an image in reciprocal space creating an electron diffraction pattern of the imaged area. A schematic of the imaging system in TEM mode is shown in Fig. 3.12. The magnetic field of the intermediate lens is tuned to form an object as focal or image plane of the objective lens, which is then further magnified via the projection lens system. When the objective focal plane is used as an object for the projection system, electron diffraction patterns are formed, while a magnified image of the specimen is seen on the detector when the objective image plane is used as an object. The detector can be a fluorescent screen or a digital camera based on CCD or CMOS technology, which is used to acquire images in modern microscopes.
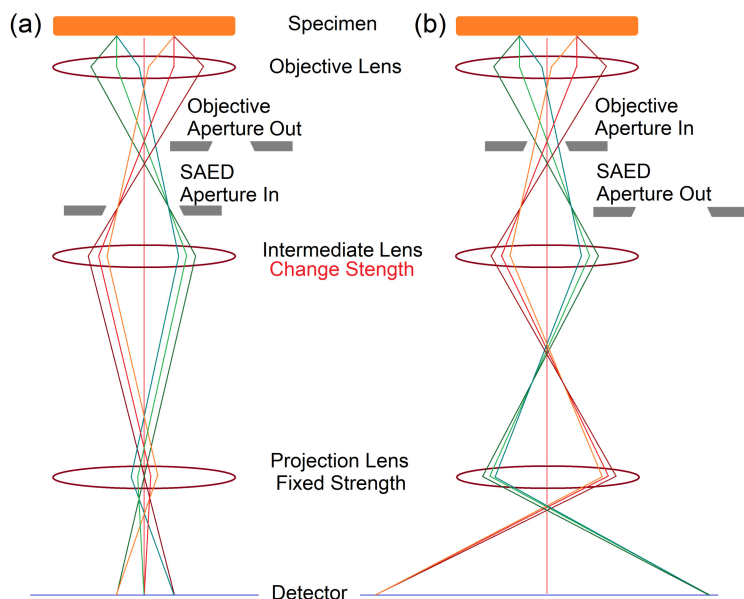
Figure 3.12: Imaging system of a transmission electron microscope in conventional TEM mode. (a) Formation of an electron diffraction pattern. (b) Formation of magnified image. The main differences between diffraction or imaging mode is in the intermediate lens, which forms the object for the projection system. SAED - selected area electron diffraction aperture is inserted in the image plane to select a region of a specimen, from which an electron diffraction pattern is acquired. Objective aperture is inserted in the back-focal plane of the objective lens. Schematic based on image from ref. [47].

In STEM mode the image formation is serial. A finely focused electron probe is scanned across the specimen usually in a raster pattern and the transmitted electrons are detected with specialized semiconductor or photo-electron multiplier detectors, Fig. 3.13. The fundamental difference between TEM and STEM modes is that in TEM mode the image is magnified with the electromagnetic lenses, while in STEM mode the magnification is achieved by scanning smaller and smaller areas with the electron probe.

STEM images can be formed by detecting either directly transmitted electrons by the bright field detector or by detecting scattered electrons by annular dark field and high angle annular dark field (HAADF) detectors, Fig. 3.13(b). An advantage of the STEM mode is that several signals can be acquired simultaneously, for example, revealing weakly absorbing features by white contrast in the bright field detector and highly scattering objects by white contrast in the annular detectors. It is noted that collection angles of the STEM detectors can be changed by virtually changing the distance (camera length) between the sample and the detectors. This is achieved by manipulating electron beams via lenses in the imaging system.

To image electromagnetic fields within specimen in STEM mode, annular seg-

mented detectors can be used. The most widespread segmented detector has four segments and is usually called DF4 (dark field 4 segment detector). Electromagnetic field imaging takes advantage of the charged nature of the electron. As the electron passes through electromagnetic fields it experiences Lorentz forces: $\mathbf{F} = q(\mathbf{E} + \mathbf{v} \times \mathbf{B})$ [68]. Assuming that the fields in the specimen are pointing in the orthogonal direction of the incoming electrons' velocity vector, then after the electrons have passed through the sample, they will have acquired additional speed component orthogonal to the initial velocity vector. That is, the internal electromagnetic fields deflect the electron beam [68]. The segments of the annular detector allows for the center of mass (COM) of the transmitted beam to be measured by the signal in each separate segment. A schematic representation of the operation of DF4 detector, when scanning a semiconductor p-n junction, is shown in Fig. 3.14 [68]. The beam deflection in the x and y directions can be calculated using the following equations:

$$W_x(\mathbf{k}) = \frac{\pi}{2\sqrt{2}} k_{BF}(W_A(\mathbf{k}) - W_C(\mathbf{k})), \tag{29}$$

$$W_y(\mathbf{k}) = \frac{\pi}{2\sqrt{2}} k_{BF}(W_B(\mathbf{k}) - W_D(\mathbf{k})), \tag{30}$$

where W_A to W_D are the signals in the respective segments of the DF4 detector (as depicted in Fig. 3.14), k_{BF} represents the convergence angle of the STEM probe, W_x and W_y are the differential phase contrast (DPC) signals in the x and y directions (measured in radians) providing a measurement of the deflection angle [69]. The electric field component perpendicular to the electron beam can then be calculated with the equation:

$$E_\perp = -\frac{\gamma m_e^* v_0^2}{et}, \tag{31}$$

where γ is the deflection angle, m_e^* is the relativistic electron mass, v_0 is the initial velocity of the incident electron, e is the electron charge and t is the thickness of the specimen [68].
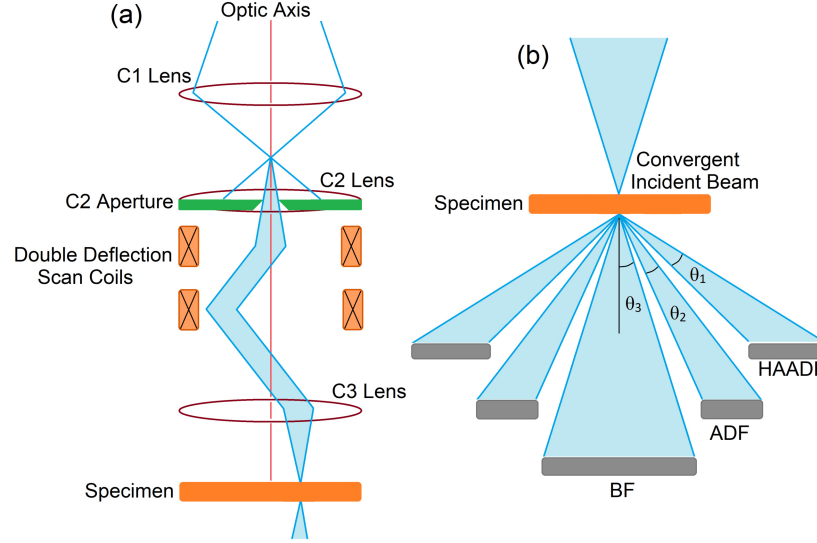
Figure 3.13: Scanning system in three condenser lens STEM system and a schematic of the typical STEM detectors. (a) A system of scanning coils is used to guide the electron probe across the specimen. In three condenser lens system C2 lens is only transferring the beam, not modifying it. (b) Typical STEM detectors - bright field (BF), annular dark field (ADF) and high angle annular dark field (HAADF). ADF and HAADF detectors have circular hole in the center. Typical angular values for the detectors are $\theta_1 > 50$ mrad, 10 mrad $< \theta_2 < 50$ mrad and $\theta_3 < 10$ mrad with respect to optical axis. Schematic based on image from ref. [47].
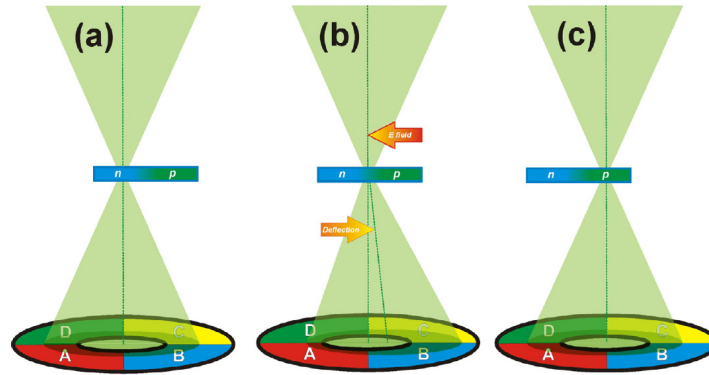
Figure 3.14: Schematic of the operation of DF4 detector. (a) The beam (green shading) is in the n-doped region of semiconductor, however there is no electric field, therefore the beam passes through the sample without deflection - all of the segments are illuminated evenly. (b) Electron beam is on the n-p junction, at this point there is electric field within the region. Electric field is pointing from right to left, consequently electrons are deflected to the right hand side and DF4 segments are not illuminated evenly. (c) Beam is in the p-doped region of the semiconductor, no internal electric field, the beam illuminates DF4 evenly. Reproduced from the ref. [68], by respecting *Creative Commons (CC-BY) license.*

49

Differential phase contrast microscopy has been validated on the p-n junctions and magnetic fields, however interpretation of the DPC contrast of the ferroelectric domain structure is not straightforward. Qualitative interpretation of the DPC signal of a ferroelectric is possible, however for its quantitative evaluation diffraction effects of the domain walls and the breakage of the Friedel's law must be taken into account (under kinematical diffraction conditions, the intensity of a reflection hkl is equal to the intensity in its opposite $\bar{h}\bar{k}\bar{l}$, which stays true for X-rays, but not for electrons due to the strong dynamic scattering) [47, 70]. Minor misalignment and the presence of a diffracted beam on the DF4 detector greatly complicates the quantitative analysis.

3.4.1   Relevant electron-matter interactions

In general, the interaction of fast electrons with matter generates a plethora of signals, which can be acquired to study the physical properties of the specimen. The most relevant physical processes are depicted in Fig. 3.15. Characteristic X-rays and
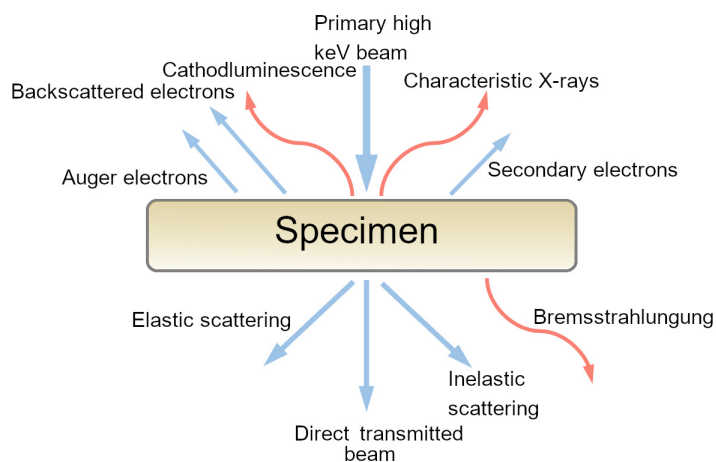
Figure 3.15: Physical processes induced by the fast incident electron beam. Blue arrow indicates that the carrier of the signal is an electron, red arrow indicates a photon.

inelastically scattered electrons carry valuable information on chemical constituents of the material and its electronic structure. The generation process of both signal carriers is linked.

Considering the characteristic X-ray signal, a fast incoming electron inelastically scatters on the electron laying in the deep K shell of the atom. During this process the fast electron loses some part of its energy. The electron from the K shell gets additional energy and is either ejected in the vacuum or is transferred to the empty states above the Fermi level. Assuming the latter, as the hole in the K shell is energetically unfavourable, an electron from either L_3 or L_2 shell transitions to lower laying K shell in the process losing energy as a photon (there are other possibilities,

but the selection rules show that the transitions from $L_{3,2}$ are most likely to happen). As the deep energy levels of the atom are very well defined, the photon carries energy characteristic to the particular element and the particular transition (Fig. 3.16). Characteristic X-rays are routinely analyzed in the TEM with Si based semiconductor detectors. The technique is called energy dispersive X-ray spectroscopy (EDS or EDX) [47].

However, if we assume that the K shell electron got ejected to an empty state within an atom, then the fast electron, which induced the X-ray emission, also carries information. It has lost kinetic energy with exact amount necessary to transfer the K shell electron to the conduction band. Such inelastically scattered electrons are probed via electron energy loss spectroscopy (EELS).
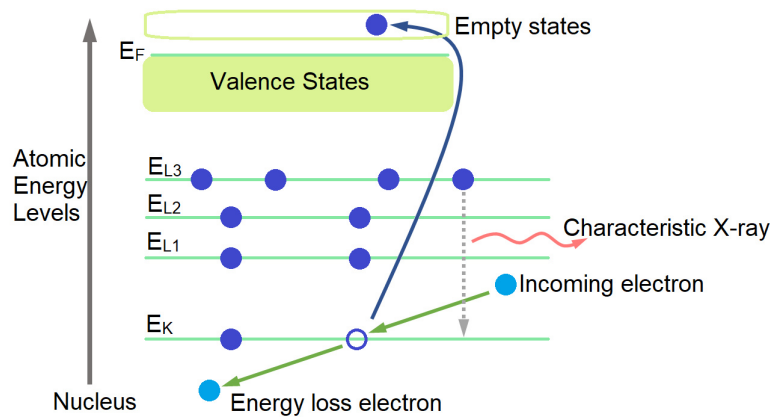
Figure 3.16: Electron scattering on the deep atomic electrons. Incoming electron loses some of the energy in the scattering process to the K shell electron, which gets transferred to the empty states above Fermi level. This induces cascade of transitions within atom. As the energy levels deep in the nucleus potential are well defined, emitted X-ray has characteristic wavelength for the particular transition for the particular element. Schematic based on image from ref. [47]

3.4.2 Measurement of transmitted electron energy

In order to probe the inelastically scattered electrons, a method to measure their kinetic energy is required. In other words, electrons must be sorted by their speed. Fortunately there are several possibilities to achieve this with the help of magnetic and electric fields.

One of the most widely used approach involves usage of so called 90° magnetic prism [71]. This device can be conveniently added to the transmission electron microscope. After the electrons have passed through the sample and some of them have interacted with the specimen and lost some of their energy, they are gathered at the last projector crossover as seen in Fig. 3.12. However, instead of being

directly projected on a screen or camera, the electrons enter the 90° magnetic prism (essentially an angled tube with constant magnetic field orthogonal to the velocity vector of the incident electrons), Fig. 3.17 [71, 72]. Impacted by the magnetic field, the electrons enter a circular trajectory with a radius of curvature given by the expression:

$$R = \left(\frac{\gamma m_0}{eB}\right)v, \tag{32}$$

where $\gamma = 1/(1 - v^2/c^2)^{1/2}$ is the relativistic correction, m_0 is the rest mass of the electron, e is the electron charge, B is the magnitude of the magnetic field in the prism and v is the speed of the electron. From this follows that slower electrons have smaller radius of curvature, therefore they are deflected more by the action of the magnetic field [71]. The magnetic prism also focuses the divergent electron beam as can be seen in Fig. 3.17. Electrons, which enter the prism on the left hand side, travel longer distance in the magnetic field as compared to ones which enter the spectrometer on the right hand side.Therefore, the left hand side of the divergent beam is deflected more, while the right hand side of the beam is deflected less. The actual spectrometers have much more optical elements, but the core working principle is as described herein.
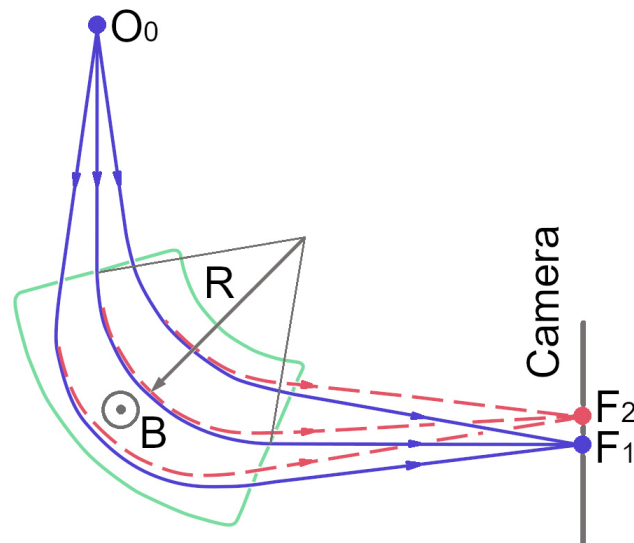
Figure 3.17: A schematic of 90° magnetic prism. O_0 is the last crossover of the imaging system of the microscope, the electrons continue the path until they encounter green region representing 90° magnetic prism, which has constant magnetic field **B** pointing out of the page. The electrons experience magnetic Lorentz force and are deflected. Faster electrons (blue) have larger radius of curvature, while electrons, which have lost comparably more energy (red dashed lines) have a trajectory with smaller radius of curvature and are deflected more. The spectrometer also focuses the sorted electron beams on the camera (F_1 and F_2), where the spectrum can be recorded.

3.5 General EELS features

A typical EELS spectrum representation with a schematic of the solid state electron energy levels is shown in Fig. 3.18. The most intense feature in the EEL spectrum (if specimen is sufficiently thin) is the zero loss peak which represents electrons that have not lost any energy. The zero loss peak (ZLP) is located at 0 eV in the energy loss scale and is used to calibrate the scale [71]. The lowest possible excitations in the EELS spectrum are atomic lattice vibrations (phonons). However they are located in the energy range of 10 - 100 meV, and specialized instruments are used to probe them [71]. In most cases these excitations are hidden by the zero loss peak as the typical full width half maximum (FWHM) of ZLP is $\sim$ 0.1 - 1 eV, therefore they are not discussed in Fig. 3.18.
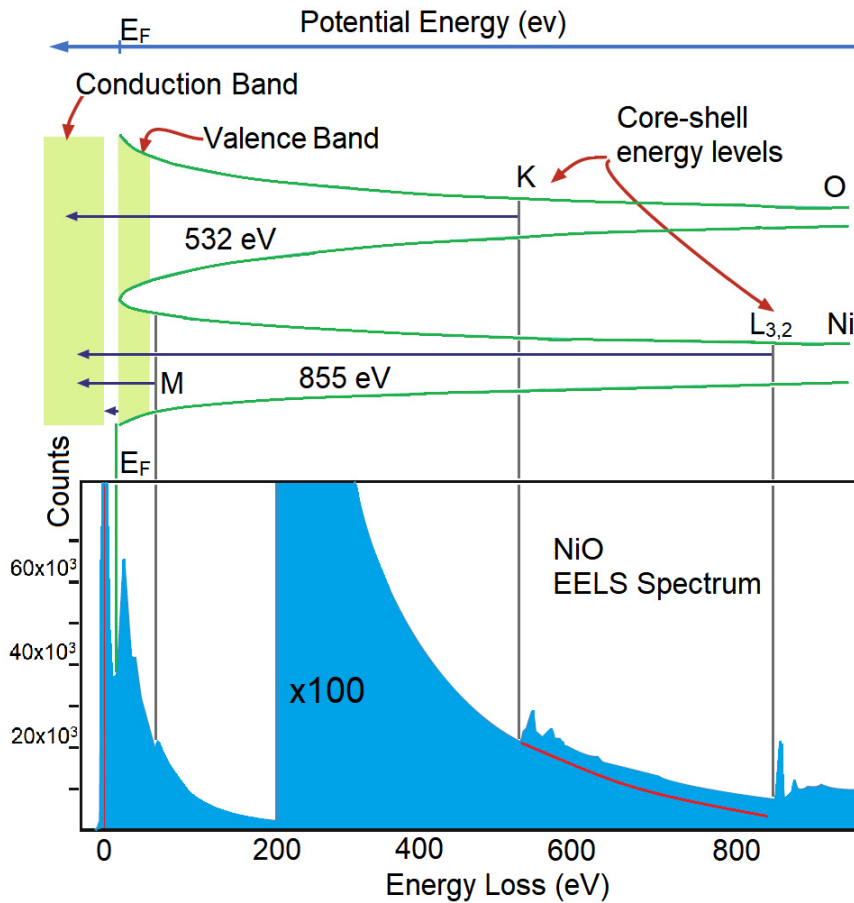
Figure 3.18: Schematic EELS spectrum (bottom) and representation of the visible core loss transitions from the atomic potential wells. At 0 eV ZLP is seen (not in full height), low loss region is dominated by the plasmon peak. Upon increasing energy losses, the count rate drops, relevant absorption edges of the oxygen and nickel atoms are seen at 532 eV and 855 eV. Schematic based on image from ref. [47].

The onset of the EEL spectrum right after the zero loss peak (shown by the green vertical line in Fig. 3.18) represents the band-gap width (for insulators or semiconductors). The onset originates from the transition between the highest band in the valence zone to the lowest band in the conduction zone. In principle, there should be no other transitions in the region between the ZLP and the bandgap onset (if the material is defect free).

The next more prominent feature is the plasmon resonance peak [71, 72]. In Fig. 3.18 it is located between lines representing E_F and M transitions. The plasmon peak corresponds to the resonant oscillation of the valence band electrons. It is noted that additional features may arise around the plasmon resonance peak due to the interband transitions. Overall, the region between 0 to 50 eV in the EELS spectrum is known as low loss region (albeit there is no strict definition as per [71] the boundary of the low loss region is somewhere in between 50 - 100 eV).

The energy loss region above $\sim$ 50 eV is known as the core loss region. The first core loss feature in the example spectrum of Fig. 3.18 is nickel $M_{3,2}$ transition (located at 68 eV), where electrons are ejected from the 3p shell and transferred to the empty states of partially filled 3d shell. Technically this would count as a core-shell transition, however the absorption edge is located close to the plasmon peak, which indicates that solid state effects may have also affected the 3p level. Although this is the first observable feature in the core loss spectrum, it does not mean it is the only one. For example there is also the transition M_1 of the nickel, located at 112 eV, but the absorption cross-section is small and the feature is very weak and not represented in the figure.

As the energy loss becomes larger, the count-rate rapidly drops and for the next features, the spectrum is magnified $\times100$. At 532 eV the oxygen K transition occurs where 1s electrons are transferred to empty density of states of 2p like orbitals. The form of the absorption edge is square like. Although from an ionic point of view the 2p shell of the oxygen atoms in a NiO compound is filled, from the perspective of solids, they form bands and hybridized orbitals/states. In the case of oxygen in NiO, there are 2p like empty states in the conduction band, which occur due to the hybridization with nickel 3d (and other) states. Therefore, the oxygen K edge reveals local electronic structure and bonding effects of the oxygen atoms. Under the oxygen K edge, the red line represents the background which is approximated by fitting a power law function ($I = A \cdot E^{-r}$, where A and r are fitting parameters and E is the energy) just before the absorption edge (end of the fitting range is usually 5 eV less than the onset of the absorption edge) and extrapolating it further down the energy scale [71]. Removal of the background is necessary for the quantitative elemental analysis as well as for extracting fine features of the absorption edge.

The final absorption edge seen in Fig. 3.18 is nickel $L_{3,2}$ edge, which corresponds to the transition from the core 2p to empty 3d states. This transition appears as two sharp peaks followed by a smooth absorption onset. The two sharp lines (also

called white lines) represent the localized empty 3d orbitals of Ni. The absorption edge appears as a doublet due to the spin orbit splitting of the initial electron orbital (2p orbital splits in to $2p_{1/2}$ and $2p_{3/2}$, where the first contains two electrons and the latter one four). The $L_{3,2}$ absorption edge contains rich information on the electronic structure of the transition metal 3d orbitals. Analysis of the onset energy and relative intensity ratio of L_3/L_2 white lines reveals information on transition metal oxidation state. Analysis of the white lines fine structure gives information on the coordination environment of the transition metal ion and the 3d density of states [71].
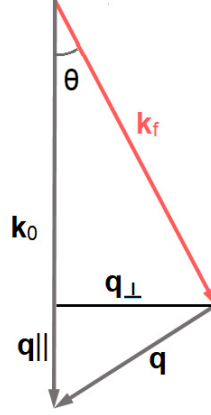
Figure 3.19: Representation of electron wave vectors before and after scattering event. As the energy is lost [magnitude of $\mathbf{k_o}$ (grey) is larger than $\mathbf{k_f}$ (red)] the momentum is transferred to the specimen. As the scattering angle (θ) is usually small, Transferred momentum can be separated in to two orthogonal components $\mathbf{q} \parallel$ and $\mathbf{q} \perp$.

During these processes the electron is scattered inelastically and, hence, the momentum of the electron not only changes direction but also magnitude. The initial wave-vector of the electron is $\mathbf{k_0} = 2\pi/\lambda_0$, where λ_0 is the initial wavelength of the electron. The final wave-vector of the electron after suffering energy loss and being scattered is $\mathbf{k_f}$. The momentum transfer suffered by the incident electron $\mathbf{q}(h/2\pi)$, and the momentum received by the sample have opposite signs: $-\mathbf{q}(h/2\pi)$, where h is Planck's constant and $\mathbf{q} = \mathbf{k_0} - \mathbf{k_f}$. A schematic representation of the scattering by the wave vectors is shown in Fig. 3.19. For fast incident electrons, $\mathbf{q}$ is much smaller than $\mathbf{k_0}$ and using the approximation $\sin(\theta) \sim \theta$ it follows:

$$q^2 = q_{\parallel}^2 + q_{\perp}^2 = k_0^2(\theta_E^2 + \theta^2), \tag{33}$$

where θ is the scattering angle and θ_E is the characteristic angle of scattering corresponding to the mean energy (E_{av}) loss: $\theta_E = E_{av}/(\gamma m_0 v^2)$, where γ is the relativistic correction for the rest mass m_0 of an electron travelling at the speed v [72]. From Eq. 33 it follows that $q_{\parallel} = k_0\theta_E$ and $q_{\perp} = k_0\theta$ (for small θ). In most experiments, electrons which have scattered close to $q_{\parallel}$ are collected and the orthogonal component

is neglected. However, measurement of EEL signal at higher scattering angles may reveal information on the anisotropic properties of the specimen and directionality of bonding (with a cost of even smaller count rates as the energy loss electrons are highly forward scattered [71]).

3.5.1 Low loss EELS

The electrons undergoing scattering in a medium obey Poisson's distribution. Assuming independent scattering events, the electron integrated intensity is given by:

$$I_n = I \cdot P_n = (I/n!)(t/\lambda)^n \exp(-t/\lambda), \tag{34}$$

where I_n is the intensity of the n-th order scattering integrated over all energy loss, I is the total integrated intensity (sum over all n scattering events), P_n is the probability of the electron scattering in the specimen n times, t is the sample thickness and λ is the mean free path of the fast electrons in the specimen [71]. If n is set to zero, then I_0 corresponds to the integrated intensity in the non-scattered, ZLP beam. As the mean free path ($\lambda \sim 100$ nm) is on the same order as the usual specimen thickness, then almost inevitably many electrons suffer two or more energy loss events. It is better to avoid multiple scattering, by using thinner specimen or by increasing the accelerating voltage of the incident electrons (i.e increasing the mean free path of the electron in the medium). However, multiple scattering allows to measure the relative thickness of the sample via the expression:

$$\frac{t}{\lambda} = \ln\left(\frac{I}{I_0}\right), \tag{35}$$

where I is the total integral intensity of the spectrum (including ZLP) and I_0 is the integral intensity of the ZLP only [71]. If λ is calibrated on a sample of known thickness or estimated from theoretical calculations, absolute thickness measurement can be done.

The effect of the multiple scattering in the EEL spectrum is the increasing intensity with increasing energy loss (blue shaded spectrum in Fig. 3.20). Precise analysis of the low loss EEL spectrum, requires knowledge of the single scattering events. The single scattering spectrum can be extracted from the raw, multiple scattering affected data by Fourier log deconvolution:

$$s_1(\nu) = z(\nu) \ln\left(\frac{j(\nu)}{z(\nu)}\right), \tag{36}$$

where $s_1(\nu)$ is the single scattering distribution in Fourier space, $z(\nu)$ is the Fourier transformed ZLP and $j(\nu)$ is the Fourier transformed EEL spectrum containing the ZLP [71]. The units of ν correspond to inverse energy. The single scattering EEL
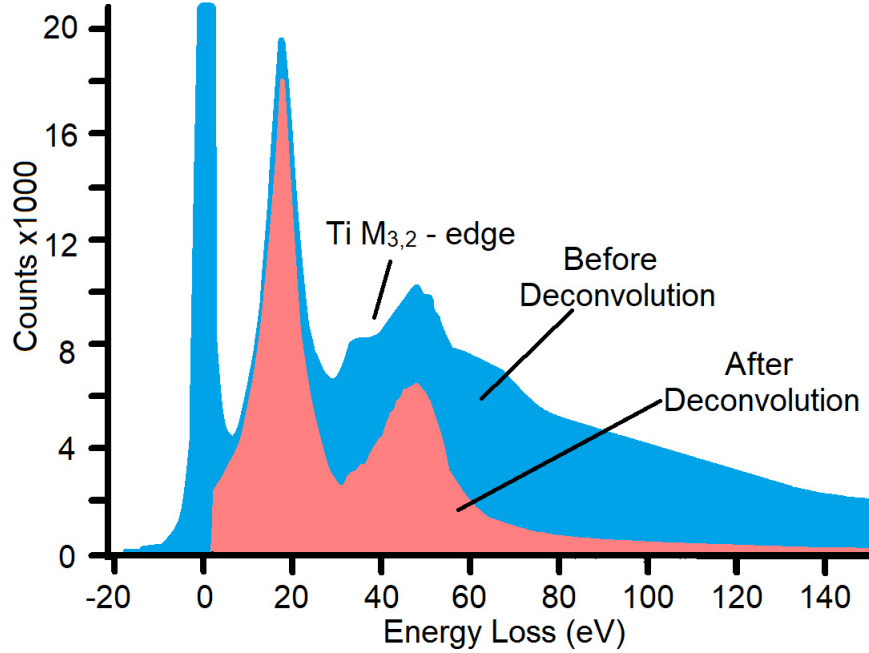
Figure 3.20: Low loss region of Ti alloy specimen. Effect of multiple scattering is seen in the spectrum before deconvolution, after deconvolution ZLP is removed as well as excess intensity at the high loss region giving single scattering distribution. Based on image from ref.[72].

distribution $[S(E)]$ is obtained by the inverse Fourier transform of $s_1(\nu)$ and taking the real part of the result. After such operation, the spectrum containing only single scattering is obtained (red-shaded spectrum of Fig. 3.20). Successful deconvolution means zero intensity of the ZLP region as well as reduced intensity at high energy loss. Simple Fourier log deconvolution is applicable to the case where $q_\perp \sim 0$.

The features of the low loss EEL spectrum can be understood via Drude's model, which approximates the valence electrons as coupled oscillators interacting with each other and with the transmitted electrons via electrostatic forces [71]. Although developed for free electron gas, it describes well low loss EELS for metals and it gives qualitative description of semiconductors and even dielectrics. Plasmons in Drude's model can be understood as collective resonance oscillation of the valance electrons. It can also be shown that the single scattering distribution is proportional to the imaginary part of the negative inverse dielectric function $S(E) \sim \mathrm{Im}\{-1/\varepsilon(E)\}$ [71]. In the general case, with $\mathbf{q} \not\sim 0$:

$$S(E, \mathbf{q}) \sim \mathrm{Im}\{-1/\varepsilon(E, \mathbf{q})\}, \tag{37}$$

with the complex dielectric function equal to $\varepsilon = \varepsilon_1 + i\varepsilon_2$, which is dependent on both energy and momentum.

The dielectric response of Drude's model is given by:

$$\varepsilon_1 = 1 - \frac{E_p^2}{E^2 + (1/\Gamma)^2}, \tag{38}$$

$$\varepsilon_2 = \frac{\Gamma}{E} \frac{E_p^2}{E^2 + (1/\Gamma)^2}. \tag{39}$$

Where E is the oscillation energy (frequency), E_p is the plasmon oscillation energy and $\Gamma = 1/\tau$ represents the damping of the oscillation and consequently FWHM of the plasmon peak by $\Delta E_p = \frac{h}{2\pi}\Gamma$ [71, 73]. If interband transitions are present, then additional terms must be appropriately added to the free electron dielectric response [71, 73]:

$$\varepsilon_b = 1 + \frac{E_p^2}{E_b^2 - E^2 - i \cdot E \cdot \Gamma_b}, \tag{40}$$

where E_b represents the energy at which the transition happens and Γ_b is the damping constant of the particular transition (Γ and Γ_b may not be equal). Previously mentioned $\mathrm{Im}\{-1/\varepsilon(E)\}$ is calculated by:

$$\mathrm{Im}\{-1/\varepsilon(E)\} = \frac{\varepsilon_2}{\varepsilon_1^2 + \varepsilon_2^2}. \tag{41}$$

Similarly $\mathrm{Re}\{1/\varepsilon(E)\}$ is calculated via:

$$\mathrm{Re}\{1/\varepsilon(E)\} = \frac{\varepsilon_1}{\varepsilon_1^2 + \varepsilon_2^2}. \tag{42}$$

To give a general representation of the dielectric response at the low loss regime, a model was simulated with two transitions, one with energy ($E_{b1} = 10$ eV) smaller than the plasmon resonance ($E_p = 16$ eV) and the other one with larger ($E_{b2} = 30$ eV). All the transitions and plasmon resonance have the same damping constant $\Gamma = 4$ eV. In Fig. 3.21(a) the interband transitions appear as peaks in the imaginary part of the dielectric response, while the plasmon resonance is located where the real part crosses zero with a positive slope and the imaginary part does not show any peaks [71]. On the other hand, Fig. 3.21(b) depicts the negative inverse imaginary part which is proportional to the EELS low loss measurement. However, the plasmon and interband transition peaks are not exactly at the transition energies set in the model. When the transition occurs below the plasmon resonance, then the plasmon resonance energy is increased (more electrons can participate in the oscillation), while the opposite is true for the transitions at the energies larger than E_p. In this case, the electrons are bound and cannot participate in the oscillation, additionally damping also influences the position of the plasmon peak in $\mathrm{Im}\{-\frac{1}{\varepsilon(E,\mathbf{q})}\}$ [71].

To obtain $\mathrm{Im}\{-1/\varepsilon\}$ from single scattering events in EELS data, appropriate
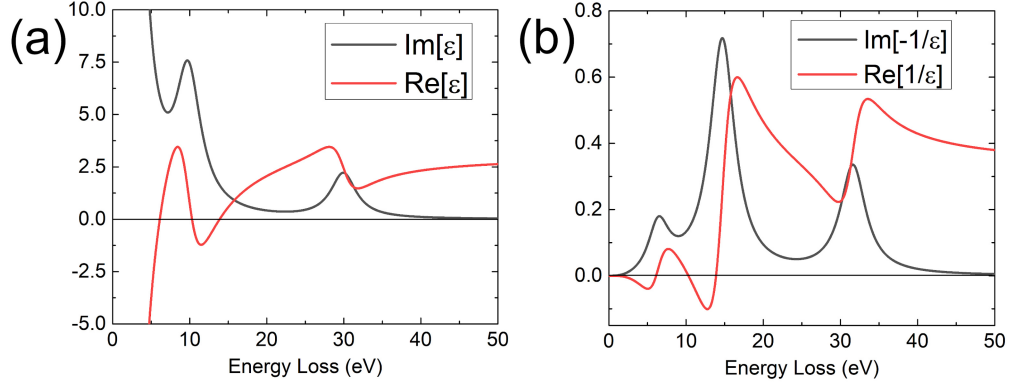
Figure 3.21: Dielectric response of a Drude's model with two transitions and a plasmon resonance. Two interband transitions are located at 10 eV and 30 eV, plasmon resonance is set at 16 eV. (a) Real and imaginary parts of the dielectric function. (b) Real and imaginary parts of the inverse dielectric functions.

scaling of $S(E)$ must be done. One option is to use Kramers-Kronig analysis, which connects real and imaginary parts of the inverse dielectric response [71]. For a general case:

$$\text{Re}\{1/\varepsilon(E, \mathbf{q})\} = 1 - \frac{2}{\pi}P\int_0^\infty \text{Im}\left\{-\frac{1}{\varepsilon(E', \mathbf{q})}\right\}\frac{E'dE'}{(E')^2 - E^2}, \qquad (43)$$

where P stands for the Cauchy principal value (necessary to deal with the singularity at $E' = E$). In the optical limit ($\mathbf{q} \sim 0$) and at at small energies ($E \sim 0$), the left hand side approximates $\text{Re}\{1/\varepsilon(0,0)\} \approx 1/\varepsilon_1(0)$, where $\varepsilon_1(0)$ is the square of the refractive index for visible light or $\varepsilon_1(0) \sim \infty$ for a metal. Therefore, the left hand side of Eq. 43 gives the scaling value, when the $\text{Im}\left\{-\frac{1}{\varepsilon(E')}\right\}$ is substituted for the measured single scattering spectrum $S(E')$.

Appropriate scaling of $S(E)$ allows to retrieve $\text{Re}\{1/\varepsilon(E)\}$ via previously shown Kramers-Kronig relation and also the complex dielectric function with:

$$\varepsilon(E) = \varepsilon_1(E) + i \cdot \varepsilon_2(E) = \frac{\text{Re}\{1/\varepsilon(E)\} + i \cdot \text{Im}\{-1/\varepsilon(E)\}}{(\text{Re}\{1/\varepsilon(E)\})^2 + (\text{Im}\{-1/\varepsilon(E)\})^2} \qquad (44)$$

3.5.2 Core loss EELS

Core loss EELS probes the empty density of states of a substance with the electrons ejected from the deep potential of the atomic levels as depicted in Fig. 3.22. For small collection angles (i.e. electrons collected with a small component of $\mathbf{q}_\perp$), the EEL signal originating from the transitions between core level to the empty density of states obeys the dipole selection rule, that is the change in the angular momentum of the states is $\Delta l = \pm 1$. Thus, K type transitions (initial electron state is 1s orbital) probe p-like empty orbitals, L_1 transitions (initial state of the electron is 2s orbital)
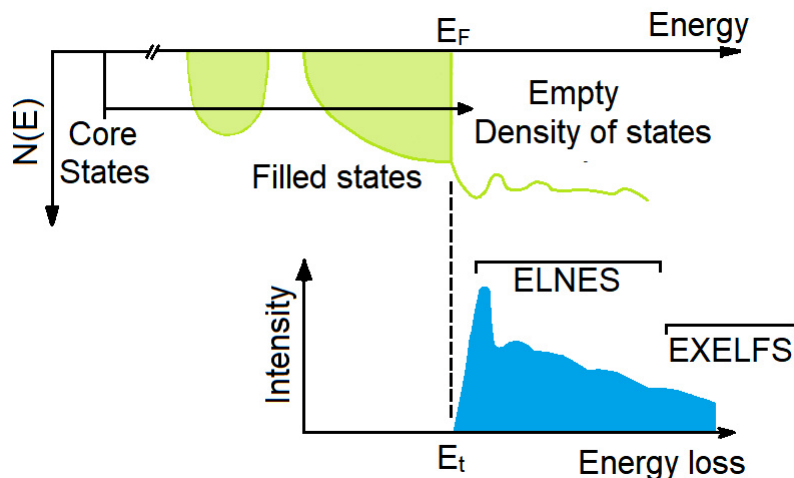
Figure 3.22: Schematic diagram of core loss EELS formation ELNES represents empty density of states probed by the electrons ejected from the deep atomic potential. EXELFS part represents interference of the ejected electrons on the neighboring atoms (appears as oscillations in the loss signal). Based on image from ref. [72].

also probe p-like empty states, while $L_{3,2}$ reflect transitions from spin-orbit split 2p core level, which probe d-like and s-like empty states [72].

Two regions of the core loss response can be isolated: the energy loss near edge structure (ELNES), which span 30 - 40 eV above the absorption edge onset (E_t in Fig. 3.22) and the extended energy loss fine structure (EXELFS), which appears at higher energy losses [72]. For the first row transition metals, ELNES of $L_{3,2}$ transitions mostly reflect localized empty states of the 3d orbitals, which appear as sharp peaks in the core loss EELS, while the empty 4s state (if the metal is in a compound) is de-localized due to solid state effects and appears as broad background on the sharp 3d response.

The transition metal $L_{3,2}$ absorption edge gives rich information on the oxidation state (i.e. filling of the 3d orbitals) and also coordination environment of the metal atom, as the 3d states are much more localized as 4s states, while still highly influenced by the ligands surrounding the transition metal atom [71]. For example, tetrahedral and octahedral coordination of the transition metal with the same oxidation state produce different ELNES shape of the $L_{3,2}$ transition.

EXELFS originates from the scattering of the ejected electron on the atoms located in the closest two to three coordination spheres. Treatment of EXELFS signal can give radial distribution function of the atoms surrounding the one that suffered the absorption event [71].

Similarly as in the case of low-loss EELS, core-loss EELS also suffer from plural scattering. For the core loss data Fourier ratio method is usually employed to remove the excess intensity after the edge onset originating from the plural scattering effects

according to the relation:

$$j_k^1(\nu) = z(\nu)[j_k(\nu)/j_l(\nu)], \tag{45}$$

where $j_k^1(\nu)$ is the single scattering spectrum of the background subtracted absorption edge in Fourier space, $z(\nu)$ is the Fourier transformed ZLP, $j_k(\nu)$ is the background subtracted absorption edge (as measured) and $j_l(\nu)$ is the Fourier transformed low loss EELS part (up to ~ 100 eV), ν is measured in units of inverse energy [71]. To retrieve single scattering spectrum in direct space, $j_k^1(\nu)$ is inverse Fourier transformed and then the real part of the result corresponds to the single scattering spectrum - $J_k(E)$.

3.5.3 Low-loss EELS modelling with density function theory

As previously discussed, EELS represents transitions to the empty density of states or the collective oscillation of the valence electrons. If the density of states for a particular material is known, then transitions can be modelled with appropriate methods.

Low-loss EELS of periodic solids can be effectively calculated with Quantum Espresso code in combination with TurboEELS package [74–76].

Quantum espresso calculates the electronic structure of the materials with the density functional theory (DFT) in reciprocal space employing plane wave self consistent field approach (PWscf). Quantum espresso uses pseudo-potentials, that is the electron DOS is calculated only for the valence and semi-core states, while the effects of core state electrons (which do not participate in bonding or band formation of a solid) are substituted with an effective potential. This readily reduces the number of electrons involved in the calculations, therefore simplifying the problem.

TurboEELS package uses time dependent density functional theory (TDDFT) to calculate low-loss EELS response of the material. The calculations involve the Liouville–Lanczos iterative approach.

3.5.4 Core-loss EELS modelling with density function theory

The EELS and x-ray absorption spectroscopy (XAS) spectral shape is given by the Fermi golden rule. The core electron is excited to an empty state where, at the edge, the lowest empty state (allowed by the selection rules) is reached. Therefore, the simulation codes developed for the XAS can be used to calculate core-loss EELS. However, effects such as very large collection angles during EELS acquisition which can lead to higher order effects beyond dipole approximation, must be taken into account when compared to simulations since they might influence the experimental

spectrum [77, 78].

The FDMNES code is designed to calculate core level XAS absorption spectra [79]. Calculations are done in real space where an atomic cluster is made from the crystallographic unit cell model at desired cut-off range. The density of states is calculated with Hedin–Lundquist density functional [79]. The calculated density of states is then used for the desired transitions and absorption spectra. FDMNES can be used in conjunction with TDDFT, which helps to calculate more precise the $L_{3,2}$ edges of the transition metals.

4 Biasing of 180° domain walls in BaTiO$_3$

Local hard and soft pinning of 180° domain walls in BaTiO$_3$ probed by *in situ* transmission electron microscopy

Reinis Ignatans, Dragan Damjanovic and Vasiliki Tileli
Institute of Materials, École Polytechnique Fédérale de Lausanne,
CH-1015 Lausanne, Switzerland

Contributions of R. Ignatans: performed sample preparation, in situ experiments, data analysis, finite element calculations and wrote the manuscript with the contributions from all authors.

4.1 Introduction

Understanding the electrical response, polarization switching, and domain wall movement processes in ferroelectric materials is important for the envisioned future applications such as field effect transistors for neuromorphic systems or the resurgence and optimization of devices including ferroelectric random access memories (FeRAMs) [15, 81]. Particularly important is polarization switching through nucleation and movement of ferroelectric 180° domain walls as they offer the least amount of emerging strain during operation, thus minimizing issues associated with mechanical failure and cracking [17]. The functionality of many ferroelectric devices depends on the speed of switching of the polarization states or domains [82, 83] and this is directly linked with the domain-wall movement. Understanding the dynamics of the domains walls is highly relevant also to already commercially applied ferroelectrics as domain wall movement contributes to the high dielectric permittivity, excellent electromechanical response and associated electrical, dielectric and mechanical loss mechanisms in ferroelectric Perovskite oxides [84, 85].

The origins of ferroelectricity at atomic scale can be understood via various quantum-mechanical, order-disorder and displacive mechanisms [86–90]. Neglecting the atomistic origins of ferroelectricity, Landau's phenomenological theory and its derivatives successfully deal with the phase transitions and the macroscopic physical properties of the material and their dependencies on the external stimuli [42, 91–95]. Between the atomic and macroscopic scale lays the domain structure of the ferroelectric that can be experimentally accessed via various microscopy and scattering techniques [17]. Dynamic studies of the ferroelectric domain structure under external electric field in the mesoscopic length-scale is relevant due to the strong influence on the macroscopic properties of the material. The domain response on the electric field is typically probed indirectly using dielectric spectroscopy, polarization- or strain- response as a function of field, current response during switching or *in situ* diffraction techniques [96, 97]. These methods reveal mostly the average behaviour of the system. Studies of the local domain response usually involve piezo-force microscopy (PFM) or *in situ* transmission electron microscopy (TEM) [61, 98, 99]. With PFM, quantitative measurements are difficult and the electric field is inherently inhomogeneous [100]. Technical requirements for interpretable *in situ* electric-field biasing results in the TEM also make the experiments challenging. For instance, specimen preparation is required to result in a sample with high electrical resistivity otherwise the current would flow across the conductive channels and the actual electric field would be smaller than the nominal (applied) field. In that case, the observed response would be dominated by Joule heating instead of the applied electric field. In most cases localized Joule heating leads to sample failure (cracking, electrode delamination due to the current surge, or complete sample disintegration). In all cases, it is necessary for the applied electric field to be homogeneous across the probed area

in order to reduce complexity in interpretation of the observed dynamic processes. To perform *in situ* electrical biasing experiments in the TEM, several methods are available. Traditionally, biasing experiments were performed on TEM holders that could accommodate mechanically polished samples connected with electrodes far away from the area of interest, which could be contacted in several ways (wire bonding, silver paste, etc.). The main advantage of this method is the excellent TEM sample quality, [56, 58, 59, 101] however, the resulting electric field in a mechanically polished sample cannot be uniform and it is also difficult to control the geometry of the region of interest with respect to the direction of the electric field [57, 59].

For better control of the applied voltage, the probe technique is used for biasing ferroelectric structures in the TEM. In this case, a metallic probe is pressed against the ferroelectric material to apply the potential [102–104]. However, since ferroelectrics are highly responsive to the applied external stress, pressing the probe against the material can adversely influence the formation and switching of the domains. Additionally, this method creates a highly inhomogeneous local electrical field, which hinders interpretation of the results. These issues can be mitigated by sandwiching the ferroelectric between conductive layers and pressing the probe on the conductor far away from the region of observation [62]. Nevertheless, such configuration is viable for thin films [63], but not for samples with larger areas such as single crystals or ceramics and restrictions imposed on the sample geometry with the addition of conductive layers can influence the inherent switching properties of the ferroelectrics through interfacial effects. More recently, advances in TEM holder instrumentation enabled microelectromechanical (MEMS) Si-based chips with patterned electrodes deposited on silicon nitride membranes to be used for heating and biasing experiments. The sample is transferred on such chips using focused ion beam (FIB) lamella-making protocols [65]. The advantages of this method involve the ability to control the sample orientation and, consequently, to control the desired electric field direction with respect to the crystallographic orientation. However, ferroelectric sample preparation is especially challenging due to possible strain fields and emerging conduction channels due to ion implantation, surface amorphization, and redeposition of residuals while polishing the lamella [105–107].

Herein, we use MEMS-based microchip TEM holder technology to systematically bias a single-crystal $BaTiO_3$ sample along the pseudocubic $[100]_{PC}$ direction. In particular, we use an optimized sample geometry that enables us to precisely control the applied voltage and, in consequence, the electric-field distribution in the probed area. The electrical performance of the device is confirmed with simulations using finite element methods. To quantitatively evaluate our results, we focused on the motion of 180° domain walls at room temperature. Local physical phenomena such as weakly charged zigzag domain walls and domain-wall pinning as a function of the applied voltage are directly probed.

4.2 Methods

4.2.1 Sample preparation

Single crystalline $BaTiO_3$ (001) (MTI Corporation) was used for the device fabrication. The largest facets of the crystal were already polished to optical grade. For the preparation of the lamella, the top surface was sputter-coated with a 30-nm-thick carbon layer (Cressington 108 series carbon coater). This step is required to dissipate the charges during electron imaging and to protect the surface from Ga ion implantation during ion-beam milling.

Inside the focused ion beam (FIB) milling instrument (Zeiss NVision 40, Ga^+ source), two site-specific carbon protective layers were additionally deposited. A thin electronbeam deposited (thickness in the range of $\sim$ 100 nm at 5 kV) was followed by a thicker ion-beam deposited protective layer (1.5 µm thickness at 30 kV and 150 pA current). Trenches around the protected area were etched consecutively with 27, 13, 6.5, and 0.7 nA ion beam currents at 30 kV. The lamella was thinned to about 1 µm prior to its transfer with a micromanipulator (Kleindiek Nanotechnik) to a four heating and two-biasing MEMS chip (DENSsolutions). Complete details of the final steps of the device fabrication and the measurement of the thickness of the final lamella can be found in the Methodology (Chapter 3).

Finally, the temperature on the heating element of the heating/biasing TEM holder was precalibrated using its electrical resistance and the electrical bias to the sample was applied with a source meter (Keithley SMU-2450) using a script to generate a triangular voltage wave shape (see Appendix A).

4.2.2 Finite element calculations

The electrostatic finite element model (FEM) of the device was created with COMSOL MULTIPHYSICS 5.4 package. Dimensions for the electrostatic model were measured from scanning electron microscopy (SEM) images. The dimensions of the simulation box were 40 µm width, 30 µm height, and 30 µm in depth. Tetrahedral adaptive mesh was used for the simulation. The general mesh element characteristics for the simulations involved the electron transparent window of 0.02 µm max and 0.008 µm min, the bulk part of the lamella of 0.05 µm max and 0.008 µm min, the surface of the electrodes of 2.2 µm max and 0.16 µm min, the SiNx membrane of 0.2 µm max and 0.008 µm min, and the vacuum region around the device 0.25 µm max and 0.008 µm min. The bulk part of the lamella was set to 1 µm thick and the electron transparent region to a thickness of 268 nm. The potential difference between the electrodes in the calculations was set to 1 V and it was used as a boundary condition.

4.2.3 Electron microscopy

Bright-field scanning transmission electron microscopy (BF-STEM) was performed on a double spherical aberration (Cs) corrected Titan Themis 60–300 (ThermoFischer Scientific) operated at 300 kV. A beam current of 100 pA was used, the beam convergence angle was 28 mrad, and the collection angle was 79 mrad. Serial STEM imaging was done with a pixel scan area of 1024 × 1024 (3.204 nm/pixel) and 2.0 µs dwell time resulting in 2.98 s/frame. The images were then cropped to 764 × 764 or 760 × 1024 pixel size. Images were cropped to remove completely dark parts from the sides of the electron transparent window. Postprocessing was performed using IMAGEJ software to enhance the domain-wall contrast. It involved the following steps: Fourier filtering to reduce the horizontal scan noise from the images, subtraction of the background (50 pixel rolling ball radius), and contrast and brightness adjustment.

The thickness of the lamella was measured using low loss electron energy-loss spectroscopy (EELS) on the same instrument. An electron-beam current of 100 pA was used. Operating conditions included 70 µm C2 aperture, beam convergence angle of 28 mrad, and collection angle of 19.8 mrad. The spectrometer dispersion was set to 0.25 eV/channel. First, a controlled experiment was performed. A $BaTiO_3$ lamella sample with known thickness was spectrally mapped at the low-loss energy region. From the acquired map, the t/λ calculation was done (where t is the thickness of the lamella and λ is the mean free path of the electrons in the specimen). The thickness of the lamella was measured with the SEM and the mean free path, at the specific conditions, was calculated to be $\lambda = 156 \pm 3$ nm. Second, the sample used in biasing experiments was mapped at the same conditions, giving t/λ measurements across the whole lamella and, by using the mean free path calculated from the control sample, the thickness map of the imaged area was measured.

4.3 Results and discussion

A six-contact MEMS chip [Fig. 4.1(a)] was used that utilizes four of the contacts for heating and precise temperature control and two for biasing [Fig 4.1(b)]. The $BaTiO_3$ lamella was FIB prepared and planar Pt contacts were ion-deposited on the two sides of the lamella as depicted by the SEM image in Fig. 4.1(c). The sample was then thinned to a final thickness of 268 nm - the thickness map is shown in Fig. 4.2. To mitigate conductive paths caused by the contaminants introduced by the ion-beam preparation method, site specific etching was performed around the area of interest [green boxes in Fig. 4.1(c)].

67
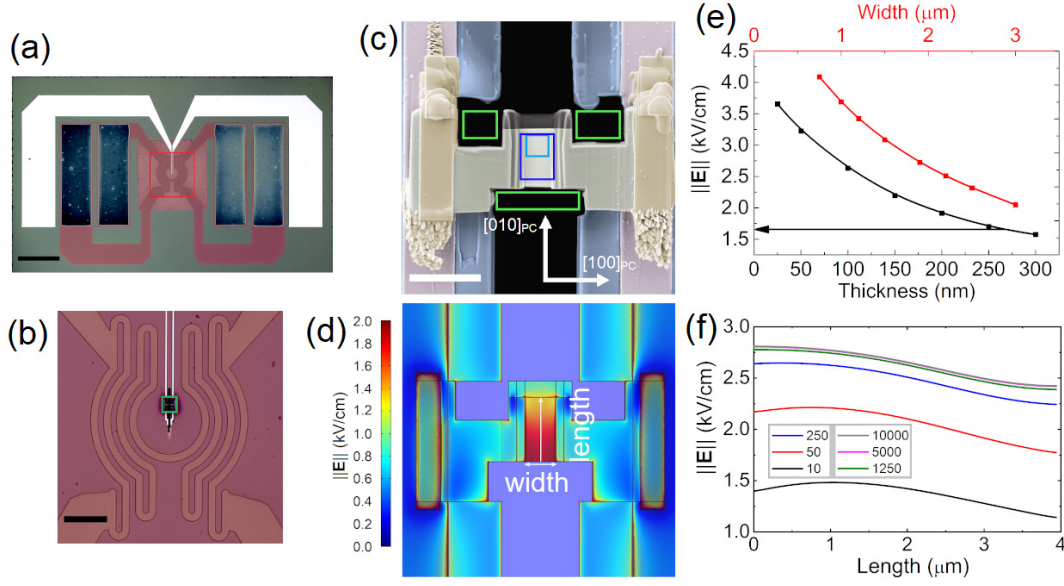
Figure 4.1: *In situ* heating/biasing MEMS chip and the results of FEM calculations. (a) Optical microscope image of the *in situ* biasing/heating TEM MEMS chip. Scale bar is 500 µm and red rectangle corresponds to the area depicted in (b). (b) SiN$_x$ membrane region with the heating spiral and two biasing electrodes (bright vertical features). Scale bar is 100 µm and small green rectangle corresponds to the location of the lamella. (c) False color SEM image of BaTiO₃ sample mounted on the MEMS chip (black area corresponds to the vacuum region, blue to the silicon nitride membrane, pink to the Pt electrodes on the membrane, yellow to the FIB deposited Pt contact electrodes, grey to the bulk part of BaTiO₃, light grey to the electron transparent window, and dark grey to the protective carbon layer). Scale bar is 5 µm. Green boxes represent the etched-out areas, dark blue rectangle represents the area for domain area—voltage loops measurements and light square shows the area imaged in Fig. 4.4. (d) Color map of the electric-field distribution within the device as calculated by finite element methods, white arrows indicate width and length directions. (e) Plot showing the dependence of the calculated electric field on the thickness and width of the electron transparent area ($\varepsilon = 1250$, for varying thickness, the width was fixed at 2.275 µm; for varying width, the thickness was fixed at 100 nm), black arrow shows the calculated electric field for the actual lamella thickness (268 nm). (f) Plot showing the dependence of the calculated electric field on the lamella's dielectric constant. In both (e) and (f) the electric field is plotted along the central part of the electron transparent region [white vertical arrow in (d)]. Reprinted figure with permission from [80]. *Copyright (2021) by the American Physical Society*

Figure 4.1(d) shows FEM calculations of the field distribution for the final geometry of the device. The resulting electric field E in the central part of the lamella is calculated to be ~ 1.65 kV/cm for 1 V applied to the electrodes. This value is the upper bound of the electric field magnitude since the simulation does not consider

leakage currents and effects of the interfaces.
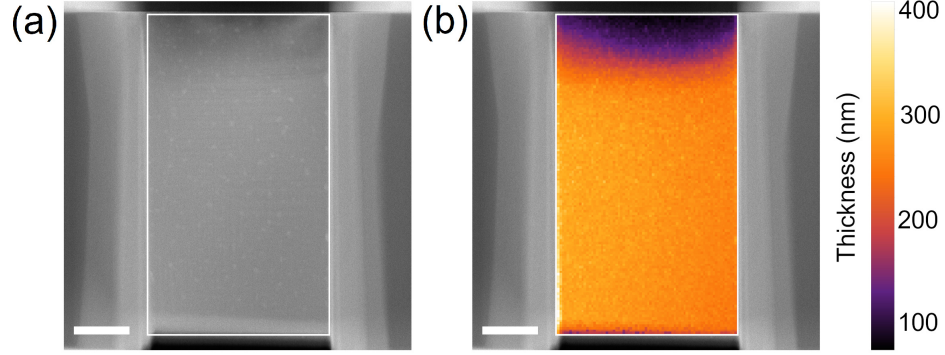
Figure 4.2: Thickness map of BaTiO₃ lamella used for the biasing experiments. (a) Annular dark field (ADF) STEM image annotated with a white rectangle which represents the low-loss EELS mapping area. (b) ADF image with overlayed thickness map. Scale bar in both images is 750 nm. Reprinted figure with permission from [80]. *Copyright (2021) by the American Physical Society.*
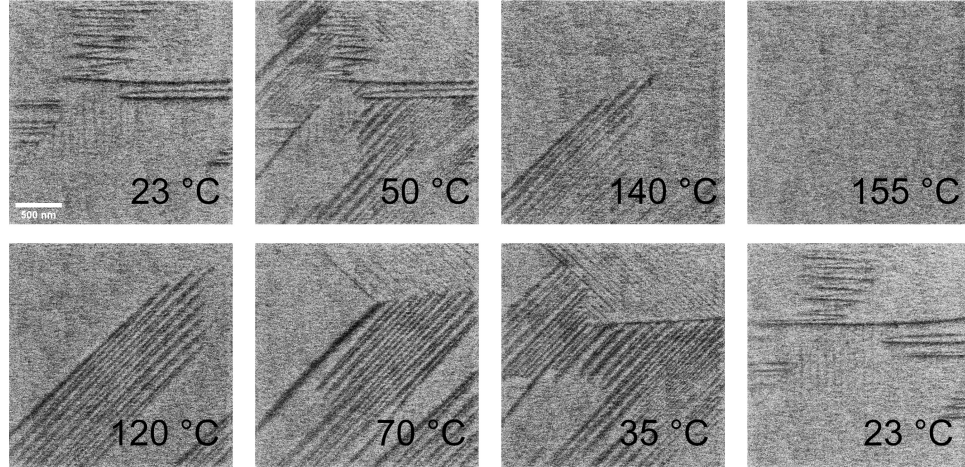
Figure 4.3: Still frames of the BaTiO₃ heating experiment video. Scale bar is 500 nm, the temperature of each frame is shown at the lower right corner. At around 50 °C morphological transition to pure 90° domain state happens. Paraelectric state signified by the lack of domain walls is achieved around 150 °C (nominal temperature). Cooling down to room temperature (bottom row) reintroduces 180° domain walls. Crystallographic axis are as depicted in the Fig. 4.1.

These effects might alter the magnitude of the applied field, however, the overall characteristics of the electric field distribution remain the same. The calculations predict a difference in the electric field of ~ 0.4 kV/cm field across the vertical direction of the lamella [white arrow in Fig. 4.1(d)]. Figure 4.1(f) depicts the magnitude of the electric field along the arrow line and its dependence on the dielectric constant of the sample. The inhomogeneity of the electric field and small gradient across the

lamella results from the etched-out regions. This inhomogeneity can be reduced by more conservative isolating cuts, however, this increases the probability of failure of the device during biasing.
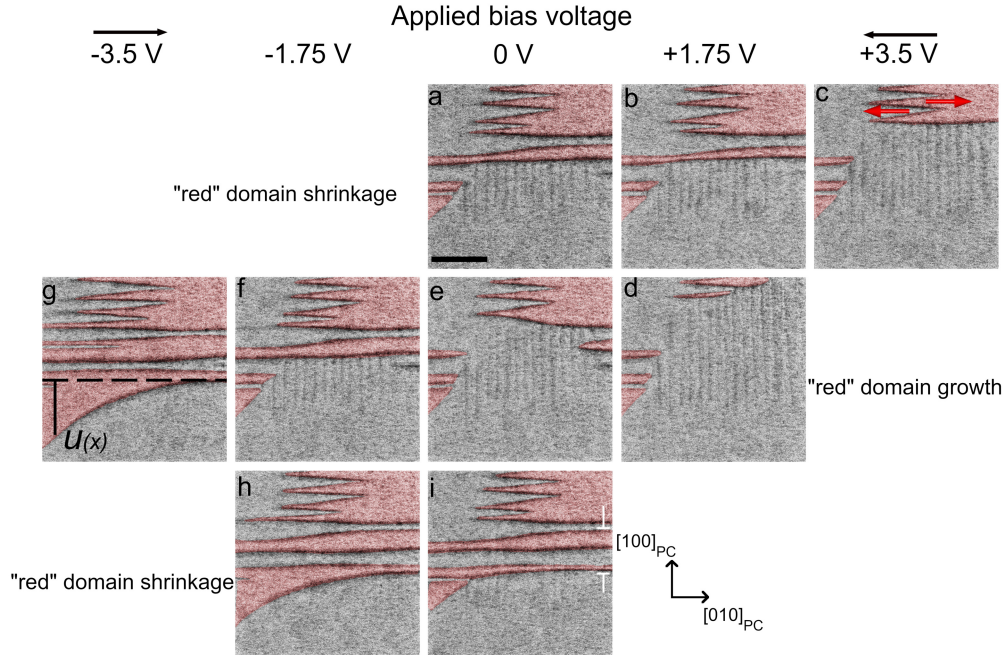
Figure 4.4: BF-STEM micrographs showing the domain structure evolution during cyclic electrical biasing. In the image, the field is oriented along the [010]$_{PC}$ and black arrows indicate the direction of the electric field. (a) Initial domain structure at 0 V bias. (b) Domain structure at +1.75 V bias with increasing electric-field strength. (c) Domain structure at maximum of +3.5 V bias. Red arrows indicate the polarization direction in the two domains. (d) Domain structure at 1.75 V with decreasing field strength. (e) Domain structure at 0 V in the middle of the cycle. (f) Domain structure at -1.75 V with increasing field strength. (g) Domain structure at minimal voltage -3.5 V. $u(x)$ represents the magnitude of domain-wall bending from the equilibrium position, which is marked with the dashed line (g). (h) Domain structure at -1.75 V with decreasing field strength. (i) Final domain configuration at the end of the cycle with 0 V. White indication lines depict the double domain that shows sideways growth and it is hysteric to the domain in (a). Red false color superimposed on all images corresponds to the domains with polarization pointing to the right. Scale bar is 500 nm [shown in (a)]. Reprinted figure with permission from [80]. *Copyright (2021) by the American Physical Society.*

Considering the geometry of the lamella, for a given applied voltage the magnitude of the electric field in the sample is mainly influenced by the width [horizontal white arrows in Fig. 4.1(d)] and thickness of the probed area. If the width of the probed area decreases [Fig. 4.1(e)], the magnitude of the electric field increases, which is similar to decreasing the plate distance in a parallel plate capacitor config-

uration. Reduction of the thickness of the lamella would also result in an increase in the magnitude of the applicable electric field [Fig. 4.1(e)] as the equipotential lines get "squeezed" together in the smaller volume. The overall electric-field distribution is also dependent on the dielectric permittivity of the sample. Figure 4.1(f) shows the dependence of E on the average dielectric constant of the probed material along the central part of the lamella [white vertical arrow in Fig. 4.1(d)]. For low values of the relative dielectric permittivity (below 100), the resulting electric field is highly dependent on the permittivity of the material. When the dielectric permittivity approaches the values corresponding to perovskite ferroelectrics (dielectric permittivity ranging between hundreds to several thousand), the dependence of the field on the permittivity becomes minimal. Thus, the dielectric properties of $BaTiO_3$ do not influence the magnitude of the electric field along the probed area.

Prior to biasing the sample, annealing above the Curie temperature (T_C) was performed inside the TEM. Heating is required to release most of the strain due to the FIB preparation process [105]. The sample was heated to 200 °C, held at this temperature for 1 min, then the temperature was lowered to 25 °C in 20 min (the heating profile and respective image sequence are shown in Supplemental Video 1 of ref. [80], still frames from the video are shown in the Fig. 4.3).

The biasing experiments were performed at room temperature where the sample is dominated by unusually stable 180° walls [108]. Figure 4.4(a) depicts bright-field scanning TEM (BF-STEM) images of the domain structure at room temperature (the full image sequence during electrical biasing is shown in Supplemental Video 2, of ref. [80]). The dark contrast in the images corresponds to the domain walls. To improve this contrast without interference due to diffraction effects, the sample was mistitled by ~ 10 mrad from the $[001]_{PC}$ zone axis. The sample was then biased with a triangular wave form starting from the positive direction to the maximum of the positive voltage [3.5 V, Fig. 4.4(c)], continuing to negative applied voltage [-3.5 V, Fig. 4.4(g)] before completing the loop at 0 V [Fig. 4.4(i)]. We note that the applied voltage of 3.5 V corresponds to electric field values of about 5.8 kV/cm, based on the FEM simulation. Considering the coercive field of $BaTiO_3$ (approximately 0.5 kV/cm), by studying the domain response we conclude that the actual applied field is within one order of magnitude of the FEM calculated one [109]. This discrepancy is attributed to the sample-electrode interface and leakage current effects, which are difficult to eliminate due to the microscopic size of the device and which are not included in the calculations of the electric field.

A schematic illustrating an equivalent circuit of the microdevice fabricated for the biasing experiments is used to comprehend the expected electron transport behavior across the biased $BaTiO_3$ sample and explain the discrepancies between the applied voltage and expected electric field as calculated with finite element methods. R1 is the electric resistance of the wires leading to the chip in addition with the resistance of the platinum electric lines of the MEMS chip - R1 = 40 Ω. Part of the system
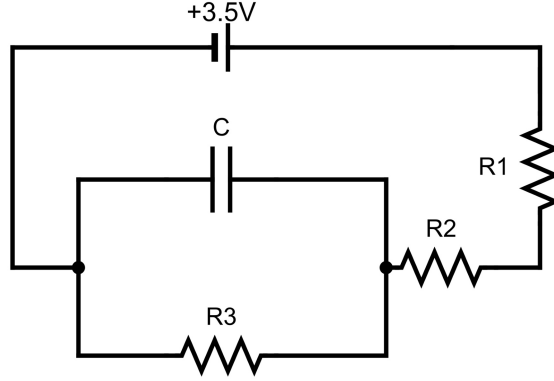
Figure 4.5: Equivalent circuit of *in situ* biasing system. R1 represents the resistance of the wires and Pt lines on the chip leading to the lamella. R2 is the resistance of the FIB deposited Pt contacting layers between the BaTiO$_3$ lamella and the Pt electric lines on the chip. C represents the insulating lamella as a capacitor and R3 is equivalent to conducting channels within this lamella. Reprinted figure with permission from [80]. *Copyright (2021) by the American Physical Society.*

consisting of R2, R3 and C is equivalent to the lamella with FIB deposited contacting layers. R2 is the electric resistance of the deposited contact layers between the MEMS Pt lines and the BaTiO$_3$ lamella. R3 is the resistance of the conductive channels within the BaTiO$_3$ lamella. Good preparation of a device should lead to a large R3 value and small R2 value. In that case, the voltage drop on C and R3 should be the same since the conductive channels can be imagined to be in a parallel geometry to a lamella (depicted as capacitor C). If R3 is large, then the applied potential drop at the lamella C is equivalent to the nominally applied potential (as in schematic +3.5 V). On the other hand, if R3 is small, comparably large current flows through the circuit and most of the potential drops within R1 and R2. Therefore, the voltage on C (and therefore electric field within lamella) is considerably smaller.

The FEM simulation is used to explore influence of the sample's geometry on the magnitude and distribution of the electric field within the lamella. It is noted that the calculated electric field values from FEM are of the same order of magnitude but due to leakage effects and non-ideal contact layers they are not expected to match one-to-one. The discrepancy between the FEM calculated electric field magnitude and the one applied during biasing experiments can be largely attributed to the FIB deposited Pt contacting layers between the BaTiO$_3$ lamella and the electric lines of the MEMS chip. In the equivalent circuit above this is represented as R2. During the experiments resistance of the system is 33 MΩ. Comparably R1 is miniscule and can be easily neglected, therefore R2+R3 = 33 MΩ. The configuration of R2 and R3 in the equivalent circuit forms a voltage divider. Voltage drop U_C on C in the equivalent circuit is as follows: $U_C = \frac{R3}{R3+R2} \times 3.5$ V. If the contacting layers are of good quality R2 is small and the voltage drop on the C is the same as the supplied

voltage to the circuit. On the other hand, if R2 ∼ R3, the voltage drop across the C is smaller than the supplied voltage. In our case, we expect R3 > R2. That is our sample preparation leads to a situation, where the resistance of the lamella is larger than the resistance of the contacting layers, and this is supported by directly observing the domain response at moderate voltages.

By examining the domain structure in the BF-STEM images, the presence of weakly charged zigzag domain walls was noticed [Fig. 4.4(a)]. It is theoretically predicted that weakly charged domain walls are more stable in $BaTiO_3$ when it is not in a bulk form and it is connected with platinum electrodes [110]. This corresponds well to the geometry of the device where the polarization is essentially confined in a thin slab within two dimensions with Pt electrodes on the sides. The transition mechanism of the strongly charged domain wall into a weakly charged zigzag domain wall and the meaning of the periodicity has been previously described by Sidorkin [27].

The polarization direction within the domains can be determined upon application of the electric field [Fig. 4.4(c)]. The domains with polarization pointing in the direction of the electric field should grow and, consequently, domains with polarization vector opposite to the applied field should shrink. By examining domain and domain-wall response on positive bias (the direction of the applied electric field is depicted with a black arrow at the start or end of the image rows in Fig. 4.4), the polarization vectors in the visible 180° domains were determined and are indicated with red arrows in Fig. 4.4(c). Consequently, red shading in the BF-STEM images of Fig. 4.4 corresponds to domains with polarization direction pointing to the right. It is noted that the periodic vertically aligned 180° domain walls, which appear as weak contrast in the central part of Figs. 4.4(a) – 4.4(f), do not respond as strongly to the external bias since the polarization and the electric-field vectors are orthogonal.

When the direction of the electric field is changed, Figs. 4.4(d) – 4.4(g), the domains that span across the whole electron transparent window as bands experience sideways growth. The observed domain-wall bending in Fig. 4.4(g) is attributed to strong domain-wall pinning possibly due to a dislocation center. The domain-wall displacement $u(x)$ from the equilibrium position (which in this case is aligned along the $[100]_{PC}$ direction) has a characteristic hyperbolic nature [theoretically $u(x) \sim 1/\sqrt{x}$] as the domain wall regains equilibrium when the distance (x) from the pinning center increases [27].

Finally, the applied bias cycle terminates after completing the full loop [Fig. 4.4(i)]. During field cycling, the domain structure exhibits hysteretic behavior at all fields by not returning to the same state for the same voltage during increasing and decreasing steps of the full cycle [for example, compare Figs. 4.4(b) and 4.4(d) for +1.75 V and Figs. 4.4(a), 4.4(e), and 4.4(i) for 0 V].

The response of the domains at different maximum applied voltages was further investigated to study the domain dynamics from weak to strong fields. The voltages

ranged from 0.25 to 3.5 V for 14 different values in total and all image sequences are shown in Supplemental Videos 3–16, of ref [80]). Analysis of the sequential BF-STEM images of the domains exhibiting the same polarization (i.e., the red shaded domains in Fig. 4.4) resulted in the domain area vs applied potential loops shown in Fig. 4.7(a) (each data point corresponds to the domain structure image at given bias potential plotted as bias voltage–domain area loops for three cases corresponding to 3.5, 2.5, and 2.0 V maximum applied voltage, the methodology of calculating the loop at 3.5 V is detailed in Fig. 4.6).
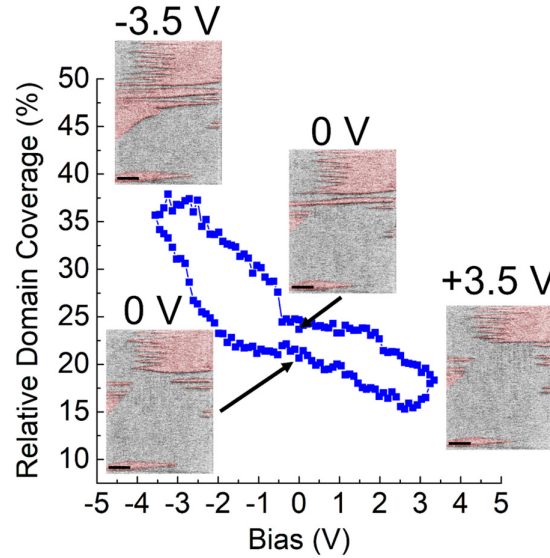
Figure 4.6: Domain area − bias loop with images at 0 and ± 3.5 V bias voltages. Each dot in the loop represents a measurement from one image. Selection of the appropriate domains (red shading in the STEM images) were made based on their response on the electric field – for example, only the domains, which grow with negative bias were measured. Domain area measurements were made manually for each image with ImageJ. The measured domain area was then divided by the total image area, which results in relative domain coverage in the given image. Scale bar is 500 nm. Reprinted figure with permission from [80]. *Copyright (2021) by the American Physical Society.*

The measured area is proportional to the polarization pointing to the right and this corresponds to domain growth with respect to negative applied voltage. The measured loops in Fig. 4.7(a) resemble the polarization-electric field (P-E) loops in "hard" ferroelectrics where P-E loops are constricted at weak fields and open at larger fields [111–114]. Remarkably, the local loops shown here reveal additional features which cannot be discerned in loops taken with classical approaches over macroscopic areas. These include domain wall pinning (weakly responsive polarization region in the -1 to 1 V interval of the measured loops) and domain nucleation annihilation accompanied with ballistic movement of domain walls. The apparent loop asymmetry
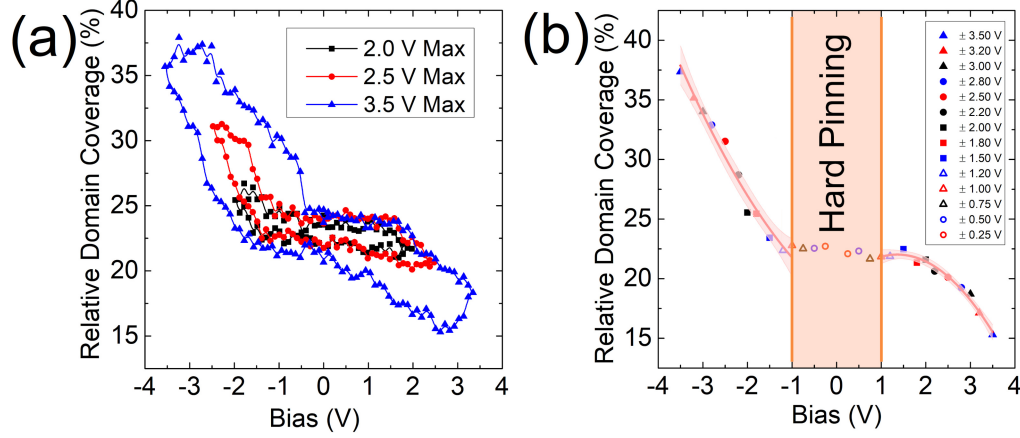
Figure 4.7: Results of image analysis. (a) Selected domain area-voltage loops using triangle wave voltages of 2, 2.5, and 3.5 V. (b) Relative domain coverage with respect to the maximal/minimal cycle voltage for the positive and negative branch of the loops (14 loops in total). The lines represent the quadratic polynomial fits for each branch and red shaded regions correspond to 95% confidence interval. Orange shading corresponds to the flat region of the plot, where hard domain-wall pinning occurs. Reprinted figure with permission from [80]. *Copyright (2021) by the American Physical Society.*

and the fact that at 0 V the relative domain coverage does not reach 50 % (which would be a requirement for electroneutrality) can be partly attributed to the nature of the local TEM measurements that do not necessarily correspond to the entire domain structure. On the other hand, the loop asymmetry and apparent pinching around 0 V bias indicate hard pinning of domain walls, which are released from pinning centers at higher fields as indicated by the loop opening. These defects exert restoring forces on the domain walls at weak fields limiting the movement of the wall and consequently pinching the loop. At higher electrical fields, the restoring forces are overcome and the domain-wall movement is controlled by pinning centers randomly distributed in space and with variable strengths [114, 115].

Figure 4.7(b) depicts the totality of the results from the loop biasing experiments plotted as the minimal and maximal cycle voltage for each loop as a function of the domain surface coverage (again, the domains corresponding to the red shading in Fig. 4.4 were measured). At low voltages, the domain coverage reveals that new domains do not nucleate and existing domain walls do not move significantly as expected for a hard domain-wall pinning [this region is marked with orange shading in Fig. 4.7(b)]. At higher applied voltages (above ±1 V), the existing domain walls experience significant forward and sideways motion and domains start to nucleate or annihilate depending on the applied voltage as previously predicted [17]. Overall, a quadratic behavior of the area ($\sim$ polarization) vs electric field relation is observed, particularly pronounced at positive applied voltages. The function $P \sim E^2$, which

essentially corresponds to classical Rayleigh's law, represents the weak domain-wall pinning on randomly distributed defects within the crystal [116, 117]. In principle, Rayleigh's law is applicable at weak field conditions in a material with a broad distribution of pinning center strengths, but in our case the local domain-wall movements are hindered by hard pinning at weak fields, therefore domain walls do not move substantially and do not experience soft pinning upon random lattice defects. Rayleigh motion is achieved only at higher fields when the domain wall is depinned and can move through the lattice with randomly distributed defects. The asymmetry of the loops indicates asymmetrical distribution of defects in the examined local area, which is again a feature that would not be necessarily noticed in a macroscopic loop measured over a much larger area. Similarly, the different slope of the positive and negative applied voltages of Fig. 4.7(c) indicates the different response of the domain walls upon reversal of the direction of the electric field.

4.4   Conclusions

In summary, a specialized sample preparation method was demonstrated, which allows to perform reliable *in situ* electrical biasing measurements in the TEM and provides the ability for interpretable physical processes of ferroelectric nanodomains. The meticulously designed and fabricated geometry of the device results in a homogeneous electric field, whose magnitude and direction are confirmed by finite element calculations. The classical ferroelectric BaTiO$_3$ was used and it was shown that precise control of the external electric field and sequential BF STEM imaging permits to locally study 180° domains and domain wall movements at room temperature. The origins and stability of weakly charged zigzag nanodomain walls are associated with the thin slab geometry of the ferroelectric and interplay of BaTiO$_3$ with Pt electrodes. Polarization–electric-field loops calculated directly from the areas of the imaged domains elucidate the relation between bulk and nanoscale ferroelectric effects. The domain-wall response at low electric field is associated with the hard pinning mechanisms on the defects within the lattice, which results in pinched and asymmetric domain area vs voltage loops. At higher fields, domain walls are depinned and localized effects such as new domain nucleation and sideways growth and domain-wall bending were observed. At such fields (above the coercive field), it was shown that the domain-wall motion follows Rayleigh-like behavior. Thus, this controlled electrical biasing method can provide unprecedented insights on dynamic domain-wall motion and domain interactions at the nanoscale.

5 Biasing of 90° ferroelastic needle domains in BaTiO$_3$

The contents of this chapter are based on the published article [118]:

Individual Barkhausen Pulses of Ferroelastic Nanodomains

Reinis Ignatans, Dragan Damjanovic and Vasiliki Tileli
Institute of Materials, École Polytechnique Fédérale de Lausanne,
CH-1015 Lausanne, Switzerland

Contributions of R. Ignatans: performed sample preparation, in situ experiments, data analysis and wrote the manuscript with the contributions from all authors.

5.1 Introduction

Polarization switching in ferroelectric crystals is akin to first order phase transition induced by an applied electric field [17]. The reorientation of the domains during switching is a response to assume the equilibrium conditions that minimize the free energies of domain configuration. The motion toward the equilibrium state is hindered by potential barriers that lead to nonmonotonous polarization change discontinuities referred to as Barkhausen effect [97, 119–122]. The accumulated probing of this effect describing the motion of many domain walls is linked to the theory of avalanches and the noise associated with it [123, 124]. More generally, crackling noise seems to be a fundamental aspect of nature and "crackles" occur in vastly different systems and processes [36, 125].

In ceramics [97] and single crystalline BaTiO$_3$ [120, 126], the origins of the Barkhausen effect are placed on nucleation of spikelike domains, pinning of domain walls due to defects in the lattice [119, 122], domain coalescence [127], and transition of the needlelike to parallelepiped domains [126]. Most electrical studies of Barkhausen jumps attempt to resolve single events from macroscopic properties of ferroelectrics (such as switching current or charge) and the different methodologies used can reveal different origins of the pulses. This is associated with variations in measurement timescales, boundary conditions, and physical dimensions of the material. Typically, to characterize these effects, *in situ* optical microscopy experiments are performed [128]. However, optical measurements are diffraction limited and fine polar regions, such as the tips of needle domains, are difficult to probe in detail. At nanoscale dimensions traditional electrical measurements become exponentially more difficult due to miniscule charges associated with individual switching events. For example, *in situ* transmission electron microscopy (TEM) experiments have been previously performed in BaTiO$_3$ single crystals to enhance the spatial resolution of the domain dynamics [57, 129–131]. In general, kinetically controlled studies of nanodomain switching and the way their interaction affects their motion in TEM are still limited due to the overall geometric confinement of the specimen, the electric field uniformity in the probed area, and the effects of the electron beam irradiation.

In the following, 90° ferroelastic nanodomains are stabilized and their movement tracked inside the TEM by applying a well-oriented electric field. Barkhausen jumps are locally probed for different potential barriers and at different electric field frequencies.

5.2 Methods

5.2.1 Sample preparation

A lamella from single crystal $BaTiO_3$ (MTI Corporation) was prepared with focused ion beam method and it was transferred to a 4 heating and 2 biasing electrode microelectromechanical (MEMS) chip provided by DENSsolutions. The Pt contacts were ion beam deposited and the lamella was thinned to a final thickness of 268 nm. A detailed description on the device fabrication can be found in the Methodology (Chapter 3) as well as in ref. [80]. The average temperature on the heating element of the MEMS chip is calculated from its electrical resistance and DENSsolutions software was used to control the temperature. Electrical bias to the sample was applied using a Keithley SMU-2450 sourcemeter.

5.2.2 Transmission electron microscopy

Imaging was performed on a double spherical aberration (Cs) corrected ThermoFischer Scientific Themis 60-300 operated at 300 kV in STEM mode using 100 pA beam current, 70 µm C2 aperture, and a beam convergence angle of 28 mrad. Serial imaging during standard biasing experiments was done in bright field (BF) mode with a collection angle of 79 mrad. The pixel size was 3.2 nm and 2.98 s was the frame time. For the low frequency biasing experiment, the pixel size was 1.1 nm and the frame time was 8.22 s.

DPC imaging was performed using a four-segment detector and the imaging conditions were 200 pm pixel size and 34.3 s frame time. The camera length was 91.1 mm, corresponding to inner and outer collection angles of 15.3 and 85.5 mrad, respectively. Beam centering and gain/offset equilibration of the segments were done in the vacuum region prior to the experiment.

Free standing lamella was investigated on ThermoFisher Talos F200S microscope operated at 200 kV in STEM mode and imaged with the high angle annular dark field (HAADF) detector. The sample was mounted on a standard grid and a Gatan single tilt furnace type heating holder was used for heating the sample.

5.2.3 Image processing

Images of the standard biasing experiment were cropped to 764×764 pixel size. Images of the low frequency field measurement were not cropped and remained at the 2048×2048 pixel size. To enhance domain wall contrast in the BF images, postprocessing using ImageJ software was performed. It involved Fourier filtering of the horizontal scan noise of the images, subtraction of background (50 pixel rolling ball

radius with sliding paraboloid enabled) followed by contrast and brightness adjustment.

DPC experimental signal processing involved the same 1024×1024 pixel region from the original set of 4 images (corresponding to the segments A, B, C, and D). The cropped region was further downsized with ImageJ to 256×256 pixel size essentially averaging out the noise. Further data processing was undertaken using a custom script written in Mathematica v.11.2. A 256×256 array was created, where each element represented a vector in the xy plane corresponding to the beam deflection. Beam deflection along the x axis is proportional to the differential signal D-B and correspondingly along the y axis it is proportional to C-A. Each element was corrected for the detector rotation with respect to the scan direction (+17°). Using this array, the vector field plots were created (Fig. 5.1 b-c). The vector field plot consists of 32×32 arrows, which are proportional to the direction and magnitude of the polarization.

5.3   Results and discussion
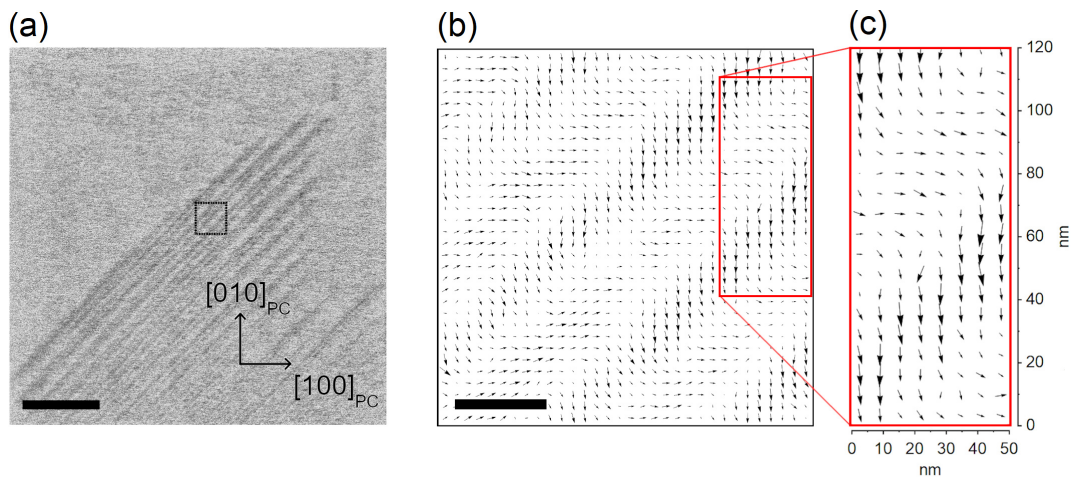
Figure 5.1: BF STEM Micrograph of BaTiO$_3$ lamella at 130 °C. (a) Domain structure at 130 °C showing periodic ferroelastic 90° needle domains with polarization direction along [100]$_{PC}$ (scale bar is 500 nm). (b) DPC image of the black dotted square area in (a) (scale bar is 50 nm). The arrows represent the polarization direction of the needle and parent domains. (c) Close-up of polarization vectors of the ferroelastic nanodomains. Reproduced from ref. [118]. By respecting *Creative Commons Attribution 4.0 International license.*

Figure 5.1(a) depicts the domain structure at nominal temperature of 130 °C, which consists of periodic 90° ferroelastic needle domain groups (the full heating profile and image series is shown in Supplemental Material, Video S1 of ref. [118]).

We note that similar domain evolution is seen in a free standing lamella (Fig. 5.2) and, hence, this behavior is not associated with the geometry of the biasing device.
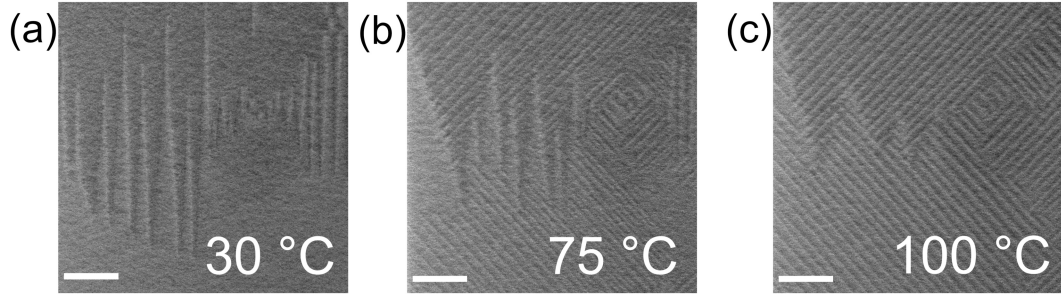
Figure 5.2: ***In situ* heating experiment of free-standing lamella** (a) Domain structure at 30 °C exhibiting 180° zig-zag domain walls. (b) At 75 °C, the sample is mostly dominated by 90° domain walls, nevertheless some character from zig-zag domain walls is still seen. (c) Domain structure at 100 °C where the specimen is dominated by 90° domain walls. The appearance of zig-zag wall vertices seems to be associated with crossing 90° domain walls. Scale bar is 250 nm. Reproduced from ref. [118]. By respecting *Creative Commons Attribution 4.0 International license.*

To characterize the ferroelastic domain structure, differential phase contrast (DPC) imaging [68] was employed. The DPC signal is directly proportional to the magnitude and direction of the local polarization [68]. Figure 5.1(b) represents the local profile of polarization directions encoded by arrows from the square region shown in Fig. 5.1(a). The size of the arrows is proportional to the magnitude of the polarization, however, absolute values are difficult to report since minor misalignment greatly affects the DPC results, which is the reason why the magnitude of the arrows in the horizontal and vertical directions are not exactly the same. Nevertheless, Fig. 5.1(c) illustrates that the 90° domain walls in tetragonal $BaTiO_3$ align with the $[110]_{PC}$ direction [17], as expected from crystallographic symmetry laws. The measured average domain width w is 33 nm. The domain walls are less than 7 nm thick and they are associated with dark contrast (i.e., high angle scattering) in bright-field scanning TEM (BF STEM) images. The appearance of the periodic domain structure in thin films results from the proportional relationship between the square of w with the slab's thickness d [29, 31, 132–134].

At 130 °C, we applied a triangular waveform voltage (see Fig. 5.3) and followed the response of several 90°, ferroelastic, a-type, needlelike domains, Fig. 5.4(a).

The full sequence of BF STEM images of a cyclic measurement for an applied bias of $\pm$ 3.5 V can be seen in Supplemental Material Video S2 of the ref. [118]. The collective statistical behavior of the system has also been analyzed by machine learning algorithms and is reported elsewhere [135]. Figures 5.4(b) and 5.4(c) depict the domain length as a function of applied potential for two needle domains. These plots highly resemble traditional polarization-electric field (PE) loops, however, while
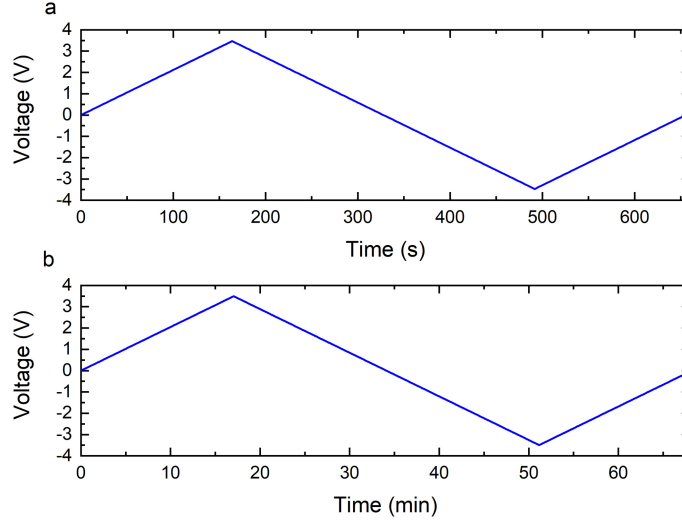
Figure 5.3: Triangular voltage profiles as a function of time. (a) Profile used for ferroelastic domain biasing of the domains in Fig. 2. (b) Profile used for the low frequency experiment. Reproduced from ref. [118]. By respecting *Creative Commons Attribution 4.0 International license.*

conventionally measured PE loops show macroscopically averaged behavior, here, we follow the response locally on a single domain basis. We have observed two distinct manifestations of the needle domain response on the electric field. When the vertex of a needle domain is located further away from the perpendicular domain walls [Fig. 5.4(b)], the measured domain length vs applied electric field loop is smeared, with reduced hysteresis, and the process is lattice-defect mediated [116, 117]. However, when the needle domain's vertex is located close to the perpendicular domain's wall [Fig. 5.4(c)] the shape of the measured loop is sharp and square-like showing pronounced hysteresis. Therefore, this domain-domain interaction mediated process seems to involve strong local strain and depolarizing fields leading to large hysteresis, unlike the lattice-defect mediated process. Measurements of the motion of perpendicular needle domains show similar behavior - see Fig. 5.5.

Closer investigation of the loop in Fig. 5.4(c) shows clear step-like features around, for example, 1 and 2 V, whereas for needle domains whose vertices lie further away from the perpendicular needle domain walls, step-like features are less pronounced. Thus, needle domains whose vertices are close to the perpendicular domain walls experience distinct non-monotonous movement during biasing [122]. These Barkhausen jumps occur when the perpendicular needle domains have contracted. In practice, needle domains do not interact directly with perpendicular domains (i.e., they are not in direct contact with them), but rather interaction of needle domains is mediated through a large parent domain [the background gray domain in the images of Fig. 5.4(a)].
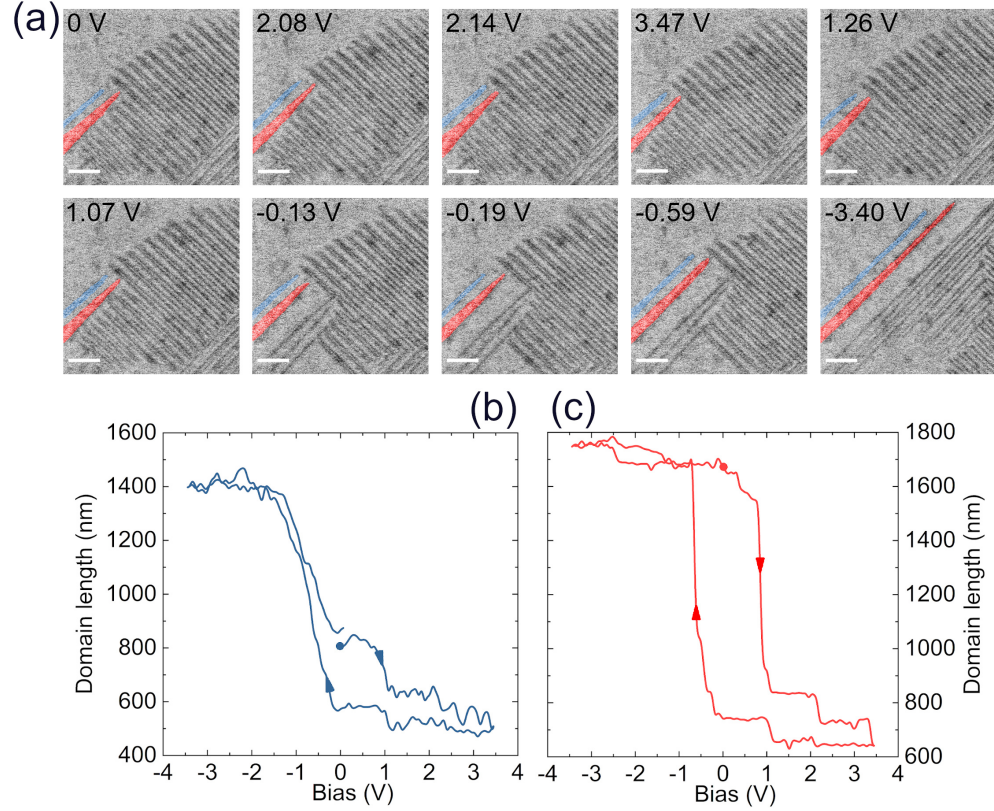
Figure 5.4: BF STEM micrographs and the measurements of the domain lengths. (a) 90° domain structure evolution during biasing recorded at 130 °C. The measured domains are overlaid with red and blue false color. The electric field is applied along the needle domains polarization direction, i.e. $[100]_{PC}$. Scale bar is 300 nm. (b) Domain length as a function of applied potential plot of a domain with weak interaction with perpendicular domain walls [blue false color in (a)]. (c) Similar loop of a domain that interacts strongly with perpendicular domain walls [red false color in (a)]. The starting point of the loops is marked with a dot and the loop rotation direction is marked with arrows. Reproduced from ref. [118]. By respecting *Creative Commons Attribution 4.0 International license.*

In general, the equilibrium position of the needle domains between Barkhausen jumps is associated with electric and mechanical compatibility [136–138]. Two possibilities can be distinguished, the first one, where the needle domain's vertex terminates next to the perpendicular needle domain's body, and the second, in which equilibrium is achieved when two or more strongly charged needle domain vertices come in contact [136]. The observed Barkhausen jumps occur among these equilibria. We note that experiments for an increasing maximum range of the applied bias were additionally performed and similar domain behavior was observed - Supplemental Material, Videos S3 to S8 of the ref. [118]

To study the time dependence of the needle domain response, similar experiments were carried out with a less steep voltage ramp (0.0034 V/s) corresponding to the
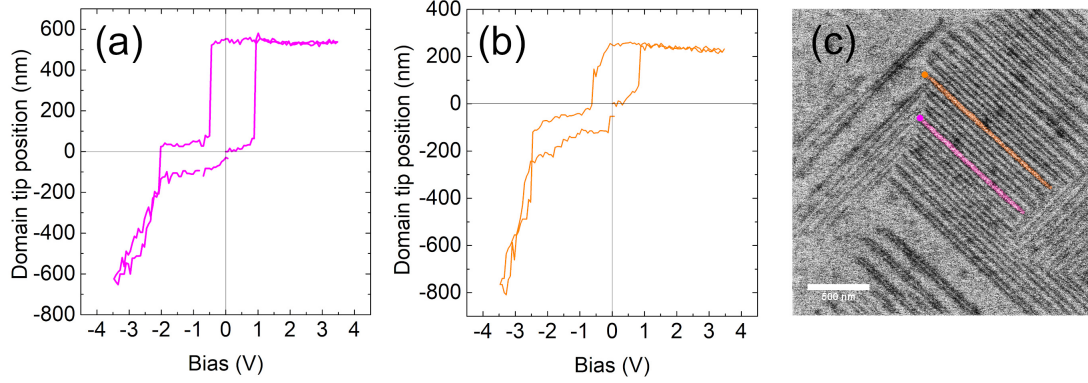
Figure 5.5: Domain tip position as a function of applied voltage for crossing domains. Loop from the pink (a) and orange (b) coloured domain tips (colored circles) shown in the BF-STEM image (c). Due to the continuous changes of the domain length, the end of the crossing domain was not constant. Therefore, the position of the needle tip with respect to applied bias was measured in this case. The positions are calculated with respect to the 0 V bias at the start of the experiment (i.e. tip position of 0 nm corresponds to the start of the experiment). Reproduced from ref. [118]. By respecting *Creative Commons Attribution 4.0 International license.*

ultralow frequency of 0.24 mHz. The hysteresis loop can be seen in Fig. 5.6, and the full sequence is shown in Video S9 of the ref. [118]. The overall domain length vs. applied voltage loop is steep and square-like and it is similar to the one in Fig. 2(c) that represents strong domain-domain interaction. Again, Barkhausen jump events associated with interacting needle domain equilibrium positions were recorded.

To compare the response of the processes leading to characteristically different domain wall motion, their length is plotted as a function of time, Fig. 5.7(a). Both time axes in the plot are rescaled to match the start and the end of the bias cycle. Domains which experience strong mutual interaction (red and green squares), exhibit distinctive step-like Barkhausen jumps (marked in the Fig. 5.7 with green and red arrows), whereas domain growth via lattice-mediated defect mechanism is considerably smoother (blue squares). The key difference observed during the low frequency measurement is the appearance of the domain relaxation events with a time constant of roughly three to five minutes. For example, one such event can be seen in Fig. 5.7(a) between 2500 and 2900 s. The measured domain first decreases in length upon applied negative voltage, then it slowly increases in length (marked with gray horizontal line), and eventually exhibits a Barkhausen jump around 2900 s, before shrinking further. After this jump, the domain again slightly increases in length, showing similar behaviour as before. Interestingly, at around 3000 – 3300 s, when the negative potential slowly returns to zero volts, the domain annihilates completely (marked with the dashed green arrow). In short, when the domain experiences large
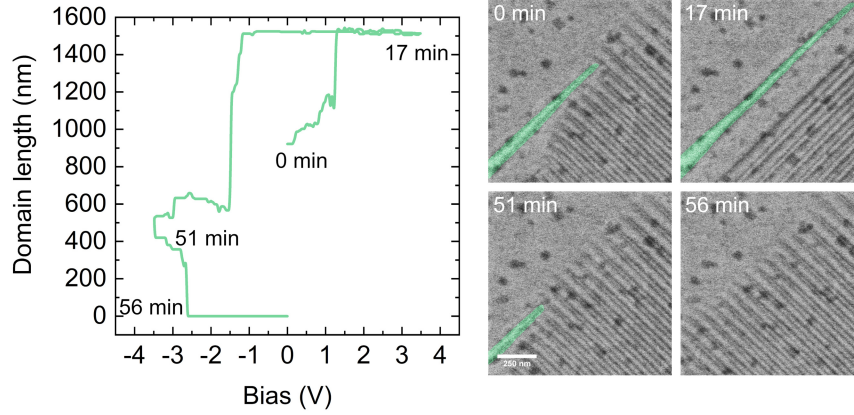
Figure 5.6: Low frequency domain motion. Domain length as a function of applied bias at 130 °C, and image sequence of the domain at 0, 17, 51, and 56 min. The orientation of the loop is opposite as in Fig. 5.4 due to the measured domain (green false color) nucleating with anti-parallel polarization compared to the ones in Fig. 5.4. The direction of the electric field is depicted with black arrows on the images. The polarization direction in the green coloured domain is the same as the field direction at t = 17 min. The dark spots in the BF-STEM images are surface contamination, which grew upon lengthy *in situ* biasing and heating experiments. These spots seem to be located at the surface inactive layers and hence do not affect the domain motion. Reproduced from ref. [118]. By respecting *Creative Commons Attribution 4.0 International license.*

applied bias, it stays intact, but on the decreasing field it slowly decreases in size and disappears, which again indicates a relaxation event with a time constant of several minutes. The observed sluggish relaxation process can be attributed to dielectric and elastic viscosity [119, 139]. According to observations from electrical measurements, the domain structure can relax up to several hours after poling. We may therefore be witnessing an individual event responsible for ageing and creep in ferroelectric materials [140–142]. Finally, when the lower frequency domain motion is compared to higher frequency ones, a time delay of the switching process was noticed, when the potential is brought back to zero. During ultralow frequency measurements, the domain remains at the same position for a significant time before it eventually switches.
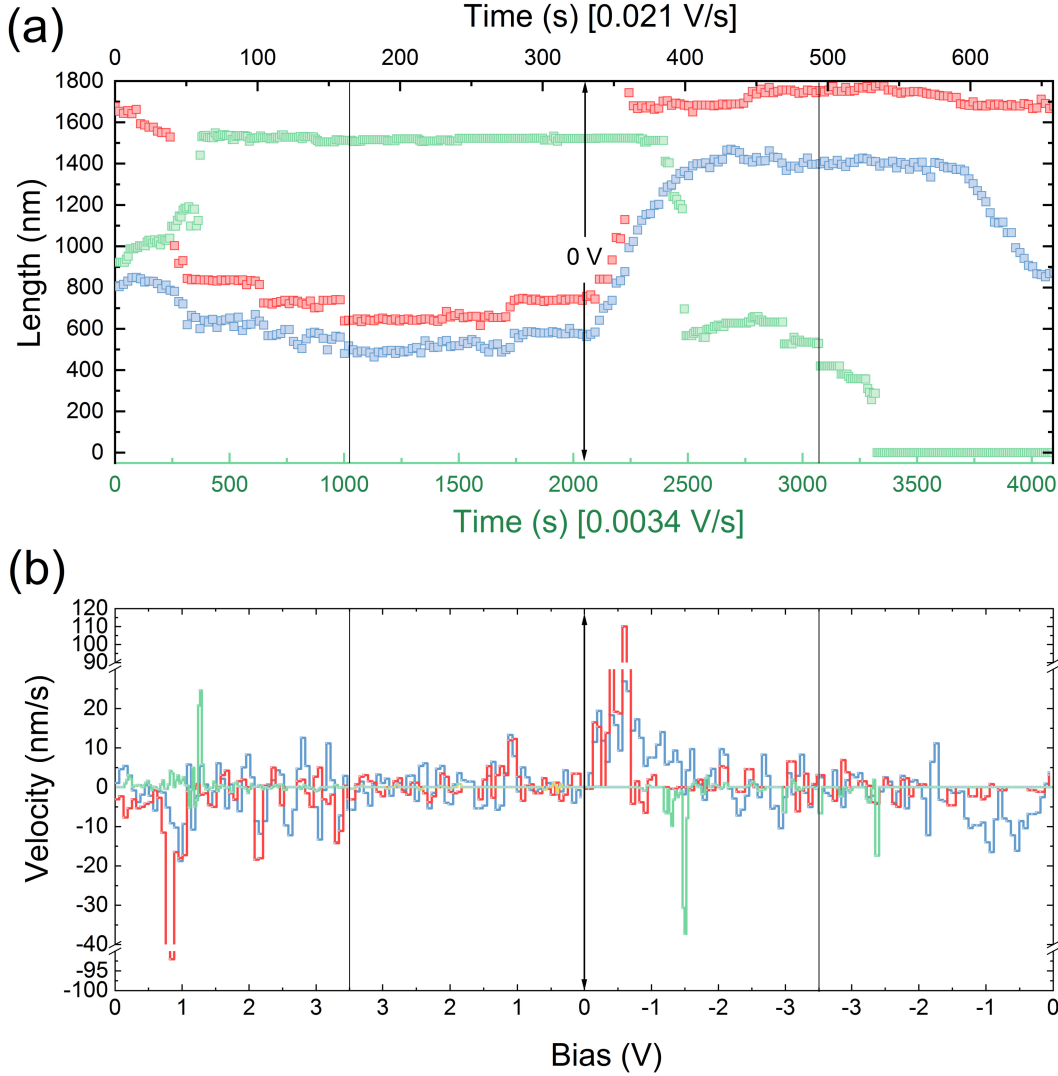
Figure 5.7: Analysis of needle domain motion. (a) Domain length plotted as a function of time. The measurements of the two domains [red and blue of Fig. 5.4(a)] correspond to the top black x axis (performed at 0.021 V/s) whereas the green squares and bottom x axis correspond to the slow domain response seen in Fig. 5.6 (performed at 0.0034 V/s). Red and green vertical arrows indicate Barkhausen events. The dashed, green arrow represents the point of annihilation of the domain. Gray dotted horizontal lines represent domain length after relaxation. The domain response of the ultralow frequency measurements is reversed, due to the spontaneous polarization direction upon domain nucleation. (b) Domain tip velocity with respect to applied bias voltage [color coding is the same as in (a)]. Time and bias x axes on the two plots are scaled in such way that they correspond to each other on the basis of the field waveform. Reproduced from ref. [118]. By respecting *Creative Commons Attribution 4.0 International license.*

By numerically differentiating the domain length vs. time data [Fig. 5.7(a)], the speed of the needle domains can be determined. Figure 5.7(b) shows the velocity as a function of applied voltage for the three distinct domains. Essentially, the speed is proportional to the local switching current (i.e., $i \sim \Delta P / \Delta t$). By comparing the lattice-mediated growth (blue line) with the domain-domain interaction (red and green lines), it is determined that the domain-tip velocity for the lattice-mediated domain is more smeared out (i.e., the vertex is almost always moving), whereas the tip velocity of domains that interact with each other is accompanied with sharp spikes and, at most times, the velocity is close to zero. This indicates that the potential well is deeper for domain domain associated pinning as compared to pinning due to the defects within the lattice [143, 144]. Additionally, in the case of the low frequency measurement (green line), the velocity spikes can be seen in the deep negative electric field region representing Barkhausen jumps due to the simultaneous effects of domain-domain interaction and slow relaxation processes.

Overall, the observed evolution and motion of ferroelectric single needle domains induced by the electric field applied in the polar direction is characteristic of a forward domain growth process [145]. However, we have previously shown that such movements follow Rayleigh-like behaviour [80] and, therefore, pinning mechanisms typically studied for lateral domain wall movements are also applicable in this high field regime. Further, we discuss the dynamic behaviour of the domains on the basis of the schematics in Fig. 5.8. Our results show that when a herringbone domain pattern is adopted, a separation between perpendicular domains that never come into contact with each other is probed [Fig. 5.8(a)]. Images associated with this phenomenon are shown and inspected in the Fig. 5.9. Moreover, the depolarizing and strain fields at the needle tip form a large potential barrier that manifests as well-defined Barkhausen jumps. The positions of these jumps are associated with the annihilation of the periodic, perpendicular domains. The motion of the domains through potentials determined by domain-domain pinning interactions leads to hysteretic behavior. A different mechanism is encountered when parallel needle domains are free to move within the lattice [Fig. 5.8(b)]. In this case, the Barkhausen pulses are rare events, and are most likely dominated by Peierls' potential barriers due to lattice potential and point defects in the non-perfect crystal [143, 144]. The associated shallow potential barrier does not affect perpendicular domain-domain motion but is dominating the jump frequency during the motion of single domains across the lattice. Therefore, at the moderate electric field and frequencies used herein, Barkhausen jumps mostly originate from domain-domain interactions without domains actually touching each other and much less from interaction of domains with point defects.
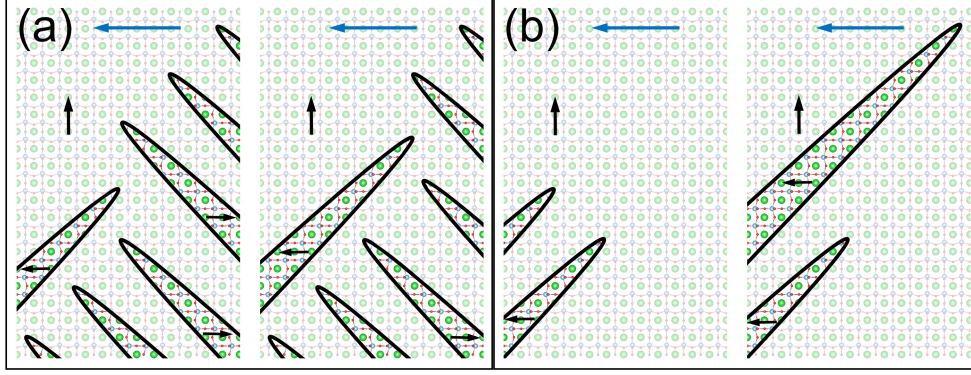
Figure 5.8: Schematic of a needle domain response with strong domain-domain interaction and weak lattice mediated pinning. (a) Needle domain configuration in a metastable electromechanical equilibrium before a Barkhausen event and new equilibrium after the application of external electric field in the polar direction of the needle domains. (b) Configuration of two needle domains located far from perpendicular domain walls. The electric field direction is depicted with blue arrows and the polarization directions in all domains are shown with black arrows. Reproduced from ref. [118]. By respecting *Creative Commons Attribution 4.0 International license.*
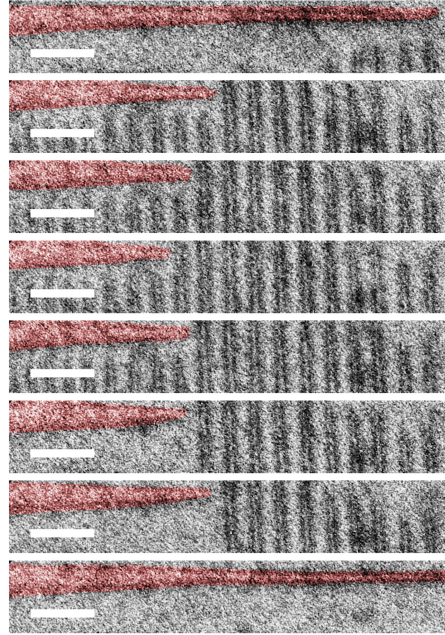
Figure 5.9: Close-up inspection of domain tip interactions. The excerpts correspond to various voltage values of the loop of Fig. 5.4 (a), which exhibits characteristic Barkhausen jumps. Light contrast is seen in-between crossing needle domains, indicating separation between them. Scale bars are 300 nm. Reproduced from ref. [118]. By respecting *Creative Commons Attribution 4.0 International license.*

5.4 Conclusions

In conclusion, individual ferroelastic needle domain response on the applied electric field was demonstrated, leading to strong pinning and consequential Barkhausen jumps in between domain structure metastable equilibria. The mechanisms of domain-domain interactions among noncontacting domains remain largely unexplored. The experimental study shows that major domain pinning and restriction to movement in a thin single crystal $BaTiO_3$ ferroelectric is predominantly associated with contactless mutual domain interaction and less with Peierls' potential pinning arising from the lattice in an undoped crystal. The shape of the measured domain length-electric bias loops hints that domain-domain interaction may be dominant in the expression of the materials properties macroscopically. Individual local relaxation events leading to aging and creep have also been observed. Such insights gained from local measurements performed in a thin ferroelectric slab, can be relevant for modern technologies related to local and global polarization switching.

6 *In situ* EELS studies of BaTiO$_3$

In this chapter *in situ* EELS studies of tetragonal and cubic BaTiO$_3$ are discussed. Core-loss EELS were acquired together with the help of Dr. Liam Spillane (EELS application specialist in Gatan, Pleasanton, USA). Angle resolved EELS were acquired by Dr. Liam Spillane.

Contributions of Reinis Ignatans: wrote data analysis and deconvolution scripts, performed DFT calculations and wrote point charge model script.

6.1 Introduction

A ferroelectric transition implies physical displacement of the atoms. However, the atomic configuration governs the electronic structure of the solid and, therefore, the structural phase transition also influences the electronic structure of the crystal.

In $BaTiO_3$, the transition at the Curie temperature occurs from paraelectric cubic $Pm\bar{3}m$, where three crystallographic axis are equivalent, to polar $P4mm$ space group, where two crystallographic axis are equivalent ($a = b$) but the polar c axis is larger ($c > a = b$). Such crystallographic configuration gives rise to anisotropic dielectric, piezoelectric, mechanical and optical properties [17]. The anisotropic optical properties is a direct evidence for the anisotropic electronic structure with respect to the crystallographic axis.

Indeed, optical spectroscopy as well as theoretical calculations reveal that change from cubic to tetragonal symmetry in $BaTiO_3$ shrinks the bandgap from ~ 3.4 to 3.2 eV [146]. Additionally, as shown by Merz, the dielectric constant along the polar axis is smaller by at least an order of magnitude ($\varepsilon_c = 100$) when compared to the one along the two equivalent directions ($\varepsilon_a = 10000$) in tetragonal $BaTiO_3$ [10].

Electron energy loss spectroscopy (EELS) probes empty density of states (DOS). Low loss EELS contains information on the valence and conduction bands, while the analysis of the core-loss EELS sheds light on the bonding between atoms and oxidation states of the atoms within the matter [71]. Accurate analysis of the EELS could bring new insights on the nature of the ferroelectric phase transition, that is, whether it comes closer to the order-disorder type or displacive. Additionally, angle resolved (or momentum resolved, which is an equivalent term) EELS could potentially resolve anisotropic properties of ferroelectric $BaTiO_3$, which could be projected further to more complex systems.

Herein, $BaTiO_3$ is probed with *in situ* electron energy loss spectroscopy techniques. Core-loss EELS is experimentally measured in $q \sim 0$ mode on the oxygen and titanium absorption edges and theoretically calculated with modern density functional theory (DFT) approach. Low loss EELS of $BaTiO_3$ is measured in angle resolved mode, which allows precise badgap measurements and provides an opportunity to extract anisotropic properties of $BaTiO_3$. Similarly, the low loss EEL spectra of $BaTiO_3$ are calculated with modern DFT approach and the theoretical spectra are compared to the experimentally obtained.

6.2 Methods

6.2.1 Sample preparation

Single crystalline BaTiO$_3$ (001) (MTI Corporation) was used for the experiments. The largest facets of the crystal were polished to optical grade. Two different samples were prepared. Sample number 1 was made on a heating/biasing MEMS chip with the FIB methodology described in Chapter 3. With a similar approach, Sample number 2 was prepared, however, it was mounted on the conventional *Omniprobe* Lift-Out grid. Sample number 1 was used for the core-loss EELS studies, but Sample number 2 was used for the low-loss EELS measurements.

6.2.2 EELS spectroscopy

Core-loss EEL spectra were acquired on a double spherical aberration (Cs) corrected Titan Themis 60–300 (ThermoFischer Scientific) operated at 300 kV, equipped with a *Gatan Image Filter* (GIF) Quantum ERS electron energy loss spectrometer. A beam current of 100 pA was used. The double tilt *in situ* biasing and heating holder by DENSsolutions was used. The microscope was operated in scanning transmission mode (STEM). The beam convergence semi-angle was 28 mrad and the spectrometer collection angle was 19.8 mrad. The microscope was set on the shortest camera length (29.5 mm) to gather as much scattered electrons as possible in the 2.5 mm entrance aperture of the spectrometer. The spectra were acquired as maps, where each scanned pixel contains an EEL spectrum from the particular region on the sample. The displayed spectra are integrated maps. The spectra were acquired in dual-eels mode (both low loss spectrum containing zero loss peak as well as core-loss regions were recorded, allowing precise energy axis calibration).

Low-loss angle resolved EELS spectra were recorded on a Jeol F200 microscope equipped with cold field emission gun (cold-FEG). The microscope was operated at 200 kV in STEM mode. The GIF Continuum K3 HR spectrometer was used. The sample was mounted in the Gatan furnace type heating holder. The scanning beam was set-up to form narrow parallel beam with an estimated convergence angle of $\sim$ 0.11 mrad. The signal entering the spectrometer corresponds to a diffraction pattern and a slit aperture (3.3 mrad wide) was used to select a direction containing $00\bar{1}$, 000 and 001 maxima, transferred in the spectrometer optics. The resulting data set contained momentum transfer - energy loss map (q-E map) from a particular region in the sample. The q-E maps were obtained in two different temperatures, 250 °C for cubic BaTiO$_3$ and at 100 ° for tetragonal BaTiO$_3$ showing ferroelastic 90° domain walls.
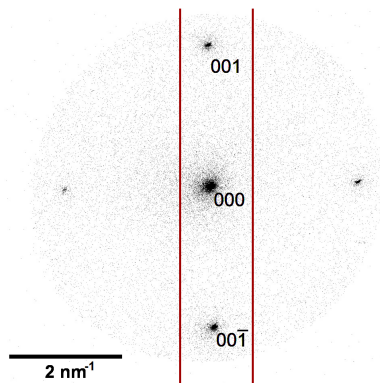
Figure 6.1: Diffraction pattern of tetragonal BaTiO$_3$, which is transferred in the EEL spectrometer. Dark spots indicate diffraction maxima from {100} planes. Red lines show the position of the slit aperture during q-E maps EELS acquisition.

6.2.3 EELS data analysis

Spectral data primary analysis, background subtraction with power law, Fourier-ratio deconvolution and primary analysis was performed in *Gatan* GMS 3 software with the methods readily available within the software suite.

Low-loss momentum resolved EELS primary data inspection was also made with GMS 3. However, there are no readily available tools for data correction (alignment of the energy axis and removal of stray X-ray effects in the q-E map). Additionally, the procedure to treat multiple scattering in angle resolved mode is different as compared to conventional angle integrated low-loss spectroscopy. Therefore, suitable data-treatment scripts were developed in *Mathematica 11.2*, which will be demonstrated in the Results and discussion section.

6.2.4 Core-loss spectra calculations

First, to understand the influence of the titanium displacement within the oxygen octahedron on the 3d density of states, a point charge model was created in *Mathematica 11.2* based on Ref. [147]. The code is provided in Appendix B. However, it was found that the parameter G_{21}^i used by [147] has an error, therefore parameters from Ref. [148] were used. A point charge model was successfully implemented in the analysis of LaMnO$_3$ EEL spectra [149].

The absorption spectra of the oxygen K edge and titanium L$_{3,2}$ edge in BaTiO$_3$ were calculated with FDMNES software package [79]. The calculations are done in direct space with the cluster based approach. A cluster with cutoff radius at 7 Å was created with crystallographic parameters from [150]. Calculations were done with the full relativistic approach. (i.e. spin up and spin down states were calculated separately). For the titanium L edge calculations, time dependent density functional

theory (TDDFT) was used, as it takes into account core-hole effects, which strongly affect the transition metal L$_{3,2}$ white line relative intensities and the overall shape of the absorption edge [151]. An example input for FDMNES package to calculate the Ti L$_{3,2}$ edge is shown in Appendix C.

6.2.5   Low-loss spectra calculations

Low-loss EEL spectra of BaTiO$_3$ were calculated with Quantum Espresso in combination with the TurboEELS package [74–76]. The work flow for the calculation was as follows: PBEsol type pseudo-potentials were used for the calculations of BaTiO$_3$ obtained from the open source library of the materials cloud [152]. The kinetic energy cutoff for the wavefunctions was set to 60 Ry while the kinetic energy cutoff for the charge density and potential was set to 600 Ry, following the suggested minimal values in the pseudopotential description. For both tetragonal and cubic BaTiO$_3$, an 8×8×8 shifted Monkhorst-Pack mesh was used. The structures were relaxed, in case of the cubic BaTiO$_3$, only the lattice parameter was varied until equilibrium was found. In the case of tetragonal BaTiO$_3$, c and a lattice parameters were varied as well as z coordinate of the Ti and O atoms. The coordinates of Ba were fixed to the origin of the unit cell (as dictated by the symmetry of the *P4mm* space group). The resulting equilibrium structures were used further for the TurboEELS package.

The Im$\{-1/\varepsilon(\mathbf{q}, E)\}$ for BaTiO$_3$ was calculated with 15 000 Liouville–Lanczos iterations, which was adequate for successful convergence. The momentum transfer vector was varied in between runs to calculate the energy loss spectra at various $\mathbf{q}$ (0.1, 0.2, 0.5 and 0.7 1/Å). The calculated energy range for the spectra was from 0 to 100 eV. The same steps were followed for the super cell (2×2×2) calculations of the spectra, with the difference being that the 4×4×4 shifted Monkhorst-Pack mesh was used. Two different calculations were performed with the expanded super cell that fixes the geometry to cubic and only relaxes the lattice parameter and another one, where a single oxygen atom was removed from the super cell and the atomic coordinates and lattice parameters were allowed to relax freely in the three dimensional space. After the structure relaxation of the super cell, the low-loss spectrum of the oxygen-vacant BaTiO$_3$ was calculated. An example work flow to calculate the vacancies in the BaTiO$_3$ energy-loss function is shown in Appendix D. To compare calculated low-loss EELS with experimental spectra at $\mathbf{q} = 0$, the calculations were performed with momentum transfer of 0.1 1/Å (as some momentum transfer must occur due to the energy loss). However, this is very close to $\mathbf{q} = 0$ and the energy loss functions are not greatly altered.

6.3 Results and discussion: Core-loss EELS

The deviation of ferroelectric $BaTiO_3$ from the symmetric cubic structure is small, therefore it is also expected that differences of the spectral features between cubic and tetragonal $BaTiO_3$ are also small. The microscope is equipped with a monochromator, which decreases the energy spread of the incident electron beam. For the particular experiment the monochromator was turned on to increase the visibility of fine details in the spectra. Excitation of the monochromator resulted in an energy resolution of 0.5 eV for the measurements of ferroelectric $BaTiO_3$ done at 100 °C and 0.6 eV for the cubic $BaTiO_3$ measurements recorded at 240 °C. The survey spectrum, containing features of the core-loss $BaTiO_3$ edges, was acquired from 600 to 910 eV energy loss with dispersion of 0.25 eV/channel. Higher energy resolution spectra containing only Ti $L_{3,2}$ and oxygen K edges were recorded from 380 eV to 585 eV energy loss with dispersion of 0.1 ev/channel. The relative indicated thickness was $t/\lambda \sim 0.97$.

The spectrum is depicted in Fig. 6.2. No impurities were detected and all of the spectral features can be assigned to $BaTiO_3$. The Ti $L_{3,2}$ and and Ba $M_{5,4}$ edges have characteristic white lines whereas the O K edge has square-like onset with rich fine structure in the ELNES region.
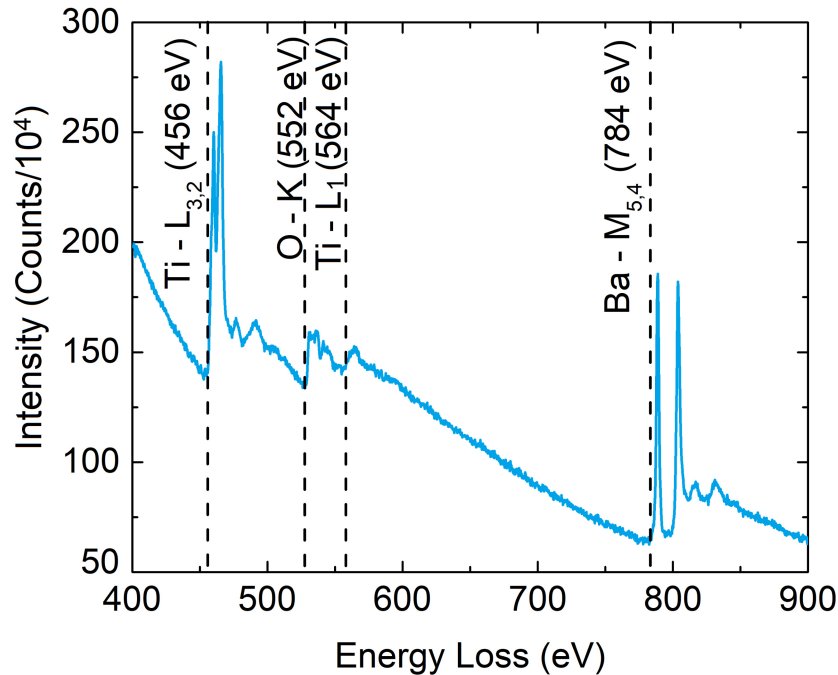

Figure 6.2: Survey spectrum of tetragonal $BaTiO_3$ The spectrum is raw data, no background subtraction or multiple scattering removal is done. All of the features can be assigned to Ba, Ti or O atoms.

The absorption edge that possible changes could occur with respect to the ferro-

electric/paraaelectric states is the Ti L$_{3,2}$. This is because this edge mostly represents electrons transferred to the 3d states. The point charge model was employed to understand the differences in 3d states between highly symmetric Ti in cubic state with respect to the tetragonally distorted oxygen octahedron (see Appendix B for the script). The model does not take into account solid-state effects, but rather it calculates perturbation of the external negative charges on the 3d orbitals of a single Ti-O$_6$ cluster (in principle a molecule). The high symmetry cubic (O_h) case produces
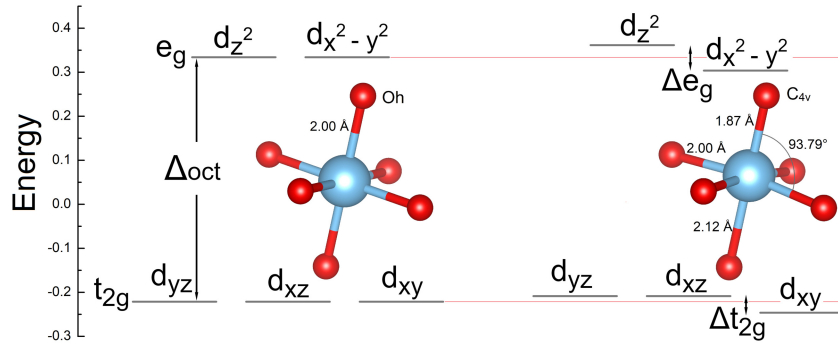
Figure 6.3: Point charge models of Ti-O$_6$ clusters and the energy of 3d electron orbitals. O_h symmetry corresponds to cubic, C_{4v} to tetragonal BaTiO$_3$. O_h symmetry produces classic e_g and t_{2g} orbital splitting pattern, while additional distortion in the tetragonal case adds additional sub-splitting in them.

classical e_g and t_{2g} orbital splitting pattern as seen in Fig. 6.3, where orbitals pointing in the direction of the oxygen anions (d_{z^2} and $d_{(x^2-y^2)}$ are destabilized and raised in the energy scale while the rest of the orbitals are pointing in between the oxygen anions and are lowered in the energy scale [147]. The tetragonal distortion (C_{4v}) leaves only the d_{yz} and d_{xz} orbitals in degenerate state. Additional splitting is seen in the e_g-like orbitals, where d_{z^2} is destabilized and $d_{(x^2-y^2)}$ are slightly stabilized with respect to the O_h state. Splitting is also expected in the t_{2g} orbitals, but it it smaller as compared to e_g ($\Delta e_g > \Delta t_{2g}$).

Examination of the EEL Ti L$_{3,2}$ edge (background subtracted, plural scattering corrected and normalized to the maximal intensity) at the ferroelectric (100 °C) and paraelectric states (240 °C) reveals two peaks on each edge corresponding to e_g/t_{2g} splitting. The octahedral field splitting in cubic state is $\Delta_{oct} = 2.02$ eV. Comparison of the spectrum measured at 100 °C with the 240 °C one shows a slight shift of the peak corresponding to the e_g orbitals, Fig. (6.4). As the observed shift is small, the e_g peaks of the L$_3$ edge at both temperatures were fitted with a Pseudo-Voigt peak function to precisely find the centers of them (note that the energy axis was very carefully adjusted so the center of zero loss peak is at 0 eV). Peak fitting reveals a 50 meV difference in the centers of the e_g peaks of tetragonal and cubic BaTiO$_3$ as shown in Fig. 6.5. Although the effect is small, it is reproducible and it has also been observed before [153]. Therefore, it is not an artifact. Although the difference in the

e_g-like orbitals corresponds well with the simple point-charge model with tetragonal distortion, it does not take into account solid state effects, electronic transitions to the empty states, or the effect of core-hole left behind in the deep atomic states.
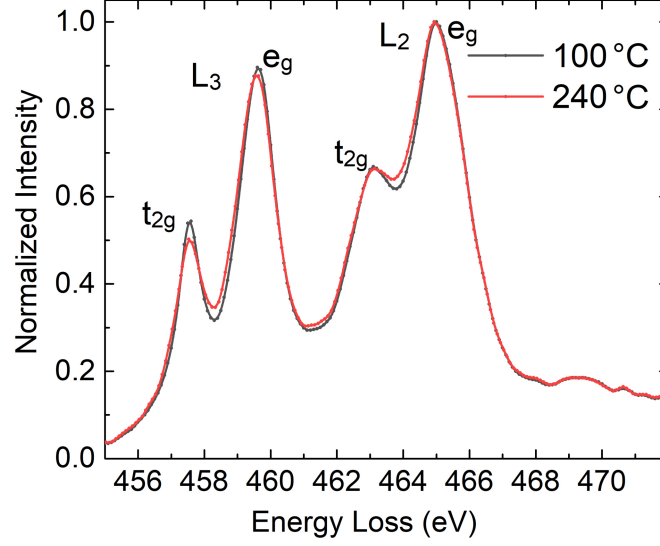
Figure 6.4: Ti $L_{3,2}$ EELS at 100 °C and 240 °C. Small dots on the lines represent data points. Both, L_3 and L_2, edges show distinct octahedral field splitting in to a doublet. Additional splitting in the e_g/t_{2g} of tetragonal (100 °C) BaTiO$_3$ is not resolved, but there is slight shift in the peak corresponding to e_g-like orbitals.
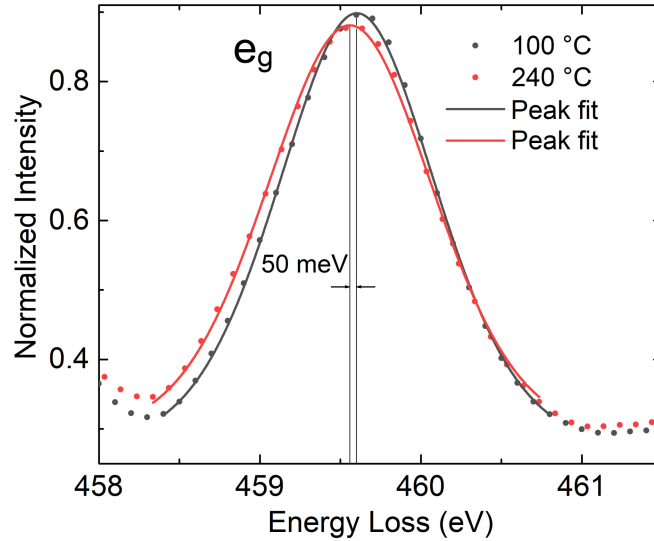
Figure 6.5: Ti L_3 e_g peak at 100 °C and 240 °C. Dots represent measurement points, the line is Pseudo-Voigt profile fitting the data.

To better understand the differences of Ti $L_{3,2}$ edge between the tetragonal and cubic states of BaTiO$_3$, the spectrum was simulated with FDMNES package em-

ploying muffin-tin approach and TDDFT. The results for both cubic and tetragonal cases are shown in Fig. 6.6.
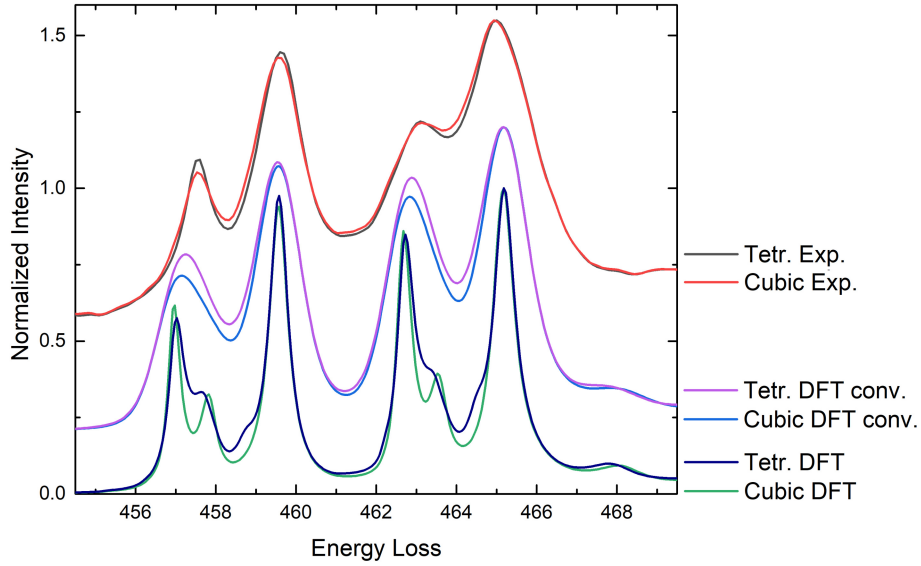
Figure 6.6: Comparison of experimental and calculated Ti L$_{3,2}$ absorption edges. Red and gray lines are experimental spectra, violet and blue lines are calculated spectra, which are convoluted with Gaussian so the L$_3$ e_g peaks are same width, dark blue and green lines are spectra without convolution.
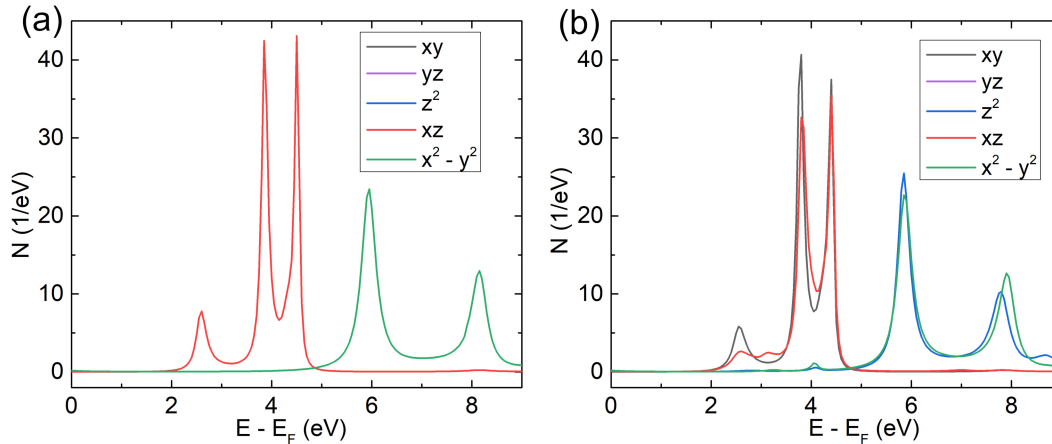
Figure 6.7: Projected density of of 3d-like states in cubic and tetragonal BaTiO₃. (a) As calculated for cubic case. (b) Tetragonal case. Seperate color coding for the five different orbitals.

The TDDFT approach has reproduced reasonably well L$_3$/L$_2$ ratio, which is usually problematic to calculate right with simpler methods [78]. Theoretically L$_3$/L$_2$ ratio should be 2 (that is, the first L$_3$ edge should be twice as intense as L$_2$ edge), because initial state $2p_{3/2}$ of the electron experiencing L$_3$ absorption has four electrons, while

$2p_{1/2}$ initial state for the L_2 edge has two electrons. The TDDFT takes into account core-hole instigated mixing of the final empty states of e_g and t_{2g}, therefore reproducing experimentally observed ratio. Interestingly in the calculated spectra a shift (~ 100 meV) is observed in the t_{2g} peak and not in the e_g. This could be attributed to the wrongly calculated L_3/L_2 transition cross-sections or overestimation of e_g/t_{2g} mixing [71, 77, 78].

Inspection of the calculated projected density of states corresponding to 3d states gives similar picture, Fig. 6.7. In the cubic case, Fig. 6.7(a), two degenerate states are seen exactly as in the point charge model, albeit the solid state effects create fine structure in them. The tetragonal case, Fig. 6.7, shows the same splitting pattern as the point charge model.

Another possibility of this discrepancy could be indicative of the order-disorder character of the phase transitions in $BaTiO_3$, where in the "cubic" case the titanium atom "rattles" around in between eight different positions in the <111> directions in the unit cell [90, 153]. In this case, the calculated density of states and the associated transitions may be calculated erroneously.
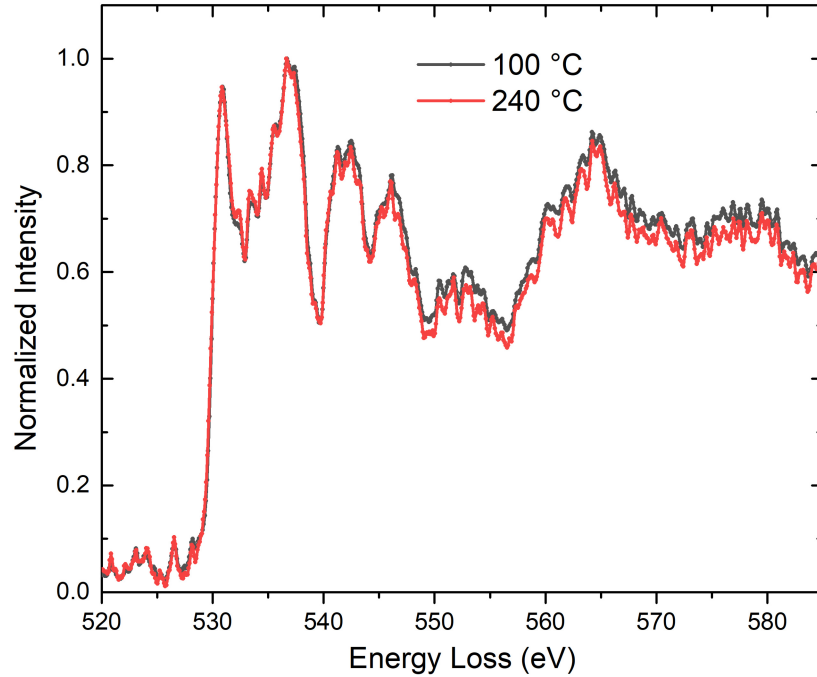
Figure 6.8: EELS of oxygen K edge at 100 °C and 240 °C of BaTiO₃.
Dots represent measurement points. The data are background subtracted, multiple scattering corrected and normalized to maximal intensity.

Inspection of the O K absorption edges does not reveal any large differences between the cubic and tetragonal states of $BaTiO_3$, Fig. 6.8. However, this could be attributed to noise in the data as the O K edge is less intense than the Ti $L_{3,2}$

(Fig. 6.2). As per Ref. [153], some differences are expected in the near vicinity of the edge onset.
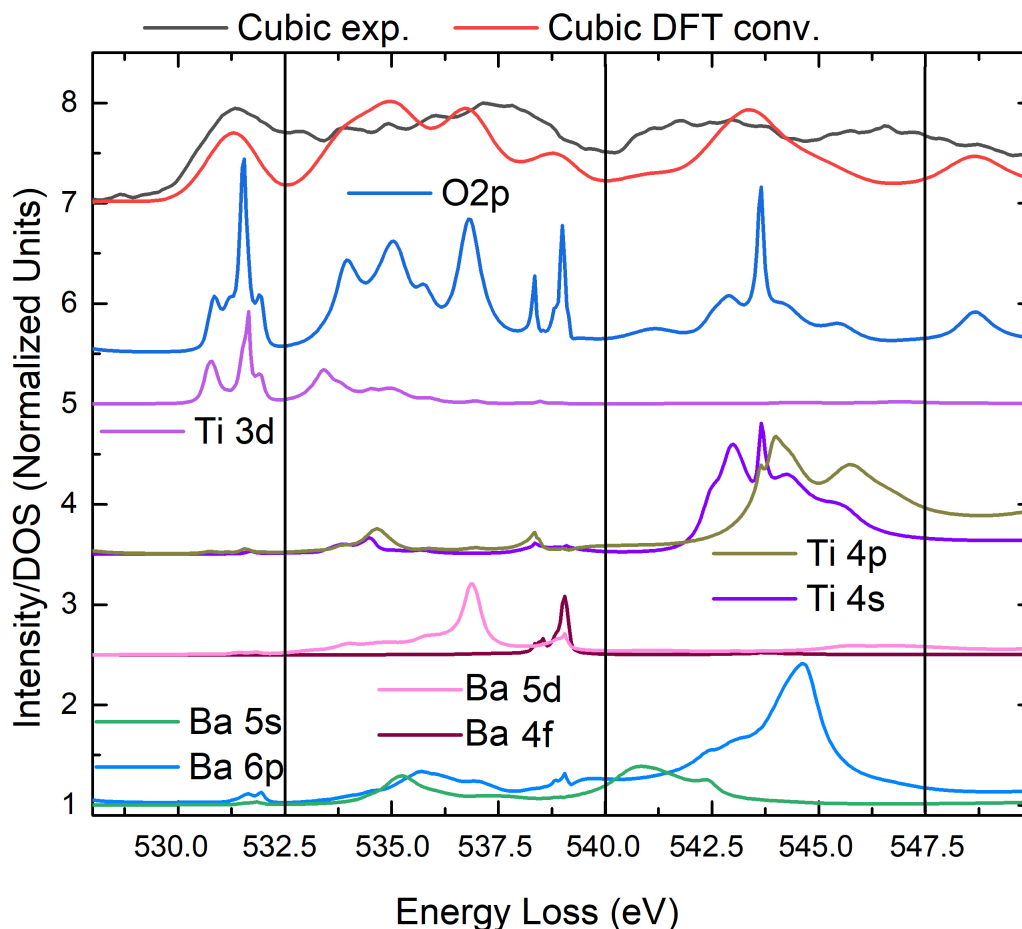
Figure 6.9: Experimental and calculated EELS of the oxygen K edge of BaTiO₃ and comparison with some projected density of states. On the top, dark grey line is the experimental spectrum red line is calculated spectrum (convolved in such way, so the peak onset of the edge would match experimental). Blue line is the empty density of states having oxygen 2p character. Underneath, projected density of states of several titanium and barium orbitals. Density of states is aligned so it would coincide with the absorption edge on the energy axis.

The O K edge represents hybridization of the oxygen empty p-like states with the titanium and barium empty states. FDMNES calculations were also performed on the O K edge to understand the origins of the various peaks. Figure 6.9 shows that the onset of the O K edge represents the Ti 3d hybrid states, indicative by the similarity of O 2p (blue line) with the Ti 3d states (violet line). The region between 532.5 to 540 eV corresponds to hybrid states with barium, while the region between 540 and 547.5 eV indicated the character of the outer, diffused Ti orbitals. Therefore,

the origins of the rich fine structure are well illustrated with the help of density of states calculations.

6.4 Results and discussion: Low-loss EELS

Experimental acquisition and data extraction from angle resolved (q-resolved) EELS data require different approaches as compared to the angle integrated data. It is noted that when **q** is mentioned herein, it indicates the momentum transfer perpendicular to the incident electron beam.

Q-resolved EELS acquisition is challenging due to the high intensity of non-scattered and weakly scattered electrons around $q \sim 0$. However, the signal rapidly drops when EEL spectra are measured at $q > 0$. Therefore, a large dynamic range of the detector collecting the signal is required. Nevertheless, even with modern detectors it is very easy to saturate the signal at $q \sim 0$, while the signal-to-noise ratio at high scattering angles is still low.

Another challenge has to do with the extraction of the q-resolved data and their analysis since there are no readily available tools or software packages. Previously, Batson and Silcox have developed a mathematical framework of data treatment [154] and herein, I will demonstrate an implementation of their method with some improvements regarding dielectric samples with high refractive index.

The extraced $\mathrm{Im}\{-1/\varepsilon(\mathbf{q}, E)\}$ at various q vectors (also along polar and non-polar directions) will be treated further to obtain the real and imaginary parts of the dielectric function. Finally, the experimental functions will be compared to the theoretically calculated ones.

6.4.1 Data treatment

The raw data are collected as q-E images, where the vertical direction (2048 pixels in height) corresponds to the angular part and the horizontal direction (3456 pixels wide) to energy loss. The dispersion in the energy range is 0.03 eV/pixel. The recorded energy range spans from -5 eV to 98 eV (for the maps containing the zero loss peak), while the q range encompasses the central, non-scattered beam surrounded by two opposite diffraction maxima (for example, 001 and 00$\bar{1}$), which are used to calibrate the momentum axis of the q-E map. The energy resolution of the q-E map is ~ 0.6 eV. An example of the recorded raw map is shown in Fig. 6.10(a).

Additionally, maps with shifted energy range were recorded in a way that the zero-loss part did not enter the spectrometer, Fig. 6.10(b). The obtainable intensity in the maps was limited by the spectrometer's shutter where the zero-loss peak quickly over-saturates the detector elements. The recorded spectrum without the ZLP (with the same acquisition time) has 5.5 times larger average intensity. To increase the signal in the low loss region, maps without the zero-loss part were "stitched" together

with the zero-loss from the maps containing it. The zero-loss part was multiplied accordingly to match the average intensity in the low-loss part.
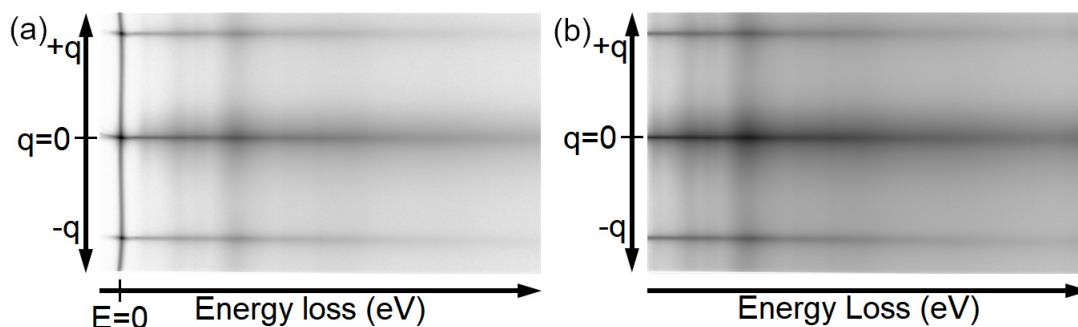
Figure 6.10: Raw recorded q-E maps (a) Map containing a zero-loss peak. (b) Recorded map without zero-loss peak. Both maps are shown in the logarithmic scale, each pixel has been added one to the recorded intensity as there were pixels with zero counts. Contrast is inverted for better visualization. Central peak corresponds to $q = 0$, top and bottom peaks are diffracted beams.
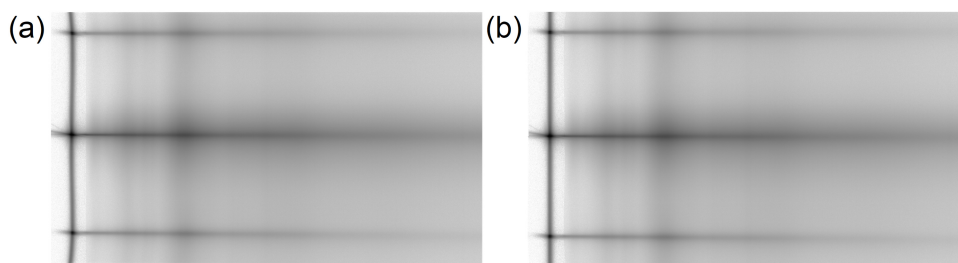
Figure 6.11: Stitched q-E maps. (a) The map contains low loss part recorded with higher shutter duty cycle [Fig. 6.10(b)], which is stitched together with the missing zero-loss (intensity accordingly multiplied) part from another measurement [Fig. 6.10(a)]. (b) The same map, but the energy scale is aligned across the whole map.

The camera used for recording the q-E map is very sensitive and stray X-rays may enter the electron sensitive detector and dissipate their energy, which results in some pixels having unreasonably high intensity. An example of one such event is shown in Fig. 6.12. To remove them, An automatic spike removal routine was written in *Mathematica 11.2* and can be seen in Appendix E. In a nutshell, the function has two inputs that includes the q-E map (named *list* in the function) and some criteria (named *crit* in the function). The script iteratively runs through every energy loss spectrum at each q value and checks each value on the energy axis with the neighbor on the left and on the right (special treatment is done if the checked value is at the start or at the end of the spectrum). If the intensity of a pixel is *criteria* times larger than the average of the neighboring ones, a spike is detected. The value of

the particular pixel is then altered to be the average value of the neighboring pixels, otherwise, no alterations are done. The result of this function is a corrected q-E map named *cor*.
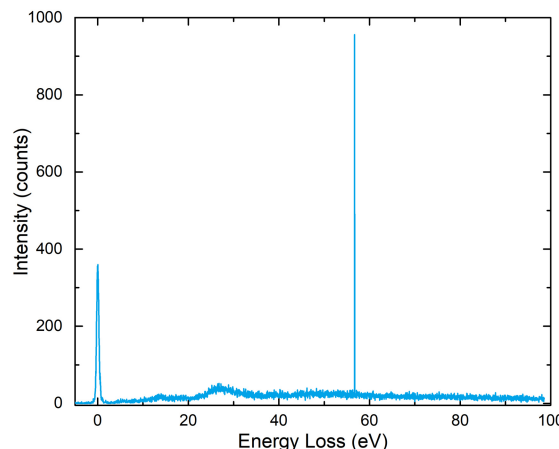
Figure 6.12: A large spike due to a stray x-ray entering the spectrometer. Example is from a spectrum row with $q >> 0$, therefore the small count statistics. Around 58 eV a large spike is seen.

By examining Figs. 6.10(a) and 6.11(a), it is apparent that the zero-loss peak is not located at the same energy channel throughout the whole map, but it rather looks "wavy". This is the result of the imperfect electron optics and residual aberrations, which cannot be avoided during acquisition. To correct for this artifact the following routine is used. For each row in the q-range, a zero-loss peak is fitted with a Gaussian function and its parameters are saved in an array. The zero-loss peak, which has the largest energy (i.e. the one which has shifted the most to the right hand side in the q-E map) is found. Every other zero-loss peak is shifted to the same energy (i.e. pixel number). The shift is accompanied by padding the left hand side with zeroes. In principle, this is permissible since there should be no intensity on the left hand side of the zero loss peak (electrons do not gain energy in the process of transmission through the specimen). The right hand side (tail at the high energy losses) of the shifted spectra is then removed to keep the original size of the q-E map.

The low-loss EELS of BaTiO$_3$ is strongly influenced by Cherenkov losses [155, 156]. In short, when a charged particle is traveling through a medium with speed $v > c/n$, where c is the speed of light and n is the refractive index, it loses energy via Cherenkov radiation. The refractive index of BaTiO$_3$ is $n \sim 2.4$ [157]. For BaTiO$_3$, Cherenkov losses occur when the electrons are accelerated over ~ 50 kV and, therefore, in any conventional TEM Cherenkov losses are inevitable. In the EEL spectra, Cherenkov losses appear close to the ZLP and are highly forward scattered, that is, almost only the $q = 0$ part is affected. However, this is also the most intense part of the q-E map. The effect of Cherenkov radiation loss can be

seen in Fig. 6.13(a). It is noted that off-axis measurements are not influenced by this effect as seen by the red line in Fig. 6.13(a). The distance in q between non-diffracted beam and 001 maximum is 1.56 1/Å, while the off axis measurement lays very close to the zero loss peak at $q = 0.07$ 1/Å. In addition, the Cherenkov loss effect is always seen in the integrated spectra case [blue line in Fig. 6.13(a)]. The affected part lays in the bandgap region, which effectively forbids precise bandgap measurements for materials with large refractive index with conventional approaches (for example, conventional STEM-EELS would produce artificially narrow bandgap measurement) [158].
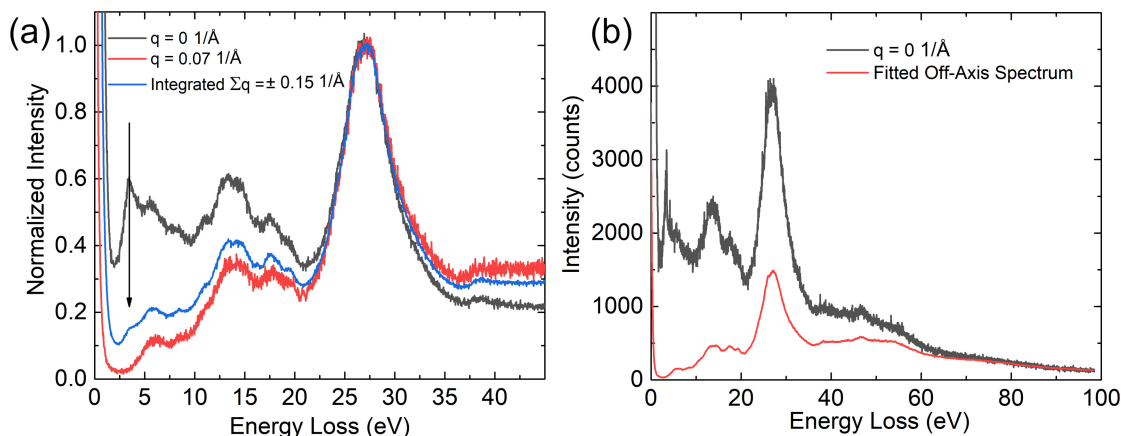
Figure 6.13: Cherenkov loss affected spectra. (a) Gray line is $q = 0$ line in the q-E map, the arrow indicates excess loss intensity, additional peak appears close to the ZLP. Red line is a spectrum measures at $q = 0.07$ 1/Å. Measurement off-axis gives the true shape of the low-loss spectra. Blue line is a spectrum obtained by integrating in the range ± 0.15 1/Å. Although the shape of the spectrum is similar to the off-axis measurements, Cherenkov losses create additional peak in the band-gap region of the low-loss. (b) Gray line is the spectrum measured at $q = 0$ Red line is a spectrum obtained by averaging 5 spectra in the q range from 0.077 to 0.087 1/Å and fitting the tail from ~ 80 eV energy loss.

As the Cherenkov losses affect the spectra close to $q = 0$ and the affected part is at smaller energies, a plan to remove this effect from the spectra was created. The Cherenkov loss affected region was separated from the q-E map, which spans across $q = \pm 0.087$ 1/Å. The spectra at the bordering region of the separated region were not affected by the Cherenkov loss and average spectrum spanning from $q = 0.077$ to $q = 0.087$ was calculated. The tail region of the region of the off-axis spectrum was fitted to each spectrum in the Cherenkov loss affected region and the excess intensity was then removed. Finally, the corrected region was added back to the q-E map. The full script is shown in Appendix G.

Fig. 6.14(a) shows the resulting map where only the $q+$ range is shown because it will be used further for the dielectric loss function extraction. To increase the

Figure 6.14: q-E maps showing the effect of Cherenkov loss correction and potential binning. (a) q-E map after Cherenkov loss correction. (b) q-E map with potential q bins, each bin is located in between dashed red lines.

signal-to-noise ratio, binning along the q direction was performed, Fig. 6.14(a). The binning is shown on the Cherenkov loss uncorrected q-E map, as it was easier to align the $q = 0$ position. The width of each bin is $\sim \Delta q = 0.05$ 1/Å. and the spectrum in each bin is the sum of the spectra. Two scripts were created, one to align the bins and $q = 0$ and the other one to perform the binning (see Appendix H). The binning script also creates the so called *Image spectrum*, which is formed by integrating along the q-direction can is used in the further stage. After all the corrections and binning, an attempt to extract the single scattering distribution can be made.

6.4.2 Single scattering q-E map extraction

In the momentum resolved EELS two unwanted scattering processes take place: the quasi-elastic multiple scattering and the usual electronic multiple scattering (i.e. electrons scattering more than once in the specimen).

The effect of quasi-elastic multiple scattering is dominant at larger momentum transfers (higher scattering angles). Essentially, spectra at $q > 0$ are convoluted with scattering from all the other momentum vectors [154]. Mathematically it is represented with the following convolution integral:

$$\int_{-\infty}^{+\infty} Q_M(\mathbf{q} - \mathbf{q}') E_M(\mathbf{q}', \omega) \, d^2\mathbf{q}', \tag{46}$$

where $Q_M(\mathbf{q} - \mathbf{q}')$ is the wide-angle multiple quasi-elastic scattering associated with small energy loss of wave vector $\mathbf{q} - \mathbf{q}'$, $E_M(\mathbf{q}', \omega)$ is the conventional multiple electronic scattering at $\mathbf{q}'$ with energy dependence ω [154]. Removal of the quasi-elastic
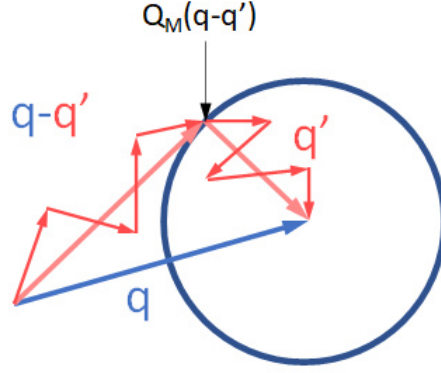
Figure 6.15: Schematic representation of the quasi-elastic multiple scattering. Geometric construction showing the composition of quasielastic plus plasmon scattering at the point q. The multiple scattering is broken up into terms involving only multiple quasielastic scattering and multiple plasmon scattering. The total intensity at q is obtained by an integration over all q'.

scattering is done mathematically via Fourier transformation:

$$\widehat{I_E}(\mathbf{q_0}, \widehat{\omega}) = \widehat{G}(\widehat{\omega}) \left(\frac{\widehat{I_M}(\mathbf{q_0}, \widehat{\omega})}{\widehat{Q_M}(\mathbf{q_0}, \widehat{\omega})} - \frac{\widehat{I_I}(\widehat{\omega})}{\widehat{Z_I}(\widehat{\omega})} \right), \tag{47}$$

where $\widehat{I_E}(\mathbf{q_0}, \widehat{\omega})$ is the elastic electronic scattering (still containing multiple electronic scattering) at particular $\mathbf{q_0}$ in Fourier space (note Fourier transform is only done along the energy axis), $\widehat{I_I}(\widehat{\omega})$ is the Fourier transformed image-spectrum (containing zero-loss), $\widehat{Z_I}(\widehat{\omega})$ is the Fourier transformed zero-loss peak of the image spectrum, $\widehat{I_M}(\mathbf{q_0}, \widehat{\omega})$ is the Fourier transformed energy loss spectrum at particular $\mathbf{q_0}$ and $\widehat{Q_M}(\mathbf{q_0}, \widehat{\omega})$ is the zero-loss peak of the spectrum at $\mathbf{q_0}$. $\widehat{G}(\widehat{\omega})$ is a re-convolution function (either Gaussian with the same FWHM as zero-loss peak or even the measured zero-loss profile $\widehat{Q_M}(\mathbf{q_0}, \widehat{\omega})$ can be used). The elastic scattering can be retrieved by taking the real part of the inverse Fourier transform of $\widehat{I_E}(\mathbf{q_0}, \widehat{\omega})$.

In practice, discrete Fourier transforms are used and some preparations of the spectra are needed. The zero-loss peak is seperated form the spectra as described in Ref. [71] (finding the minimum on the right hand side of the ZLP, selecting that as the cutoff for the measured ZLP and padding further it to go to zero). Additionally, the tails of the spectra should go smoothly to zero and this is done by increasing the length of the energy scale by two and fitting the right hand side to go to zero with the cosine-bell function of $f(m) = a[1 - \cos(r(n - m))]$, where n is the length of the energy axis (in channels/pixels), a and r are fitting parameters and m is the channel/pixel number [71]. Padding is necessary to avoid artificially induced oscillations in the filtered spectrum, which occur when there is non-zero intensity at the end of the spectrum [71]. It is noted that all of the Fourier transforms are done

on plain data, that is on the matrices, which do not carry any information on the q or energy scales. Re-scaling is done at the very end. All of the arrays used in the discrete Fourier transform must be the same size (i.e same number of entries in the spectrum list). The script can be found in Appendix I.
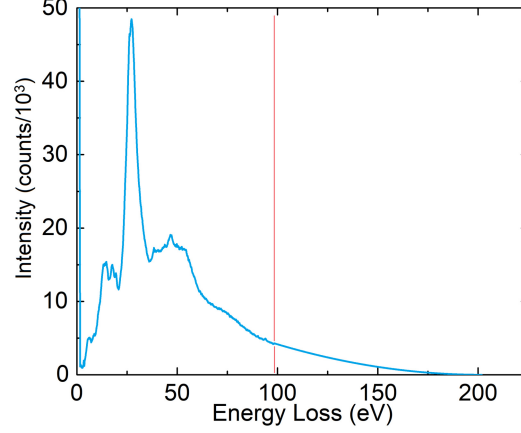
Figure 6.16: Example of padded spectrum. Red vertical line indicates start of the cosine-bell padding, energy range is increased two times to ~ 200 eV.

If the operations are successful, then $I_E(\mathbf{q_0}, \omega)$ is obtained, however it is still affected by conventional multiple electron scattering. Single scattering distribution can be formally retrieved by:

$$\widehat{S}(\widehat{\mathbf{q}}, \widehat{\omega}) \propto \widehat{G}(\widehat{\mathbf{q}}, \widehat{\omega}) \ln\left(\frac{\widehat{I_E}(\widehat{\mathbf{q}}, \widehat{\omega})}{\widehat{G}(\widehat{\mathbf{q}}, \widehat{\omega})} \right), \tag{48}$$

where $\widehat{S}(\widehat{\mathbf{q}}, \widehat{\omega})$ is the single scattering distribution (in Fourier space) and $\widehat{I_E}(\widehat{\mathbf{q}}, \widehat{\omega})$ is the q-E map containing only elastic scattering and $\widehat{G}(\widehat{\mathbf{q}}, \widehat{\omega})$ is the re-convolution function (either standardized Gaussian or the measured ZLP) [154]. It is noted that the form of the function is very similar to the conventional angle integrated case (Fourier Log method) [71]. However, the difference is that here the Fourier transform is two-dimensional. Proportionality in the equation 48 is used deliberately since the single scattering spectrum's absolute intensity is dependent on the thickness of the sample, but the main goal is to get correct shape of the distribution. The single scattering spectrum in direct space is retrieved by taking the real part of the inversely Fourier transformed $\widehat{S}(\widehat{\mathbf{q}}, \widehat{\omega})$.

In practice, the functions $\widehat{I_E}(\widehat{\mathbf{q}}, \widehat{\omega})$ and $\widehat{G}(\widehat{\mathbf{q}}, \widehat{\omega})$ should be even and periodic otherwise, due to the logarithm, artificial phase jumps occur (Fourier transform produces also imaginary part). Additionally, it is important that the zero-loss is located at the first channel/pixel of the q-E map [71], otherwise similar phase problems occur. Moreover, the intensity in the q-direction should smoothly go to zero. To achieve all of these requirements, $I_E(\mathbf{q}, \omega)$ and $G(\mathbf{q}, \omega)$ are modified accordingly. First, the

107

energy range is increased by two while the right hand half of the spectrum is filled with zeros, which artificially creates an even function along the energy axis [71]. The q-range is also increased by two times while the last measured spectrum is identified (last used q bin) and multiplied with a function, which smoothly reaches zero at the end of the new q-range (it can also be a cosine-bell function).
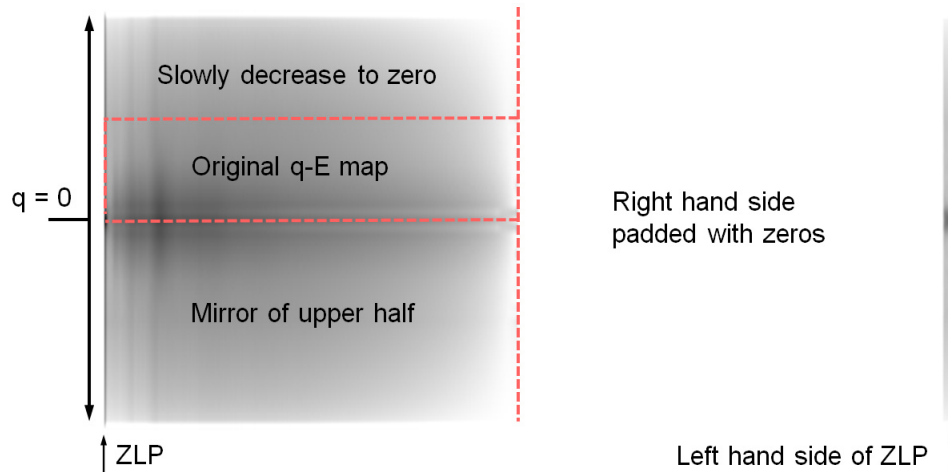
Figure 6.17: Altered q-E map to produce even periodic function. Map is shown in logarithmic scale, the original q-E map is located in the rectangle formed by red, dashed lines.
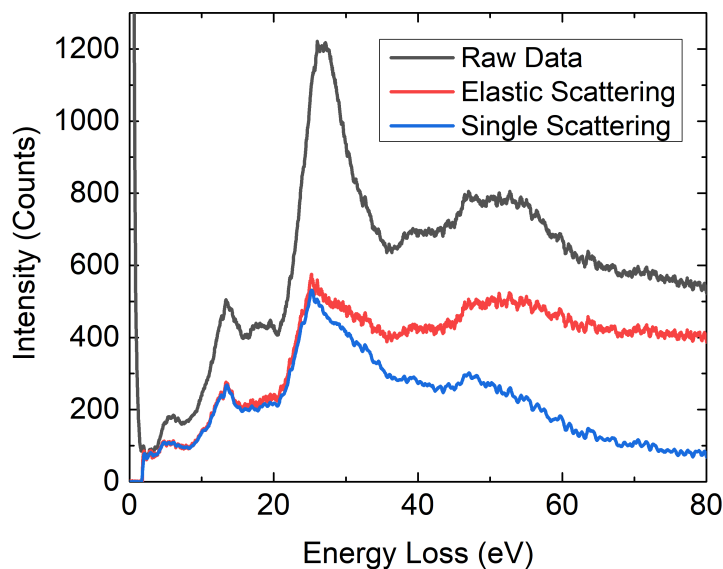
Figure 6.18: Comparison of raw spectrum, quasi-elastic corrected and single scattering distribution. The spectra shown here are recorded at $q = 0.6$ 1/Å. Raw spectrum (gray) has character similar as for $q \sim 0$. Filtering of quasi-elastic scattering reveals true shape of the spectrum at high q. Removal of multiple scattering affects mostly higher loss part of the spectrum as expected.

Then, a mirror image is created along $q = 0$, which is followed by shifting the center of zero loss peak to the first entry in the array and pushing the left hand side of the ZLP to the end of the array. Visually these operations produce a q-E map similar to the one seen in Fig 6.17. The same procedure is done to the array containing only the ZLP of the q-E map. Previous removal of Cherenkov radiation is crucial to get correct single scattering distribution since strong Chernkov losses in the $q \sim 0$ vicinity alters the plural scattering statistics and the formula 48 gives erroneous results. The comparison of the raw spectrum with elastic and single scattering distributions is depicted in Fig. 6.18. The *Mathematica* script to retrieve single scattering distribution is also included in Appendix I.

6.4.3 Retrieval of scaled energy-loss function

The single scattering distribution is directly proportional to the negative-inverse-imaginary part of the dielectric function: $S(\mathbf{q}, E) \propto \text{Im}\left\{-\frac{1}{\varepsilon(\mathbf{q},E)}\right\}$. To retrieve the true $\text{Im}\left\{-\frac{1}{\varepsilon(\mathbf{q},E)}\right\}$, the single-scattering distribution $S(\mathbf{q}, E)$ must be appropriately scaled. For $q \sim 0$, the Kramers-Kronig relationship is utilized (Eq. 43) by using the following approximation: $\text{Re}\{1/\varepsilon(\mathbf{0},0)\} \approx 1/\varepsilon_1(\mathbf{0},0) \approx 1/n^2$ [71].

$$1 - \frac{1}{n^2} = \frac{2}{\pi} \int_0^\infty \text{Im}\left\{-\frac{1}{\varepsilon(\mathbf{0}, E)}\right\} \frac{dE}{E}. \tag{49}$$

The left-hand side of Eq. 49 is known and can be used to calculate the scaling constant for $S(\mathbf{0}, E)$:

$$C_0 = \left(1 - \frac{1}{n^2}\right) \Big/ \left(\frac{2}{\pi} \int_0^{E_f} S(\mathbf{0}, E) \frac{dE}{E}\right). \tag{50}$$

The integral of Eq. 50 has to be calculated numerically. The boundary condition E_f is the final measured energy. After obtaining C_0, the energy-loss function can be obtained:

$$\text{Im}\left\{-\frac{1}{\varepsilon(\mathbf{0}, E)}\right\} = C_0 \cdot S(\mathbf{0}, E) \tag{51}$$

Tetragonal $BaTiO_3$ has ordinary and extra-ordinary optical axis with refractive indices $n_o = 2.42$ and $n_e = 2.36$ (extra-ordinary axis corresponds to polar axis in $BaTiO_3$) [157]. The polarization vector is locked in-plane in a thin TEM specimen, therefore, the direct incident electron beam goes along the ordinary axis and the n_o value should be used. In the case of cubic $BaTiO_3$, there exists a single value $n = 2.52$ (in the temperature interval, where the EELS measurements were done) according to Ref. [159].

For the spectra measured at $q > 0$, Bethe's f-sum rule must be applied to re-scale them to the energy-loss function [71, 76]. Bethe's f-sum rule allows calculation of the

effective number of electrons per unit volume, which participate in the formation of the energy-loss function up to E_f:

$$n_{eff} = \frac{2m_e\varepsilon_0}{\pi e^2} \int_0^{E_f} \mathrm{Im}\left\{-\frac{1}{\varepsilon(\mathbf{q}, E)}\right\} E dE. \tag{52}$$

Note that on the right hand side, the integral contains the energy-loss function with arbitrary $\mathbf{q}$, but the left hand side is independent of it (same electron density form the energy-loss function at $\mathbf{q} = 0$ and $\mathbf{q} > 0$). Therefore, n_{eff} can be calculated by inserting Eq. 51 in the integral of Eq. 52. Then, the re-scaling constant for each separate spectrum measured at arbitrary $\mathbf{q}$ can be obtained:

$$C_q = \left(\frac{\pi e^2 n_{eff}}{2m_e\varepsilon_0}\right) \bigg/ \int_0^{E_f} S(\mathbf{q}, E) E dE. \tag{53}$$

Finally, the integral in the Eq. 53 is calculated numerically and the energy-loss function at some arbitrary $\mathbf{q}$ is obtained via:

$$\mathrm{Im}\left\{-\frac{1}{\varepsilon(\mathbf{q}, E)}\right\} = C_q \cdot S(\mathbf{q}, E) \tag{54}$$

6.4.4 Bandgap measurement
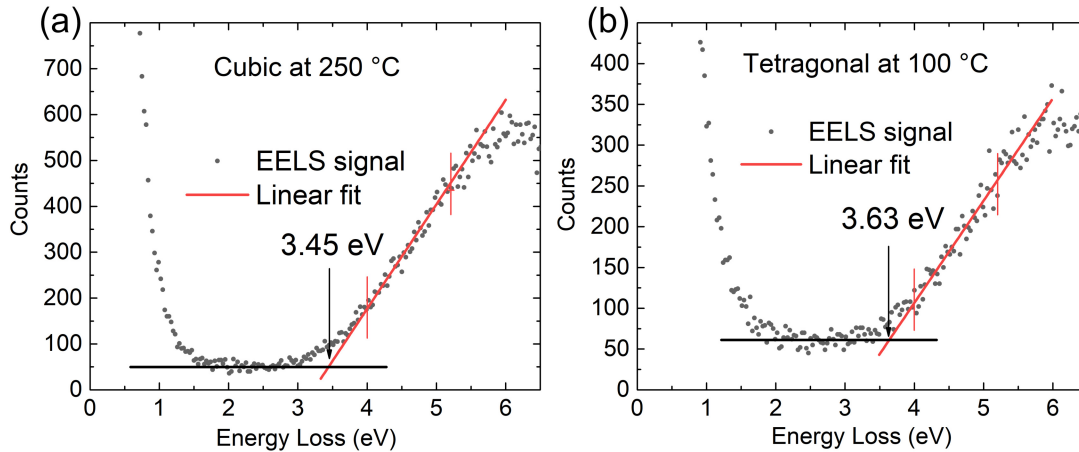
Figure 6.19: Bandgap measurement of cubic and tetragonal BaTiO$_3$ with off-axis EELS. (a) Cubic phase measured at 250 °C, $E_g = 3.45$ eV. (b) Tetragonal phase measured at 100 °C, $E_g = 3.63$ eV.

Measurement of the bandgap does not require any pre-processing and can be used to quickly check whether changes in the electronic structure upon phase transitions in BaTiO$_3$ are reflected in the low-loss EELS. Additionally, the angle resolved low-loss EELS measurements permit precise bandgap determination, which is unaltered

by Cherenkov losses [158]. For this, the method described in Ref. [160] was used. Two linear fits are made in the vicinity of the first low-loss intensity onset. The first one determines the background level by fitting a linear function in the 2 to 3 eV region. The other one fits the onset of the low loss spectra. Fitting is done using a linear function in the range from 4 to 5.25 eV. This function is then extrapolated to lower energies and the cross-point with the background is found. The cross-point corresponds to the bandgap of the material. The spectra are measured off-axis at $q = 0.07$ 1/Å, where Cherenkov losses do not affect the spectra. The momentum transfer is small, therefore, it corresponds to the "optical limit" [158].

The bandgaps of cubic ($E_g = 3.45$ eV) and tetragonal ($E_g = 3.64$ eV) BaTiO$_3$ correspond well to the values previously reported (both experimentally and theoretically) [146]. The relative difference between cubic and tetragonal bandgaps is ~ 0.2 eV and it is also reflected in the theoretically calculated values [146]. Off-axis EELS bandgap measurements has already proven valuable in detecting effects such as bandgap shrinkage due to phase transition and it can also indicate possible changes in the overall shape of the dielectric function.

6.4.5 Dielectric functions of BaTiO$_3$ at q $= 0$

The tetragonal and cubic energy loss functions and imaginary part of dielectric function (Im$\{\varepsilon\}$ of $\varepsilon = \varepsilon_1 + i\varepsilon_2$) are compared in Fig. 6.20. Transformations between various representations of the dielectric function are achieved with Eqs. 43, 41, 42 and 44 found in Chapter 3. The Im$\{\varepsilon\}$ parameter of cubic BaTiO$_3$ is slightly overestimated up to ~ 10 eV in the energy-loss range due to the slightly faulty ZLP removal during deconvolution [there is an artificial tiny step very close to the onset of the low-loss EELS in Fig. 6.20(a)].

The most prominent features in the energy-loss loss function are marked with capital letters in Fig. 6.20(a). According to ref. [161], the onset (A) of the energy-loss corresponds to the excitation from 2p to 3d bands, (B) is the collective excitation, (C) is the barium O$_{3,2}$ excitation in to conduction band, (D) corresponds to the plasmon resonance peak, (E$_1$) is the Ba O$_1$ excitation into the conduction band and (E) is the titanium M$_{3,2}$ excitation (arguably, E$_1$ is also titanium M$_{3,2}$, because the absorption edge is located at 35 eV, however the more intense features of the edge are seen at E). According to ref. [162], the slight increase of Im$\{\varepsilon\}$ in Fig. 6.20(c) around 11 eV is characteristic of the cubic phase. This peak originates from transitions within bands of O 2p to Ba 4d character.

However, it seems that (E$_1$) and (E) are more sensitive to the ferroelectric-paraelectric transition, which can be seen in the insets of Fig. 6.20(c-d). This is attributted to the Ti 3d orbital representation in this region.

Figure 6.21 compares the theoretically calculated dielectric function and experimentally obtained one for cubic BaTiO$_3$. Overall, the features match quite well,
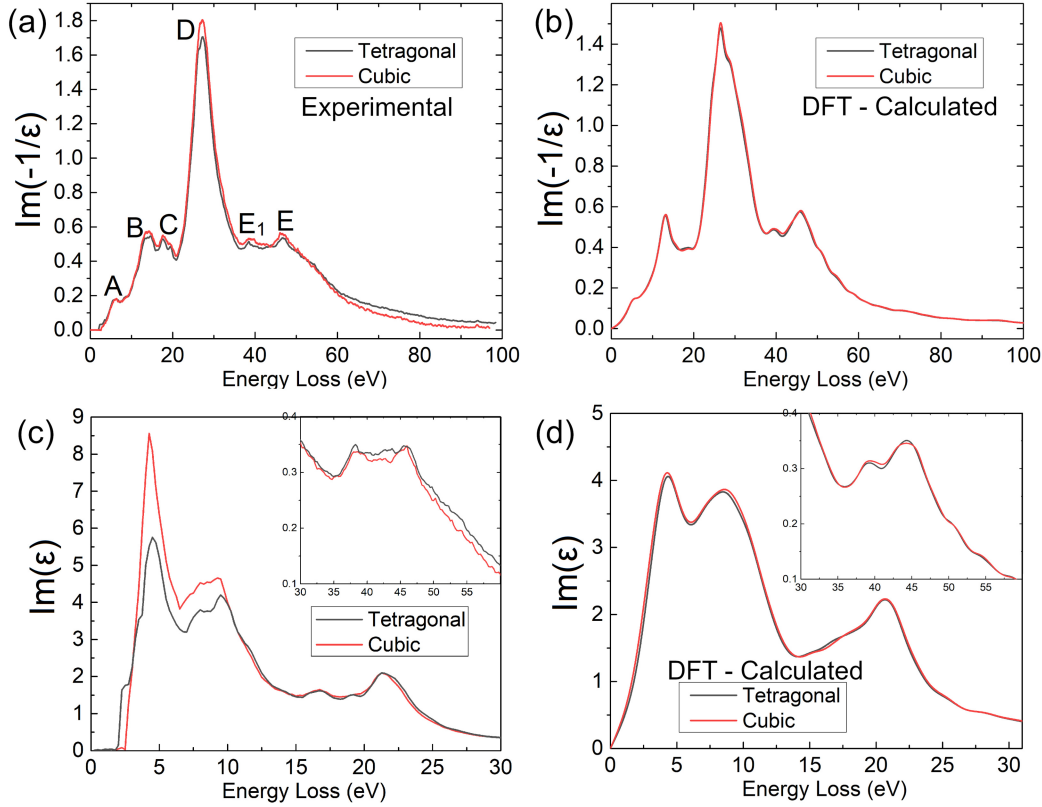
Figure 6.20: Experimental and theoretical energy-loss functions and imaginary part of dielectric function of cubic and tetragonal BaTiO$_3$. Tetragonal phase measured at 100 °C, Cubic phase measured at 250 °C, functions at $\mathbf{q} = \mathbf{0}$ 1/Å. (a) Experimental energy-loss functions. (b) Theoretical energy-loss functions. (c) Experimental imaginary part of dielectric function. (d) Theoretical imaginary part of dielectric function.

except for the ones very close to $E = 0$ (due to the erroneous ZLP deconvolution). The inverse functions in Fig. 6.21 are less sensitive to this artifact and show excellent match.

Designation of the peak (B) in Fig. 6.20 is difficult. According to Ref. [162] B in Fig. 6.20 represents the collective plasmon oscillation, while authors from ref. [161] claim that it originates from the surface plasmon oscillation. However, surface plasmon should appear at energy $E_{sp} = E_p/\sqrt{2}$, where E_p is the volume plasmon oscillation energy and E_{sp} is the surface plasom oscillation energy [71]. For BaTiO$_3$, E_{sp} is at ~ 19.6 eV and B is located at 14 eV. Another argument against its origins due to the collective oscillation can be made with the help of Fig. 6.21. Although, the experimental Re$\{\varepsilon\}$ in Fig. 6.21(c) crosses zero with positive slope in the vicinity of ~ 12 eV, which can be an indication of plasmon oscillation, such condition is not sufficient since in Fig.6.21(d) the experimental Im$\{\varepsilon\}$ has the peak at ~ 15 eV. The argument is made stronger by referring to the DFT calculated Re$\{\varepsilon\}$, which does
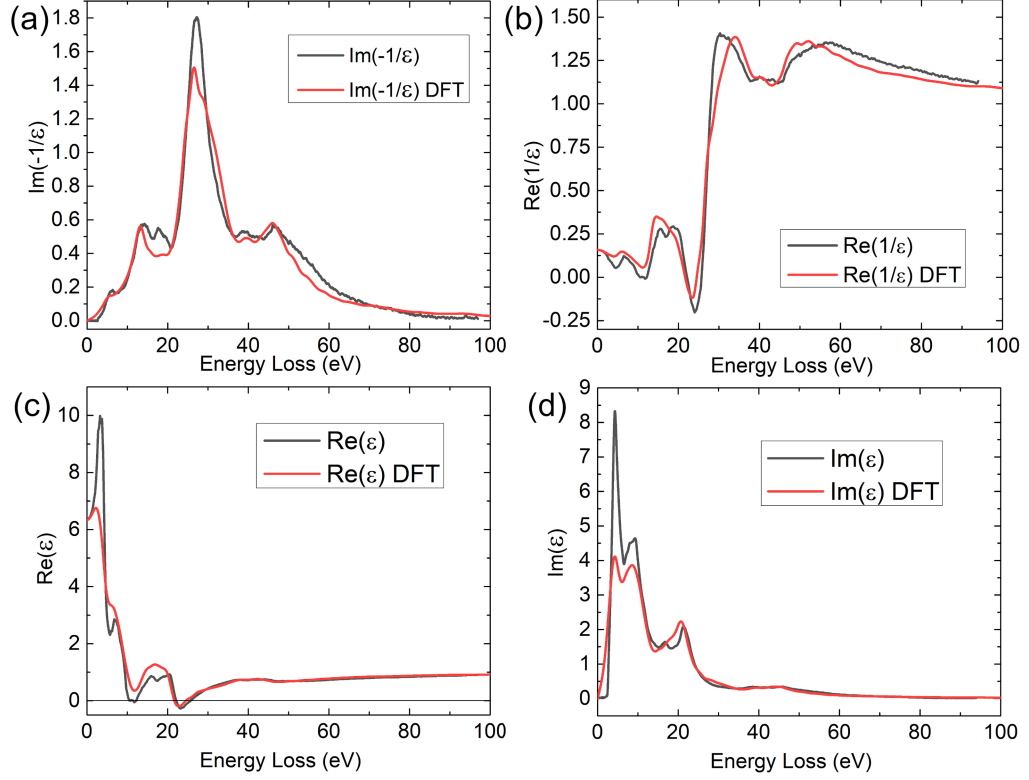
Figure 6.21: Direct comparison of experimentally obtained (at 250 °C) dielectric functions and theoretically calculated ones for cubic BaTiO$_3$ at q = 0 1/Å. Gray lines are experimental functions, red lines are calculated with DFT. (a) energy-loss function. (b) Inverse real part of dielectric function. (c) Real part of dielectric function. (d) Imaginary part of dielectric function.

not cross zero, and the DFT calculated Im$\{\varepsilon\}$, which shows a distinct shoulder at $\sim$ 15 eV. Therefore, the origins of peak B are attributed to electron transitions, which could be collective in between several bands.

Although, an attempt to retrieve the momentum resolved EELS of cubic BaTiO$_3$ was made, it was not successful since at several $q > 0$ channels the periodic spike-like oscillations were prominent which rendered the $q > 0$ range difficult to analyze. However, the experiments on tetragonal BaTiO$_3$ at 100 °C were more successful.

6.4.6   Q-resolved EELS of ferroelectric BaTiO$_3$

Deeper analysis of the **q** = 0 1/Å case is done for tetragonal BaTiO$_3$ as the retrieved single scattering function is more qualitative due to the successful deconvolution process. First, precise plasmon oscillation energy and damping constant can be
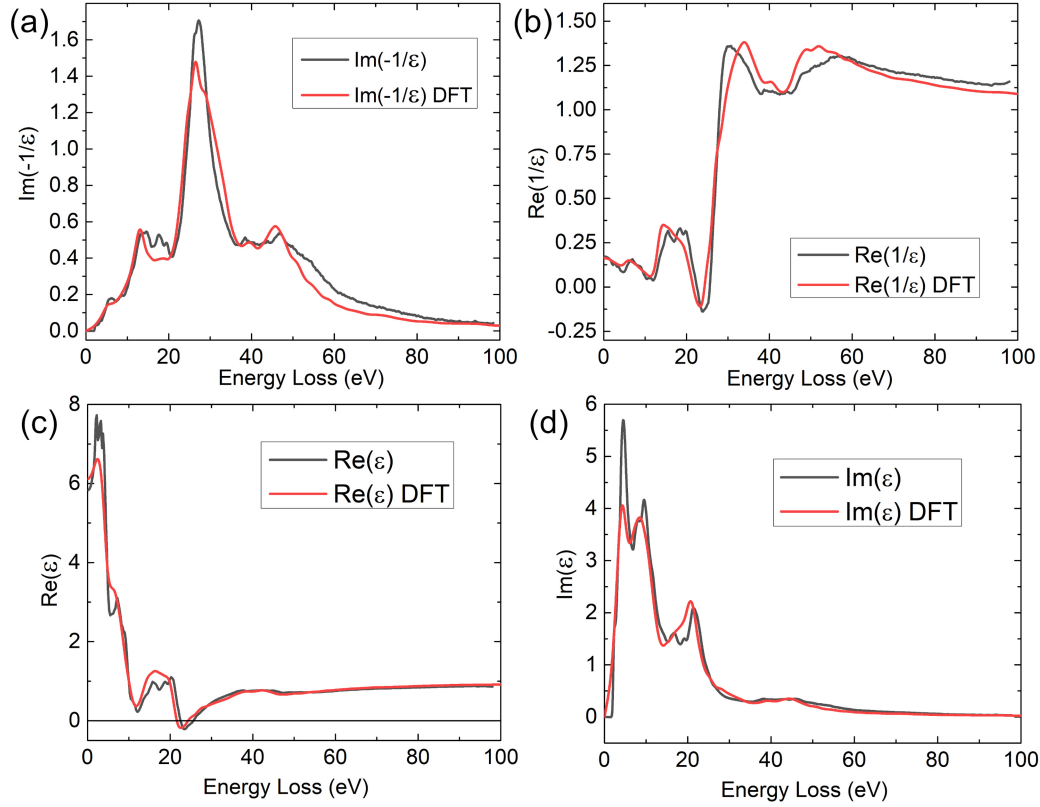
Figure 6.22: Direct comparison of experimentally obtained (at 100 °C) dielectric functions and theoretically calculated ones for tetragonal BaTiO₃ at q = 0 1/Å. Gray lines are experimental functions, red lines are calculated with DFT. (a) energy-loss function. (b) Inverse real part of dielectric function. (c) Real part of dielectric function. (d) Imaginary part of dielectric function.

determined by solving the following equation system [71]:

$$\begin{cases} E_{max} = \sqrt{E_p^2 - (\Delta E_p^2)/2} \\ E_{\varepsilon_1=0} = \sqrt{E_p^2 - \Delta E_p^2} \end{cases} \quad (55)$$

where E_{max} is the energetic position of the plasmon maximum in the energy-loss spectrum and $E_{\varepsilon_1=0}$ is the energy, where $\mathrm{Re}\{\varepsilon\}$ crosses zero (in the vicinity of the plasmon) and $\Delta E_p = \hbar\Gamma = \hbar/\tau$ is the FWHM of the plasmon peak. Γ is the damping constant and τ is the relaxation time (it represents the time for plasma oscillations to decay in amplitude by a factor $e^{-1} = 0.37$). It is noted that the maximum position of the plasmon peak due to the damping of the oscillations does not correspond to the actual plasmon oscillation energy. For tetragonal BaTiO₃, $E_{max} = 27.2$ eV and $E_{\varepsilon_1=0} = 25.6$, which yields $E_p = 28.7$ eV and $\Delta E_p = 12.9$ eV. The number of

oscillations within a relaxation time τ can be calculated by:

$$\frac{\omega_p \tau}{2\pi} = \frac{1}{2\pi}\left(\frac{E_p}{\Delta E_p}\right), \tag{56}$$

which gives 0.36 oscillations per τ. This corresponds to heavily damped oscillations and it is as expected in good insulators. For example, in diamond this value is 0.4 and in a good conductor such as aluminium it is 4.6 [71].

To calculate, how many electrons each unit cell of BaTiO$_3$ can provide for the excitations in the 0 to 100 eV range, n_{eff} is multiplied by the volume of the unit cell $n_{eff} \cdot V_{BaTiO_3} \approx 37$, while the value for the DFT calculated spectrum is 33. Both theoretical and experimental evaluated n_{eff} indicate that the chosen valence configurations for Ba ($5s^2\,5p^6\,6s^2$), Ti ($3s^2\,3p^6\,3d^2\,4s^2$) and O ($2s^2\,2p^4$) of the pseudo-potentials is adequate for energy-loss calculations, but it could probably benefit by addition of deeper atomic levels for barium. Nevertheless, the calculated energy-loss function corresponds well to the experimental one, therefore most of the excitations originate from previously mentioned valence/semi-core states.
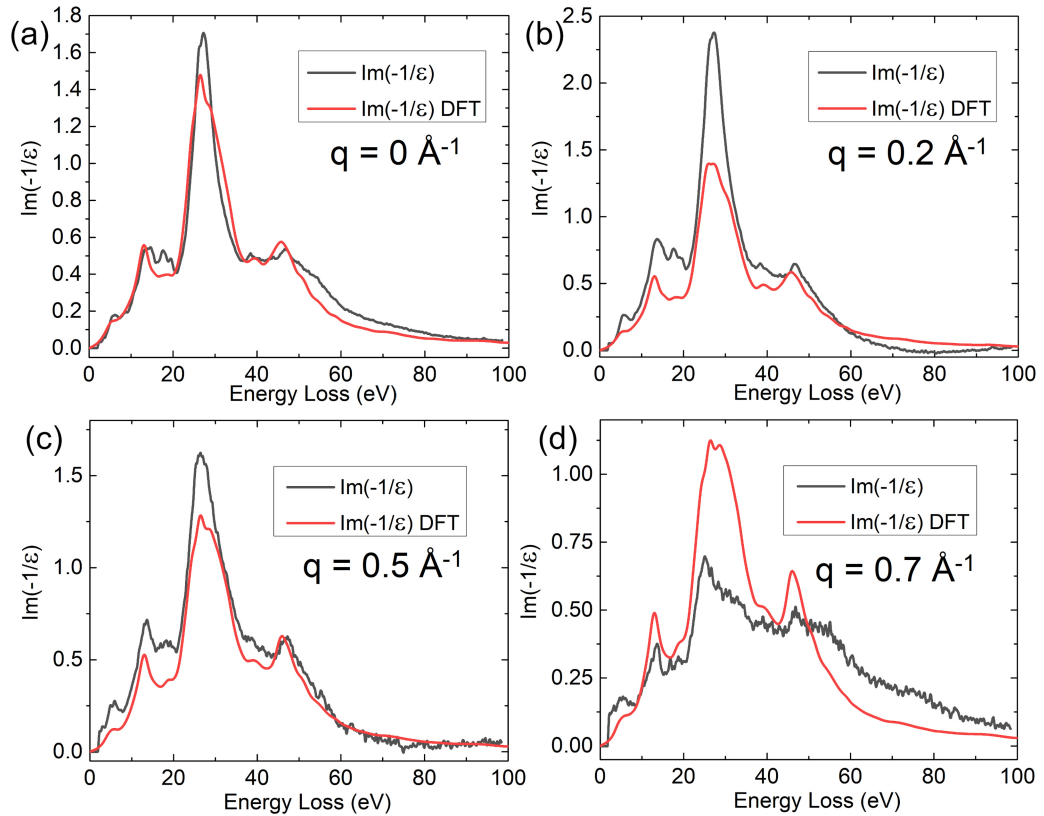
Figure 6.23: Momentum resolved experimental ant theoretical energy-loss functions of BaTiO$_3$. q change direction corresponds to tetragonal [100]. Gray lines are experimental functions, red lines are calculated with DFT. (a) $\mathbf{q} = 0$ 1/Å. (b) $\mathbf{q} = 0.2$ 1/Å. (c) $\mathbf{q} = 0.5$ 1/Å. (d) $\mathbf{q} = 0.7$ 1/Å.

The momentum resolved energy-loss function measured in the non-polar direction [100] of tetragonal BaTiO$_3$ is shown in Fig. 6.23. Removal of the quasi-elastic and multiple scattering from the measured spectra seems to have worked well as the overall shape of the measured energy-loss function resembles the calculated ones shown in Fig. 6.23. Admittedly, there are issues with the correct scale of the energy-loss functions at higher scattering angles. At $\mathbf{q} = 0.2$ 1/Å, the experimentally measured energy-loss function is overestimated, but at $\mathbf{q} = 0.7$ 1/Å it is underestimated. This is most likely associated with small number of bins in the q range of the q-E map and the usage of the two-dimensional Fourier transform to remove plural scattering (i.e. the method would work better with higher number of bins). Note the deficient intensity in the 60 to 100 eV range in Fig. 6.23(b) in contrast to the excess in (d). Such discrepancies alter the absolute scale of the energy-loss function. This could originate from the lack of resolution in the q range due to binning. However binning is necessary, otherwise the signal-to-noise ratio is poor. Another factor influencing the absolute scale of the energy-loss functions is the low signal at high scattering angles (for example, see the noise level of $\mathbf{q} = 0.7$ 1/Å). The signal at smaller scattering angles is measured at several thousands counts while at high scattering angles it reaches ~ 1000 counts at maximum after deconvolution.
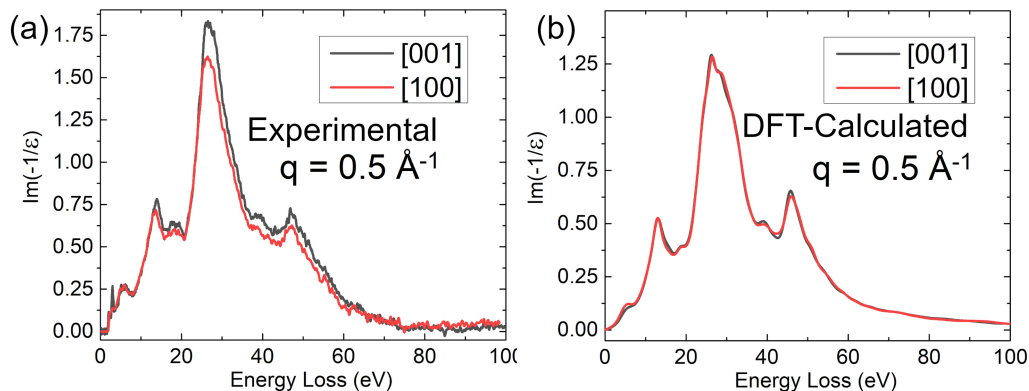
Figure 6.24: Momentum resolved experimental and theoretical energy-loss functions of BaTiO$_3$. along [001] and [100] directions at q $= 0.5$ 1/Å. (a) Experimentally obtained energy-loss functions. (b) Theoretically calculated energy loss functions.

Nevertheless, the general features of the measured function agree. Dispersion of the plasmon oscillation energy with respect to momentum transfer is not detected, which seems reasonable as the electrons are strongly bound (indicated by the large damping constant). The increase of the plasmon oscillation peak's width with respect to the increasing momentum transfer is seen in both, experimentally and theoretically obtained energy loss functions. Interestingly, at higher scattering angles, the feature close to 35 eV (Ti M$_{3,2}$ edge) becomes relatively more intense. This could indicate preferential excitation of the electrons in the empty 3d states "pointing" in

the direction of the Ti-O bond [71, 72].

A similar q-E map was acquired in the adjacent domain and the crystallographic directions were determined by carefully measuring the distance between diffracted spots. Smaller distance corresponds to polar [001] direction while larger diffracted beam spot distance corresponds to the [100] non-polar direction. Two orthogonal measurement directions are compared in Fig. 6.24(a).

Theoretically differences in the directionality of the Ti $M_{3,2}$ edge ($\sim$ 35 eV) may arise [Fig. 6.24(b)], but the quality of the experimental loss-functions [Fig. 6.24(a)] does not permit to detect such small features.

6.4.7 The effect of oxygen vacancies

Oxygen vacancies strongly influence the ferroelectric properties of perovskite oxides [163–165]. They are especially important to screen charged domain walls [17]. However, in many cases, the detection and interpretation of their distribution in ferroelectric materials is elusive.

To explore the effect of oxygen vacancies on the energy-loss function, a cubic $2 \times 2 \times 2$ $BaTiO_3$ super-cell was created. The unit cell was translated in a manner so the central atom in the super-cell is oxygen. The energy-loss function was calculated and was compared to the conventional unit cell to make sure the results matched. Further, the central oxygen atom in the super-cell was removed and the structure was relaxed. The resulting structure is comparable with similar results
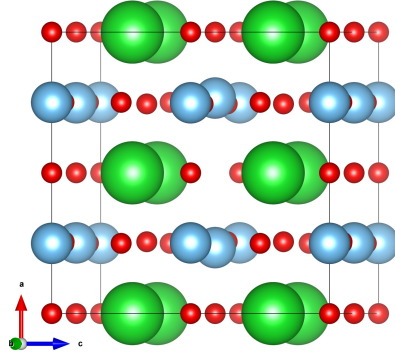
Figure 6.25: Relaxed super-cell of BaTiO₃ with oxygen vacancy. The central oxygen atom is removed, relaxed structure shows surrounding Ti atoms moving outward.

found in Refs. [166, 167] and it is shown in Fig. 6.26. The calculation of the energy-loss function according to this structure resulted in the energy-loss and imaginary part of the dielectric function as depicted in Fig. 6.26. It is clear, that single cell and super-cell calculations match, which indicates, that the super-cell approach produces interpretable and reproducible results. Addition of oxygen vacancies alters the
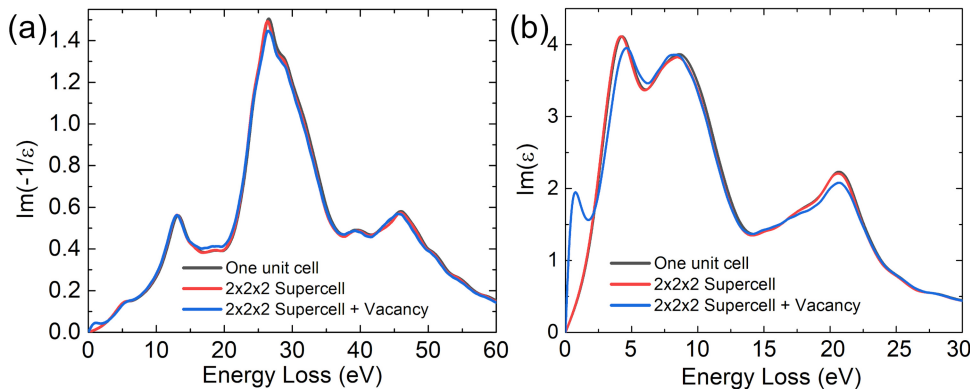
Figure 6.26: Energy-loss function and imaginary part of dielectric function of BaTiO$_3$ for single unit cell, super-cell and super-cell with vacancy. (a) Energy-loss function. (b) Imaginary part of dielectric function.

energy-loss function with an additional peak appearing in the bandgap region, Fig. 6.26(a). This corresponds to transitions in the so-called defect levels, which appear in the bandgap region of pristine BaTiO$_3$ [168]. Upon application of Kramers-Kronig relations, the imaginary part of the dielectric function is retrieved. There is a distinct peak seen in Fig. 6.26(b), indicating electronic transitions to the defect-levels. However, caution is advised when interpreting the experimental data since the vacancy altered energy-loss function is very similar to the angle integrated EELS spectrum, which is influenced by Cherenkov losses, Fig. 6.13. For that reason, assessment of the possible vacancies also must be made with an off-axis measurement. Therefore, a possible sensitive measurement of the oxygen vacancies in the ferroelectric perovskite oxide is demonstrated by theoretical calculation. Interpretable experimental measurements of oxygen vacancies require highly monochromatic incident beam. A possible, future *in situ* TEM experiment could include heating of BaTiO$_3$ at very high temperature to induce extensive vacancy formation in the pristine crystal, which would be easier to detect with low-loss EELS.

6.4.8 Conclusions

Core-loss EELS revealed changes within the Ti L$_{3,2}$ edge upon phase transition between tetragonal and cubic states of BaTiO$_3$. The changes in the L-edge could be understood with a simple point-charge model, but could not directly be reproduced with more complicated DFT methods. More elaborate calculations are needed to reproduce and understand the origins of the absorption edge changes. One of the approaches may involve usage of Bethe-Salpeter calculations [169]. The other possibility of such discrepancy is the possibility of order-disorder character of the phase transition. Measurement of the O K edge revealed that it is less sensitive to the ferroelectric phase transition, however its calculation revealed the origins of the rich

fine structure. All features have been assigned corresponding to Ba and Ti atoms.

Moreover, momentum resolved low-loss EELS allowed precise bandgap measurements of cubic and tetragonal $BaTiO_3$, which were not influenced by strong Cherenkov losses due to the large refractive index of $BaTiO_3$. The change in the bandgap is indicative of the change in the electronic structure of the $BaTiO_3$ upon the phase transition.

Concerning the low-loss EELS, the origins of the spectral features have been discussed aided by DFT calculations. Momentum-resolved low-loss EELS of tetragonal $BaTiO_3$ has been measured along polar and non-polar axis. The deconvolution algorithms and the experimental measurements need to be improved to achieve more concrete results. It is suggested that momentum resolved EELS deconvolution should be tested on a metallic system to reveal distinct plasmon dispersion with respect to the momentum transfer vector. The overall impression is that the changes in the EEL spectra of $BaTiO_3$ upon phase transition is always associated with the titanium 3d states.

A method to quantitatively measure oxygen vacancies with low loss EELS in perovskite oxides is theoretically shown. Future EELS experiments influenced by oxygen vacancies must be made carefully in order to distinguish Cherenkov loss from intrinsic material effects in the bandgap region.

7 Conclusions and outlook

Rich dynamic behavior of ferelectric materials upon electrical and temperature stimuli has always attracted attention from both a fundamental and practical point of view. State-of-the-art *in situ* TEM methods based on silicon MEMS technology are becoming more widespread and more available to the scientists enabling dynamic studies of ferroelectrics at nanoscale. However, in the case of ferroelectrics, specimen preparation and the strict requirements for non-conductive samples for *in situ* biasing experiments make them especially challenging.

Here, a reliable sample preparation method based on focused ion beam technology was described and demonstrated on the classical ferroelectric $BaTiO_3$. The microscopic size of the sample and the non-conventional geometry needed for MEMS based chips require precise assessment of the electric field magnitude. This was evaluated by using finite element electrostatic calculations. The results of the finite element calculations were compared to biasing experiments of $BaTiO_3$ at room temperature and observing the domain response at reasonable field values. Distinctively different domain response on the electric fields with opposite directions ensure that the effect is not induced by Joule heating. Biasing of the $BaTiO_3$ not only showed that the specimen preparation is successful, but also gave new scientific results.

$BaTiO_3$ specimen with FIB deposited platinum electrodes spontaneously formed charged zig-zag domain walls. At lower electric fields the domain walls were non-responsive, indicating strong pinning, however high fields depinned them and the motion of the domain walls followed Rayleigh-like behavior. Room-temperature biasing experiments permitted direct measurement of P-E like loops by directly measuring the domain areas with the same polarization direction.

The ability to heat and bias at the same time with the *in situ* TEM system proved extremely useful even in the case of $BaTiO_3$, which upon heating transformed its morphological state from 180° to pure 90° domain walls, which formed in groups of needle domains. Biasing of 90° needle domains revealed two very distinct mechanisms of their movement. The domains, which do not encounter perpendicularly oriented "needles" can move relatively freely and do not show large hysteresis. However, needle domains, which encounter perpendicular domain walls, show very distinct, square like domain length vs. applied voltage loops with strong hysteresis. Additionally, a new manifestation of Barkhausen jumps was directly observed, due

to strong domain-domain interaction. These observations point to the fact that the switching in $BaTiO_3$ at these conditions is hindered not by lattice defects, but mostly due to domain self-interaction.

An attempt was made to study changes in the density of the states of $BaTiO_3$ induced by ferroelectric phase transition by *in situ* EELS. Changes in the Ti $L_{3,2}$ edge were observed and qualitatively understood, but DFT calculations do not yield the same results indicating to either wrongly calculated transitions or incorrect assumption of displacive phase transition mechanism. One of these possibilities must be eliminated to achieve precise interpretation.

Momentum resolved EELS was used to probe cubic and tetragonal $BaTiO_3$. It allowed precise bandgap measurements, however, the measurement of q-E maps can be improved to enhance the limiting factor of the low spectrum intensity at higher scattering angles. The extracted momentum-resolved energy loss functions of $BaTiO_3$ were qualitatively similar to the DFT calculated ones. The extraction could be further improved regarding issues with the absolute scale of the extracted function. Smaller binning could be beneficial, however this also requires more signal at higher scattering angles. Nevertheless, the experimental and DFT approaches showed that almost every observable change in EELS is associated with the titanium 3d orbitals.

Similar *in situ* heating and biasing approaches can be used to more exotic ferroelectric materials. Although, here the viability of the sample preparation technique was demonstrated on $BaTiO_3$, which has comparably small coercive field of $0.5\,kV/cm^2$, the experiments were performed on $Na_{1/2}Bi_{1/2}TiO_3$, which requires large electric field to induce the phase transition between relaxor and ferroelectric states. Several successful *in situ* biasing experiments were made, where the maximum applied voltage was 30 V. The analysis of the data is undergoing. However, if the applied voltage is recalculated to the magnitude of the electric field, then $E \sim 60$ kV/cm^2 was applied. This indicates that the sample preparation procedure is robust to sustain even strong electric fields and can be used to study materials that require such strong fields.

Herein, differential phase contrast imaging was used to qualitatively gain insight of the 90° needle domains, but quantitative analysis was hindered by coupling of the electric field induced effects and diffraction effects produced by breakage of the Friedel's law. Nowadays, the 4D-STEM technique is gaining popularity due to the commercially available STEM pixelated detectors. It seems that 4D-STEM can be used to decouple electric field induced effects and diffraction effects, which would permit quantitative differential phase contrast imaging for ferroelectrics in the future.

Finally, *in situ* MEMS based biasing and heating in a TEM could prove to be a valuable tool in understanding non-conventional binary oxide piezoelectrics/ferroelectrics such as HfO_2 and defective CeO_2. It is believed that oxygen vacancies play a critical role in the physical properties of these materials (i.e. they break the inversion symmetry). As, in principle, they are charged, there must be some response on

the external electric field (i.e. vacancy movement). Additionally, DFT calculations showed that low-loss EELS is sensitive to formation of oxygen vacancies and could be used to spatially map the distribution of them and, therefore, would give better understanding of their influence.

A Voltage control script

This is custom made script for Keithley SMU-2450 to create triangular voltage shape and measure current. Parameters *dv* and *vmax* are controlling the discrete size of the voltage step and maximum of the applied voltage. The script, at first, runs to the positive side and achieves +*vmax*, returns to zero, then goes to -*vmax*, then returns again to zero and the execution is finished. The parameter *nstep* is number of steps necessary to achieve *vmax* with given *dv*. Parameter *dt* controls a pause in-between each successive voltage step, therefore it is convenient to adjust the speed of the voltage sweep for given TEM imaging conditions. After the voltage sweep, voltage, current and time-stamps are printed out on the screen of the computer.

```
--Sweep voltage and measure current in a two electrode configuration
--Instrument reset and clearing the buffer
reset()
defbuffer1.clear()
--Measurement settings
smu.measure.func = smu.FUNC_DC_CURRENT
smu.measure.autorangelow = 1e-6
smu.measure.autorange = smu.ON
smu.measure.nplc = 1
smu.measure.terminals = smu.TERMINALS_REAR
smu.measure.sense = smu.SENSE_2WIRE
--Source settings
smu.source.func = smu.FUNC_DC_VOLTAGE
smu.source.highc = smu.OFF
smu.source.range = 20
smu.source.ilimit.level = 0.01
--Voltage and timing setups
dv=0.01
vmax=5.0
nstep=(vmax/dv)+1
dt=0.5
--Linear sweep setup
smu.source.sweeplinear('Data', 0, vmax, nstep, dt, 1, smu.RANGE_BEST,
    ↪   smu.ON, smu.ON)
--Run trigger model and wait for it to complete
trigger.model.initiate()
```

```
waitcomplete()
--Print Results
if defbuffer1.n == 0 then
       print("Buffer is empty\n")
else
       print("Voltage\tCurrent\tTime")
       for i=1,defbuffer1.n do
              print(string.format("%g\t%g\t%s", defbuffer1.
                  ↪ sourcevalues[i], defbuffer1.readings[i],
                  ↪ defbuffer1.timestamps[i]))
       end
end

defbuffer1.clear()
smu.source.sweeplinear('Data', 0, -vmax, nstep, dt, 1, smu.RANGE_BEST
    ↪ , smu.ON, smu.ON)
trigger.model.initiate()
waitcomplete()
if defbuffer1.n == 0 then
       print("Buffer is empty\n")
else
       print("Voltage\tCurrent\tTime")
       for i=1,defbuffer1.n do
              print(string.format("%g\t%g\t%s", defbuffer1.
                  ↪ sourcevalues[i], defbuffer1.readings[i],
                  ↪ defbuffer1.timestamps[i]))
       end
end
```

B Point charge model for 3d orbitals

Positions of the charges surrounding transition metal are given in polar coordinates. Coordinates are parsed in an array, each array element consists of three numbers: angles θ and ϕ, and normalized radius (normalization, for example, can be done with respect to the longest bond). Some examples of the input are given at the start of the script. The positions of the charges are given to the *Lig* array. Output of the code contains three matrices (at the very end). The first one is eigenvalue matrix, showing energy of the particular orbital. The other one is eigenvector matrix, which gives information on which orbital exactly has particular energy. Each element of the eigenvector list contains five entries corresponding to five possible orbitals. Starting from position one: $1 \rightarrow d_{x^2-y^2}$, $2 \rightarrow d_{xz}$, $3 \rightarrow d_{z^2}$, $4 \rightarrow d_{yz}$, $5 \rightarrow d_{xy}$. Asymmetric fields may induce mixing of the 3d orbitals. Then the character (for example, how much d_{z^2} is mixed in the $d_{x^2-y^2}$ orbital) can be calculated from the convectional normalization rule, please see [147, 149] for further information.

```
(*Ligand coordinates \[Theta]i \[Phi]i Ri (normalized to one)*)
(*Octahedral field \
{{0,0,1},{180,0,1},{90,0,1},{90,180,1},{90,270,1},{90,90,1}}*)
(*Square planar {{90,0,1},{90,180,1},{90,270,1},{90,90,1}}*)
(*Tetrahedral with bad choice of the reference axis \
{{ArcCos[-1/3]*180/Pi,0,1},{ArcCos[-1/3]*180/Pi,120,1},{ArcCos
    ↪ [-1/3]*\
180/Pi,240,1},{0,0,1}}*)
(*Tetrahedral with proper choice of the axis \
{{(ArcCos[-1/3]*180/Pi)/2,45,1},{(ArcCos[-1/3]*180/Pi)
    ↪ /2,225,1},{180-(\
ArcCos[-1/3]*180/Pi)/2,135,1},{180-(ArcCos[-1/3]*180/Pi)/2,315,1}}*)
(*Tetra {{(ArcCos[Sqrt[1/3]]*180/Pi),45,1},{(ArcCos[Sqrt[1/3]]*180/
    ↪ Pi)\
,225,1},{(ArcCos[-Sqrt[1/3]]*180/Pi),135,1},{(ArcCos[-Sqrt
    ↪ [1/3]]*180/\
Pi),315,1}}*)

(*12 - coordinated site \
{{45,0,1},{45,90,1},{45,180,1},{45,270,1},{90,45,1},{90,135,1},{90,\
```

```
225,1},{90,315,1},{135,0,1},{135,90,1},{135,180,1},{135,270,1}}*)
(*C4v as in BaTiO3 - \
{{0,0,0.9339},{180,0,1.060239},{93.7921,0,1},{93.7921,180,1},{93.7921,\
    ↪
270,1},{93.7921,90,1}}*)

Lig = {{0, 0, 1.060239}, {180, 0, 0.9339}, {93.7921, 0, 1}, {93.7921,
    180, 1}, {93.7921, 270, 1}, {93.7921, 90, 1}};
(*Coordination number equals to the ligand number*)
cn = Length[Lig];
(*Functions to extract necessary values*)
\[Alpha]0[i_] := 0(*1/Lig[[i]][[3]]*);
\[Alpha]2[i_] := 1/(Lig[[i]][[3]])^3;
\[Alpha]4[i_] := 1/(3*(Lig[[i]][[3]])^3);
\[Theta][i_] := Lig[[i]][[1]]*Pi/180;
\[Phi][i_] := Lig[[i]][[2]]*Pi/180;
(*Ligand position functions*)
D00i = Table[\[Alpha]0[i], {i, 1, cn}];
D00 = Sum[D00i[[i]], {i, 1, cn}];
D20i = Table[\[Alpha]2[i]*(3*(Cos[\[Theta][i]]^2) - 1), {i, 1, cn}];
D20 = Sum[D20i[[i]], {i, 1, cn}];
D40i = Table[\[Alpha]4[
    i]*((35/3)*(Cos[\[Theta][i]]^4) - 10*(Cos[\[Theta][i]]^2) +
    1), {i, 1, cn}];
D40 = Sum[D40i[[i]], {i, 1, cn}];
D21i = Table[\[Alpha]2[i]*Sin[\[Theta][i]]*Cos[\[Theta][i]]*
    Cos[\[Phi][i]], {i, 1, cn}];
D21 = Sum[D21i[[i]], {i, 1, cn}];
D22i = Table[\[Alpha]2[i]*(Sin[\[Theta][i]]^2)*Cos[2*\[Phi][i]], {i,
    1, cn}];
D22 = Sum[D22i[[i]], {i, 1, cn}];
D41i = Table[\[Alpha]4[i]*Sin[\[Theta][i]]*
    Cos[\[Theta][i]]*((7/3)*(Cos[\[Theta][i]]^2) - 1)*
    Cos[\[Phi][i]], {i, 1, cn}];
D41 = Sum[D41i[[i]], {i, 1, cn}];
D42i = Table[\[Alpha]4[
    i]*(Sin[\[Theta][i]]^2)*(7*(Cos[\[Theta][i]]^2) - 1)*
    Cos[2*\[Phi][i]], {i, 1, cn}];
D42 = Sum[D42i[[i]], {i, 1, cn}];
D43i = Table[\[Alpha]4[i]*(Sin[\[Theta][i]]^3)*(Cos[\[Theta][i]])*
    Cos[3*\[Phi][i]], {i, 1, cn}];
D43 = Sum[D43i[[i]], {i, 1, cn}];
D44i = Table[\[Alpha]4[i]*(Sin[\[Theta][i]]^4)*Cos[4*\[Phi][i]], {i,
    1, cn}];
D44 = Sum[D44i[[i]], {i, 1, cn}];
```

```
G21i = Table[\[Alpha]2[i]*Sin[\[Theta][i]]*Cos[\[Theta][i]]*
    Sin[\[Phi][i]], {i, 1, cn}];
G21 = Sum[G21i[[i]], {i, 1, cn}];
G22i = Table[\[Alpha]2[i]*(Sin[\[Theta][i]]^2)*Sin[2*\[Phi][i]], {i,
    1, cn}];
G22 = Sum[G22i[[i]], {i, 1, cn}];
G41i = Table[\[Alpha]4[i]*Sin[\[Theta][i]]*
    Cos[\[Theta][i]]*((7/3)*(Cos[\[Theta][i]]^2) - 1)*
    Sin[\[Phi][i]], {i, 1, cn}];
G41 = Sum[G41i[[i]], {i, 1, cn}];
G42i = Table[\[Alpha]4[
     i]*(Sin[\[Theta][i]]^2)*(7*(Cos[\[Theta][i]]^2) - 1)*
    Sin[2*\[Phi][i]], {i, 1, cn}];
G42 = Sum[G42i[[i]], {i, 1, cn}];
G43i = Table[\[Alpha]4[i]*(Sin[\[Theta][i]]^3)*Cos[\[Theta][i]]*
    Sin[3*\[Phi][i]], {i, 1, cn}];
G43 = Sum[G43i[[i]], {i, 1, cn}];
G44i = Table[\[Alpha]4[i]*(Sin[\[Theta][i]]^4)*Sin[4*\[Phi][i]], {i,
    1, cn}];
G44 = Sum[G44i[[i]], {i, 1, cn}];
(*Integrals*)
H11 = D00 - (1/7)*D20 + (1/56)*D40 + (5/24)*D44;
H22 = D00 + (1/14)*D20 - (1/14)*D40 + (3/14)*D22 + (5/42)*D42;
H33 = D00 + (1/7)*D20 + (3/28)*D40;
H44 = D00 + (1/14)*D20 - (1/14)*D40 - (3/14)*D22 - (5/42)*D42;
H55 = D00 - (1/7) D20 + (1/56)*D40 - (5/24)*D44;
H12 = (3/7)*D21 - (5/28)*D41 + (5/12)*D43;
H13 = (-Sqrt[3]/7)*D22 + (5*Sqrt[3]/84)*D42;
H14 = (-3/7)*G21 + (5/28)*G41 + (5/12)*G43;
H15 = (5/24)*G44;
H23 = (Sqrt[3]/7)*D21 + (5*Sqrt[3]/14)*D41;
H24 = (3/14)*G22 + (5/42)*G42;
H25 = (3/7)*G21 - (5/28)*G41 + (5/12)*G43;
H34 = (Sqrt[3]/7)*G21 + (5*Sqrt[3]/14)*G41;
H35 = (-Sqrt[3]/7)*G22 + (5*Sqrt[3]/84)*G42;
H45 = (3/7)*D21 - (5/28)*D41 - (5/12)*D43;
(*Matrix creation, finding eigenvalues and eigenvectors*)
m = {{H11, H12, H13, H14, H15}, {H12, H22, H23, H24, H25}, {H13, H23,
   H33, H34, H35}, {H14, H24, H34, H44, H45}, {H15, H25, H35, H45,
   H55}};
Eigenvalues[m]
Eigenvectors[m]
ListPlot[Eigenvalues[m]]
(*Position of eigenvector 1 \[Rule] dx^2-y^2 2 \[Rule] xz 3 \[Rule]
```

```
     ↪ \
dz^2 4 \[Rule] dyz 5 \[Rule] dxy*)


  {0.360051, 0.304357, -0.246349, -0.209029, -0.209029}

  {{0., 0., 1., 0., 0.}, {1., 0., 0., 0., 0.}, {0., 0., 0., 0.,
  1.}, {0., 1., 0., 0., 0.}, {0., 0., 0., 1., 0.}}
```

C FDMNES input example

An example of Ti $L_{3,2}$ edge calculation with FDMNES code. Green functions are used to calculate absorption spectrum within multiple-scattering approach. Density of states is calculated (*SCF* flag) for the cluster in the radius of 7 Å. Absorber is Ti atom ($Z = 22$), self absorption correction is employed. *Density all* flag requests to output projected density of states, *Relativism* and *Spinorbit* flags request relativistic approach to calculate the density of states and the transitions. This is followed by atom electron configuration (which is optimized during SCF cycles) and the description of the unit cell and space group.

```
Filout
   /home/xeon/parallel_fdmnes/BTO/cubic/mst_7_Barium_TiL

 Range
 -10. 0.05 20.


 Green
 SCF
 !P_self_max
 !0.1
 N_self
 300
 Quadrupole

 !NRIXS
 !0. 0.1 0.2 0.35 0.7 1.35

 Z_absorber
 22

 Edge
 L23

 !Eimag
 !0.1
```

```
Excited

Self_abs

Double_cor

Radius
7.0

!Hubbard
 !3.0

Density_all

Relativism
Spinorbit
TDDFT

 Atom
  22 3 3 2 0. 0. 4 0 1. 1. 4 1 1. 1.
  56 3 5 2 0. 0. 6 0 0. 0. 6 1 1. 1.
   8 0

Spgroup
221

Crystal
 4.00730 4.00730 4.00730 90. 90. 90. ! = a, b, c, alpha, beta, gamma

      1 0.500000000000000 0.500000000000000 0.500000000000000
      2 0.000000000000000 0.000000000000000 0.000000000000000
      3 0.000000000000000 0.500000000000000 0.500000000000000

Convolution

Estart
-10.0
E_cut
-2.0
!Gamma_hole
!0.01

End
```

D   Quantum Espresso input

Work flow to calculate vacancy affected $BaTiO_3$ low-loss spectrum. First part is used for general electronic structure calculation with pw.x code. celldm(1) is unit cell dimension in Bohr radius units. The actual unit cell is defined as a matrix CELL_PARAMETERS followed by the atomic positions.

```
&control
calculation = 'scf'
title = 'BTcubic'
prefix='BTC'
pseudo_dir = './pseudo'
outdir='./out'
/
&system
ibrav = 0,
celldm(1) =15.102008388,
nat = 39,
ntyp = 3,
ecutwfc = 60,
ecutrho = 600,
nosym=.false.,
noinv=.false.,
/

&electrons
conv_thr = 1.0d-10,
diagonalization = 'david',
mixing_mode = 'plain',
mixing_beta = 0.05,
electron_maxstep = 1000,
/
ATOMIC_SPECIES
 Ba 137.327 Ba.pbesol-spn-rrkjus_psl.1.0.0.UPF
 Ti 47.88 Ti.pbesol-spn-rrkjus_psl.1.0.0.UPF
 O 15.9994 O.pbesol-n-rrkjus_psl.1.0.0.UPF
CELL_PARAMETERS {alat}
   1.003900033 0.000000000 0.000000000
```

```
   0.000000000 0.993557359 0.000000000
   0.000000000 0.000000000 0.993557359
ATOMIC_POSITIONS {crystal}
Ba 0.0000000000 0.2467657266 0.2467657266
Ba 0.5000000000 0.7534477699 0.2465522301
Ba 0.5000000000 0.2465522301 0.2465522301
Ba 0.0000000000 0.7532342734 0.7532342734
Ba 0.0000000000 0.2467657266 0.7532342734
Ba 0.5000000000 0.7534477699 0.7534477699
Ba 0.5000000000 0.2465522301 0.7534477699
Ba 0.0000000000 0.7532342734 0.2467657266
Ti 0.2494395705 0.0000000000 0.0000000000
Ti 0.7488224440 0.5000000000 0.0000000000
Ti 0.7505604295 0.0000000000 0.0000000000
Ti 0.2343169934 0.5000000000 0.5000000000
Ti 0.2511775560 0.0000000000 0.5000000000
Ti 0.7656830066 0.5000000000 0.5000000000
Ti 0.7488224440 0.0000000000 0.5000000000
Ti 0.2511775560 0.5000000000 0.0000000000
O 0.0000000000 0.0000000000 0.0000000000
O 0.2495843452 0.2498821721 0.0000000000
O 0.2495843452 0.0000000000 0.2498821721
O 0.5000000000 0.5000000000 0.0000000000
O 0.5000000000 0.0000000000 0.0000000000
O 0.0000000000 0.5000000000 0.5000000000
O 0.0000000000 0.0000000000 0.5000000000
O 0.5000000000 0.0000000000 0.5000000000
O 0.0000000000 0.5000000000 0.0000000000
O 0.7504156548 0.7501178279 0.0000000000
O 0.7504156548 0.2498821721 0.0000000000
O 0.2552037577 0.7459970280 0.5000000000
O 0.2552037577 0.2540029720 0.5000000000
O 0.7447962423 0.7459970280 0.5000000000
O 0.7447962423 0.2540029720 0.5000000000
O 0.2495843452 0.7501178279 0.0000000000
O 0.7447962423 0.5000000000 0.2540029720
O 0.7504156548 0.0000000000 0.2498821721
O 0.2552037577 0.5000000000 0.7459970280
O 0.2495843452 0.0000000000 0.7501178279
O 0.7447962423 0.5000000000 0.7459970280
O 0.7504156548 0.0000000000 0.7501178279
O 0.2552037577 0.5000000000 0.2540029720
K_POINTS {automatic}

4 4 4 1 1 1
```

Input for turbo_EELS.x. Same *prefix* and *outdir* must be used as before, *restart step* is usefeul in case computer halts, as the calculation can be restarted at the last full thousand iteration. Maximal iteration number *itermax* and lastly definition of momentum transfer vector (in the units of $2\pi/celldm$).

```
&lr_input
    prefix="BTC",
    outdir='./out',
    restart_step=1000,
    restart=.false.
/
&lr_control
    approximation = 'TDDFT',
    itermax = 15000,
    q1 = 0.000,
    q2 = 0.000,
    q3 = 0.12656,
/
```

Input for turbo_spectrum.x. Same *prefix* and *outdir* must be used as before. *itermax0* - how many Lanczos will be read from previous output. *itermax* - how many coefficients will be used to calculate energy-loss spectrum and associated physical values (dielectric function, absorption coefficients etc.).

```
&lr_input
  prefix='BTC',
  outdir='./out',
  eels=.true.
  ipol = 4
  itermax0 = 15000,
  itermax = 15000,
  extrapolation = 'osc'
  epsil = 0.08
  units = 1
  start = 0.0d0
  increment = 0.01d0
  end = 100
  verbosity = 0
/
```

E   q-E map spike removal

```
Despike[list_, crit_] := (
  Print["This␣function␣produces␣q-E␣map,␣which␣is␣corrected␣for␣\
spikes.␣New␣corrected␣array␣is␣named␣cor"];
  cor = list;
  Do[
   Do[
    Which[
     i == 1,
     If[(((list[[k]][[i]]) + 1)/((list[[k]][[i + 1]]) + 1)) > crit,
      cor[[k]][[i]] = list[[k]][[i + 1]];
      Print["Position␣k"];
      Print[k];
      Print["position␣i"];
      Print[i];
      ],
     i == Length[list[[1]]],

     If[(((list[[k]][[i]]) + 1)/((list[[k]][[i - 1]]) + 1)) > crit,
      cor[[k]][[i]] = list[[k]][[i - 1]];
      Print["Position␣k"];
      Print[k];
      Print["position␣i"];
      Print[i];
      ],

     (((list[[k]][[i]]) +
           1)/((1 + list[[k]][[i - 1]] + list[[k]][[i + 1]])/2)) >
       crit && i != 1 && i != Length[list[[1]]],
     cor[[k]][[i]] = ((list[[k]][[i - 1]] + list[[k]][[i + 1]])/2);
     Print["Position␣k"];
     Print[k];
     Print["position␣i"];
     Print[i];

     ], {i, 1, Length[list[[1]]]}], {k, 1, Length[list]}])
```

F   q-E map zero loss alignment

A Gaussian function is defined with *gf*, function to correct zero-loss peak positions is named *zerocor*. This function takes three parameters, q-E map (*list*) and initial values for the gaussian function fit. Result of the function is an array named *zcor* - zero-loss corrected q-E map.

```
gf[x_, a_, b_, c_] := a*Exp[-(((x - b)^2)/(2*c^2))];

zerocor[list_, binit_, cinit_] := (
  zcor = list;
  zero = Table[k, {k, 1, Length[list]}];
  Do[
   fit = FindFit[list[[i]][[1 ;; 300]],
     gf[x, a, b, c], {a, {b, binit}, {c, cinit}}, x];
   zero[[i]] = b /. fit;

   ,
   {i, 1, Length[list]}];
  Print[Max[zero]];
  Print[Min[zero]];
  maxv = Max[zero];
  len = Length[zcor[[1]]];

  Do[
   pad = Round[maxv - zero[[j]]];
   zcor[[j]] = PadLeft[zcor[[j]], len + pad];
   zcor[[j]] = Drop[zcor[[j]], -pad];
   , {j, 1, Length[list]}];
  )
```

G   Cherenkov loss correction

List named *av* is the off-axis averaged spectrum, function *rcher* takes four parameters; averaged off-axis spectrum *av*, Cherenkov loss affected region *qlist*, fittting start channel/pixel (i.e. ~ 80 eV), *cutout* is a channel/pixel value close to the ZLP peak, bellow this energy channel spectrum is not altered. Fitting start channel is selected in such way to keep the zero-loss peak unaffected. Output of the function is the corrected selected region named *chremoved*.

```
av = MovingAverage[(ch[[ench]] + ch[[ench - 1]] + ch[[ench - 2]] +
     ch[[ench - 3]] + ch[[ench - 4]])/5, 11];

rcher[av_, qlist_, startfit_, cutout_] := (
  chremoved = qlist;
  excessive = qlist;
  chfix = qlist;
  avlen = Length[av];
  Do[
   itlist = MovingAverage[qlist[[i]], 11];
   excess =
    itlist - av*a /.
     mini[itlist[[startfit ;;]], av[[startfit ;;]], a][[2]];
   excess = PadLeft[excess, avlen + 5];
   excess = PadRight[excess, avlen + 10];
   excessive[[i]] = excess;
   chremoved[[i]] = qlist[[i]] - excess;
   chfix[[i]] =
    Join[qlist[[i]][[1 ;; cutout]], chremoved[[i]][[cutout + 1 ;;]]];
   , {i, 1, Length[qlist], 1}]
  )
```

H   Binning of the q-E map

At the start, check function (*checkbins*), which is used to visually check bins and adjust the parameters for q binning. It takes as parameters q-E map (*list*), number of preferred bins (*nbins*) (actual bin number could be slightly different at the end, because q0 bin will be adjusted in such way, that it is the first one), q0 position (*q0*), end end-energy (*endene*) - energy somewhere near the ZLP (used to plot zoom in region of the zlp for centering).

```
checkbins[list_, nbins_, q0_, endene_] := (
   qbin = Floor[Length[list]/nbins];
   Print["Channels␣in␣a␣bin"];
   Print[qbin];
   Print["Q␣=␣0␣channel␣with␣full␣energy␣scale"];
   Print[ColorNegate[
     Image[Rescale[
       Log[(list[[
           Length[list] - (q0 + Round[0.5*qbin]) ;;
            Length[list] - (q0 - Round[0.5*qbin])]] + 1)]],
      ImageSize -> 1000]]];
   Print["Q␣=␣0␣channel␣around␣ZLP,␣use␣this␣to␣adjust␣zlp␣more␣or␣\
less␣in␣the␣center␣by␣selecting␣q0␣value"];
   Print[ArrayPlot[Log[list + 1],
     PlotRange -> {{Length[list] - (q0 + Round[0.5*qbin]),
        Length[list] - (q0 - Round[0.5*qbin])}, {1, endene}}]];
   Print["Max␣number␣of␣bins"];
   maxbin = Floor[(Length[list] - Round[(q0 - 0.5*qbin)])/qbin];
   Print[maxbin];
   lines =
    Table[Line[{{1,
        q0 - Round[0.5*qbin] + i*qbin}, {Length[list[[1]]],
        q0 - Round[0.5*qbin] + i*qbin}}], {i, 0, maxbin, 1}];
   Print["Expected␣bins␣look␣like␣this"];
   Print[Show[imgb, Epilog -> {Red, Dashed, lines}]];
   );
```

Actual binning function *bin*. It takes three parameters, q-E map (*list*), preferred number of channels (*chan*) and the position of the $q = 0$ position of the q axis. Output of the function is a binned q-E map and image-spectrum, which is calculated by integrating along the q-axis.

```
bin[list_, chan_, q0_] := (
   rlist = Reverse[list];
   maxbinr = Floor[(Length[list] - Round[(q0 - 0.5*chan)])/chan];
   binned =
    Table[Total[
      rlist[[q0 - Round[0.5*chan] + i*chan ;;
        q0 - Round[0.5*chan] + i*chan + chan]]], {i, 0, maxbinr - 1,
      1}];
   imagespectrum = Total[list];
   );
```

I Retrieval of single scattering distribution within q-E map

At the start, definition of Pseudo-Voigt function (*pv*), it used to fit zero-loss peaks and scale the spectra accordingly. Function *elastic* takes four parameters image spectrum *image*, image spectrum zero-loss peak list *imagez*, binned q-E map *qlist*, zero-loss peaks of the q-E map *qzlp* and some reconvolution function *recon*. The function returns *elasticlist[[k]]*, which contains only elastic scattering of the q-E map, parameter k is equivalent to the bin number.

```
pv[x_, x0_, \[CapitalGamma]_, \[Eta]_,
  int_] := (int*(\[Eta]*((1/((\[CapitalGamma]/(2*Sqrt[2*Log[2]]))*
            Sqrt[2*Pi]))*
        Exp[-(((x -
              x0)^2)/(2*(\[CapitalGamma]/(2*
                Sqrt[2*Log[2]]))^2))]) + (1 - \[Eta])*((1/
          Pi)*((\[CapitalGamma]/
            2)/((x - x0)^2 + (\[CapitalGamma]/2)^2)))));


elastic[image_, imagez_, qlist_, qzlp_, recon_] :=
 (
  newlen = 2*Length[image];
  elasticlist = Table[{}, {i, 1, Length[qlist], 1}];
  iimg = pv[x0, x0, \[CapitalGamma], \[Eta], int] /. fitimage;
  paddedimage = PadRight[image, newlen];
  paddedimagezlp = PadRight[imagez, newlen];
  reconvolution = PadRight[recon, newlen];

  Do[
   iq = pv[x0, x0, \[CapitalGamma], \[Eta], int] /. zlpparam[[k]];
   rescale = iimg/iq;
   paddedq = PadRight[qlist[[k]], newlen];
   paddedqzlp = PadRight[qzlp[[k]], newlen];
   elasticlist[[k]] =
    Re[InverseFourier[
```

```
    Fourier[(paddedqzlp),
      FourierParameters -> {1,
        1}]*((Fourier[paddedq, FourierParameters -> {1, 1}]/
         Fourier[paddedqzlp,
          FourierParameters -> {1, 1}]) - (Fourier[(paddedimage),
          FourierParameters -> {1, 1}]/
         Fourier[(paddedimagezlp), FourierParameters -> {1, 1}])),
     FourierParameters -> {1, 1}]];
  , {k, 1, Length[qlist]}];
 )
```

Single scattering distribution can be obtained by follwing operation. Arrays *qepad* and zlpqepad are q-E map and its ZLP array padded in the q and energy ranges to form artificial periodic even functions. The added parts to the q-E map must be removed afterwards.

```
dsingle =
  Re[InverseFourier[
    Fourier[zlpqepad, FourierParameters -> {1, 1}]*
     Log[Fourier[qepad, FourierParameters -> {1, 1}]/
       Fourier[zlpqepad, FourierParameters -> {1, 1}]],
    FourierParameters -> {1, 1}]];
```

Bibliography

[1] J. Valasek, "Piezo-Electric and Allied Phenomena in Rochelle Salt," *Phys. Rev.*, vol. 17, pp. 475–481, Apr 1921. [Online]. Available: https://link.aps.org/doi/10.1103/PhysRev.17.475

[2] "A century of ferroelectricity," *Nature Materials*, vol. 19, no. 2, pp. 129–129, Jan 2020. [Online]. Available: https://doi.org/10.1038/s41563-020-0611-1

[3] C. Kittel, *Introduction to Solid State Physics*, 7th ed.   John Wiley & Sons, Inc., 1996.

[4] G. Busch and P. Scherrer, "Eine neue seignette-elektrische Substanz," *Die Naturwissenschaften*, vol. 23, no. 43, pp. 737–737, Oct 1935. [Online]. Available: https://doi.org/10.1007/bf01498152

[5] A. von Hippel, R. G. Breckenridge, F. G. Chesley, and L. Tisza, "High dielectric constant ceramics," *Industrial & Engineering Chemistry*, vol. 38, no. 11, pp. 1097–1109, Nov 1946. [Online]. Available: https://doi.org/10.1021/ie50443a009

[6] "Stealing a lead on lead," *Nature Materials*, vol. 9, no. 2, pp. 98–98, Feb 2010. [Online]. Available: https://doi.org/10.1038/nmat2618

[7] Y. Xu, *Ferroelectric materials and their applications.*   Amsterdam New York New York, NY, USA: North-Holland Sole distributors for the USA and Canada, Elsevier Science Pub. Co, 1991.

[8] A. L. Thornton, "Electro-optic shutter devices utilizing lead lanthanum zirconate titanate (PLZT) ceramic wafers," in *Polarizers and Applications*, G. B. Trapani, Ed. SPIE, May 1982. [Online]. Available: https://doi.org/10.1117/12.965902

[9] A. J. Bell and D. Damjanovic, "Balancing hyperbole and impact in research communications related to lead-free piezoelectric materials," *Journal of Materials Science*, vol. 55, no. 25, pp. 10 971–10 974, May 2020. [Online]. Available: https://doi.org/10.1007/s10853-020-04721-4

[10] W. J. Merz, "The Electric and Optical Behavior of $BaTiO_3$ Single-Domain Crystals," *Phys. Rev.*, vol. 76, pp. 1221–1225, Oct 1949. [Online]. Available: https://link.aps.org/doi/10.1103/PhysRev.76.1221

[11] "DIRECTIVE 2002/95/EC OF THE EUROPEAN PARLIAMENT AND OF THE COUNCIL of 27 January 2003 on the restriction of the use of certain hazardous substances in electrical and electronic equipment," *OJ L*, vol. 37, pp. 19–23, Feb 2003. [Online]. Available: https://eur-lex.europa.eu/LexUriServ/LexUriServ.do?uri=OJ:L:2003:037:0019:0023:EN:PDF

[12] S. Zhang, B. Malič, J.-F. Li, and J. Rödel, "Lead-free ferroelectric materials: Prospective applications," *Journal of Materials Research*, vol. 36, no. 5, pp. 985–995, Mar 2021. [Online]. Available: https://doi.org/10.1557/s43578-021-00180-y

[13] X. Yan, M. Zheng, X. Gao, M. Zhu, and Y. Hou, "High-performance lead-free ferroelectric BZT–BCT and its application in energy fields," *Journal of Materials Chemistry C*, vol. 8, no. 39, pp. 13 530–13 556, 2020. [Online]. Available: https://doi.org/10.1039/d0tc03461d

[14] B. N. Rao and R. Ranjan, "Electric-field-driven monoclinic-to-rhombohedral transformation in $Na_{1/2}Bi_{1/2}TiO_3$," *Phys. Rev. B*, vol. 86, p. 134103, Oct 2012. [Online]. Available: https://link.aps.org/doi/10.1103/PhysRevB.86.134103

[15] H. Mulaosmanovic, T. Mikolajick, and S. Slesazeck, "FeFETs for neuromorphic systems," in *Topics in Applied Physics*. Springer Singapore, 2020, pp. 399 – 411. [Online]. Available: https://doi.org/10.1007/978-981-15-1212-4_20

[16] J. Zhang, X. Hou, Y. Zhang, G. Tang, and J. Wang, "Electrocaloric effect in ferroelectric materials: From phase field to first-principles based effective hamiltonian modeling," *Materials Reports: Energy*, vol. 1, no. 3, p. 100050, Aug 2021. [Online]. Available: https://doi.org/10.1016/j.matre.2021.100050

[17] A. K. Tagantsev, L. E. Cross, and J. Fousek, *Domains in Ferroic Crystals and Thin Films*. Springer New York, 2010. [Online]. Available: https://doi.org/10.1007/978-1-4419-1417-0

[18] M. Ichikawa, T. Gustafsson, and I. Olovsson, "Is $NaNO_2$ a pure order–disorder type ferroelectric?" *Solid State Communications*, vol. 123, no. 3, pp. 135–139, Jul 2002. [Online]. Available: https://www.sciencedirect.com/science/article/pii/S0038109802002077

[19] K. Momma and F. Izumi, "*VESTA3* for three-dimensional visualization of crystal, volumetric and morphology data," *Journal of Applied Crystallography*, vol. 44, no. 6, pp. 1272–1276, Dec 2011. [Online]. Available: https://doi.org/10.1107/S0021889811038970

[20] M. I. Kay, "The structure of sodium nitrite at 150°, 185°, 225° C," *Ferroelectrics*, vol. 4, no. 1, pp. 235–243, Mar 1972. [Online]. Available: https://doi.org/10.1080/00150197308235765

[21] J. E. Tibballs, R. J. Nelmes, and G. J. McIntyre, "The crystal structure of tetragonal KH_2PO_4 and KD_2PO_4 as a function of temperature and pressure," *Journal of Physics C: Solid State Physics*, vol. 15, no. 1, pp. 37–58, Jan 1982. [Online]. Available: https://doi.org/10.1088/0022-3719/15/1/004

[22] W. Cochran, "Crystal stability and the theory of ferroelectricity," *Phys. Rev. Lett.*, vol. 3, pp. 412–414, Nov 1959. [Online]. Available: https://link.aps.org/doi/10.1103/PhysRevLett.3.412

[23] I. Bersuker, "On the origin of ferroelectricity in perovskite-type crystals," *Physics Letters*, vol. 20, no. 6, pp. 589–590, Apr 1966. [Online]. Available: https://doi.org/10.1016/0031-9163(66)91127-9

[24] F. A. Rabuffetti and R. L. Brutchey, "Structural evolution of $BaTiO_3$ nanocrystals synthesized at room temperature," *Journal of the American Chemical Society*, vol. 134, no. 22, pp. 9475–9487, May 2012, pMID: 22587702. [Online]. Available: https://doi.org/10.1021/ja303184w

[25] M. S. Senn, D. A. Keen, T. C. A. Lucas, J. A. Hriljac, and A. L. Goodwin, "Emergence of long-range order in $BaTiO_3$ from local symmetry-breaking distortions," *Phys. Rev. Lett.*, vol. 116, p. 207602, May 2016. [Online]. Available: https://link.aps.org/doi/10.1103/PhysRevLett.116.207602

[26] M. C. Gupta and J. Ballato, Eds., *The Handbook of Photonics*. CRC Press, 2018. [Online]. Available: https://doi.org/10.1201/9781315222103

[27] A. Sidorkin, *Domain Structure in Ferroelectrics and Related Materials*, ser. EngineeringPro collection. Cambridge International Science Publishing, 2006. [Online]. Available: https://books.google.ch/books?id=jnXRp3qJxA4C

[28] T. Mitsui and J. Furuichi, "Domain structure of rochelle salt and KH_2PO_4," *Phys. Rev.*, vol. 90, pp. 193–202, Apr 1953. [Online]. Available: https://link.aps.org/doi/10.1103/PhysRev.90.193

[29] C. Kittel, "Theory of the structure of ferromagnetic domains in films and small particles," *Phys. Rev.*, vol. 70, pp. 965–971, Dec 1946. [Online]. Available: https://link.aps.org/doi/10.1103/PhysRev.70.965

[30] A. Kopal, T. Bahnik, and J. Fousek, "Domain formation in thin ferroelectric films: The role of depolarization energy," *Ferroelectrics*, vol. 202, no. 1, pp. 267–274, Oct 1997. [Online]. Available: https://doi.org/10.1080/00150199708213485

[31] A. Schilling, T. B. Adams, R. M. Bowman, J. M. Gregg, G. Catalan, and J. F. Scott, "Scaling of domain periodicity with thickness measured in $BaTiO_3$ single crystal lamellae and comparison with other ferroics," *Phys. Rev. B*, vol. 74, p. 024115, Jul 2006. [Online]. Available: https://link.aps.org/doi/10.1103/PhysRevB.74.024115

[32] V. K. Wadhawan, "Ferroelasticity," *Bulletin of Materials Science*, vol. 6, no. 4, pp. 733–753, Sep 1984. [Online]. Available: https://doi.org/10.1007/bf02744001

[33] G. Arlt, "Twinning in ferroelectric and ferroelastic ceramics: stress relief," *Journal of Materials Science*, vol. 25, no. 6, pp. 2655–2666, Jun 1990. [Online]. Available: https://doi.org/10.1007/bf00584864

[34] E. K. H. Salje, S. A. Hayward, and W. T. Lee, "Ferroelastic phase transitions: structure and microstructure," *Acta Crystallographica Section A Foundations of Crystallography*, vol. 61, no. 1, pp. 3–18, Dec 2004. [Online]. Available: https://doi.org/10.1107/s0108767304020318

[35] P. S. Bednyakov, B. I. Sturman, T. Sluka, A. K. Tagantsev, and P. V. Yudin, "Physics and applications of charged domain walls," *npj Computational Materials*, vol. 4, no. 1, Nov 2018. [Online]. Available: https://doi.org/10.1038/s41524-018-0121-8

[36] G. F. Nataf, M. Guennou, J. M. Gregg, D. Meier, J. Hlinka, E. K. H. Salje, and J. Kreisel, "Domain-wall engineering and topological defects in ferroelectric and ferroelastic materials," *Nature Reviews Physics*, vol. 2, no. 11, pp. 634–648, Sep 2020. [Online]. Available: https://doi.org/10.1038/s42254-020-0235-z

[37] L. Jin, F. Li, and S. Zhang, "Decoding the fingerprint of ferroelectric loops: Comprehension of the material properties and structures," *Journal of the American Ceramic Society*, vol. 97, no. 1, pp. 1–27, Dec 2013. [Online]. Available: https://doi.org/10.1111/jace.12773

[38] J. Akimoto, Y. Gotoh, and Y. Oosawa, "Refinement of hexagonal $BaTiO_3$," *Acta Crystallographica Section C*, vol. 50, no. 2, pp. 160–161, Feb 1994. [Online]. Available: https://doi.org/10.1107/S0108270193008637

[39] G. H. Kwei, A. C. Lawson, S. J. L. Billinge, and S. W. Cheong, "Structures of the ferroelectric phases of barium titanate," *The Journal of Physical Chemistry*, vol. 97, no. 10, pp. 2368–2377, Mar 1993. [Online]. Available: https://doi.org/10.1021/j100112a043

[40] H. Kay and P. Vousden, "XCV. symmetry changes in barium titanate at low temperatures and their relation to its ferroelectric properties," *The London, Edinburgh, and Dublin Philosophical Magazine and Journal of Science*, vol. 40, no. 309, pp. 1019–1040, Oct 1949. [Online]. Available: https://doi.org/10.1080/14786444908561371

[41] H. H. Wieder, "Electrical behavior of barium titanatge single crystals at low temperatures," *Phys. Rev.*, vol. 99, pp. 1161–1165, Aug 1955. [Online]. Available: https://link.aps.org/doi/10.1103/PhysRev.99.1161

[42] A. Devonshire, "XCVI. theory of barium titanate," *The London, Edinburgh, and Dublin Philosophical Magazine and Journal of Science*, vol. 40, no. 309, pp. 1040–1063, Oct 1949. [Online]. Available: https://doi.org/10.1080/14786444908561372

[43] ——, "CIX. theory of barium titanate-part II," *The London, Edinburgh, and Dublin Philosophical Magazine and Journal of Science*, vol. 42, no. 333, pp. 1065–1079, Oct 1951. [Online]. Available: https://doi.org/10.1080/14786445108561354

[44] A. P. Levanyuk, I. B. Misirlioglu, and M. B. Okatan, "Landau, ginzburg, devonshire and others," 2020.

[45] L. Eric Cross, "Ferroelectric ceramics: Tailoring properties for specific applications," in *Ferroelectric Ceramics*, N. Setter and E. L. Colla, Eds. Basel: Birkhäuser Basel, 1993, pp. 1–85.

[46] L. X. Zhang and X. Ren, "In situ observation of reversible domain switching in aged Mn-doped $BaTiO_3$ single crystals," *Phys. Rev. B*, vol. 71, p. 174108, May 2005. [Online]. Available: https://link.aps.org/doi/10.1103/PhysRevB.71.174108

[47] D. Williams, *Transmission electron microscopy : a textbook for materials science.* New York: Springer, 2009.

[48] J. Ricote, R. W. Whatmore, and D. J. Barber, "Studies of the ferroelectric domain configuration and polarization of rhombohedral PZT ceramics," *Journal of Physics: Condensed Matter*, vol. 12, no. 3, pp. 323–337, Dec 1999. [Online]. Available: https://doi.org/10.1088/0953-8984/12/3/311

[49] M. Foeth, A. Sfera, P. Stadelmann, and P.-A. Buffat, "A comparison of HREM and weak beam transmission electron microscopy for the quantitative measurement of the thickness of ferroelectric domain walls," *Journal of Electron Microscopy*, vol. 48, no. 6, pp. 717–723, Jan 1999. [Online]. Available: https://doi.org/10.1093/oxfordjournals.jmicro.a023740

[50] L. Li, P. Gao, C. T. Nelson, J. R. Jokisaari, Y. Zhang, S.-J. Kim, A. Melville, C. Adamo, D. G. Schlom, and X. Pan, "Atomic scale structure changes induced by charged domain walls in ferroelectric materials," *Nano Letters*, vol. 13, no. 11, pp. 5218–5223, Oct 2013. [Online]. Available: https://doi.org/10.1021/nl402651r

[51] D. Szwarcman, A. Lubk, M. Linck, K. Vogel, Y. Lereah, H. Lichte, and G. Markovich, "Ferroelectric effects in individual $BaTiO_3$ nanocrystals investigated by electron holography," *Phys. Rev. B*, vol. 85, p. 134112, Apr 2012. [Online]. Available: https://link.aps.org/doi/10.1103/PhysRevB.85.134112

[52] H. Lichte, M. Reibold, K. Brand, and M. Lehmann, "Ferroelectric electron holography," *Ultramicroscopy*, vol. 93, no. 3-4, pp. 199–212, Dec. 2002. [Online]. Available: https://doi.org/10.1016/s0304-3991(02)00277-2

[53] C. W. Tai, S. H. Choy, and H. L. W. Chan, "Ferroelectric domain morphology evolution and octahedral tilting in lead-free $(Bi_{1/2}Na_{1/2})TiO_3$ - $(Bi_{1/2}K_{1/2})TiO_3$ - $(Bi_{1/2}Li_{1/2})TiO_3$ - $BaTiO_3$ ceramics at different temperatures," *Journal of the American Ceramic Society*, vol. 91, no. 10, pp. 3335–3341, Oct 2008. [Online]. Available: https://doi.org/10.1111/j.1551-2916.2008.02592.x

[54] N. Petkov, "In situ real-time TEM reveals growth, transformation and function in one-dimensional nanoscale materials: From a nanotechnology perspective," *ISRN Nanotechnology*, vol. 2013, pp. 1–21, Jan 2013. [Online]. Available: https://doi.org/10.1155/2013/893060

[55] H. Saka, T. Kamino, S. Ara, and K. Sasaki, "In situ heating transmission electron microscopy," *MRS Bulletin*, vol. 33, no. 2, pp. 93–100, Feb 2008. [Online]. Available: https://doi.org/10.1557/mrs2008.21

[56] X. Tan, H. He, and J.-K. Shang, "In situ transmission electron microscopy studies of electric-field-induced phenomena in ferroelectrics," *Journal of Materials Research*, vol. 20, no. 7, pp. 1641–1653, Jul 2005. [Online]. Available: https://doi.org/10.1557/jmr.2005.0213

[57] E. Snoeck, L. Normand, A. Thorel, and C. Roucau, "Electron microscopy study of ferroelastic and ferroelectric domain wall motions induced by the *in situ* application of an electric field in $BaTiO_3$," *Phase Transitions*, vol. 46, no. 2, pp. 77–88, Jan 1994. [Online]. Available: https://doi.org/10.1080/01411599408200317

[58] Z. Xu, X. Tan, P. Han, and J. K. Shang, "In situ transmission electron microscopy study of electric-field-induced microcracking in single crystal $Pb(Mg_{1/3}Nb_{2/3})O_3$ - $PbTiO_3$," *Applied Physics Letters*, vol. 76, no. 25, pp. 3732–3734, Jun. 2000. [Online]. Available: https://doi.org/10.1063/1.126765

[59] M. Zakhozheva, L. A. Schmitt, M. Acosta, W. Jo, J. Rödel, and H.-J. Kleebe, "In situ electric field induced domain evolution in $Ba(Zr_{0.2}Ti_{0.8})O_3$-$0.3(Ba_{0.7}Ca_{0.3})TiO_3$ ferroelectrics," *Applied Physics Letters*, vol. 105, no. 11, p. 112904, Sep. 2014. [Online]. Available: https://doi.org/10.1063/1.4896048

[60] P. Gao, C. T. Nelson, J. R. Jokisaari, S.-H. Baek, C. W. Bark, Y. Zhang, E. Wang, D. G. Schlom, C.-B. Eom, and X. Pan, "Revealing the role of defects in ferroelectric switching with atomic resolution," *Nature Communications*, vol. 2, no. 1, Sep 2011. [Online]. Available: https://doi.org/10.1038/ncomms1600

[61] P. Gao, J. Britson, C. T. Nelson, J. R. Jokisaari, C. Duan, M. Trassin, S.-H. Baek, H. Guo, L. Li, Y. Wang, Y.-H. Chu, A. M. Minor, C.-B. Eom,

R. Ramesh, L.-Q. Chen, and X. Pan, "Ferroelastic domain switching dynamics under electrical and mechanical excitations," *Nature Communications*, vol. 5, no. 1, May 2014. [Online]. Available: https://doi.org/10.1038/ncomms4801

[62] M.-G. Han, M. S. Marshall, L. Wu, M. A. Schofield, T. Aoki, R. Twesten, J. Hoffman, F. J. Walker, C. H. Ahn, and Y. Zhu, "Interface-induced nonswitchable domains in ferroelectric thin films," *Nature Communications*, vol. 5, no. 1, Aug 2014. [Online]. Available: https://doi.org/10.1038/ncomms5693

[63] C. T. Nelson, P. Gao, J. R. Jokisaari, C. Heikes, C. Adamo, A. Melville, S.-H. Baek, C. M. Folkman, B. Winchester, Y. Gu, Y. Liu, K. Zhang, E. Wang, J. Li, L.-Q. Chen, C.-B. Eom, D. G. Schlom, and X. Pan, "Domain dynamics during ferroelectric switching," *Science*, vol. 334, no. 6058, pp. 968–971, Nov 2011. [Online]. Available: https://doi.org/10.1126/science.1206980

[64] S. Vijayan, J. R. Jinschek, S. Kujawa, J. Greiser, and M. Aindow, "Focused ion beam preparation of specimens for micro-electro-mechanical system-based transmission electron microscopy heating experiments," *Microscopy and Microanalysis*, vol. 23, no. 4, pp. 708–716, Jun 2017. [Online]. Available: https://doi.org/10.1017/s1431927617000605

[65] M. Duchamp, Q. Xu, and R. E. Dunin-Borkowski, "Convenient preparation of high-quality specimens for annealing experiments in the transmission electron microscope," *Microscopy and Microanalysis*, vol. 20, no. 6, pp. 1638–1645, Nov 2014. [Online]. Available: https://doi.org/10.1017/s1431927614013476

[66] P. R. N. Childs, J. R. Greenwood, and C. A. Long, "Review of temperature measurement," *Review of Scientific Instruments*, vol. 71, no. 8, pp. 2959–2978, Aug 2000. [Online]. Available: https://doi.org/10.1063/1.1305516

[67] "Zeiss crossbam description," https://www.zeiss.de/mikroskopie/produkte/fib-sem-instruments/crossbeam/crossbeam-technology.html, accessed: 2021-11-01.

[68] B. Haas, J.-L. Rouvière, V. Boureau, R. Berthier, and D. Cooper, "Direct comparison of off-axis holography and differential phase contrast for the mapping of electric fields in semiconductors by transmission electron microscopy." *Ultramicroscopy*, vol. 198, pp. 58–72, Mar. 2019. [Online]. Available: https://doi.org/10.1016/j.ultramic.2018.12.003

[69] I. Lazic and E. G. Bosch, "Analytical review of direct stem imaging techniques for thin samples," in *Advances in Imaging and Electron Physics*. Elsevier, Mar 2017, pp. 75–184. [Online]. Available: https://doi.org/10.1016/bs.aiep.2017.01.006

[70] I. MacLaren, L. Wang, D. McGrouther, A. J. Craven, S. McVitie, R. Schierholz, A. Kovács, J. Barthel, and R. E. Dunin-Borkowski,

"On the origin of differential phase contrast at a locally charged and globally charge-compensated domain boundary in a polar-ordered material," *Ultramicroscopy*, vol. 154, pp. 57–63, Jul. 2015. [Online]. Available: https://doi.org/10.1016/j.ultramic.2015.03.016

[71] R. F. Egerton, *Electron energy-loss spectroscopy in the electron microscope.* New York: Springer, 2011.

[72] R. Brydson, *Electron Energy Loss Spectroscopy.* Garland Science, Jul. 2020. [Online]. Available: https://doi.org/10.1201/9781003076858

[73] J. Daniels, C. v. Festenberg, H. Raether, and K. Zeppenfeld, "Optical constants of solids by electron spectroscopy," in *Springer Tracts in Modern Physics.* Springer Berlin Heidelberg, 1970, pp. 77–135. [Online]. Available: https://doi.org/10.1007/bfb0045980

[74] P. Giannozzi, S. Baroni, N. Bonini, M. Calandra, R. Car, C. Cavazzoni, D. Ceresoli, G. L. Chiarotti, M. Cococcioni, I. Dabo, A. D. Corso, S. de Gironcoli, S. Fabris, G. Fratesi, R. Gebauer, U. Gerstmann, C. Gougoussis, A. Kokalj, M. Lazzeri, L. Martin-Samos, N. Marzari, F. Mauri, R. Mazzarello, S. Paolini, A. Pasquarello, L. Paulatto, C. Sbraccia, S. Scandolo, G. Sclauzero, A. P. Seitsonen, A. Smogunov, P. Umari, and R. M. Wentzcovitch, "QUANTUM ESPRESSO: a modular and open-source software project for quantum simulations of materials," *Journal of Physics: Condensed Matter*, vol. 21, no. 39, p. 395502, Sep 2009. [Online]. Available: https://doi.org/10.1088/0953-8984/21/39/395502

[75] P. Giannozzi, O. Baseggio, P. Bonfà, D. Brunato, R. Car, I. Carnimeo, C. Cavazzoni, S. de Gironcoli, P. Delugas, F. F. Ruffino, A. Ferretti, N. Marzari, I. Timrov, A. Urru, and S. Baroni, "QuantumESPRESSO toward the exascale," *The Journal of Chemical Physics*, vol. 152, no. 15, p. 154105, Apr 2020. [Online]. Available: https://doi.org/10.1063/5.0005082

[76] I. Timrov, N. Vast, R. Gebauer, and S. Baroni, "turboEELS—a code for the simulation of the electron energy loss and inelastic x-ray scattering spectra using the liouville–lanczos approach to time-dependent density-functional perturbation theory," *Computer Physics Communications*, vol. 196, pp. 460–469, Nov 2015. [Online]. Available: https://doi.org/10.1016/j.cpc.2015.05.021

[77] E. Stavitski and F. M. de Groot, "The CTM4XAS program for EELS and XAS spectral shape analysis of transition metal L edges," *Micron*, vol. 41, no. 7, pp. 687–694, Oct 2010. [Online]. Available: https://doi.org/10.1016/j.micron.2010.06.005

[78] F. de Groot and A. Kotani, *Core Level Spectroscopy of Solids.* CRC Press, Mar 2008. [Online]. Available: https://doi.org/10.1201/9781420008425

[79] O. Bunău and Y. Joly, "Self-consistent aspects of x-ray absorption calculations," *Journal of Physics: Condensed Matter*, vol. 21, no. 34, p. 345501, Aug 2009. [Online]. Available: https://doi.org/10.1088/0953-8984/21/34/345501

[80] R. Ignatans, D. Damjanovic, and V. Tileli, "Local hard and soft pinning of 180° domain walls in BaTio₃ probed by in situ transmission electron microscopy," *Phys. Rev. Materials*, vol. 4, p. 104403, Oct 2020. [Online]. Available: https://link.aps.org/doi/10.1103/PhysRevMaterials.4.104403

[81] D. A. Buck, "Ferroelectrics for digital information storage and switching," Massachusetts Institute of Technology, Department of Electrical Engineering, Tech. Rep., 1952.

[82] J. F. Scott, "Ferroelectric memories today," *Ferroelectrics*, vol. 236, no. 1, pp. 247–258, Jan 2000. [Online]. Available: https://doi.org/10.1080/00150190008016056

[83] V. Garcia and M. Bibes, "Inside story of ferroelectric memories," *Nature*, vol. 483, no. 7389, pp. 279–280, Mar 2012. [Online]. Available: https://doi.org/10.1038/483279a

[84] O. V. Malyshkina, A. Y. Eliseev, and R. M. Grechishkin, "Dispersion of switching processes in ferroelectric ceramics," *Advances in Condensed Matter Physics*, vol. 2017, pp. 1–5, Jul 2017. [Online]. Available: https://doi.org/10.1155/2017/2507808

[85] S. Trolier-McKinstry, F. Griggio, C. Yaeger, P. Jousse, D. Zhao, S. S. N. Bharadwaja, T. N. Jackson, S. Jesse, S. V. Kalinin, and K. Wasa, "Designing piezoelectric films for micro electromechanical systems," *IEEE Transactions on Ultrasonics, Ferroelectrics and Frequency Control*, vol. 58, no. 9, pp. 1782–1792, Sep 2011. [Online]. Available: https://doi.org/10.1109/tuffc.2011.2015

[86] W. Cochran, "Crystal stability and the theory of ferroelectricity," *Advances in Physics*, vol. 9, no. 36, pp. 387–423, Oct 1960. [Online]. Available: https://doi.org/10.1080/00018736000101229

[87] J. Harada, J. D. Axe, and G. Shirane, "Neutron-scattering study of soft modes in cubic BaTiO₃," *Phys. Rev. B*, vol. 4, pp. 155–162, Jul 1971. [Online]. Available: https://link.aps.org/doi/10.1103/PhysRevB.4.155

[88] Y. Luspin, J. L. Servoin, and F. Gervais, "Soft mode spectroscopy in barium titanate," *Journal of Physics C: Solid State Physics*, vol. 13, no. 19, pp. 3761–3773, Jul 1980. [Online]. Available: https://doi.org/10.1088/0022-3719/13/19/018

[89] W. Cochran, "Neutron scattering and dielectric properties of perovskite-type crystals," *Physica Status Solidi (b)*, vol. 30, no. 2, pp. K157–K160, 1968. [Online]. Available: https://doi.org/10.1002/pssb.19680300267

[90] V. Polinger, P. Garcia-Fernandez, and I. Bersuker, "Pseudo jahn–teller origin of ferroelectric instability in BaTiO$_3$ type perovskites: The Green's function approach and beyond," *Physica B: Condensed Matter*, vol. 457, pp. 296–309, Jan 2015. [Online]. Available: https://www.sciencedirect.com/science/article/pii/S0921452614007935

[91] A. Devonshire, "Theory of ferroelectrics," *Advances in Physics*, vol. 3, no. 10, pp. 85–130, Apr 1954. [Online]. Available: https://doi.org/10.1080/00018735400101173

[92] Q. M. Zhang, W. Y. Pan, S. J. Jang, and L. E. Cross, "Domain wall excitations and their contributions to the weak-signal response of doped lead zirconate titanate ceramics," *Journal of Applied Physics*, vol. 64, no. 11, pp. 6445–6451, Dec 1988. [Online]. Available: https://doi.org/10.1063/1.342059

[93] W. Cao, "Constructing Landau-Ginzburg-Devonshire type models for ferroelectric systems based on symmetry," *Ferroelectrics*, vol. 375, no. 1, pp. 28–39, Sep 2008. [Online]. Available: https://doi.org/10.1080/00150190802437845

[94] M. Dawber, K. M. Rabe, and J. F. Scott, "Physics of thin-film ferroelectric oxides," *Rev. Mod. Phys.*, vol. 77, pp. 1083–1130, Oct 2005. [Online]. Available: https://link.aps.org/doi/10.1103/RevModPhys.77.1083

[95] X. Lu, H. Li, and W. Cao, "Landau expansion parameters for BaTiO$_3$," *Journal of Applied Physics*, vol. 114, no. 22, p. 224106, Dec 2013. [Online]. Available: https://doi.org/10.1063/1.4838456

[96] J. L. Jones, E. Aksel, G. Tutuncu, T.-M. Usher, J. Chen, X. Xing, and A. J. Studer, "Domain wall and interphase boundary motion in a two-phase morphotropic phase boundary ferroelectric: Frequency dispersion and contribution to piezoelectric and dielectric properties," *Phys. Rev. B*, vol. 86, p. 024104, Jul 2012. [Online]. Available: https://link.aps.org/doi/10.1103/PhysRevB.86.024104

[97] C. D. Tan, C. Flannigan, J. Gardner, F. D. Morrison, E. K. H. Salje, and J. F. Scott, "Electrical studies of barkhausen switching noise in ferroelectric PZT: Critical exponents and temperature dependence," *Phys. Rev. Materials*, vol. 3, p. 034402, Mar 2019. [Online]. Available: https://link.aps.org/doi/10.1103/PhysRevMaterials.3.034402

[98] A. Gruverman and S. V. Kalinin, "Piezoresponse force microscopy and recent advances in nanoscale studies of ferroelectrics," in *Frontiers of Ferroelectricity.* Springer US, 2007, pp. 107–116. [Online]. Available: https://doi.org/10.1007/978-0-387-38039-1_10

[99] L. Li, L. Xie, and X. Pan, "Real-time studies of ferroelectric domain switching: a review," *Reports on Progress in Physics*, vol. 82, no. 12, p. 126502, Nov 2019. [Online]. Available: https://doi.org/10.1088/1361-6633/ab28de

150

[100] A. N. Morozovska, S. V. Svechnikov, E. A. Eliseev, and S. V. Kalinin, "Extrinsic size effect in piezoresponse force microscopy of thin films," *Phys. Rev. B*, vol. 76, p. 054123, Aug 2007. [Online]. Available: https://link.aps.org/doi/10.1103/PhysRevB.76.054123

[101] H. He and X. Tan, "In situ transmission electron microscopy study of the electric field-induced transformation of incommensurate modulations in a Sn-modified lead zirconate titanate ceramic," *Applied Physics Letters*, vol. 85, no. 15, pp. 3187–3189, Oct 2004. [Online]. Available: https://doi.org/10.1063/1.1805179

[102] H. Chang, S. V. Kalinin, S. Yang, P. Yu, S. Bhattacharya, P. P. Wu, N. Balke, S. Jesse, L. Q. Chen, R. Ramesh, S. J. Pennycook, and A. Y. Borisevich, "Watching domains grow: In-situ studies of polarization switching by combined scanning probe and scanning transmission electron microscopy," *Journal of Applied Physics*, vol. 110, no. 5, p. 052014, Sep 2011. [Online]. Available: https://doi.org/10.1063/1.3623779

[103] T. Denneulin, N. Wollschläger, and M. Hÿtch, "Piezoelectric thin films investigated by dark-field electron holography and in-situ biasing," pp. 1068–1069, Dec 2016. [Online]. Available: https://doi.org/10.1002/9783527808465.emc2016.6496

[104] J. F. Scott, A. Hershkovitz, Y. Ivry, H. Lu, A. Gruverman, and J. M. Gregg, "Superdomain dynamics in ferroelectric-ferroelastic films: Switching, jamming, and relaxation," *Applied Physics Reviews*, vol. 4, no. 4, p. 041104, Dec 2017. [Online]. Available: https://doi.org/10.1063/1.5005994

[105] F. Hofmann, E. Tarleton, R. J. Harder, N. W. Phillips, P.-W. Ma, J. N. Clark, I. K. Robinson, B. Abbey, W. Liu, and C. E. Beck, "3D lattice distortions and defect structures in ion-implanted nano-crystals," *Scientific Reports*, vol. 7, no. 1, Apr 2017. [Online]. Available: https://doi.org/10.1038/srep45993

[106] R. P. Babu, S. Irukuvarghula, A. Harte, and M. Preuss, "Nature of gallium focused ion beam induced phase transformation in 316l austenitic stainless steel," *Acta Materialia*, vol. 120, pp. 391–402, Nov 2016. [Online]. Available: https://doi.org/10.1016/j.actamat.2016.08.008

[107] M. Suess, E. Mueller, and R. Wepf, "Minimization of amorphous layer in Ar^+ ion milling for UHR-EM," *Ultramicroscopy*, vol. 111, no. 8, pp. 1224–1232, Jul. 2011. [Online]. Available: https://doi.org/10.1016/j.ultramic.2011.03.004

[108] T. Matsumoto and M. Okamoto, "Ferroelectric 180° a-a nanostripe and nanoneedle domains in thin $BaTiO_3$ films prepared with focused-ion beam," *IEEE Transactions on Ultrasonics, Ferroelectrics and Frequency Control*, vol. 57, no. 10, pp. 2127–2133, Oct 2010. [Online]. Available: https://doi.org/10.1109/tuffc.2010.1668

[109] M. Acosta, N. Novak, V. Rojas, S. Patel, R. Vaish, J. Koruza, G. A. Rossetti, and J. Rödel, "BaTiO$_3$-based piezoelectrics: Fundamentals, current status, and perspectives," *Applied Physics Reviews*, vol. 4, no. 4, p. 041305, Dec 2017. [Online]. Available: https://doi.org/10.1063/1.4990046

[110] M. Y. Gureev, A. K. Tagantsev, and N. Setter, "Head-to-head and tail-to-tail 180° domain walls in an isolated ferroelectric," *Phys. Rev. B*, vol. 83, p. 184104, May 2011. [Online]. Available: https://link.aps.org/doi/10.1103/PhysRevB.83.184104

[111] T. Granzow, E. Suvaci, H. Kungl, and M. J. Hoffmann, "Deaging of heat-treated iron-doped lead zirconate titanate ceramics," *Applied Physics Letters*, vol. 89, no. 26, p. 262908, Dec 2006. [Online]. Available: https://doi.org/10.1063/1.2425035

[112] Q. Tan, J. Li, and D. Viehland, "Role of lower valent substituent-oxygen vacancy complexes in polarization pinning in potassium-modified lead zirconate titanate," *Applied Physics Letters*, vol. 75, no. 3, pp. 418–420, Jul 1999. [Online]. Available: https://doi.org/10.1063/1.124394

[113] K. Carl and K. H. Hardtl, "Electrical after-effects in Pb(Ti, Zr)O$_3$ ceramics," *Ferroelectrics*, vol. 17, no. 1, pp. 473–486, Jan 1977. [Online]. Available: https://doi.org/10.1080/00150197808236770

[114] D. Damjanovic, *The science of hysteresis.* Oxford: Academic Press, 2006.

[115] T. Rojac, S. Drnovsek, A. Bencan, B. Malic, and D. Damjanovic, "Role of charged defects on the electrical and electromechanical properties of rhombohedral Pb(Zr,Ti)O$_3$ with oxygen octahedra tilts," *Phys. Rev. B*, vol. 93, p. 014102, Jan 2016. [Online]. Available: https://link.aps.org/doi/10.1103/PhysRevB.93.014102

[116] D. Damjanovic, "Ferroelectric, dielectric and piezoelectric properties of ferroelectric thin films and ceramics," *Reports on Progress in Physics*, vol. 61, no. 9, pp. 1267–1324, Sep 1998. [Online]. Available: https://doi.org/10.1088/0034-4885/61/9/002

[117] L. Mitoseriu, V. Tura, D. Ricinschi, and C. Harnagea, "Grain size dependence of the Rayleigh coefficients in barium titanate ceramics," *Ferroelectrics*, vol. 240, no. 1, pp. 1317–1324, Jan 2000. [Online]. Available: https://doi.org/10.1080/00150190008227952

[118] R. Ignatans, D. Damjanovic, and V. Tileli, "Individual barkhausen pulses of ferroelastic nanodomains," *Phys. Rev. Lett.*, vol. 127, p. 167601, Oct 2021. [Online]. Available: https://link.aps.org/doi/10.1103/PhysRevLett.127.167601

[119] V. M. Rudyak, "THE BARKHAUSEN EFFECT," *Soviet Physics Uspekhi*, vol. 13, no. 4, pp. 461–479, Apr 1971. [Online]. Available: https://doi.org/10.1070/pu1971v013n04abeh004681

[120] A. G. Chynoweth, "Barkhausen pulses in barium titanate," *Phys. Rev.*, vol. 110, pp. 1316–1332, Jun 1958. [Online]. Available: https://link.aps.org/doi/10.1103/PhysRev.110.1316

[121] W. J. Merz, "Domain formation and domain wall motions in ferroelectric $BaTiO_3$ single crystals," *Phys. Rev.*, vol. 95, pp. 690–698, Aug 1954. [Online]. Available: https://link.aps.org/doi/10.1103/PhysRev.95.690

[122] C. Flannigan, C. D. Tan, and J. F. Scott, "Electrical studies of barkhausen switching noise in ferroelectric lead zirconate titanate (PZT) and $BaTiO_3$: critical exponents and temperature-dependence," *Journal of Physics: Condensed Matter*, vol. 32, no. 5, p. 055403, Nov 2019. [Online]. Available: https://doi.org/10.1088/1361-648x/ab4d87

[123] Y. Xu, Y. Zhou, D. Xue, X. Ding, J. Sun, and E. K. H. Salje, "Anisotropic avalanche dynamics during ferroelectric switching in $BaTiO_3$ and $0.7Pb(Mg_{2/3}Nb_{1/3})O_3$ - $0.3PbTiO_3$," *Applied Physics Letters*, vol. 117, no. 17, p. 172901, Oct 2020. [Online]. Available: https://doi.org/10.1063/5.0027752

[124] E. K. H. Salje, D. Xue, X. Ding, K. A. Dahmen, and J. F. Scott, "Ferroelectric switching and scale invariant avalanches in $BaTiO_3$," *Phys. Rev. Materials*, vol. 3, p. 014415, Jan 2019. [Online]. Available: https://link.aps.org/doi/10.1103/PhysRevMaterials.3.014415

[125] E. K. Salje and K. A. Dahmen, "Crackling noise in disordered materials," *Annual Review of Condensed Matter Physics*, vol. 5, no. 1, pp. 233–254, Mar 2014. [Online]. Available: https://doi.org/10.1146/annurev-conmatphys-031113-133838

[126] B. BŘezina, J. Fousek, and A. Glanc, "Barkhausen pulses in $BaTiO_3$ connected with 90° switching processes," *Czechoslovak Journal of Physics*, vol. 11, no. 8, pp. 595–601, Aug 1961. [Online]. Available: https://doi.org/10.1007/bf01689156

[127] R. C. Miller, "On the origin of barkhausen pulses in $BaTiO_3$," *Journal of Physics and Chemistry of Solids*, vol. 17, no. 1-2, pp. 93–100, Dec 1960. [Online]. Available: https://doi.org/10.1016/0022-3697(60)90180-3

[128] P. Potnis and J. Huber, "In-situ observation of needle domain evolution in barium titanate single crystals," *Journal of the European Ceramic Society*, vol. 33, no. 2, pp. 327–333, Feb 2013. [Online]. Available: https://doi.org/10.1016/j.jeurceramsoc.2012.08.026

[129] M. He, M. Wang, and Z. Zhang, "Electric-field-induced domain intersection in $BaTiO_3$ single crystal," *Japanese Journal of Applied Physics*, vol. 56, no. 3, p. 031501, Feb 2017. [Online]. Available: https://doi.org/10.7567/jjap.56.031501

[130] X. Y. Qi, H. H. Liu, and X. F. Duan, "In situ transmission electron microscopy study of electric-field-induced 90° domain switching in BaTiO$_3$ single crystals," *Applied Physics Letters*, vol. 89, no. 9, p. 092908, Aug 2006. [Online]. Available: https://doi.org/10.1063/1.2345231

[131] Z. Zhang, X. Qi, and X. Duan, "Two-step evolution mechanism of multi-domains in BaTiO$_3$ single crystal investigated by in situ transmission electron microscopy," *Scripta Materialia*, vol. 58, no. 6, pp. 441–444, Mar 2008. [Online]. Available: https://www.sciencedirect.com/science/article/pii/S1359646207007725

[132] A. L. Roitburd, "Equilibrium structure of epitaxial layers," *Physica Status Solidi (a)*, vol. 37, no. 1, pp. 329–339, Sep 1976. [Online]. Available: https://doi.org/10.1002/pssa.2210370141

[133] J. S. Speck and W. Pompe, "Domain configurations due to multiple misfit relaxation mechanisms in epitaxial ferroelectric thin films. i. theory," *Journal of Applied Physics*, vol. 76, no. 1, pp. 466–476, Jul 1994. [Online]. Available: https://doi.org/10.1063/1.357097

[134] J. S. Speck, A. Seifert, W. Pompe, and R. Ramesh, "Domain configurations due to multiple misfit relaxation mechanisms in epitaxial ferroelectric thin films. II. experimental verification and implications," *Journal of Applied Physics*, vol. 76, no. 1, pp. 477–483, Jul 1994. [Online]. Available: https://doi.org/10.1063/1.357098

[135] R. Ignatans, M. Ziatdinov, R. Vasudevan, M. Valleti, V. Tileli, and S. V. Kalinin, "Latent mechanisms of polarization switching from in situ electron microscopy observations," 2020. [Online]. Available: https://arxiv.org/abs/2011.11869

[136] D. Sui and J. E. Huber, "Modelling and interaction of needle domains in barium titanate single crystals," *European Journal of Mechanics - A/Solids*, vol. 80, p. 103919, Mar 2020. [Online]. Available: https://doi.org/10.1016/j.euromechsol.2019.103919

[137] E. K. H. Salje and Y. Ishibashi, "Mesoscopic structures in ferroelastic crystals: needle twins and right-angled domains," *Journal of Physics: Condensed Matter*, vol. 8, no. 44, pp. 8477–8495, Oct 1996. [Online]. Available: https://doi.org/10.1088/0953-8984/8/44/004

[138] S. Puchberger, V. Soprunyuk, W. Schranz, A. Tröster, K. Roleder, A. Majchrowski, M. A. Carpenter, and E. Salje, "The noise of many needles: Jerky domain wall propagation in PbZrO$_3$ and LaAlO$_3$," *APL Materials*, vol. 5, no. 4, p. 046102, Apr 2017. [Online]. Available: https://doi.org/10.1063/1.4979616

[139] R. J. Harrison, S. A. T. Redfern, and E. K. H. Salje, "Dynamical excitation and anelastic relaxation of ferroelastic domain walls in LaAlO$_3$," *Phys. Rev. B*, vol. 69, p. 144101, Apr 2004. [Online]. Available: https://link.aps.org/doi/10.1103/PhysRevB.69.144101

[140] B. Ziegler, K. Martens, T. Giamarchi, and P. Paruch, "Domain wall roughness in stripe phase BiFeO$_3$ thin films," *Phys. Rev. Lett.*, vol. 111, p. 247604, Dec 2013. [Online]. Available: https://link.aps.org/doi/10.1103/PhysRevLett.111.247604

[141] P. Paruch, T. Giamarchi, and J.-M. Triscone, "Domain wall roughness in epitaxial ferroelectric PbZr$_{0.2}$O$_3$ - PbTi$_{0.8}$O$_3$ thin films," *Phys. Rev. Lett.*, vol. 94, p. 197601, May 2005. [Online]. Available: https://link.aps.org/doi/10.1103/PhysRevLett.94.197601

[142] T. Tybell, P. Paruch, T. Giamarchi, and J.-M. Triscone, "Domain wall creep in epitaxial ferroelectric Pb(Zr$_{0.2}$Ti$_{0.8}$)O$_3$ thin films," *Phys. Rev. Lett.*, vol. 89, p. 097601, Aug 2002. [Online]. Available: https://link.aps.org/doi/10.1103/PhysRevLett.89.097601

[143] K. S. Novoselov, A. K. Geim, S. V. Dubonos, E. W. Hill, and I. V. Grigorieva, "Subatomic movements of a domain wall in the Peierls potential," *Nature*, vol. 426, no. 6968, pp. 812–816, Dec 2003. [Online]. Available: https://doi.org/10.1038/nature02180

[144] H. Ma, W.-J. Kim, J. S. Horwitz, S. W. Kirchoefer, and J. Levy, "Lattice-scale domain wall dynamics in ferroelectrics," *Phys. Rev. Lett.*, vol. 91, p. 217601, Nov 2003. [Online]. Available: https://link.aps.org/doi/10.1103/PhysRevLett.91.217601

[145] V. Y. Shur and A. R. Akhmatkhanov, "Domain shape instabilities and dendrite domain growth in uniaxial ferroelectrics," *Philosophical Transactions of the Royal Society A: Mathematical, Physical and Engineering Sciences*, vol. 376, no. 2113, p. 20170204, Jan 2018. [Online]. Available: https://doi.org/10.1098/rsta.2017.0204

[146] D. I. Bilc, R. Orlando, R. Shaltaf, G.-M. Rignanese, J. Íñiguez, and P. Ghosez, "Hybrid exchange-correlation functional for accurate prediction of the electronic and structural properties of ferroelectric oxides," *Phys. Rev. B*, vol. 77, p. 165107, Apr 2008. [Online]. Available: https://link.aps.org/doi/10.1103/PhysRevB.77.165107

[147] A. L. Companion and M. A. Komarynsky, "Crystal field splitting diagrams," *Journal of Chemical Education*, vol. 41, no. 5, p. 257, May 1964. [Online]. Available: https://doi.org/10.1021/ed041p257

[148] G. Landrum, C. Ekberg, and J. Whittaker, "A ligand field model for MCD spectra of biological cupric complexes," *Biophysical Journal*,

vol. 69, no. 2, pp. 674–689, Aug 1995. [Online]. Available: https://doi.org/10.1016/s0006-3495(95)79943-x

[149] R. Ignatans, G. Mallia, E. A. Ahmad, L. Spillane, K. A. Stoerzinger, Y. Shao-Horn, N. M. Harrison, and V. Tileli, "The effect of surface reconstruction on the oxygen reduction reaction properties of LaMnO$_3$," *The Journal of Physical Chemistry C*, vol. 123, no. 18, pp. 11 621–11 627, Apr 2019. [Online]. Available: https://doi.org/10.1021/acs.jpcc.9b00458

[150] E. K. Al-Shakarchi and N. B. Mahmood, "Three techniques used to produce BaTiO$_3$ fine powder," *Journal of Modern Physics*, vol. 02, no. 11, pp. 1420–1428, Nov 2011. [Online]. Available: https://doi.org/10.4236/jmp.2011.211175

[151] O. Bunău and Y. Joly, "Time-dependent density functional theory applied to x-ray absorption spectroscopy," *Physical Review B*, vol. 85, no. 15, Apr 2012. [Online]. Available: https://doi.org/10.1103/physrevb.85.155121

[152] G. Prandini, A. Marrazzo, I. E. Castelli, N. Mounet, E. Passaro, and N. Marzari, "A standard solid state pseudopotentials (SSSP) library optimized for precision and efficiency," 2021. [Online]. Available: https://archive.materialscloud.org/record/2021.76

[153] M. Bugnet, G. Radtke, S. Y. Woo, G.-z. Zhu, and G. A. Botton, "Temperature-dependent high energy-resolution EELS of ferroelectric and paraelectric BaTiO$_3$ phases," *Phys. Rev. B*, vol. 93, p. 020102, Jan 2016. [Online]. Available: https://link.aps.org/doi/10.1103/PhysRevB.93.020102

[154] P. E. Batson and J. Silcox, "Experimental energy-loss function, Im$[-\frac{1}{\epsilon}(q,\omega)]$, for aluminum," *Phys. Rev. B*, vol. 27, pp. 5224–5239, May 1983. [Online]. Available: https://link.aps.org/doi/10.1103/PhysRevB.27.5224

[155] P. Cerenkov, "Visible glow under exposure of gamma radiation," in *Dokl, Akad, Nauk, SSSR*, vol. 2, 1934, p. 451.

[156] I. Tamm and I. Frank, "Coherent in-medium fast-electron radiation," in *Dokl. Akad. Nauk USSR*, vol. 14, 1937, pp. 109–114.

[157] X. C. T. Ph.D, *Advanced Materials for Integrated Optical Waveguides*. Springer International Publishing, 2014. [Online]. Available: https://doi.org/10.1007/978-3-319-01550-7

[158] M. Stöger-Pollach, H. Franco, P. Schattschneider, S. Lazar, B. Schaffer, W. Grogger, and H. Zandbergen, "Čerenkov losses: A limit for bandgap determination and Kramers–Kronig analysis," *Micron*, vol. 37, no. 5, pp. 396–402, Jul 2006. [Online]. Available: https://doi.org/10.1016/j.micron.2006.01.001

156

[159] P. Konsin and B. Sorkin, "Temperature dependence of the refractive index in BaTiO$_3$ and photorefraction in perovskite oxides," *Ferroelectrics*, vol. 257, no. 1, pp. 269–274, Jan 2001. [Online]. Available: https://doi.org/10.1080/00150190108016309

[160] J. Park, S. Heo, J.-G. Chung, H. Kim, H. Lee, K. Kim, and G.-S. Park, "Bandgap measurement of thin dielectric films using monochromated STEM-EELS," *Ultramicroscopy*, vol. 109, no. 9, pp. 1183–1188, Aug 2009. [Online]. Available: https://doi.org/10.1016/j.ultramic.2009.04.005

[161] K. S. Katti, M. Qian, F. Dogan, and M. Sarikaya, "Dopant effect on local dielectric properties in barium titanate based electroceramics determined by transmission EELS," *Journal of the American Ceramic Society*, vol. 85, no. 9, pp. 2236–2243, Sep 2002. [Online]. Available: https://doi.org/10.1111/j.1151-2916.2002.tb00441.x

[162] V. Gallegos-Orozco, R. Martínez-Sánchez, and F. Espinosa-Magaña, "In situ characterization of the ferroelectric transition in BaTiO$_3$ by EELS and comparison with ab initio methods," *Phys. Rev. B*, vol. 77, p. 045128, Jan 2008. [Online]. Available: https://link.aps.org/doi/10.1103/PhysRevB.77.045128

[163] M. D. Glinchuk, E. A. Eliseev, G. Li, J. Zeng, S. V. Kalinin, and A. N. Morozovska, "Ferroelectricity induced by oxygen vacancies in relaxors with perovskite structure," *Phys. Rev. B*, vol. 98, p. 094102, Sep 2018. [Online]. Available: https://link.aps.org/doi/10.1103/PhysRevB.98.094102

[164] T. Rojac, M. Kosec, B. Budic, N. Setter, and D. Damjanovic, "Strong ferroelectric domain-wall pinning in BiFeO$_3$ ceramics," *Journal of Applied Physics*, vol. 108, no. 7, p. 074107, Oct 2010. [Online]. Available: https://doi.org/10.1063/1.3490249

[165] Y. Noguchi, H. Matsuo, Y. Kitanaka, and M. Miyayama, "Ferroelectrics with a controlled oxygen-vacancy distribution by design," *Scientific Reports*, vol. 9, no. 1, Mar 2019. [Online]. Available: https://doi.org/10.1038/s41598-019-40717-0

[166] M. Choi, F. Oba, and I. Tanaka, "Electronic and structural properties of the oxygen vacancy in BaTiO$_3$," *Applied Physics Letters*, vol. 98, no. 17, p. 172901, Apr 2011. [Online]. Available: https://doi.org/10.1063/1.3583460

[167] H. Donnerberg and A. Birkholz, "Ab initiostudy of oxygen vacancies in BaTiO$_3$," *Journal of Physics: Condensed Matter*, vol. 12, no. 38, pp. 8239–8247, Sep 2000. [Online]. Available: https://doi.org/10.1088/0953-8984/12/38/301

[168] R. Scharfschwerdt, A. Mazur, O. F. Schirmer, H. Hesse, and S. Mendricks, "Oxygen vacancies in BaTiO$_3$," *Physical Review B*, vol. 54, no. 21, pp. 15 284–15 290, Dec 1996. [Online]. Available: https://doi.org/10.1103/physrevb.54.15284

[169] J. Vinson, J. J. Rehr, J. J. Kas, and E. L. Shirley, "Bethe-Salpeter equation calculations of core excitation spectra," *Phys. Rev. B*, vol. 83, p. 115106, Mar 2011. [Online]. Available: https://link.aps.org/doi/10.1103/PhysRevB.83.115106

Curriculum Vitae

Reinis Ignatans

École polytechnique fédérale de Lausanne, MXD 220 (Bâtiment MXD) Station 12, Lausanne, CH-1015, Switzerland.

Phone number: (+41) 787 238 597, (+371) 28 345 386
e-mail: reinis.ignatans@epfl.ch, reinis.ignatans@gmail.com

ResearchGate: https://www.researchgate.net/profile/Reinis-Ignatans
ORCID: 0000-0002-0871-4994

Education

[01/09/2017 - Current] **PhD Studies - Materials Science**

- École Polytechnique Fédérale de Lausanne (EPFL)
  https://www.epfl.ch/en/
  EPFL STI IMX INE, Station 12, CH-1015, Lausanne, Switzerland

[01/09/2013 – 01/06/2015] **Master's Degree in Physics**

- University of Latvia
  https://www.lu.lv/
  Raiņa bulvāris, 19, LV-1586, Riga, Latvia

[01/09/2010 – 01/06/2013] **Bachelor's degree - Physics**

- University of Latvia
  https://www.lu.lv/
  Raiņa bulvāris, 19, LV-1586, Riga, Latvia

Work experience

[01/09/2017 - Current] **PhD Student/Scientific Assistant**

- **École Polytechnique Fédérale de Lausanne (EPFL)**
  City: Lausanne
  Country: Switzerland

  Main activities and responsibilities:
  Study of ferroelectric materials with in situ Transmission electron microscopy techniques. Focused ion beam (FIB) machining. Teaching - Thermodynamics for materials science.

[01/10/2015 – 01/06/2017] **Scientific Assistant**

- **Institute of Solid State Physics - University of Latvia**
  City: Riga
  Country: Latvia
  Main activities and responsibilities:

  X-Ray Diffraction (XRD) measurements and analysis, crystal structure refinement. Elemental composition determination with X-Ray Fluorescence (XRF). Scanning Electron Microscopy (SEM).

[01/10/2011 – 01/10/2015] **Engineer**

- **Institute of Solid State Physics - University of Latvia**
  City: Riga
  Country: Latvia
  Main activities and responsibilities:

  Upkeep and maintenance of X-ray diffractometer. X-ray diffraction measurements.

Language skills

Mother language: Latvian

Other Languages:

- **English**
  Listening C2 | Reading C2 | Writing C2 | Spoken production |
  C2 Spoken interaction C2

- **Russian**
  Listening C2 | Reading C1 | Writing A2 | Spoken production B2 |
  Spoken interaction B2

- **German**
  Listening B1 | Reading B1 | Writing B1 | Spoken production B1 |
  Spoken interaction B1

Digital skills

- **Programming Languages**
  Mathematica | C | Python

- **Word processing and Office Skills**
  Linux | Windows | LaTeX | Origin | MS Word | MS Excel | MS Powerpoint

- **X-Ray Diffraction**
  Profex | FullProf

- **Electron Microscopy**
  GMS | Dr. Probe | JEMS | QSTEM | Image Processing (ImageJ, GIMP)

- ***Ab Initio* Simulation Software**
  Quantum Espresso | FDMNES | GAMESS

- **Finite Element Calculations**
  FEMM | COMSOL

- **Crafts and Hardware**
  Fusion 360 | Arduino

Work related skills

- **Transmission Electron Microscopy (TEM)**
  Extensive experience of running FEI/Thermo Fisher transmission electron microscopes. Hands on experience on operating double C_s corrected ThermoFisher Titan Themis. Experience of running complex *in situ* TEM measurements with applied electric field, heating and cooling.

  Electron Energy Loss Spectroscopy (EELS) measurements, analysis and spectral simulations from the first principle calculations.

  Automatic image analysis with custom made scripts.

- **Focused Ion Beam (FIB) machining**
  Knowledge of FIB sample preparation for TEM measurements. Extensive experience of complex sample preparation for *in situ* measurements based on the microelectromechanical system (MEMS) chips.

- **Microstructure and composition**
  Hands on experience with Scanning Electron Microscope (SEM) equipped with Energy-Dispersive X-Ray Spectrometer (EDS) and the analysis of the data. Knowledge of sample preparation for the SEM-EDS measurements. Experience with quantitative X-Ray Fluorescence measurements and analysis.

- **X-Ray diffraction**
  Several years experience of running and maintaining an XRD machine. Crystal structure refinement from the powder diffraction data with Rietveld method. Quantitative phase analysis. *In situ* XRD measurements (electrical field, heating/cooling).

- **Computer Skills**
  Knowledge of several programming and scripting languages, which I use for automatic data analysis of large data quantities. Knowledge and understanding of first principle (ab initio) calculations and working mechanisms. Simulation of EELS and X-ray Absorption (XAS) spectra from first principles.

Selected publications

- **Individual Barkhausen Pulses of Ferroelastic Nanodomains**
  https://doi.org/10.1103/PhysRevLett.127.167601
  R. Ignatans, D. Damjanovic, and V. Tileli, *Phys. Rev. Lett.* **127**, 167601 (2021).

- **Local hard and soft pinning of 180° domain walls in BaTiO₃ probed by *in situ* transmission electron microscopy**
  https://doi.org/10.1103/PhysRevMaterials.4.104403
  R. Ignatans, D. Damjanovic, and V. Tileli, *Phys. Rev. Mater.* **4**, 104403 (2020).

- **The Effect of Surface Reconstruction on the Oxygen Reduction Reaction Properties of LaMnO₃**
  https://doi.org/10.1021/acs.jpcc.9b00458
  R. Ignatans, G. Mallia, E.A. Ahmad, L. Spillane, K. A. Stoerzinger, Y. Shao-Horn, N. M. Harrison, and V. Tileli, *J. Phys. Chem. C* **123**, 11621 (2019).

- **Novel octahedral tilt system a⁺ b⁺ c⁺ in (1-x)Na₀.₅Bi₀.₅TiO₃ - xCdTiO₃ solid solutions**
  https://doi.org/10.1007/s10853-017-0950-8
  R. Ignatans, M. Dunce, E. Birks, and A. Sternberg, *J. Mater. Sci.* **52**, 7149 (2017).

- **Structured nanoscale metallic glass fibres with extreme aspect ratios**
  https://doi.org/10.1038/s41565-020-0747-9
  W. Yan, I. Richard, G. Kurtuldu, N.D. James, G. Schiavone, J.W. Squair, T. Nguyen-Dang, T. Das Gupta, Y. Qu, J.D. Cao, R. Ignatans, S.P. Lacour, V. Tileli, G. Courtine, J.F. Löffler, and F. Sorin, *Nat. Nanotechnol.* **15**, 875 (2020).

- **Structure and dielectric properties of Na₀.₅Bi₀.₅TiO₃-CaTiO₃ solid solutions**
  https://doi.org/10.1063/1.4942221
  E. Birks, M. Dunce, R. Ignatans, A. Kuzmin, A. Plaude, M. Antonova, K. Kundzins, and A. Sternberg, *J. Appl. Phys.* **119**, 074102 (2016).

- **Full publication list:**
  https://orcid.org/0000-0002-0871-4994

Confrences and seminars

[01/12/2019 – 06/12/2019] **MRS 2019 Fall Meeting** Boston, USA

- Talk: "An *In Situ* Electron Microscopy Study of Nanodomain Polarization-Electric Field Curves in $BaTiO_3$"

[14/07/2019 – 19/07/2019] **F2Cp2 Joint Conference - European Meeting on Ferroelectricity** Lausanne, Switzerland

- Poster: Structural and chemical characterization of $BaTiO_3$ phases - from low to high temperatures.
  Best poster award by Institute of Electrical and Electronics Engineers (IEEE).

[24/04/2017 – 27/04/2017] **Functional Materials and Nanotechnology (FM&NT) 2017** Tartu, Estonia

- Guest

[28/06/2015 – 03/07/2015] **European Meeting on Ferroelectricity 2015** Porto, Portugal

- Co-author of poster: "Phase transitions in $Na_{0.5}Bi_{0.5}TiO_3$ - $(Sr_{0.7}Bi_{0.2})TiO_3$-$PbTiO_3$ solid solutions".

Hobbies and interests

- Ultimate Frisbee
  I have played Ultimate Frisbee for 15 years, Staff member of World Junior Ultimate Championship 2010 (Heilbronn, Germany). Nowadays I enjoy training new members of the community and social games.

- Electric Guitar
  Self taught guitar player. Additionally, I use my knowledge of electronics to make guitar amplifiers and effect pedals.